



Bernhard Gadermaier, MSc

**Li<sup>+</sup> ion dynamics in glassy, crystalline, and amorphous biotemplated  
solids for energy storage systems**

**DOCTORAL THESIS**

to achieve the university degree of  
Doktor der technischen Wissenschaften

submitted to

**Graz University of Technology**

**Supervisor**

Univ.-Prof., Martin Wilkening

Institute of Chemistry and Technology of Materials

Graz, June 2021

## **AFFIDAVIT**

I declare that I have authored this thesis independently, that I have not used other than the declared sources/resources, and that I have explicitly indicated all material which has been quoted either literally or by content from the sources used. The text document uploaded to TUGRAZonline is identical to the present doctoral thesis.

---

Date, Signature



## Abstract

The movement of our society from its dependence on fossil fuels to regenerative energy sources is tightly associated with the movements of ions in the solid-state. In typical mobile energy storage devices such as Li-ion batteries (LIB), these ions must move to allow efficient energy storage and they must be able to move fast to allow fast energy release and storage. This diffusion or conduction of the mobile  $\text{Li}^+$  ions was studied primarily by impedance spectroscopy but also by NMR relaxation measurements to gain a deeper understanding of the basic relations dictating fast ion diffusion in glassy, crystalline, and amorphous materials with ionic conductivity. While high-energy ball milling decreases the diffusivity in some solid electrolytes (SE) such as a high-entropy-glass like petalite ( $\text{LiAlSi}_4\text{O}_{10}$ ), it increased it by orders of magnitude in the model compound  $\text{LiTaO}_3$ . Solid electrolytes additionally need to be excellent electronic insulators; a property that was determined for the fast ion conductor LLZO. Finally, the Li diffusion was also studied in electrode active materials that need to store and release the ions as quickly as possible. While in the conventional anode material  $\text{Li}_4\text{Ti}_5\text{O}_{12}$ , indications for a universal fast diffusion process were found, the conductivity of the environmentally friendly cathode active material  $\text{LiFePO}_4$  was assessed. Using a viral template, a low-energy consuming synthesis route gave way to a promising cathode material in the shape of nanowires.

## Kurzfassung

Die Bewegung unserer Gesellschaft von ihrer Abhängigkeit von fossilen Brennstoffen zu regenerativen Energiequellen ist eng mit der Bewegung von Ionen in Festkörpern verbunden. In typischen mobilen Energiespeichern wie Li-Ionen-Batterien (LIB) müssen sich diese Ionen bewegen, um eine effiziente Energiespeicherung zu ermöglichen, und sie müssen sich schnell bewegen können, um eine schnelle Energiefreisetzung und -speicherung zu ermöglichen. Diese Diffusion oder Leitung der mobilen  $\text{Li}^+$ -Ionen wurde hauptsächlich mittels Impedanzspektroskopie, aber auch durch NMR-Relaxationsmessungen untersucht, um ein tieferes Verständnis der grundlegenden Beziehungen zu erhalten, die eine schnelle Ionendiffusion in glasartigen, kristallinen und amorphen Materialien mit Ionenleitfähigkeit ermöglichen. Während das Hochenergie-Kugelmahlen das Diffusionsvermögen von  $\text{Li}^+$  in einigen Festelektrolyten (SE) wie dem hochentropischen, gläsernen Petalit ( $\text{LiAlSi}_4\text{O}_{10}$ ) verringert, erhöht es dieses in der Modellverbindung  $\text{LiTaO}_3$  um Größenordnungen. Festelektrolyte müssen außerdem hervorragende elektronische Isolatoren sein; eine Eigenschaft, die für den schnellen Ionenleiter LLZO bestimmt wurde. Schließlich wurde die Li-Diffusion auch in den elektrochemisch aktiven Materialien der Elektroden untersucht, die die Ionen so schnell wie möglich speichern und freisetzen müssen. Während im herkömmlichen Anodenmaterial  $\text{Li}_4\text{Ti}_5\text{O}_{12}$  Hinweise auf einen universellen schnellen Diffusionsprozess gefunden wurden, wurde die Leitfähigkeit des umweltfreundlichen Kathodenmaterials  $\text{LiFePO}_4$  untersucht. Unter Verwendung einer viralen Matrize führt ein energiearmer Syntheseweg zu einem vielversprechenden Kathodenmaterial in der Form von Nanodrähten.



## Table of content

1	Introduction.....	1
2	Theory and Methods.....	4
2.1.	Different kinds of solids.....	4
2.1.1.	Crystalline materials.....	5
2.1.1.	Amorphous or glassy.....	5
2.1.2.	Defects.....	7
2.2.	Diffusion.....	10
2.2.1.	Diffusion mechanisms.....	13
2.2.2.	Diffusion in the solid state.....	14
2.3.	Impedance spectroscopy.....	17
2.3.1.	Basics of impedance spectroscopy.....	18
2.3.2.	(Di)electric relaxation.....	23
2.3.3.	The effective medium theory.....	26
2.3.4.	Polarisation effects.....	27
2.3.5.	Charge carrier density and velocity.....	27
2.3.6.	Interpretation of the results.....	32
2.4.	Structural characterization.....	35
2.4.1.	X-ray powder diffraction.....	36
2.4.2.	Extended X-ray Absorption Fine Structure (EXAFS).....	38
2.5.	Positron Annihilation Lifetime Spectroscopy (PALS).....	41
2.6.	Synthesis of solids via precipitation.....	43
2.7.	Microbiological and molecular biological methods.....	46
2.7.1.	The bacteriophage M13.....	46
2.7.2.	Cultivation of <i>E. coli</i> and amplification of M13.....	48

2.7.3.	Cloning and genetic engineering.....	50
2.7.4.	Culture media, buffer solutions and general stock solutions.....	54
3	Results and Discussion.....	56
3.1.	Glass in Two Forms: Heterogeneous Electrical Relaxation in Nanoglassy Petalite .....	57
3.2.	Influence of defects on ionic transport in $\text{LiTaO}_3$ – a study using EXAFS and positron annihilation lifetime spectroscopy.....	72
3.3.	The Electronic Conductivity of Single Crystalline Ga-Stabilized Cubic $\text{Li}_7\text{La}_3\text{Zr}_2\text{O}_{12}$ — A Technologically Relevant Parameter for All-Solid-State Batteries .....	83
3.4.	Fast $\text{Li}^+$ transport in $\text{Li}_4\text{Ti}_5\text{O}_{12}$ — Conductivity spectroscopy reveals two distinct Li ion dynamic processes in lithium pentatitanate .....	98
3.5.	NMR spectroscopic investigations into the $\text{Li}^+$ dynamics of $\text{Li}_4\text{C}_{60}$ .....	120
3.6.	Nanostructured M13 bio templated amorphous $\text{FePO}_4$ as green cathode for Li-ion batteries .....	137
4	Conclusion and Outlook.....	160
5	Appendix.....	164
5.1.	Equipment.....	164
5.2.	Software.....	166
5.3.	List of Publications .....	167
6	Bibliography: .....	171





# 1 Introduction

---

We live in a very energy demanding society. Most of this energy is provided by the combustion of fossil fuels.<sup>3</sup> While the high energy density of these fuels made them an attractive choice, the conversion of the energy from chemical to mechanical and electrical energy, the one that is needed the most by our society, is possible only with low efficiency.<sup>4</sup> Whereas thermal energy released during the combustion in stationary systems may be used in a profitable way, this is not the case in automotive applications. A large fraction of the chemically stored energy is simply lost in the form of heat while exhaust gases and nanoparticles pollute our atmosphere.

A possible mitigation strategy is offered by the electrification of the automotive sector, *i.e.* the exchange of combustion engines to electric motors, the replacement of the gear box with a battery pack of similar weight. Here, the Li-ion batteries (LiB), a technology commercialized by Sony in 1991, are anticipated to be the key technology. These batteries have been continuously developed and improved since their commercialization to increase their energy density, their power and most importantly, their safety. In this continuous development, we saw a transition from generation 1 batteries to the currently employed generation 3 batteries with much higher energy density. However, with their increasing energy density, despite ongoing improvements, their hazardousness has also increased. Especially, in the automotive sector, where accidents may exert incredible forces on batteries, the safety aspect of the battery has become more important than ever.

A significant increase in safety as well as energy density is believed to be achievable if the liquid electrolyte, currently employed in LiB, is replaced by a solid electrolyte (SE). Since the liquid electrolyte is based on flammable organic solvents, overheating of a battery may result in ignition of the volatile components. While the solid inorganic electrolytes significantly reduce the risk of ignition, they are also envisaged to even then function properly if metallic lithium, with its superior energy density, is employed.

When replacing the liquid with a solid electrolyte, and the ion storing anode with a metallic lithium anode, several new problems arise. These problems range from the processing of the materials to the chemical and electrochemical stability of the materials at every interface. Processing might be significantly eased if glassy, or amorphous, materials, which do not suffer from highly resistive grain

boundaries, are used. These materials will show bulk-like properties even if simple isostatic pressing is used and may even be obtained in the desired shape directly from the melt (see publication 1). Other problems arise from the chemical incompatibility due to for example interdiffusion of transition metals from the active materials into the solid electrolyte.<sup>5</sup> To overcome such problems specific coating materials, such as  $\text{LiTaO}_3$  may be applied as diffusion-inhibiting layers.<sup>6</sup> Obviously, such layers have to permit Li ion diffusion and will most likely be very defect rich. While ionic conductivity is very low in  $\text{LiTaO}_3$ , introducing defects significantly increases this value by many orders of magnitude. Most importantly, we found that the ionic-conductivity increasing bond-disorder is rather insensitive to thermal annealing which may be necessary in all-solid-state battery (ASSB) production<sup>7-9</sup> (see publication 2).

However, even if many challenges are eased by specific processing and coating procedures, others are even less clearly defined. The influence of electronic conductivity in solid electrolytes is a unique problem to ASSB compared to conventional LiB as the electronic conductivity in liquid electrolytes is many orders of magnitude lower than the corresponding ionic conductivity. As the electronic conductivity in practically any ionic conductor is a quantity sensitive to many parameters and influences such as impurities, defects and any kind of discontinuity in the materials, we chose a single crystal to estimate the electronic conductivity in a well-studied representative oxide-based solid electrolyte. While SE employed in ASSB will be polycrystalline, we see the electronic conductivity in the single crystal as a lower limit obtainable in the pure material. Such information is important and has to be considered in strategies focusing on reducing the thickness of the SE (see publication 3). Clearly, also new classes of solid electrolytes have to be investigated and their properties have to be studied in order to find even better suited materials. Such an example is represented by the peculiar lithium Buckminster fullerenes ( $\text{Li}_4\text{C}_{60}$ ) which show a rather complex ion dynamic (see draft 1).

If we now turn our considerations to ASSB with lithium metal anodes, we realize the fact that every active material currently used in LiB is a cathode. Therefore, also the currently employed anode materials such as  $\text{Li}_4\text{Ti}_5\text{O}_{12}$  (LTO) have to be considered as cathodes if used in combination with metallic lithium. Interestingly, especially LTO is known as a power electrode active material as its electrochemical kinetic is incredibly fast. Together with nanosized carbon coated  $\text{LiFePO}_4$ , it forms a well-known power couple enabling batteries with incredibly high charging rates of up to 10C.<sup>10</sup>

Intriguingly, the starting material,  $\text{Li}_4\text{Ti}_5\text{O}_{12}$  was shown to have a very poor conductivity, in terms of ionic as well as in terms of electronic conductivity. Considering the poor conductivity, it is surprising that this material offers such fast reaction kinetics.<sup>11</sup> We revisited this state of the active material and took another, closer look on the ionic conductivity in that material (see draft 2). Nevertheless, such a material would give rise to a very low cell voltage of about 1.5 V.<sup>12</sup> Other active materials offer much higher voltages vs lithium. However, cobalt containing active materials are less likely to be used in the future due to increasing socioeconomic cost and limited availability of cobalt.<sup>13</sup> High-voltage spinels such as manganese-oxides on the other hand are less stable and may thus pose critical safety issues for the batteries.<sup>14</sup> Thus, these materials are either potentially very hazardous, directly or indirectly by poisoning the environment, or not sustainable, neither environmentally nor financially.

The probably most benign active material is  $\text{LiFePO}_4$ .<sup>15</sup> Its constituents are very abundant in the earth's crust, and they are not toxic (except  $\text{FePO}_4$  is a molluscicide, *i.e.*, it is toxic for snails). However, if used in combination with metallic lithium it could be helpful to use the oxidized form,  $\text{FePO}_4$ , in order to produce charged Li-metal cells. However,  $\text{LiFePO}_4$  has its own drawbacks which are its very low ionic conductivity as well as its low electronic conductivity. Without carbon-coating, this material is, due to its two-phase behaviour<sup>16-19</sup> in its crystalline state, almost uncyclable within reasonable timeframes.<sup>20</sup> Furthermore, the very flat voltage plateau poses a critical problem in estimating the state-of-charge (SOC) of a cell.<sup>21</sup> We synthesised amorphous  $\text{FePO}_4$ , which shows a gradual change of voltage with SOC. Using a bio template, we could achieve the synthesis of nanowires of this active material. Surprisingly, this material could be cycled very well in its amorphous form without the need for additional carbon coating (see draft 3).

## 2 Theory and Methods

---

This chapter will give a brief introduction of the classes of materials and biological templates used within this thesis. Furthermore, the most important methods used to study those materials will be briefly discussed. In addition to that, the most important theories and concepts used to interpret the obtained data will be introduced.

### 2.1. Different kinds of solids

The basic characteristic of a solid is that its form does not change freely in order to fill an empty space. In the solid state, the atoms are confined to local potential minima with time-invariant locations. However, the atoms oscillate around their equilibrium position with temperature dependent amplitudes. In rare cases, the energy of an atom will be so high that its oscillation amplitude exceeds the size of its potential well resulting in the atom leaving its current site. The atom may encounter another local energy minimum and reside in it. This is the fundamental aspect of diffusion in solids and will be treated in chapter 2.2. The rigid nature of the solid state is its

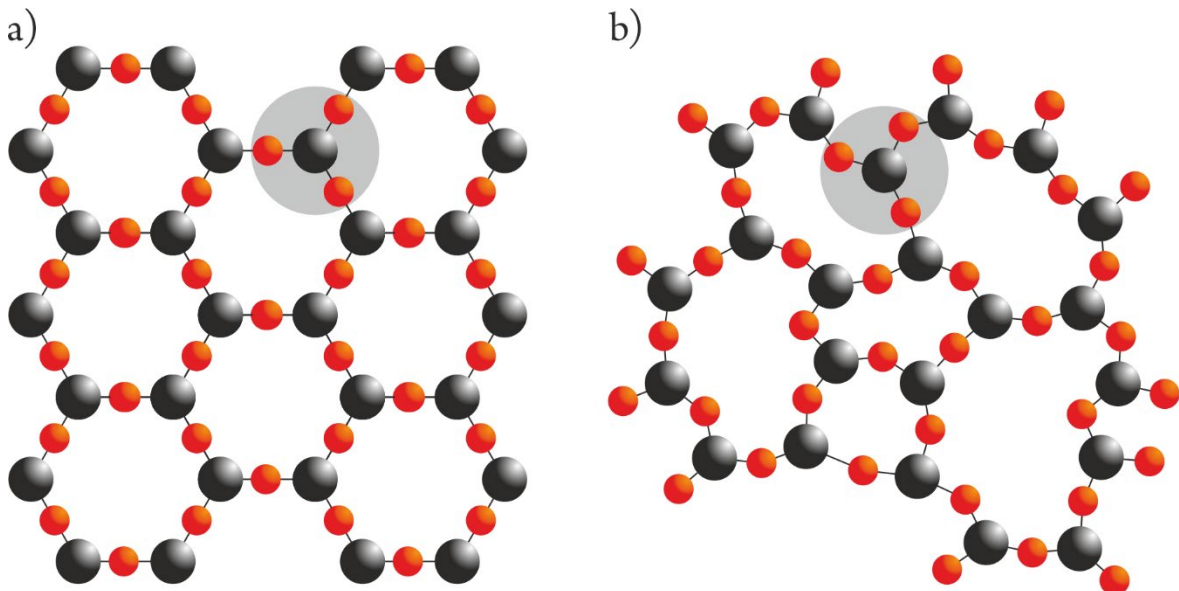


Figure 1: Schematic representation of fictive  $A_2O_3$  in its crystalline state (a) and in its glassy state. Note that the average interatomic distance is similar in both. Furthermore, both states show characteristic short-range order in the form of  $AO_3$  triangles (highlighted by grey circles). Large black circles represent the cations ( $A^{3+}$ ) and small red circles represent oxygen ( $O^{2-}$ ). After W. H. Zachariasen.<sup>1</sup>

essential characteristic whereas we will distinguish between solids with a microscopic long-range order (crystals) and those without a long-range order (glasses), see Figure 1.

Albeit the atomic long-range order is only present in the crystalline state, it is important to note that the short-range order is present and almost identical in both the crystalline and the glassy state. Most importantly, this short-range order is also present in the liquid state due to the chemical bonding of the atoms. In the following subsections details about the crystalline and glassy state will be given followed by the introduction of the basic concepts of defects in solids.

### 2.1.1. Crystalline materials

Crystalline materials certainly belong to the most important materials in our world. They fascinate us in the form of diamonds, garnets and rubies by their beauty. They are important components of our skeleton and protect our teeth from degradation. Crystalline materials also shape our world as minerals in the form of mountains. What all these representatives of crystalline materials have in common is the nature of their microscopic atomic arrangement. The nature of a crystalline solid is that the constituent atoms have a well-defined arrangement extending over many nearest neighbours. Due to this long-range repetitive ordering, the organization can be reduced to a unique repetitive unit, the unit cell. A crystalline solid constitutes a distinct phase with well-defined thermodynamic properties depending on the respective modification. The influence of the atomic arrangement, *i.e.*, the crystal structure is of tremendous importance for the diffusion of atoms and the discussion of diffusion will be exemplified on a simple crystal structure in chapter 2.2. It is important to note that most of the solid ion conductors are crystalline materials. As the atomic arrangement is well defined and periodic, also the potential wells in which the ions reside are very similar and the energy barrier separating these wells is rather homogeneous.

### 2.1.2. Amorphous or glassy

Glasses are part of our everyday life. They help people suffering from ametropia see clearly. They let light pass into our offices and living rooms while keeping the warmth in. Glasses are essentially solids in terms of rigidity but similar to liquids in terms of local atomic arrangement. Glasses are per definition a supercooled liquid. The first coordination shell of an atom or ion in a glass resembles

that of the one found in crystals (see Figure 1). This is not surprising as the interatomic forces pose certain restrictions to the microscopic arrangement of atoms and ions. Therefore, the interatomic distances in a specific material are similar in its glassy state and in its crystalline state but also in the liquid state. However, in the glassy state, the interatomic distances are subjected to a broader distribution than in the crystalline state. Furthermore, the bond angles show a much greater variation in glasses compared to crystals. It is this distribution of bond-lengths and bond-angles that reflects the major microscopic difference between a material in its glassy and crystalline state. This distribution is thermodynamically not stable but the relaxation to the thermodynamical stable configuration, *i.e.*, the crystallization, is hindered by slow kinetics.

As mentioned above, a glass is metastable, and its Gibbs free energy depends on the thermal history and on the cooling-rate used to obtain it.<sup>22,23</sup> The general phase transformation from the liquid state to the crystalline and glassy state is exemplarily shown in Figure 2a. In the liquid state, the entropy is highest. Allowing the liquid to slowly cool leads to crystallization whereby the heat of fusion is released. The process of crystallization requires the formation of nuclei, a process that takes time. Therefore, crystallization is not only a matter of thermodynamics but also a matter of kinetics. If the liquid is cooled fast enough, *i.e.*, so fast that the atoms are “frozen” in their momentary position, the obtained solid resembles the liquid state in its short-range order. Albeit cooling rates may be very

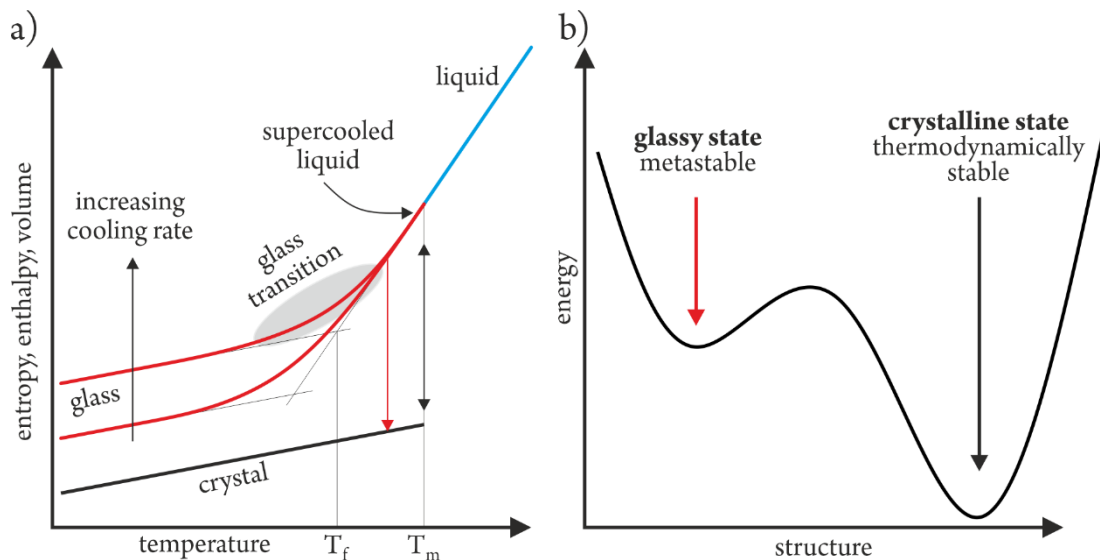


Figure 2: Glass-transition (a) and relation between the structure and the state (b). If a melt is cooled slowly, it arrests and crystallizes by a first order phase transition. If the cooling process is sufficiently fast a supercooled liquid is obtained. Importantly, the properties of the glass depend on the cooling rate. b) The glassy state is metastable and the glass in general has a higher free energy than the thermodynamically stable crystalline state does. After Chandra et al.<sup>2</sup>

high, up  $10^6$  K/sec<sup>24</sup> some relaxation of the atomic arrangement, will take place, *i.e.*, a shift of the atoms equilibrium positions to their thermodynamically most stable positions, and thus, the properties of the glass depend on the thermal history.

A glass obtained by melt quenching will be metastable, *i.e.*, it is characterized by a higher Gibbs free energy than its crystalline counterpart (see Figure 2b). This is important as it will also affect diffusion in the glass as we will see in the example of petalite (see P1). It is well known that a glass will relax if heated near to its glass transition temperature and if cooled again will show slightly different properties than before. Such a relaxation will lead to changes of the fictive temperature ( $T_f$ ) which is used to describe a glass by thermodynamic means;  $T_f$  also marks the transition from the liquid to the solid (glassy) state, *i.e.* the temperature at which the melt was “frozen”.<sup>25</sup> Relaxation of a glass is accompanied by a decrease of the Gibbs free energy and this has implications for the diffusion of ions in a glass. For example, the diffusion of  $\text{Ag}^+$  ions in silver metaphosphate ( $\text{AgPO}_3$ ) is decreased after the glass is annealed slightly below its glass transition.<sup>23</sup>

### 2.1.2. Defects

Defects in crystals refer to deviations from the ideal crystal structure. As they are defined with respect to the crystal structure, one would assume that defects only exist in a crystalline solid but not in amorphous or glassy materials. However, defects are also present in amorphous materials where they exist in the form of missing bond partners (vacancies). Apart from the missing of atoms which is known as vacancy, the displacement of atoms, by lengths smaller than their diameter, may also be considered as a defect, known as bond disorder.

As there are many different forms of defects it is useful to categorize them by their extent in dimensions as well as by their cause, *i.e.* intrinsic and extrinsic defects. Defects may be zero dimensional (0D), 1D, 2D and even 3D. For diffusion in the bulk, the 0D defects (point defects) are probably the most important ones. However, also dislocations (1D defects) and grain boundaries (2D defects) may serve as pathways for diffusion. Voids and larger agglomerates of 0D defects can be considered as 3D defects. Apart from their extension in terms of dimensions and scale, is also helpful to distinguish between intrinsic and extrinsic defects. Intrinsic defects are present even in pure single crystals and their appearance in the form of point-defects is thermodynamically driven. Extrinsic defects may be introduced by incorporation of foreign atoms



in the crystal structure or by processing. Aliovalent doping for example will lead to the formation of vacancies or interstitials; as a result of electroneutrality. By processing, however, also more complex defect types will be introduced which also include higher dimensional defects. One common way to introduce defects into crystalline materials is high-energy ball-milling.<sup>26-28</sup>

Point defects are by far the most important class of defects in crystalline solids associated with diffusion. Point defects are intrinsic to any real crystal as their presence, up to certain concentrations, leads to a decrease of the free energy (see Figure 3a). Creating a vacancy requires energy,  $\Delta H_f$ , but increases the configurational entropy,  $\Delta S_c$  and thus, according to the Gibbs-Helmholtz equation, decreases the free energy of the system.

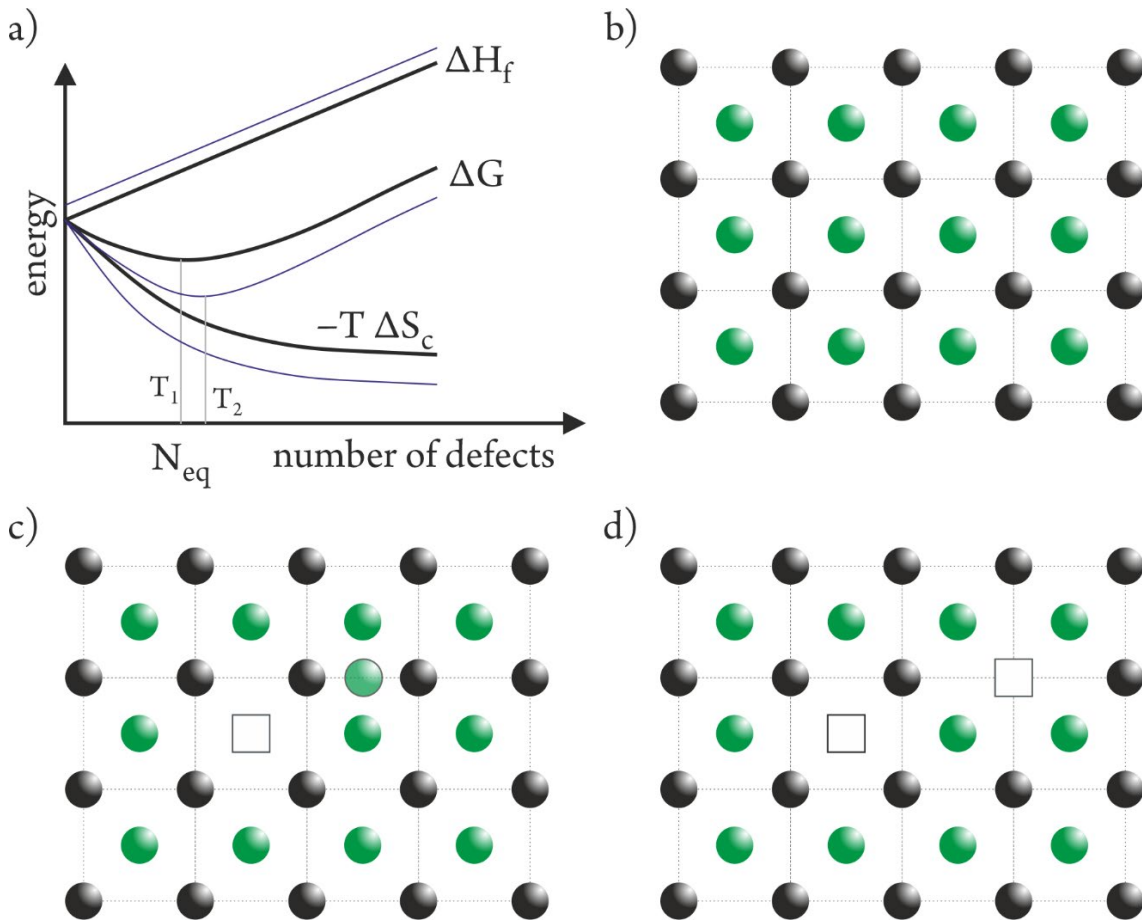


Figure 3 a) Thermodynamic equilibrium defect concentration. b) Defect-free face-centred cubic crystal lattice. c) A cation is misplaced at an interstitial position in the lattice (Frenkel defect). d) A cation and an anion are lacking (Schottky defect).

In a perfect crystal, *i.e.* without any defects (see Figure 3b) the interatomic distance is equal between every pair of atoms and all sites are occupied. As outlined above, in thermodynamic equilibrium, a crystal always contains some defects, more so at higher temperatures (see Figure 3a). Among the

most common types of point defects are the Frenkel and Schottky defects as exemplarily shown in Figure 3c and d, respectively. These two types of point defects are referred to as intrinsic defects as they do not change the stoichiometry of the crystal. In contrast, extrinsic defects are associated with a certain level of non-stoichiometry.<sup>29</sup>

For point defects, it is useful and common to use the Kroeger-Vink notation<sup>30</sup>. According to this notation, every species (M) in a crystal is accompanied by a subscript (S), indicating its site on the crystal lattice, and a superscript (C) that indicates the uncompensated, site-dependent electric charge. Some examples are presented in the following for a NaCl crystal doped by CaCl<sub>2</sub>.  $\text{Na}_{\text{Na}}^{\times}$  represents a Na ion in the correct position and thus the relative charge is 0; denoted by the superscript x. A calcium ion in a Na ion position is represented by  $\text{Ca}_{\text{Na}}^{\cdot}$  where the superscript indicates the excess positive charge. Electroneutrality demands charge compensation and thus the incorporation of the divalent cation Ca will create a vacancy  $\text{V}_{\text{Na}}^{\prime}$  with an excessive negative charge. A Frenkel defect as shown in Figure 3a is represented by  $\text{Na}_{\text{Na}}^{\times} \rightarrow \text{V}_{\text{Na}}^{\prime} + \text{Na}_{\text{i}}^{\cdot}$  where the Na ion moved from its regular lattice site to an interstitial site creating a vacancy. Note that the interstitial site is characterized by an excessive positive charge while the vacancy shows an excessive negative charge. Similarly, a Schottky defect as shown in Figure 3b is represented by  $\text{nil} \rightarrow \text{V}_{\text{Na}}^{\prime} + \text{V}_{\text{Cl}}^{\cdot}$ . Especially in transition metal oxides such as Li<sub>4</sub>Ti<sub>5</sub>O<sub>12</sub> oxygen vacancies may be created at elevated temperatures and low oxygen partial pressure according to:  $\text{O}_{\text{O}}^{\times} \rightarrow \text{V}_{\text{O}}^{\ddot{\cdot}} + 2e^{\prime} + \frac{1}{2}\text{O}_2$ . Additionally, the oxidation state of certain constituent elements might be changed and could be considered as a defect.

## 2.2. Diffusion

Diffusion is a term characterizing the movement of single particles (molecule, atom, etc.) in the most general case. It is a fundamental phenomenon present in any state of matter. The models developed to describe diffusion do not only apply to the microscopic motion but also to macroscopic motion. Self-diffusion is a randomized process with no net flux and is based on Brownian motion.<sup>31</sup> Diffusion may also be gradient-driven. However, while gradient driven diffusion will eventually cease, self-diffusion will continue.

The gradient of a concentration, a chemical or an electrochemical potential is the driving force of diffusion and eventually leads to an equilibrium and thus a minimum of energy in the system. This very simple but nonetheless very important fact relates the flux of particles to the gradient and was formalized by A. Fick as the first law of diffusion.

$$J = -D \cdot \nabla c \quad (1)$$

where  $J$  is the flux,  $D$  is the diffusion coefficient and  $\nabla c$  is the concentration gradient. If considered for only one dimension, the equation simplifies to (see Figure 4a)

$$J_x = -D \cdot \frac{dc}{dx} \quad (2)$$

Fick's second law of diffusion can be derived from the first law of diffusion when considering the conservation of mass.

$$\frac{\partial c}{\partial t} = -\nabla J = -\nabla(-D \cdot \nabla c) = -D \cdot \Delta c \quad (3)$$

where  $\Delta$  is the Laplace operator. For the one-dimensional case Fick's second law reads

$$\frac{\partial c}{\partial t} = -\frac{\partial}{\partial x} J = -\frac{\partial}{\partial x} \left( -D \cdot \frac{\partial c}{\partial x} \right) = -D \cdot \frac{\partial^2 c}{\partial x^2} \quad (4)$$

If the diffusing species is an ion, also electric forces will influence its behaviour. The dependency of the electric field and ionic movement is well described by the Nernst-Planck equation:

$$J = -D \cdot \left( \nabla c + \frac{cz\theta E}{k_B T} \right) \quad (5)$$

Here  $c$ ,  $z$ ,  $e$  and  $E$  denote the concentration, the valence of charge, the elementary charge and the electric field, respectively.  $k_B$  and  $T$  denote Boltzmann's constant and the absolute temperature. This can be interpreted as an electric field creating and sustaining a concentration gradient and vice-versa.

While the flux linearly depends on the concentration gradient, it has an exponential temperature dependence. The diffusion coefficient is generally temperature dependent and usually follows the well-known Arrhenius law:

$$D = D_0 \cdot \exp\left(\frac{-\Delta H_m}{k_B T}\right) \quad (6)$$

with  $D_0$  and  $\Delta H_m$  being the pre-exponential factor and the activation enthalpy of migration (activation energy,  $E_m$ ). Plotting the logarithm of the diffusion coefficient at different temperatures, vs. the inverse temperature, gives a straight line (see Figure 4b). From the slope of this line, the activation enthalpy of migration is obtained. Extrapolation of this line to  $1/T \rightarrow 0$  yields the pre-exponential factor. It is important to note that  $D \propto \exp\left(\frac{\Delta G}{k_B T}\right)$  where  $\Delta G = \Delta H - T\Delta S$  is the Gibbs free energy of activation. It follows that the pre-exponential factor  $D_0$  depends also on the diffusion entropy. It can be written as  $D_0 = gf v_0 a^2 \cdot \exp\left(\frac{\Delta S}{k_B}\right)$  where the

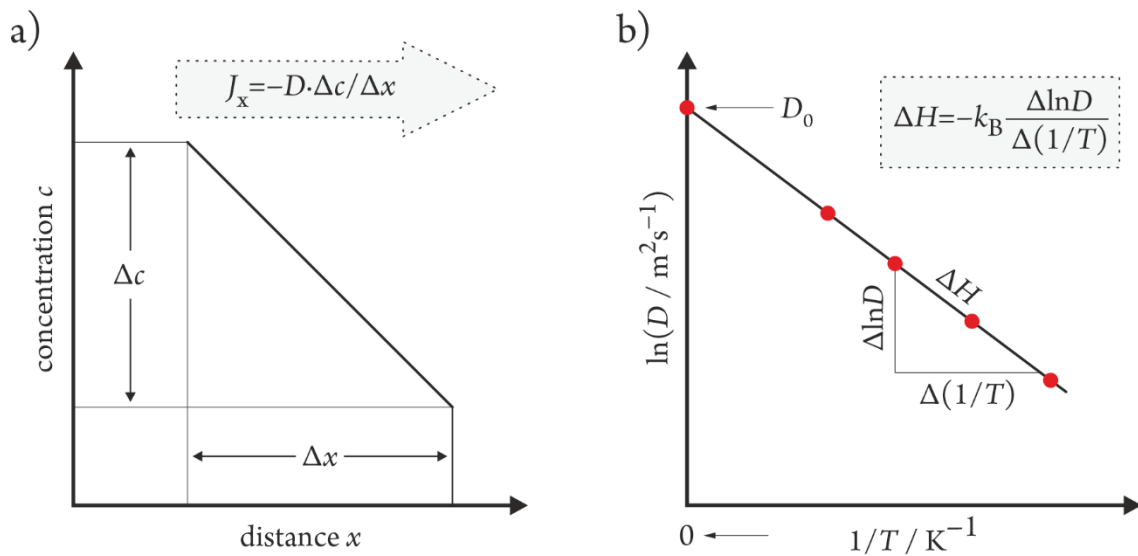


Figure 4: a) Graphical representation of Fick's first law of diffusion. b) Arrhenius plot of the diffusion coefficient highlighting its temperature dependence.

symbols have the following meaning:  $g$  is a geometric factor,  $f$  is a correlation factor and  $\nu_0$  is the attempt frequency<sup>1</sup>.<sup>32</sup> The correlation factor accounts for correlations between the directions of two successive atomic jumps processes and depends on the diffusion mechanism at play.<sup>33</sup> For vacancy-based diffusion in a cubic lattice, it can be expressed as  $f = \frac{1+\langle\cos\theta\rangle}{1-\langle\cos\theta\rangle}$  where  $\langle\cos\theta\rangle$  is the average angle between two consecutive jumps.<sup>34,35</sup>

The macroscopic diffusion in a solid is the cumulative result of many microscopic, discrete jump processes. Therefore, it is possible to link the microscopic jump processes to the macroscopic transport of ions. This relation is usually developed in the basis of the random walker, *i.e.* a single particle that walks, step-by-step, on 2-dimensional lattice without any memory about where it came from and thus the direction of every step is completely independent of, and therefore uncorrelated to, the direction of the previous step.

If the trace of such a particle is recorded over time, it will become evident that there is no correlation between the distance the particle moved from its origin and the passed time, but a clear correlation between the area it covered in time. This is formulated as  $\langle x^2 \rangle \propto t^\alpha$  where  $x$  is the length of a step and  $t$  is the time and shows that the root-mean square displacement (MSD)  $\langle x^2 \rangle$  scales with time. The temporal evolution of the MSD depends on the exponent  $\alpha$ . In normal diffusion, the MSD scales linearly with time and  $\alpha = 1$ . Anomalous diffusion is characterized by  $\alpha \neq 1$  and subdivided into subdiffusive ( $\alpha < 1$ ) and superdiffusive ( $\alpha > 1$ ) behaviour.

A limiting case is the ballistic diffusion regime in which  $\alpha$  equals 2. The latter is a rare case observable if diffusion and drift collude.<sup>36</sup> Most of the diffusive processes in solids can be well described by normal diffusion. Knowing this, we can go back to the random walker, in the case of dilute interstitial atoms on a simple cubic lattice. At equilibrium, the interstitial atoms are equally distributed such that no concentration gradient or any other driving force exists. Thus, there is no net flux of atoms. If we draw a fictive straight line to separate two areas, an artificial boundary, the randomly moving atoms will from time-to-time, pass this line by jumping from one area into the other, and vice-versa. Since there is no net flux, the number of particles jumping into the area and the number of particles jumping out of the area have to be equal: Thus,  $J = \Gamma n_1 - \Gamma n_2 = 0$  where

---

<sup>1</sup> The attempt frequency is in the order of the Debye frequency.

$n_{1,2}$  and  $\Gamma$  are the number of atoms and the jump rate. Furthermore, assuming that these areas are separated by a single jump length, we can relate the number of particles to a concentration according to  $C_i = \frac{n_i}{a}$  where  $a$  is the jump length, *i.e.* the distance between two lattice sites. Substitution then yields:  $J = \Gamma \cdot a \cdot (C_1 - C_2)$  where the term in brackets can be interpreted as a concentration gradient according to  $C_1 - C_2 = -a \frac{\partial C}{\partial x}$ . After substitution, the equation reads as  $J = -\Gamma a^2 \nabla c$  which resembles Fick's first law of diffusion:  $J = D \cdot \nabla c$ . Therefore, using this simplified derivation, we find that the diffusion coefficient describing Fick's macroscopic law of diffusion depends on the microscopic hopping rate and the respective jump distance according to  $D = \frac{\Gamma a^2}{2 \cdot d}$  where  $d$  is the number of dimensional degrees of freedom; for the 1D-case we considered so far, this yields exactly what was shown above. However, if the correlation factor is taken into account, the tracer diffusion coefficient is given by  $D^* = f \frac{\Gamma a^2}{2 \cdot d}$ . If this diffusion coefficient is used to derive specific conductivity values, another correction value, the Haven Ratio,  $H_R$ , has to be taken into account; it is defined as  $H_R = D^*/D_\sigma$  where  $D_\sigma$  is the apparent diffusion coefficient.

### 2.2.1. Diffusion mechanisms

As the arrangement of atoms in solids is rather dense, the possible direction of a jump process is restricted. In crystalline materials, atoms can only jump to certain positions of the crystal lattice and thus the jump-length is dictated by the crystal structure. Nevertheless, even in a regular arrangement, different mechanisms of diffusion can be distinguished. Some of the most important mechanisms are detailed below.

#### **Vacancy mechanism**

This mechanism relies on the presence of defects which, for  $T > 0$  K, are always present. Only few atoms will have an empty site, *i.e.* a vacancy, as its nearest-neighbour and thus only few atoms will have access to this diffusion mechanism. If an atom jumps from its current, regular lattice position into a vacant position, it leaves a vacant position behind, *i.e.* the atoms and the vacancy have changed positions. We may also consider the vacancy as a mobile species, which is surrounded by atoms, and may thus jump to any of them with equal probability. However, immediately after switching its

position with an atom, the probability for the atom to jump back is increased. Therefore, the correlation factor for vacancy-based diffusion is always smaller than unity and is approximately given by  $f \approx 1 - 2/Z$  where  $Z$  is the number neighbouring sites. Another important feature of the vacancy-based diffusion mechanism is that the activation energy of the jump-rate depends on the migration energy and the vacancy formation energy.

### **Direct interstitial mechanism**

The direct interstitial mechanism is based on the random walk of an atom residing on an interstitial position in the crystal structure. Such interstitial sites are often found in fcc and bcc lattices. Especially small foreign atoms seem to diffuse via this mechanism. In the dilute case, where every interstitial is surrounded only by empty interstitial sites, the jump probability is equal for every possible direction. The jump sequence is completely uncorrelated, and the correlation factor is given by  $f=1$ . This comparatively fast diffusion mechanism is independent of vacancies and thus the activation energy describing the temperature dependence of the jump-rate contains no defect formation energy.

### **Interstitialcy mechanism**

This mechanism is similar to the direct interstitial mechanism but is more common for self-interstitials, *i.e.* when the interstitial atom is similar in size to the matrix atoms constituting the crystal. The interstitial atom may move to a regular site whereby the former occupant of the regular site is moved to a different interstitial site. This movement of the interstitial and the regular atom may be collinear or non-collinear.

#### 2.2.2. Diffusion in the solid state

In solids however, the ions will not migrate continuously, but will perform discrete hops, jumping from one position to another. To perform the jump, the ion needs a specific amount of energy that is usually termed activation energy ( $E_a$ ). This is the energy required by the ion to overcome the energy barrier separating its current position, a local energy minimum, from an adjacent position, another local energy minimum. In the simplest case, all positions are on equal energy levels and

thus, the energy barriers separating these positions are symmetric. Considering a one-dimensional energy landscape, the energy barrier for an ion to jump from site A to site B is the same as jumping from B to A; the energy barriers are symmetric. However, not all energy barriers have to be of equal height. Such a case, where all positions are energetically equivalent but separated by non-equal energy barriers is represented by the “random barrier” model, RBM (see Figure 5a).<sup>37</sup> This model is based on an invariant energy landscape, *i.e.* no interaction between the energy landscape and the moving ion is present. Albeit rather primitive, the RBM captures one of the most important features of diffusion in solids which is the activated jump process necessary to overcome the energy barrier separating two local minima. The occurrence of a jump process  $\Gamma$  can be described by a temperature dependent hopping rate:  $\nu = \nu_0 \cdot \exp(-E_a/(k_B T))$  where  $\nu$ ,  $\nu_0$  are the hopping rate (hopping frequency) and the attempt frequency of the ion while  $k_B$  and  $T$  have the usual meaning.

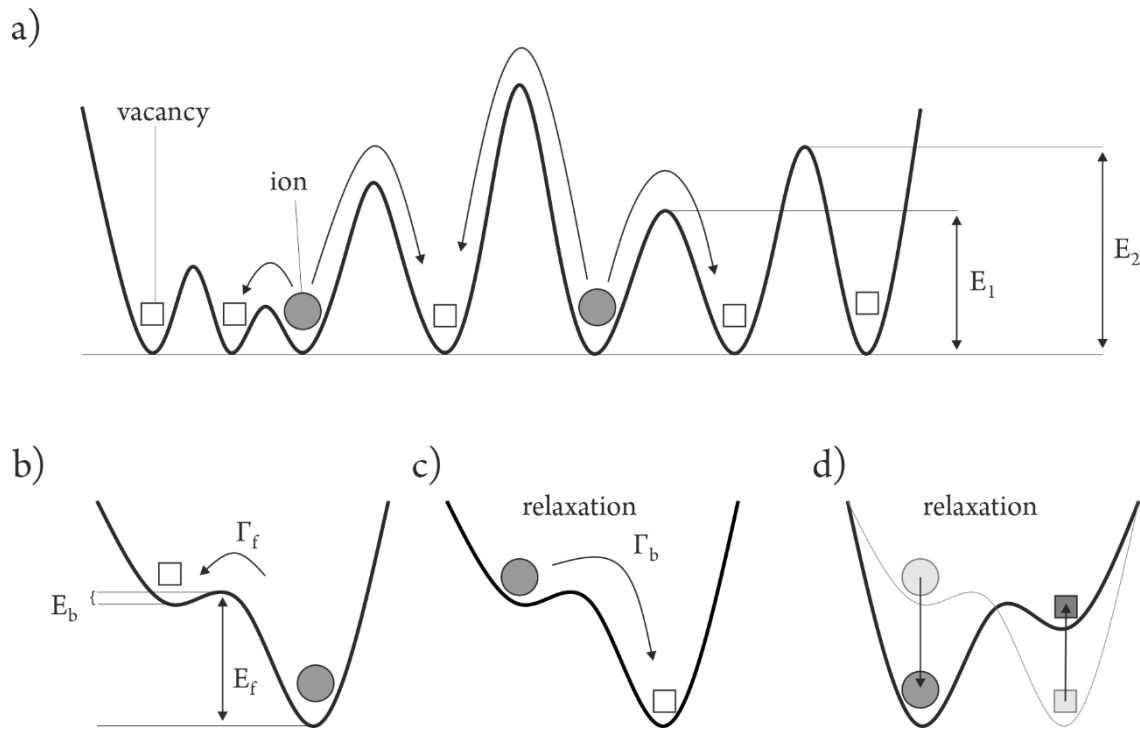


Figure 5: a) The random energy barrier (RBM) landscape model showing two ions and several vacant positions at equivalent energy levels separated by energy barriers of differing heights, *i.e.* energy barrier,  $E_1$  and  $E_2$ . b-c) Graphical representation of the jump relaxation model. b) The ion has to overcome a large energy barrier,  $E_f$ , to perform a jump,  $\Gamma_f$ , to the vacant position. After surmounting the energy barrier, the vacancy and the ion have switched place and the ion is separated by its former position only by a very small energy barrier  $E_b$ . The backward jump,  $\Gamma_b$ , is thus very probable (c) unless the lattice relaxes around the new ion and vacancy position leading to an accommodation and a stabilization, *i.e.* decrease of position energy, of the ion in its new site (d).



However, a more elaborate model also includes the effect of the ion on the energy landscape itself by Coulomb interactions. It assumes that not all positions are equal in terms of energy and that the framework surrounding the diffusing ion is accommodating the ion in its position by relaxation. This jump-relaxation model was introduced by K. Funke.<sup>38</sup> First, it assumes asymmetric energy barriers and thus anisotropic jump rates (Figure 5). Secondly, it accounts for two different types of relaxation. The ion which has just jumped from a local minimum to a site of higher energy may either jump back or reside long enough for the framework to relax around it. As shown in Figure 5b, the forward jump,  $\Gamma_f$ , is characterized by a higher energy barrier,  $E_f$ , than the energy barrier for the backward jump,  $E_b$ . Therefore, often the ion will jump back to its previous site (Figure 5c).

In contrast to this unsuccessful jump process, the ion may successfully leave its position if the framework relaxes before it jumps back. This second relaxation process is exemplified in Figure 5d and results in a successful jump by stabilizing the ion in its new position through relaxation of the framework. Usually, relaxation by backward hopping is more probable than relaxation of the framework and thus, most jump processes are unsuccessful. For the sake of completeness, it is also worth mentioning that a different, albeit in many aspects similar<sup>39</sup> model was developed by K. Ngai, the Coupling Model.<sup>40</sup>

### 2.3. Impedance spectroscopy

Impedance spectroscopy is a non-destructive analysis method to analyse the impedance of a material, *i.e.* the current response to a voltage stimulus. Practically, the voltage stimulus is a sinusoidal signal with a fixed small amplitude at a defined frequency with discrete values between very low, 10 mHz, and comparatively high, 10 MHz frequencies. The impedance is generally a function of the frequency and, if we consider the frequency as the inverse probing time, it will give information about the temporal evolution of the current. As this behaviour is very similar to the behaviour of resistor and capacitor networks (RC-units), the obtained spectra are often interpreted with the help of equivalent circuits.

One of the most important concepts of impedance spectroscopy and its use for the analysis of (solid) electrolytes is that the current is carried by moving ions. Keeping in mind that an ion has to overcome an energy barrier, separating its current position from another location, in order to follow the electric field, the influence of the electric field on the ion is best represented by an asymmetrical change of the activation barrier resulting from the overlay of an electric potential gradient. In the direction of the electric field, the energy barrier will be decreased by a factor proportional to the

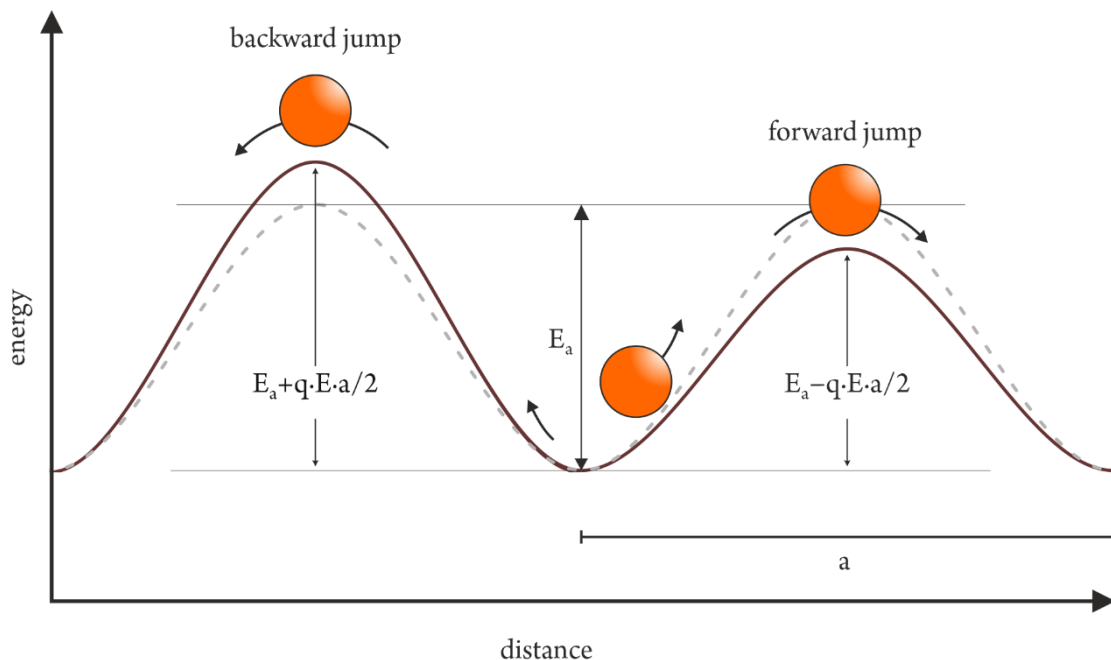


Figure 6: Energy landscape as perceived by an ion that is subjected to an electric field. The dashed line represents the energy landscape in the absence of an external electric field; a symmetrical dale in which the ion rests. The probability for the ion to jump is isotropic. However, if an electric field is applied, the energy barrier will be lowered for one side and increased for the other. Hence, the probability for the ion to jump along the field is increased. Figure adopted from reference <sup>41</sup>.

electric field, the charge of the ion as well as half the distance between the two sites (see Figure 6). In the direction opposing the electric field, the ion will face an increased energy barrier. Therefore, the probability for a forward jump in the direction of the electric field will be increased whereas the probability for a backward jump opposing the direction of the electric field will be decreased.

Hence, the conductivity is proportional to the diffusivity of these charge carriers. Within the frame of certain models, based on a few assumptions, this method is very powerful as it allows to gain information about the microscopic diffusion coefficient by measuring a macroscopic quantity. In the following sections, the basic concepts of impedance spectroscopy will be reiterated very briefly followed by a detailed delineation of the relationship between the impedance and the microscopic diffusion of ions in the solid state.

### 2.3.1. Basics of impedance spectroscopy

As mentioned in section 2.2 the Fickian diffusion is a response to a concentration or electrochemical gradient. By applying a potential difference across the material under study, any mobile charge within that material will follow the gradient according to Fick's law. Since the mass transport is directly linked to a charge transport, the former can be analysed by measuring the current. For this reason, the formalism used to describe and analyse alternating current in response to alternating voltage can be applied to study diffusion of charged species in ionic conductors.

Applying a small sinusoidal perturbation signal, that is an oscillating electric field, to an ionic conductor will result in an electric current due to moving charges in the form of mobile ions. The current and its phase with respect to the sinusoidal voltage are recorded. These two quantities are the only ones directly measured by impedance spectroscopy. As mentioned above, the current is directly linked to the mass transport, *i.e.* the transport of ions by diffusion. As diffusion is temperature dependent, such measurements are generally carried out at different temperatures (isotherms). From the frequency dependent current and its phase, the impedance is calculated and may be interpreted in the context of equivalent circuits composed of resistive and capacitive elements. In principle, impedance may be measured at samples with any arbitrary shape. However, interpretation is much more straightforward if the sample has two parallel sides to which the potential difference is applied to, *i.e.* between which the electric field is applied. Powder samples are pressed to form a cylinder and ion-blocking electrodes are applied to the parallel surfaces (see

Figure 7a). Therefore, the sample is in the arrangement of a parallel plate capacitor with the ion conductor as the separating dielectric.

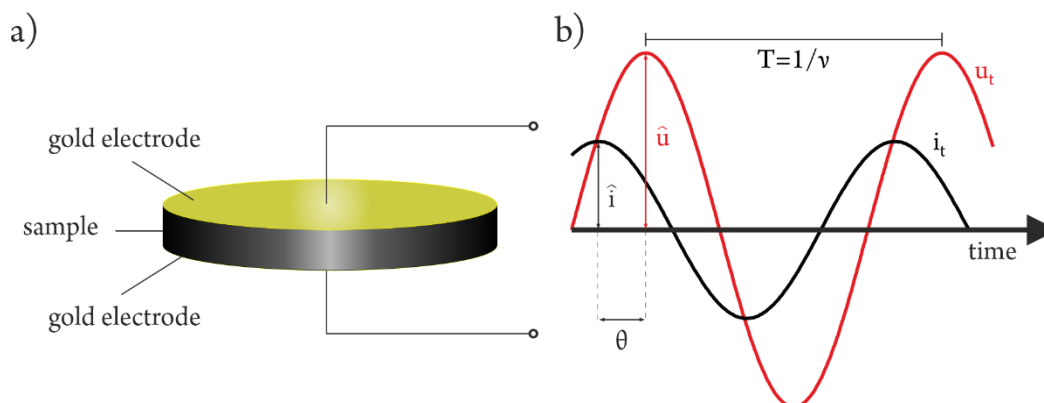


Figure 7: a) Typical shape of a powder sample equipped with ion-blocking gold electrodes. b) Schematics of the current voltage dependence with an out-of-phase contribution. The phase shift, theta, as well as the amplitudes are shown.

As the contact between the solid ion conductor and the metallic gold electrode is non-Ohmic, due to the different nature of the charge carriers, capacitive effects will arise at low frequencies in samples with high ionic conductivity.

The basic quantities, current and phase, can be used to calculate different quantities such as the impedance, the specific conductivity, and the relative permittivity. Knowing the sample geometry, also specific properties, independent of the sample's geometry, can be calculated. Since all these quantities are derived from the same data, they also contain the same information. However, for visual inspection of the data it is often important to show the data in ways highlighting different features to help with interpreting the data. Thus, there are different established plots like the conductivity isotherm plot, the Nyquist plot and more general, the Argand plot, next to the Bode plot. The impedance  $Z(\omega)$  is often analysed in the form of a complex plane plot termed Nyquist plot. Furthermore, another practical representation is to plot the real part of the complex specific conductivity,  $\sigma(\omega)$ , as a function of the frequency and as a function of temperature (isotherms) in a log-log plot. The great advantage is that all isotherms are visible in one plot and all processes, from dispersive regime to electrodes polarization, are visible. This is not always the case for the linear-scale plots like the Nyquist plot as the change in conductivity and therefore impedance often spans more than one decade; hard to visualize in a linear representation. Thus, Nyquist plots often show only a single or a few isotherms. As mentioned above, these quantities are interrelated. Using the

complex impedance  $\mathbf{Z}$  and taking the samples geometry into account, the specific conductivity, a material constant, is then calculated via Eq. (8).

$$\sigma = \frac{1}{Z} \cdot \frac{h}{A} \quad (7)$$

where  $h$  is the thickness of the sample and  $A$  is the area of electrodes.

As mentioned above, the impedance of a solid electrolyte is often interpreted in the context of an equivalent circuit consisting of basic passive circuit elements such as resistors and capacitors but also lumped circuit elements such as the constant phase element (CPE) are used. In the most general case, a time dependent voltage in the form of a sinus wave can be expressed as  $u_t = \hat{u} \cdot \sin(\omega \cdot t)$ . The corresponding current response in the most general form will be given by  $i_t = \hat{i} \cdot \sin(\omega \cdot t + \varphi)$  and is characterized by the amplitude of the current  $\hat{i}$  as well as the phase shift  $\varphi$  with respect to  $u_t$ . Depending on the tested component, the phase angle will be 0 for a resistor,  $+\frac{\pi}{2}$  ( $90^\circ$ ) for an inductance, and  $-\frac{\pi}{2}$  ( $-90^\circ$ ) for a capacitance.

For the resistor, we find that Ohm's law holds.

$$R = \frac{u_t}{i_t} = \frac{\hat{u} \cdot \sin(\omega \cdot t)}{\hat{i} \cdot \sin(\omega \cdot t)} = \frac{\hat{u}}{\hat{i}} \quad (8)$$

Since the phase angle  $\varphi = 0$ , we find that the time dependent current follows exactly the time dependent excitation signal, the voltage, and that the resistance is independent of the applied frequency.

For a capacitance, a phase shift will adopt  $-\frac{\pi}{2}$  and result in a frequency dependent resistance as shown below. The time dependent charge stored in a capacitor is proportional to the capacitance  $C$  and the applied time dependent potential  $Q_t = C \cdot u_t$ . For the time dependent current, we can derive the following equation that shows its dependence on the capacitance, the voltage amplitude as well as the frequency  $i_t = \frac{\partial Q_t}{\partial t} = C \cdot \frac{\partial u_t}{\partial t} = C \cdot \frac{\partial(\hat{u} \cdot \sin(\omega \cdot t))}{\partial t} = C \cdot \hat{u} \cdot \frac{\partial(\sin(\omega \cdot t))}{\partial t}$ . This results in  $i_t = C \cdot \hat{u} \cdot \omega \cdot \cos(\omega \cdot t) = C \cdot \hat{u} \cdot \omega \cdot \sin\left(\omega \cdot t - \frac{\pi}{2}\right)$  and shows that the amplitude of the current is given by  $\hat{i} = C \cdot \hat{u} \cdot \omega$ . Accordingly, we can derive the equation for the reactance of the capacitance as

$$\chi_c = \frac{\hat{u}}{\hat{i}} = \frac{1}{\omega \cdot C}. \quad (9)$$

In a coil, the magnetic field which accompanies moving charges superimposes to a much larger magnetic field. The interaction of this magnetic field and the electric field is described by the Maxwell-Faraday equation. In brief, the magnetic field will delay the current response to a changing electric field. Therefore, the current will not instantly follow the change in the potential but will be delayed. This self-inductance results in the frequency dependent resistance of an inductive coil and can be formulated as follows: considering  $L$  as the inductance  $u_t = L \cdot \frac{\partial i_t}{\partial t} = L \cdot \frac{\partial(\hat{i} \cdot \sin(\omega \cdot t))}{\partial t} = \hat{i} \cdot L \cdot \frac{\partial \sin(\omega \cdot t)}{\partial t}$ . This results in  $u_t = \hat{i} \cdot L \cdot \omega \cdot \cos(\omega \cdot t) = \hat{i} \cdot L \cdot \omega \cdot \sin\left(\omega \cdot t + \frac{\pi}{2}\right)$  and shows that the amplitude of the potential is given by  $\hat{u} = \hat{i} \cdot L \cdot \omega$ . Accordingly, we can derive the equation for the reactance of the inductance as

$$\chi_L = \frac{\hat{u}}{\hat{i}} = \omega \cdot L. \quad (10)$$

The resistance of a solid ionic conductor is associated with mobility of the ions in the solid while the capacitive contributions usually arise by charge accumulation at interfaces such as grain boundaries, or in general phase or domain boundaries such as the electrode electrolyte interface. Inductivity, however, is less intuitive and the reasons for inductivity are manifold. If solid electrolytes with ion-blocking electrodes are analysed, inductive effects are most often artefacts<sup>42</sup>.<sup>43</sup> Resistive and capacitive effects on the other hand are real but give rise to imaginary components of the response. Therefore, the use of equivalent circuits to model the electric response usually contains a network of resistors and capacitances only.

In impedance spectroscopy as well as in the field of circuit analysis it is unpractical to work with the trigonometric functions as they are not as handy as the Euler representation is, especially when it comes to complicated equations. The Euler representation is used as an alternative way of representing complex numbers, that is numbers with a real as well as an imaginary part. A general complex number “ $Z$ ” can be represented as

$$Z = Re(Z) + j \cdot Im(Z) \quad (11)$$

with  $Re(\mathbf{Z})$  representing the real part and  $Im(\mathbf{Z})$  representing the imaginary part which is declared by the “j” which is the imaginary unit defined by  $j = \sqrt{-1}$ . If plotted in a complex plane plot showing the real part as a function of the imaginary part the quantity  $\mathbf{Z}$  is represented by a vector (see Figure 8a). The length of this vector is given  $|\mathbf{Z}| = \sqrt{Re(\mathbf{Z})^2 + Im(\mathbf{Z})^2}$  and its projection along the abscissa and ordinate are given by  $|\mathbf{Z}| \cdot \cos(\theta)$  and  $|\mathbf{Z}| \cdot \sin(\theta)$  respectively. Thus, the complex number can be represented by  $\mathbf{Z} = |\mathbf{Z}| \cos(\theta) + j|\mathbf{Z}| \sin(\theta)$  or, in the Euler representation by  $\mathbf{Z} = |\mathbf{Z}|e^{-j\theta}$ .

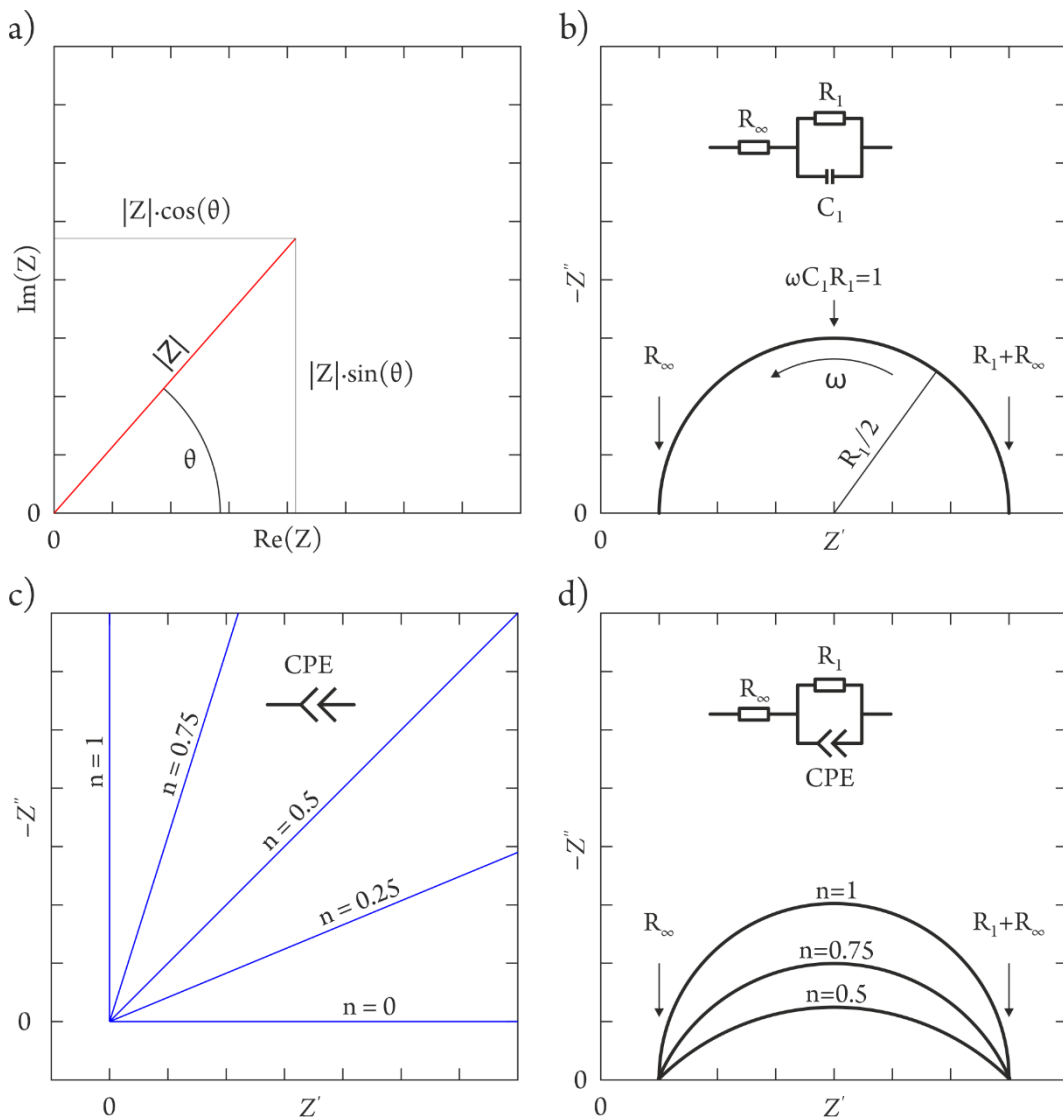


Figure 8: a) General complex plane plot showing a complex vector at one frequency. b) Complex plan plot of the impedance (Nyquist plot) and the corresponding equivalent circuit. The RC unit shows a single relaxation time and a perfect semi-circle. c) Nyquist plot of CPE with different values of  $n$ . d) Nyquist plot of a R-RCPE network with different values for  $n$ . For  $n < 1$  the semi-circle is depressed, i.e. its centre is underneath the abscissa.

The response of a simple ionic conductor may be modelled by a single RC-unit in series with a resistor,  $R_\infty$  (see Figure 8b). The impedance of such a material is then given by  $\mathbf{Z} = R_\infty + R_1 \cdot (j\omega R_1 C_1)^{-1}$ , that is the sum of the series resistor and the resistance of the RC-unit. Separation to obtain the real and imaginary part by expansion yields  $\mathbf{Z} = R_\infty + R_1 \cdot (1 + \omega^2 R_1^2 C_1^2)^{-1} - j \cdot R_1 (\omega R_1 C_1)^{-1}$ . At very high frequencies,  $\nu = \omega/(2\pi)$ , the capacitor acts as a shunt and  $|\mathbf{Z}| \approx Z' \approx R_\infty$ . At very low frequencies, the capacitor blocks the current and  $|\mathbf{Z}| \approx Z' \approx R_\infty + R_1$ . At a specific intermediate frequency, the relaxation frequency, the term  $\omega R_1 C_1$  will be 1 and therefore the real and imaginary parts are given by  $Z' = R_\infty + R_1/2$  and  $Z'' = -R_1/2$ .

The impedance will show a semicircle in the Nyquist plot where the specific relaxation frequency can be derived from the apex of the circle (see Figure 8b). The RC-unit has single relaxation frequency or relaxation time  $\tau = RC$ . Apart from these “real” circuit elements also the constant phase element (CPE) is often used to model the electric response of solid ion conductors. The CPE is best interpreted as an imperfect capacitor and while a single RC-unit is suitable to fit only a single relaxation time, a CPE allows to model a distribution or relaxation times. The CPE is characterized by the empirical impedance function  $\mathbf{Z} = A \cdot (j\omega)^{-n}$  where  $n$  is a parameter between 0 and 1. For  $n = 0$  the CPE behaves like a resistor, for  $n = 1$  it behaves like a capacitor (see Figure 8c).

Most real ionic conductors, however, show a distribution of relaxation times, a feature that can be modelled by many RC-units with different relaxation times or by a single RCPE-unit (Figure 8d). The resultant depressed semicircle is the sum of many individual relaxation processes which are caused by different resistances rather than variations in capacitances.

### 2.3.2. (Di)electric relaxation

#### **Dielectric relaxation**

In a perfect dielectric all charges are bound, and no long-range conduction is observable. However, such a material will show some electric relaxation if an electric field is applied. As a response to the electric field, the material will be polarized, and the charges displaced. The polarization  $P_{(\omega)}$  is a function of the frequency and depends on the electric susceptibility  $\chi_{(\omega)}$  as given by:

$$\mathbf{P}_{(\omega)} = \varepsilon_0 \cdot \chi_{(\omega)} \cdot E_{(\omega)} \quad (12)$$



where  $\epsilon_0$  is the vacuum permittivity. It follows from causality and the linear response of the sample that the polarisation depends only on the electric field at previous times. Consequently, the real and imaginary parts of the polarisation are related to each other and must satisfy the well-known Kramers-Kronig relations.<sup>41</sup> The electric displacement  $D(\omega)$  is analogously obtained taking the relative dielectric permittivity  $\epsilon(\omega) = 1 + \chi(\omega)$  into account.

$$\mathbf{D}(\omega) = \epsilon_0 \cdot \mathbf{E}(\omega) + \mathbf{P}(\omega) = \epsilon_0 \epsilon(\omega) \mathbf{E}(\omega) \quad (13)$$

The frequency dependence of the susceptibility gives rise to a frequency dependence of the relative permittivity and it is the root of the dispersion properties in dielectrics. The frequency dependent displacement is a complex quantity related to the microscopic movement of charges. Its behaviour may be modelled as a relaxation process following the applied electric field. One of the simplest models of dielectric relaxation is the Debye model which is characterized by an exponential decay of the response function. Importantly, the response is characterized by a single (Debye) relaxation time constant  $\tau_D$  ( $\tau_D = R_1 C_1$ ). The permittivity of the ideal Debye relaxation process is shown in

Figure 9 and is given by  $\epsilon(\omega) = \epsilon_\infty + \frac{\Delta\epsilon}{1+j\omega\tau_D}$ .

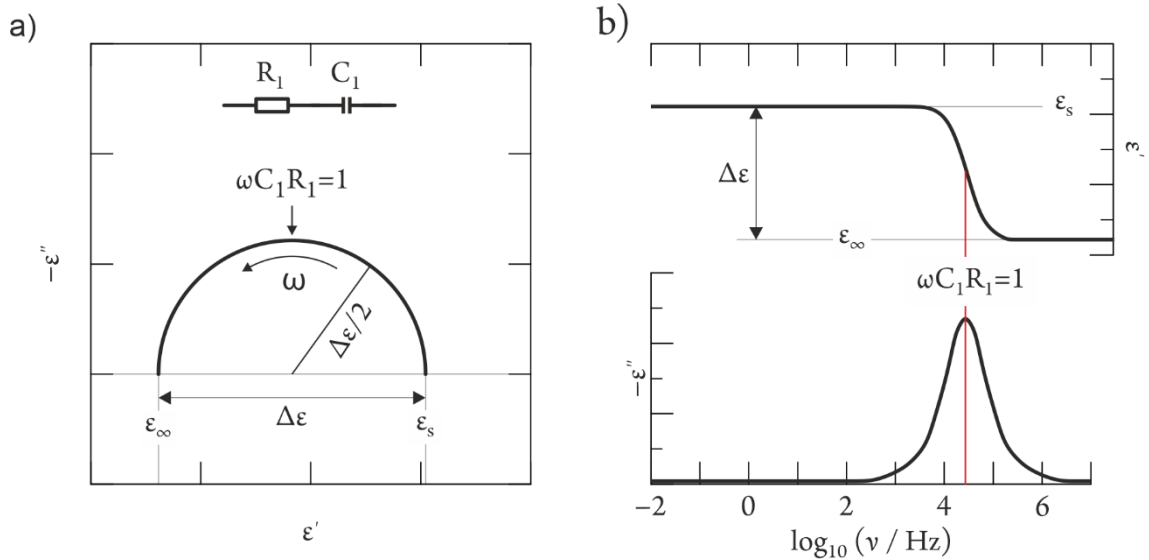


Figure 9: Dielectric relaxation for an ideal Debye process. a) The response is in the form of a perfect semi-circle with one characteristic relaxation frequency at the apex of the semicircle and the relaxation strength  $\Delta\epsilon$ . b) The same relaxation process shown as the real part of the permittivity ( $\epsilon'$ ) and the imaginary part of the permittivity ( $\epsilon''$ ) as function of the frequency.

However, real systems usually show deviations from the Debye relaxation<sup>44</sup> and empirical models, modifications of the Debye model, are used to approximate relaxation times of more complex

processes. The most important one is the Havriliak-Negami function (Eq. 14) with its limiting cases, the Cole-Cole and, the Cole-Davidson equation.

$$\epsilon(\omega) = \epsilon_{\infty} + \frac{\Delta\epsilon}{(1 + (j \cdot \omega \cdot \tau_i)^{\alpha})^{\beta}} \quad (14)$$

For  $\beta = 1$  the Cole-Cole function is obtained. For  $\alpha = 1$  the Cole-Davidson function is obtained and for  $\alpha = \beta = 1$  the original Debye function is obtained. The exponent  $0 < \alpha \leq 1$  characterizes the symmetrical broadening of the dielectric relaxation function whereas the exponent  $0 < \beta \leq 1$  describes the asymmetric broadening. It is important to note that the deviation from  $\alpha\beta = 1$  allows to model a distribution of relaxation times. Further detailed information can be found in reference<sup>45</sup>.

### Conductivity relaxation

In ionic conductors, not all charges are as tightly bound as in a perfect dielectric and therefore another relaxation process will be present in such materials: the conductivity relaxation. This relaxation process is the decay of the electric field in the ion conductor caused by the displacement of mobile charges. It is important to note that dielectric relaxation takes also place in ionic conductors albeit it is most often concealed by the conductivity relaxation. Such a behaviour is seen in  $\text{Li}_4\text{Ti}_5\text{O}_{12}$  (see Figure 10).

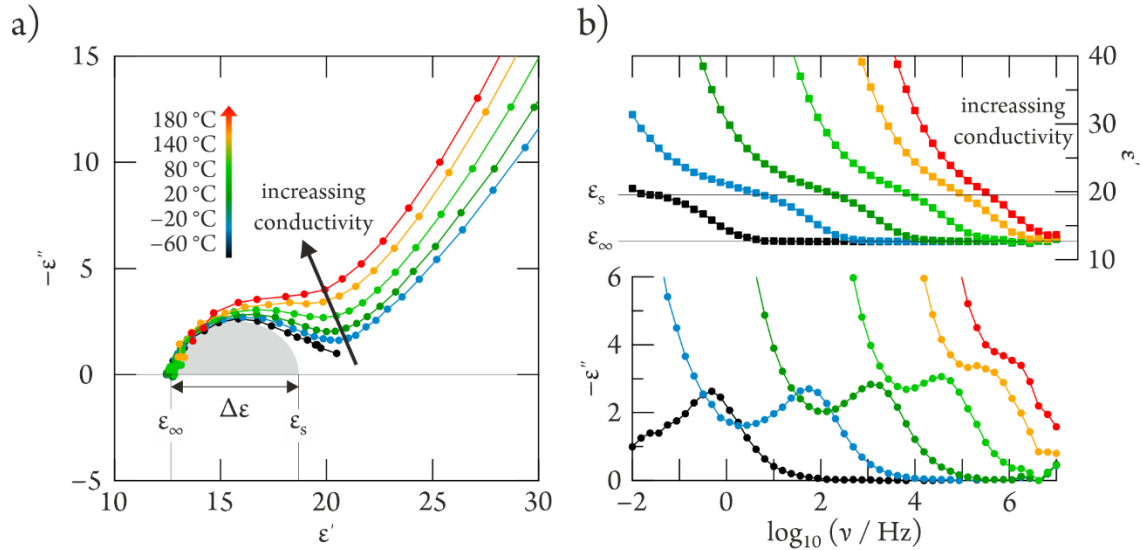


Figure 10: Isotherms of  $\text{Li}_4\text{Ti}_5\text{O}_{12}$  showing the complex permittivity in an Argand plot (a) and as a function of the frequency (b). Note how the dielectric relaxation process is increasingly overshadowed by the increasing conductivity at higher temperatures. The high and low-frequency limits of the real part of the permittivity,  $\epsilon'$ , are denoted by  $\epsilon_{\infty}$  and  $\epsilon_s$ , respectively

The complex plane plot of the permittivity shows a semicircle characteristic for Debye-like relaxation. As the temperature of the sample increases, so does the ionic conductivity and the dielectric relaxation process becomes almost hidden by the conduction relaxation. It is important to note that the time-derivative of the displacement,  $d\mathbf{D}_{(\omega)}/dt$ , resulting from an alternating electric field  $E_{(\omega)} = \hat{E} \cdot \sin(\omega \cdot t)$  is equal to the current density  $\mathbf{J}$ .

$$\mathbf{J}_{(\omega)} = \frac{d\mathbf{D}_{(\omega)}}{dt} = j \cdot \omega \cdot \boldsymbol{\varepsilon} \cdot \varepsilon_0 \cdot E_{(\omega)} \quad (15)$$

According to Ohm's law,  $\mathbf{J}_{(\omega)} = \boldsymbol{\sigma}_{(\omega)} \cdot E_{(\omega)}$ , the specific conductivity is related to the permittivity and thus given by  $\boldsymbol{\sigma}_{(\omega)} = j \cdot \omega \cdot \varepsilon_0 \cdot \boldsymbol{\varepsilon}_{(\omega)}$ . The real and imaginary part of the conductivity are then given by  $\sigma' = \omega \varepsilon_0 \varepsilon''$  and  $\sigma'' = \omega \varepsilon_0 \varepsilon'$  respectively.

### 2.3.3. The effective medium theory

A homogeneous specimen, without any significant defects, can be described by a single permittivity. However, next to single crystals, only glasses will show such properties. Most samples are heterogeneous in nature. As such, any polycrystalline material is essentially a two-domain material. The polycrystalline material, even if free from any impurity will have the interior of the grains, where every unit cell of the crystal is perfectly aligned with the adjacent one, and the contact regions with adjacent crystallites. Albeit the ionic conductivity in the ideal crystallites is identical in all crystallites, the contribution of the grain boundaries, *i.e.* the contact with the next crystallite will be very heterogeneous, even for materials characterized by three-dimensional isotropic diffusion. The grain boundaries will often be present as a large resistance. The large resistance is not only evoked by the reduced contact area, considering spherical particles with little contact area, but also by the irregularity of the anion-framework between two crystallites with different crystallographic orientations. If ionic conductivity is anisotropic, the geometric contact area between crystallites seems to have a higher impact on the resistance of grain boundaries. However, the effective medium theory may be used to deconvolute the contribution of phases, or in the more general case, volumes, with different permittivities in a composite or mixture. If the volumes differ sufficiently in their properties and the corresponding volume fractions are within reasonable limits, the effective media theory can be used to assign for example, two conduction processes to two different regions. If so the individual permittivities of the different volumes (or regions within a heterogeneous sample) may be extracted.<sup>46, 47</sup> In the case of the (nano)glassy petalite study, for example, we found two

regions with different conductivities, however, due to the low volume fraction, we were not able to extract the true permittivity values of these structurally slightly relaxed regions.

#### 2.3.4. Polarisation effects

Polarisation can be understood in terms of charge accumulation at interfaces and leads to a localized concentration gradient. As such, the polarization effects are very similar to the charge accumulation at the electrodes' surfaces in a capacitor. Polarisation effects in impedance spectroscopy and more general, in the study of conductivity, can arise from various causes.<sup>48</sup> If sufficient knowledge about the sample is given, it is possible to ascribe the polarisation effects to physical processes or locations in the sample. For example, one of the polarisation effects with the largest associated capacitance, is the electrode polarisation.<sup>49</sup> Furthermore, in polycrystalline samples, or in the more general case, in heterogeneous samples where the two electrodes are not directly connected by a single, homogeneous phase, charges can accumulate at the interfaces within the material, the grain boundaries<sup>50</sup>. This is very well exemplified by comparing oxide-based ionic conductors with sulfide-based ionic conductors. The former material often exhibits much higher rigidity than the latter does, *i.e.* oxides are harder than sulfides. If such a material is pressed into the shape of a tablet and analysed by impedance spectroscopy, the effect of grain-boundaries is often much higher in the oxide compared to the sulfide. However, if the material is sintered after pressing into tablets, the grain boundary resistance decreases largely in oxides. The sintering process allows higher diffusion, also of elements in their anion framework, and thus in general, grain growth and results in tighter connections between the individual grains. Polarisation effects arise at locations where a mismatch of resistance is present. If for example, a region with high ionic mobility is surrounded by a region of low ionic mobility (core-shell model) the ions will accumulate at this interface when following an external electric field.

#### 2.3.5. Charge carrier density and velocity

The specific ionic conductivity,  $\sigma_{DC}$ , linearly depends on the product of the actively participating charge carriers,  $N$ , as well as their mean electronic mobility,  $\mu$ :

$$\sigma_{DC} = z \cdot e \cdot N \cdot \mu \quad (16)$$

The electronic mobility  $\mu$  is defined as the mean ion velocity per electric field strength;  $\mu = v/E$ . While  $\sigma_{DC}$  can be measured easily, the determination of  $N$  or  $\mu$  is fraught with difficulties. The

accurate determination of  $\sigma_{DC}$  is sufficient if one is only seeking fast ionic conductors. However, to understand why a specific ionic conductor permits fast conduction while another does not, it is important to gain access to fundamental quantities such as the electric mobility or the charge carrier concentration. Albeit this is not easily attainable, there are some models and theories that allow to identify one of these quantities, within the limits imposed by the model. Obviously, the other quantity can then be calculated. In principle, the quantification of these two factors separately, requires a function linking the measurable, macroscopic quantities with the underlying unobservable microscopic processes. In the following, three different methods for the quantification of the charge carrier density will be introduced.

### **Quantification within the Almond-West Model**

While the model developed by Almond and West (AW-Formalism) was heavily criticized for lacking a complete physical foundation<sup>51</sup>, it accurately determines the charge carrier density from estimating the mean hopping rate of the ions from impedance spectra. According to that model, the mean hopping rate of the ions can be deduced from the transition between the diffusive and the dispersive regime.<sup>52, 53</sup> While the diffusive regime is observable in impedance spectroscopy at frequencies lower than the mean hopping rate, the dispersive regime designates the regime at frequencies higher than the mean hopping rate. At this frequency, the response of the ionic conductor to an oscillating electric field changes from foremost capacitive to foremost conductive (see Figure 11). The crossover frequency identified as the mean hopping frequency is the frequency at which the capacitive and resistive contributions are equal and the real part of the conductivity  $\sigma'_{(\nu)}$  is twice that of  $\sigma_{DC}$ . The frequency can be identified by making use of Jonscher's power law.

$$\sigma'_{(\nu)} = \sigma_{DC} \cdot \left(1 + \left(\frac{\nu}{\nu_c}\right)^\alpha\right) \quad (17)$$

The fitting parameters  $\nu_c$  and  $\alpha$  are adapted to reproduce the DC plateau and the dispersive regime. While  $\nu_c$  is the crossover frequency identified as the mean ion hopping frequency,  $\alpha$  is a dispersion parameter and usually adopts values between zero and one. Sidebottom could show that the dispersion parameter is associated with the degree of translational freedom of the ions.<sup>54</sup>

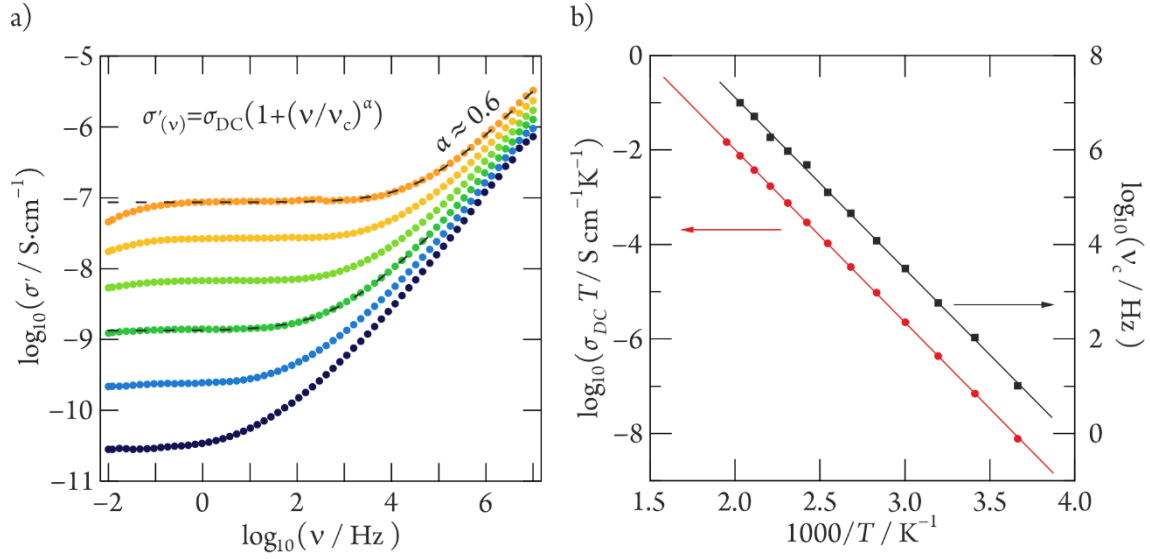


Figure 11: a) Exemplary conductivity isotherms with a power-law fit (dashed lines) according to the indicated formula. b) Arrhenius plot for the conductivity as well as the extracted crossover frequencies. The linear fits to both quantities (solid lines) show identical slopes; i.e. are equally thermally activated.

Extracting the mean hopping frequency of the ions gives access to their diffusion coefficient via the Einstein-Smoluchowski equation or alternatively, via the Green-Kubo relation. According to the Einstein-Smoluchowski equation, the MSD is proportional to the diffusion coefficient and the time.

$$\langle a^2 \rangle = D \cdot t \cdot 2 \cdot F \quad (18)$$

Here the MSD,  $\langle a^2 \rangle$ , is expressed in the context of ion diffusing in a simple cubic crystal system with the jump length  $a$ . The translational degrees of freedom,  $F$ , are counted twice since the ion can move in two directions in every dimension. The MSD will increase with time in discrete steps, the jump length is constant, and so one could express the MSD as a function of the discrete time intervals between two jump processes. This time interval between two hops is the mean residence time,  $\tau$ , of the ion on its position and is the inverse of its mean hopping rate:  $\tau = \nu^{-1}$ . For 3D isotropic diffusion, the diffusion coefficient is then given by.

$$D = \frac{\langle a^2 \rangle}{6} \cdot \nu_c \quad (19)$$

The electric mobility,  $\mu$ , is related to the diffusion coefficient of ions via the Einstein-Smoluchowski equation

$$\mu = \frac{D \cdot z \cdot e}{k_B \cdot T} \quad (20)$$

Using this formalism, one can rewrite Eq. 16 to depend on deducible quantities using Eqs. 19&20

$$\sigma_{DC} = \frac{e^2 \cdot \langle a^2 \rangle \cdot z \cdot N \cdot \nu_c}{6 \cdot k_B \cdot T} \quad (21)$$

Now the charge carrier density can be calculated if the specific conductivity, the jump length and the hopping frequency are known. It is important to note that charge carrier density calculated via this formalism usually equals the theoretical charge carrier density, *i.e.* every mobile ion participates in the conduction process. However, for ions in a crystal with a heterogeneous energy landscape not all the positions are energetically equivalent. A very stable position, *i.e.* at a low energy level, might be interpreted as a trap. If a non-negligible fraction of the mobile ions is captured in such traps, their participation in the conduction process will depend on the fraction of charge carriers having sufficient energy to leave these traps.<sup>55-57</sup> In such a system, the charge carrier density can be interpreted as a thermally activated process formulated as:  $N = N_0 \cdot \exp(-E_N/(k_B T))$ . The hopping frequency, in any case, is thermally activated:  $\nu = \nu_0 \cdot \exp(-E_M/(k_B T))$ . Within this framework, the well-known Arrhenius equation for ionic conductivity is obtained:

$$\sigma_{DC} = \left( \frac{e^2 \cdot \langle a^2 \rangle \cdot z \cdot N_0 \cdot \nu_0}{6 \cdot k_B} \right) \cdot \frac{1}{T} \cdot \exp\left( \frac{-(E_N + E_m)}{k_B \cdot T} \right) \quad (22)$$

Here, the first term in the equation is the pre-exponential factor,  $\sigma_0$ , while the activation energy,  $E_a$ , is the sum of the activation energies of the de-trapping of ions and the activation energy of migration. If the charge carrier concentration is independent of temperature all charge carriers are participating in conduction and the activation energy  $E_N$  equals zero, *i.e.*  $E_a \approx E_M$ .

However, it is important to consider the difference between the chemical and the self-diffusion mechanism. The ratio of these two is given by the Haven-ratio defined as  $H_R = D^*/D_\sigma$  where  $D^*$  is the tracer diffusion coefficient while  $D_\sigma$  is the charge diffusion coefficient.<sup>58</sup> Also correlation factors have to be taken into account. For simplicity, both have been treated as unity in the above deductions.

### **Quantification from electrode polarisation**

Another method is based on determining the charge carrier density from the capacitance of the electrode polarization. After sufficient polarization time, only negligible current flows through an ionic conductor if ion blocking electrodes and low potentials are used. If one integrates the current over time, the charge that moved can be calculated. From that charge, the charge carrier density is calculated. Albeit this model was extensively used to study the charge carrier density in glass electrolytes, it is not well suited for ceramic electrolytes as in the latter the charge carrier density is of similar magnitude in even very different ion conductors. In glasses however, the charge carrier density can be manipulated easily by changing the stoichiometry of the constituent educts and thus, the method could be rationalized. This method was successfully used to extract the effective charge carrier density in alkali metaphosphate glasses.<sup>59</sup> The concepts are treated in detail in the work of Beaumont and Jacobs<sup>60</sup> as well as by Tomozawa *et al.*<sup>61</sup>.

### **Direct quantification by Hall effect measurements**

Especially for materials with comparatively high charge carrier mobility one method is outstanding in determining the concentration of the charge carriers: Hall effect measurement. The Hall effect allows to determine not only the concentration of charge carriers but also their mobility. It was discovered by E. Hall in 1979 and is physically based on the Lorentz force. The Lorentz force acts on charges that move within a magnetic field if the velocity vector and the magnetic field vector are not parallel. In brief, a sample in the form of a bar is used and four electrodes are applied. Two electrodes are used to apply an electric field orthogonal to the magnetic field. The other two electrodes are placed, opposite to each other, on the side of the bar and aligned to be orthogonal to the electric as well as to the magnetic field. In such an arrangement, the charge carriers follow the externally applied electric field. But as they move, the Lorentz force exerts a force and pushes them to one side of the bar. Thereby a gradient of charge carriers develops until the electric field exerts a force equal to the Lorentz force and an equilibrium is obtained (see Nernst-Planck equation (5)). This electric field can be measured as a potential difference between the two other electrodes and is proportional to the velocity of the charge carriers.

This method was used by few researchers to determine the charge carrier density in ion conductors. Only few materials were studied by this method as high ionic conductivities, *i.e.* fast mean velocities



of the charge carriers are necessary. However, it was successfully employed in the fast  $\text{Ag}^+$ -ion conductors  $\alpha\text{-AgI}$ <sup>62</sup>,  $\text{AgRb}_4\text{I}_5$ <sup>63</sup> and some  $\text{Ag}^+$  conducting glasses<sup>64,65</sup>.

### 2.3.6. Interpretation of the results

Using a broadband dielectric spectroscope, or impedance analyser, provides access to a large frequency window to probe dielectric dynamics. However, for the time window accessible still being limited, not all processes, especially very fast ones cannot be detected. Among these very fast processes are the electronic and atomic polarization of the material. These processes are probed by other methods such as IR-spectroscopy and THz-spectroscopy<sup>66</sup> and it is possible to use data obtained by applying these methods to complement the data obtained from impedance spectroscopy. We have to recall, that the mobile ions are actually immobile most of the time, that is, they reside in their crystallographic positions where they oscillate around their time-averaged centre of gravity. Those vibrational frequencies are usually obtained as the pre-exponential factor of the dielectric relaxation in solid electrolytes. This is a clear indication that the origin of the jump process allowing diffusion in the solid state originates from the oscillation of the ions, *i.e.* is coupled to the phonon frequencies.

Plotting the admittance, or its geometry related quantity, the specific conductivity, vs. the frequency in a spectroscopic plot, reveals different regimes to the eye. A theoretical ion conductor would show a dispersive regime at high frequencies. In this regime, the admittance is proportional to the frequency and usually follows a power-law.<sup>67</sup> This range, characterized by nearly-constant loss (NCL) shows almost frequency-independent imaginary part of the permittivity and is often associated with cage-like ion dynamics.<sup>68</sup> At lower frequencies a regime with almost frequency independent admittance appears. This regime is a diffusive regime where ionic motion over many lattice sites is involved. The ions are therefore diffusing within the particles until they are subjected to a barrier which alters their diffusive behaviour. Such a barrier could be either an ion-blocking electrode or a different phase, with significantly differing conduction properties. In the most general case, a break in the periodicity the diffusing ion is exposed to, is often sufficient to result in some kind of polarization (see 2.3.4). This polarisation always sets in if the ions approximate and enter a phase with a much lower diffusion coefficient for the ion. This simple mismatch of diffusion coefficients leads to an accumulation of charge carriers at the boundary and gives rise to the capacitance. Usually, this charge accumulation is reflected in a steady decrease of the conductivity

(shielding of the electric field), often following an exponential decrease with frequency. At even lower frequencies, a second plateau is revealed which is characterized by the long-range motion, *i.e.* diffusion through the grains and the grain boundaries (g.b.). If ion-blocking electrodes are employed, another apparent decrease in the conductivity will show up at even lower frequencies due to the accumulation of diffusing ions at the electrolyte-electrode interface. The shape of the electrode polarisation curve is highly sensitive to surface impurities and depends on the electrode material and the true contact area between the electrode and the solid electrolyte. In addition, the g.b. plateau is often not a straight line but shows a small frequency dependency.<sup>69</sup>

### **DC-Polarisation**

We have to recall that impedance spectroscopy is non-discriminative of charge carriers and is thus, in the most general case, a technique that measures the total conductivity of a sample. In many solid electrolytes only one charge carrier is mobile, *i.e.* its diffusion coefficient is orders of magnitudes higher than that of any other constituent of the material. However, some ion conductors are mixed ionic electronic conductors (MIEC). Albeit the ionic conductivity can be determined by impedance spectroscopy with sufficient accuracy if the electronic conductivity is uncorrelated to the ionic conductivity and order of magnitude lower, *i.e.*  $\sigma_{\text{ion}} = 10^2 \cdot \sigma_{\text{eon}}$  only a 1% error is made but the electronic conductivity might be detrimental for the technical application of such a material as solid-electrolyte in electrochemical cells. Some methods have been established to measure partial conductivities in MIEC in a time consuming manner and might fail in the extreme limits, *i.e.* where one conduction process is almost negligible. However, especially in solid electrolytes, the residual electronic might be detrimental even if many orders of magnitudes smaller than the ionic conductivity. Recent reports highlighted the importance of the residual electronic conductivity in solid electrolytes and suggested a close association of electronic conductivity and the formation of Li dendrites.<sup>70</sup>

The method used to study the electronic conductivity relies on the blockage of any other charge carrier other than electrons (polarons) by ion-blocking gold electrodes. An ionic conductor is contacted by gold electrodes by means of sputtering to form an intimate contact between the microscopically rough surface of the electrolyte and electrodes. A small potential difference is applied to these two electrodes. Every mobile charge carrier will try to follow this electric field, according to its charge. Thus, at the beginning of the polarisation, every mobile charge carrier will

follow the electric field gradient in a direction according to its specific charge. However, while electrons and polarons may pass the Au electrodes, ions cannot. Thus, an ionic concentration gradient builds up until reaching a steady state in which the net movement of the ions is zero, or at least negligibly small. In this steady state, the residual current can only be carried by electrons or polarons, which are electrode-passing charge carriers. This rather simplified model holds if no electrochemical reactions take place. At low potentials, the latter condition is expected to be fulfilled. As the method relies on the measurement of a DC current, it is of utmost importance to have well defined ohmic contacts between the sample and the electrodes. It resembles the method known as Bruce-Vincent methods which is used to determine the transference number of a charge carrier that is not blocked by the electrode in the presence of charge carriers which are blocked by the electrode.

A very important assumption in this theory is that the electric field is only marginally shielded by the ionic charges. If the concentration gradient formed by the ions would not be restricted by crystal chemical constraints, the external electric field could be shielded almost completely. Then, the residual electric current would be caused by a reduced electric field and the calculated resistance would be greater than it is. A contrasting example are liquid electrolytes. As liquid electrolytes permit larger concentration gradients, the electric field is efficiently shielded at the electrodes and the interior of the liquid electrolyte is essentially free of any electric field. The ionic current is driven by the concentration gradient. However, in a solid electrolyte, especially if it is of very high purity and low defect concentration, a case expected for a single crystal, the shielding of the electric field will be negligible and the assumption that the internal electric field equals the externally applied electric field is adequate.

---

*Mit dem Wissen wächst der Zweifel.*  
— Johann Wolfgang von Goethe

---

## 2.4. Structural characterization

X-rays are high-energy photons with wavelengths in the order of 100 pm (1 Å). They are produced by bombarding a target, e.g. copper, with charged high-energy particles, usually electrons. X-rays produced in such a manner will show a broad spectrum of wavelengths superimposed by a certain number of high intensity monochromatic wavelengths (see Figure 12a). The former is known as white radiation (*Bremsstrahlung*) and arises from the collision of electrons with the target whereby some of the electron's kinetic energy is released in the form of X-rays. The lowest wavelength of this continuous spectrum is limited and depends on the highest energy of the electrons. It corresponds to a complete conversion of the electron's kinetic energy to a photon. Higher wavelengths arise from slowing down the electron by collision whereby only a fraction of its kinetic energy is released as a photon.

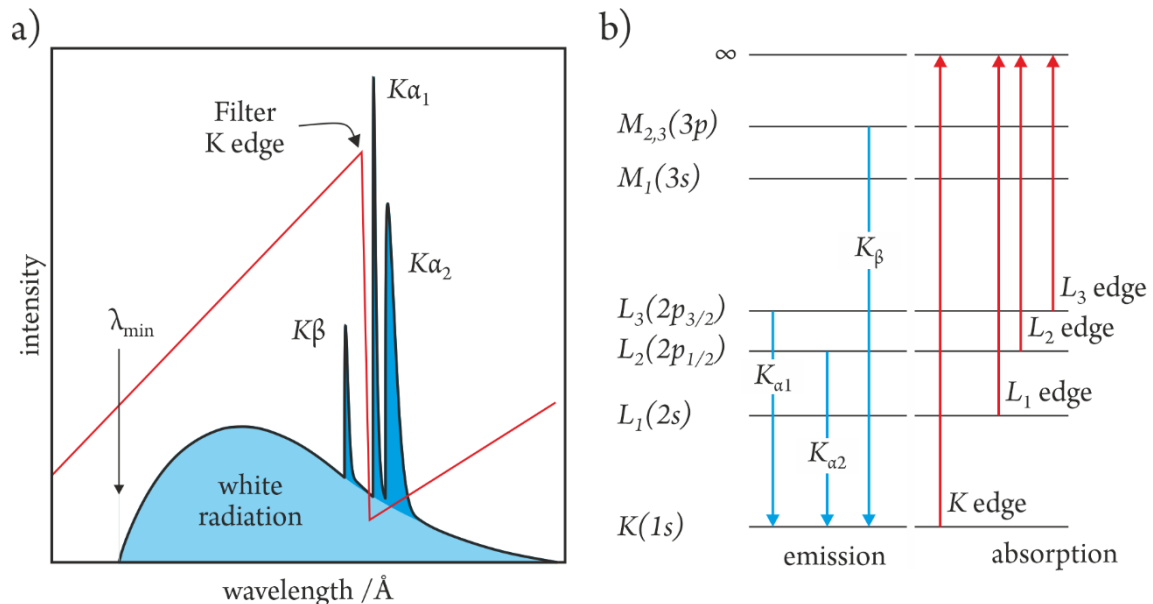


Figure 12: a) Schematic X-ray emission spectrum of Cu (blue area) comprised of white radiation and the characteristic  $\alpha$ - and  $\beta$ -transitions of electrons. The thin red line shows the absorption spectrum near the K edge of a filter (Ni). b) Electronic energy levels of an atom and the characteristic transitions for X-ray emission and X-ray absorption.

The characteristic monochromatic wavelengths, however, are characteristic for the target and the wavelength corresponds to the energy difference between the energy levels of 1s electrons and higher shell electrons. High energetic electrons may ionize the targets' atoms by ejecting an electron from the K shell (1s). Then, an electron from a higher energy level drops down to this energy level and emits the energy difference between the states in the form of an X-ray (see Figure 12b). For X-ray diffraction it is necessary to have monochromatic, or at least dichromatic, wavelengths. The

unwanted white radiation as well as the Cu  $K\beta$  radiation is filtered using a suitable absorption filter, *i.e.* a material with an absorption edge located next to the wavelengths of the Cu  $K\alpha_{1,2}$  radiation (see Figure 12). The X-ray absorption by the filter is based on the famous photoelectric effect. However, if the energy of the incident X-ray is below the ionization energy, the absorption may promote a core electron to a higher, unoccupied, energy level. This excited electron returns to the core shell whereby the excessive energy is released as a photon. This is known as fluorescence and it is a source of secondary X-rays which produce an additional background scattering in X-ray diffraction patterns. For X-ray diffraction an X-ray source with a filter is sufficient while for X-ray absorption spectroscopy a monochromatic, tuneable X-ray source is necessary, *e.g.* from a synchrotron. Monochromatic X-rays are used to study materials making use of their interaction with solids, that is scattering, coherent and non-coherent, and absorption. In X-ray diffraction it is the coherent scattering of X-rays that allows to determine the crystal structure.

#### 2.4.1. X-ray powder diffraction

X-ray powder diffraction is a versatile method to determine the structure, that is the long-range order of solid crystalline materials. The method relies on the scattering of X-rays by the interaction with atoms and may be interpreted in the context of semi-transparent mirror planes. These mirror or lattice planes ( $hkl$  planes) are periodic and intersect the Bravais lattice. Depending on the incident angle,  $\theta$ , of the X-rays and the distance between these planes,  $d_{hkl}$ , the scattering of the photons is either destructive or constructive. Only the latter leads to a strong signal, characteristic reflexes, which can be detected. As exemplified in Figure 13a, an X-ray diffracted at deeper  $hkl$  plane travels a longer way compared to one reflected at the same, but higher located, plane. Only if the extra path, according to Figure 13a, is a whole-number multiple,  $n$ , of the wavelength,  $\lambda$ , constructive interference occurs. This is fulfilled if  $n\lambda = 2a$  where  $2a = 2d_{hkl} \sin \theta$  and directly leads to the famous Bragg law:  $n\lambda = 2d_{hkl} \sin \theta$ . For simplicity, only two planes are shown in Figure 13a and a single angle for which Bragg's law is fulfilled is shown. For all other angles, destructive interference prevails if a sufficient number of  $hkl$  planes are present. However, if only a few  $hkl$  planes are present, as in the case of nanocrystalline materials, the reflexes will be broad, as too few parallel  $hkl$  planes are present to enable complete destructive interference at angles close to Bragg angles. Interestingly this broadening may be used to estimate the crystallite size of nanocrystals according to the Scherrer equation.<sup>71,72</sup>

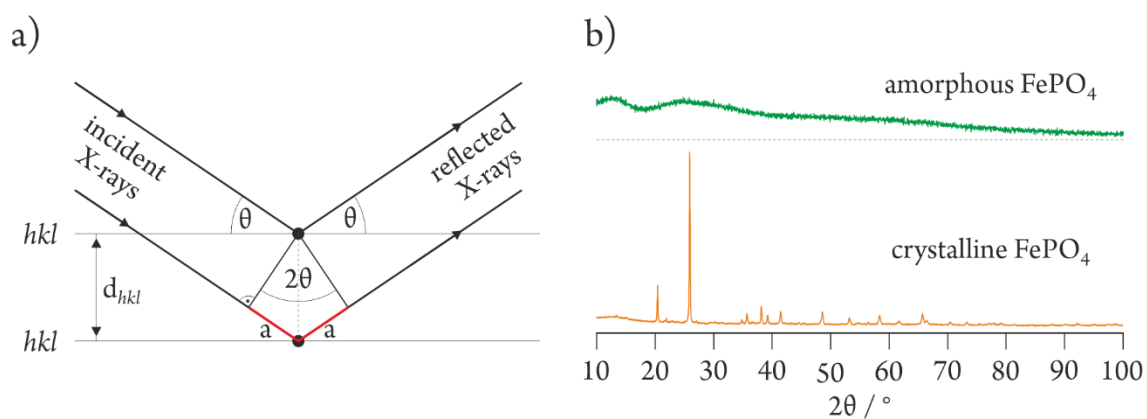


Figure 13: a) Schematic representation of the scattering of monochromatic X-rays at atoms on parallel  $hkl$ -planes. b) Exemplary X-ray powder diffraction pattern of  $\text{FePO}_4$  in its amorphous (top) and crystalline (bottom) state. Only in the crystalline state exhibits strong reflexes are obtained due to the fulfilment of Bragg's law.

In addition to that, Bragg's law is not fulfilled if no  $hkl$  planes are present at all, as in the case of an amorphous sample without any long-range ordering, and thus constructive interference is not given at any angle (see Figure 13a top pattern). This  $\text{FePO}_4$  will, after crystallization, show characteristic reflexes as the atoms are well ordered in the crystalline phase (Figure 13b bottom pattern). The location, breadth, and intensity of the reflexes can be compared to reference patterns and additional information about the cell parameters may be obtained from such patterns via Rietveld refinement. This analysis method is in principle based on the comparison of the observed quantities with modelled or expected quantities deduced from a structural model. During refinement, this model is slightly modified until the observed and expected quantities match, *i.e.* after the fitting routine found a global minimum of deviations between model and measurement.<sup>73</sup> The quality of a fit, and therefore of the refined model, is usually expressed in terms of the goodness of fit (GOF) and the R values it depends on, the weighted profile R value ( $R_{wp}$ ) and the expected R value ( $R_{exp}$ ). As a rule of thumb, a very good fit has been obtained if the R values are below 5% while the GOF should be below 10. However, it is important to note that the obtained structural model must be chemically plausible and that even R values larger than 5% may correspond to a very good model. An excellent discussion about R values and their implications for a model is given in Toby B. H., 2012.<sup>74</sup>

## 2.4.2. Extended X-ray Absorption Fine Structure (EXAFS)

If a material is illuminated with X-rays, some of these X-rays will be absorbed. The absorption coefficient,  $\mu(E)$ , for a given material will vary with the X-ray photon energy,  $E$ . If the energies of the photons are continuously increased, starting from a photon energy where few photons are absorbed, at some energy, the absorption coefficient will rise very sharply. This rise happens at the absorption edge where the energy of the photons is equal to or higher than the binding energy of a core electron of a specific element within the sample (Figure 14). This famous effect, where an electron absorbs a photon and is promoted out of the atom, is known as the photoelectric effect for the description of which Einstein received the Nobel Prize. If the energy of the photons is increased even further,  $\mu(E)$  will decrease and the absorption will show a fine structure which can be deconvoluted in a smooth background and superimposed oscillations. This X-ray absorption fine structure (XAFS) is very rich in information and can be used to quantify atomic distances, coordination number, oxidation state and even the species of the atoms surrounding the absorbing atom. As the absorption edge of an element is located, in terms of photon energy, at the binding

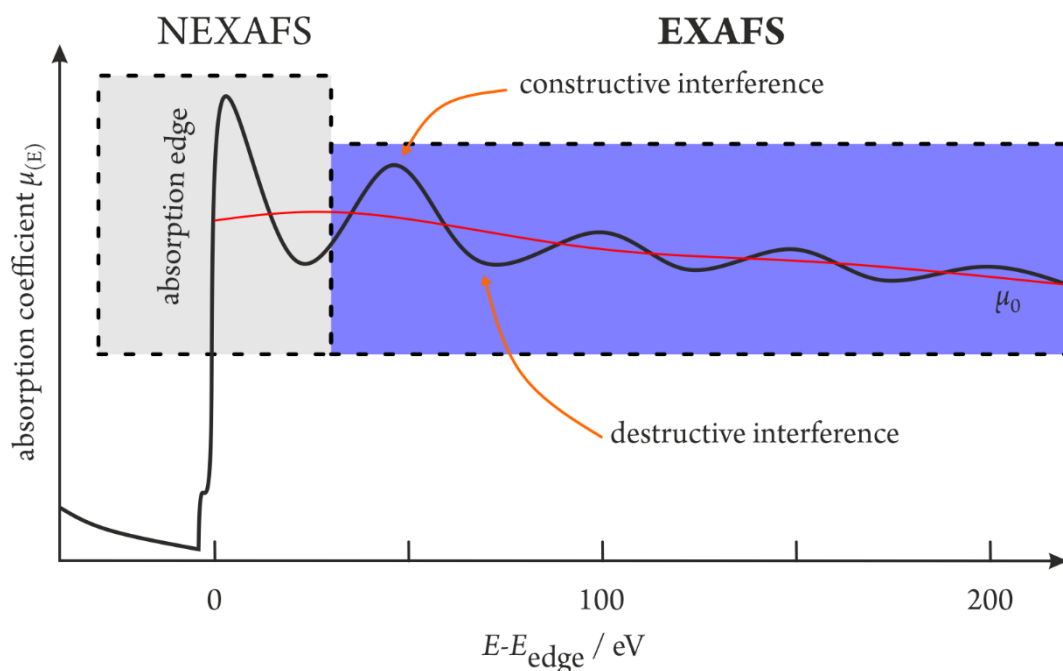


Figure 14: Schematic XAFS showing the absorption coefficient  $\mu(E)$  vs the X-ray photon energy referenced to the absorption edge. At energies slightly below the absorption edge a pre-absorption edge appears as a small bump. At energies above the absorption edge  $\mu(E)$  decreases and shows a fine structure. This fine structure is composed of a smooth background  $\mu_0$  and oscillations resulting from constructive and destructive interference. The area near the absorption edge is called the near edge XAFS (NEXFAS) and the area further away from the absorption edge is the extended XAFS (EXFAS).

energy of the core electrons, XAFS is elemental sensitive. Another very important feature is that crystallinity is not required for XAFS measurements.

Now, there is a very important feature of the absorption coefficient that has not been mentioned so far. The absorption of an X-ray photon by a core electron depends on the availability of a corresponding state for the photoelectron to occupy. That is, the electron has to go somewhere and the absorption of a photon can only occur if a state with the right energy and angular momentum exists. Therefore, the energy of the absorbed photon has to fulfil specific criteria; its energy has to allow the transition between two states. The primary state is well defined by the binding energy of the electron to the atom and is hardly changed by the atomic neighbourhood. The second state, however, is highly influenced by the imminent surrounding of the absorbing atom. This becomes clear if we consider that a photoelectron could be scattered back to the electron-emitting atom, by the neighbour atoms. This interaction of the neighbouring atoms with the photoelectrons will alter the states that can possibly be occupied and therefore, will influence the absorption coefficient  $\mu(E)$ . This relation lies at the heart of XAFS.<sup>75</sup>

Without going further into details of the physical relations governing the XAFS it has to be mentioned that XAFS is a local probe that does not see much further than about 1 nm from the absorbing atom.<sup>76</sup> Most importantly, the oscillations seen in XAFS consist of different frequencies that correspond to different distances for the coordination shells. Therefore, the Fourier transform is an important method for analysing the XAFS data.<sup>77</sup>

For EXAFS, the oscillations of the absorption coefficient at energies above the absorption edge are defined by the fine-structure function  $\chi(E) = (\mu(E) - \mu_0(E))/\Delta\mu_0(E)$  where  $\Delta\mu_0(E)$  is the difference between the baseline  $\mu_0(E)$  at the absorption edge (see Figure 14). For a better understanding and representation, the energy of the X-ray as well as the energy of the photoelectron is best represented as a wave with a wavenumber  $k$  given by  $k = \sqrt{2 \cdot m \cdot (E - E_0)}/\hbar$  where  $m$  is the mass of the electron,  $E_0$  is the absorption edge energy and  $\hbar$  is the reduced Planck constant. Now the oscillations can be represented as a function of the wave vector  $k$  as  $\chi(k)$ . The oscillations seen in  $\chi(k)$  correspond to the near-neighbour coordination shells and can be modelled by  $\chi(k) = \sum_j \left( N_j f_j e^{-2k^2 \sigma_j^2} / k R_j^2 \right) \sin[2k R_j + \delta_j(k)]$  where  $N$  is the number of neighbouring atoms,  $f(k)$  and  $\delta(k)$  are scattering factors of the atoms surrounding the excited atom,  $R$  is the distance between



the excited atom and the surrounding atoms and  $\sigma^2$  describes the disorder of the distance  $R$  and can be interpreted as a mean-square relative displacement.<sup>78</sup> Taken together, the information that can be derived from EXAFS are the number of the nearest-neighbours,  $N$ , the radial distance between the absorbing atom and its neighbours,  $R$ , as well as the disorder of this distance,  $\sigma^2$ , *i.e.* its variation. Realizing that  $\chi(k)$  is proportional to  $R^{-2}$  justifies calling EXAFS a method that is most sensitive to the imminent surrounding of the absorbing atoms and is thus very helpful in investigating local disorder.

## 2.5. Positron Annihilation Lifetime Spectroscopy (PALS)

A positron is the antielectron characterized by the same spin ( $1/2$ ) and the same mass as the electron but with opposite charge. In the radioactive  $\beta^+$  decay of certain elements like  $^{22}\text{Na}$  high-energy positrons are emitted. Along with the positron, a high-energy photon with energies in the order of MeV is emitted. This photon marks the “birth” of a positron and is important for the measurement of its lifetime as also the “death” of a positron is accompanied by the emission of photons. The lifetime of a positron is very short, in the order of a few 100 ps to a few ns, and it highly depends on its imminent surroundings, *i.e.* the local electron density. After radiation of positrons into a solid, these high-energy particles are thermalized by e.g. inelastic scattering and diffuse within the solid in their ground state. These ground state positrons will most probably annihilate by recombining with an electron, in the electron-positron-annihilation process, in which the particles' masses are converted to two photons with 511 KeV. These photons are emitted in opposite directions, and small deviations from this  $180^\circ$  geometry can be correlated with the angular momentum of the annihilating electron; the contribution of the positron is negligible. The interaction of a positron with an ionic solid, from entering the solid to annihilation, is exemplarily shown in Figure 15a. The lifetime of the positrons in the studied material highly depends on its nanoscopic structure and electron density. Recalling that the thermalized positron diffuses in the solid we can easily think of two fates for the positron. One is the annihilation with an electron in the bulk, and the other is the trapping of the positron in a region of decreased electron density, *i.e.* vacancies. The latter case will typically postpone the annihilation of the positron and the resulting lifetime depends on the nature of the trap, *i.e.* it can be correlated with charge and size of the trap. Raw lifetime spectra are qualitatively shown in Figure 15b for two cases. In the first case (blue squares), positrons only annihilate in delocalized states, that is, in the bulk and the spectrum shows only one component. In the second case (red circles), only a fraction of the positrons annihilates in the bulk with the characteristic lifetime. The rest of the positrons are trapped in vacancies where they annihilate after a prolonged lifetime.

In a typical PALS experiment the annihilation of at least  $10^6$  positrons is recorded. Conveniently, the generation as well as the annihilation of a positron is accompanied by the emission of at least one photon. Detecting these photons in a time-dependent manner allows to easily determine the lifetime of a single positron. However, this requires the activity of the source to be sufficiently low,

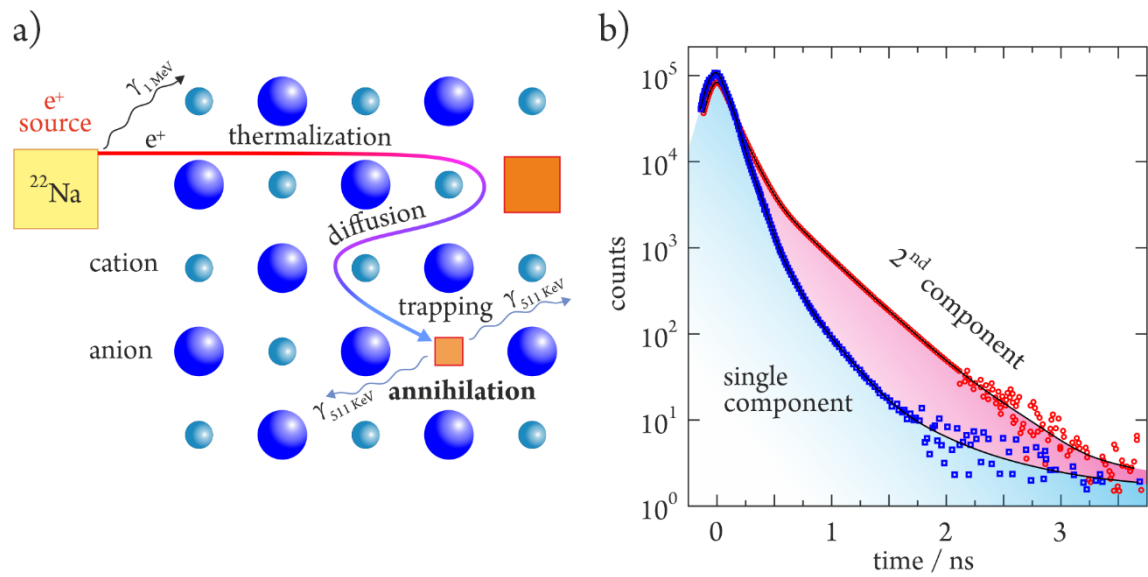


Figure 15: a) Schematic representation of the lifecycle of a typical positron injected into an ionic solid in a typical PALS experiment. After thermalization, simply speaking slowing down, of the positron, it diffuses within the solid until it annihilates with an electron. The lifetime-prolonging trapping of a positron in a localized state, a negatively charged cation vacancy, is shown. In any case, the annihilation leads to the emission of two photons. b) Exemplary lifetime spectrum of a PALS experiment. The histogram shows the counts of death-rays, emitted during annihilation, as a function of the positron lifetime. In one case, only a single component, that is a single Gaussian distribution of lifetimes is shown (blue squares). In the other case, a superposition of two Gaussian lifetime distributions is shown (red circles).

*i.e.* the mean time between the generation of the positrons must be much longer than the positron lifetime. After background correction, the lifetime spectra can be deconvoluted into specific components. Within the PALSfit software, this is done on the basis of an exponential decay model.<sup>79</sup> Considering the spectrum with two components as shown in Figure 15b the analysis would yield a lifetime and relative intensity for both components.

## 2.6. Synthesis of solids via precipitation

Precipitation is the formation of insoluble salts from a solution. It occurs when the solubility limit of a dissolved species is exceeded. The solubility of a species in a specific liquid depends on many chemical and physical factors such as temperature, polarity of the solvent, and the presence of other solubilized species. Furthermore, the solubility limit can be achieved by evaporating the solvent, which leads to an increase of the concentration. Also, the addition of flocculants may lead to precipitation. Furthermore, precipitation can occur if an antisolvent, which significantly decreases the solubility of the dissolved species, is added. A prominent example is the precipitation of DNA by the addition of EtOH. In general, the precipitation describes the process in which soluble species become insoluble by forming a salt. The formation of a solid compound decreases the concentration of solubilized species until a steady state equilibrium is attained. At this equilibrium, the species concentrations are at their solubility limits. For a chemical equilibrium  $A_xB_y \rightleftharpoons xA + yB$  the solubility product,  $K_{sp}$  for the compound  $A_xB_y$ , is defined as follows  $K_{sp} = [A]^x[B]^y$  where  $[A]$  and  $[B]$  are the concentrations of A and B in a saturated solution.

The precipitation follows a two-step mechanism. First, a solid phase has to be formed in the nucleation step. Nucleation requires energy for the formation of a new phase boundary. These nuclei will subsequently grow in size and often form agglomerates.

Also, growth of nuclei is a thermodynamically driven process. The higher the volume-to-surface ratio of a spherical particle is, the lower the energy. Thus, with time, large particles grow larger on the expense of small particles, which dissolve completely. This process of precipitate ageing is known as Ostwald ripening. Nucleation is a process determined by kinetic and its rate constant depends on the different factors, factors that can be controlled. Nucleation may start at nucleation sites at interfaces, heterogeneous nucleation, and within the liquid phase by forming a solid phase. Albeit nucleation is a stochastic process and occurs randomly its occurrence may be increased by decreasing the nucleation energy barrier. Within the classical nucleation theory, the rate of nucleation,  $R$ , can be expressed by

$$R = N \cdot Z_f \cdot r \cdot \exp\left(\frac{-\Delta G^*}{k_B \cdot T}\right) \quad (23)$$

Where  $N$ ,  $Z_f$  and  $r$  are the number of nucleation sites, the Zeldovich factor and the rate constant of the species flux attaching to the nuclei.  $\Delta G^*$  is the free energy of the nucleation barrier and  $k_B \cdot T$  are the Boltzmann constant and the absolute temperature. Additionally, it is important to note that formed nuclei are metastable until reaching a critical size. This is due to the fact of two separable thermodynamic contributions to the total Gibbs free energy, the interface energy, and the bulk free energy (see Figure 16a).

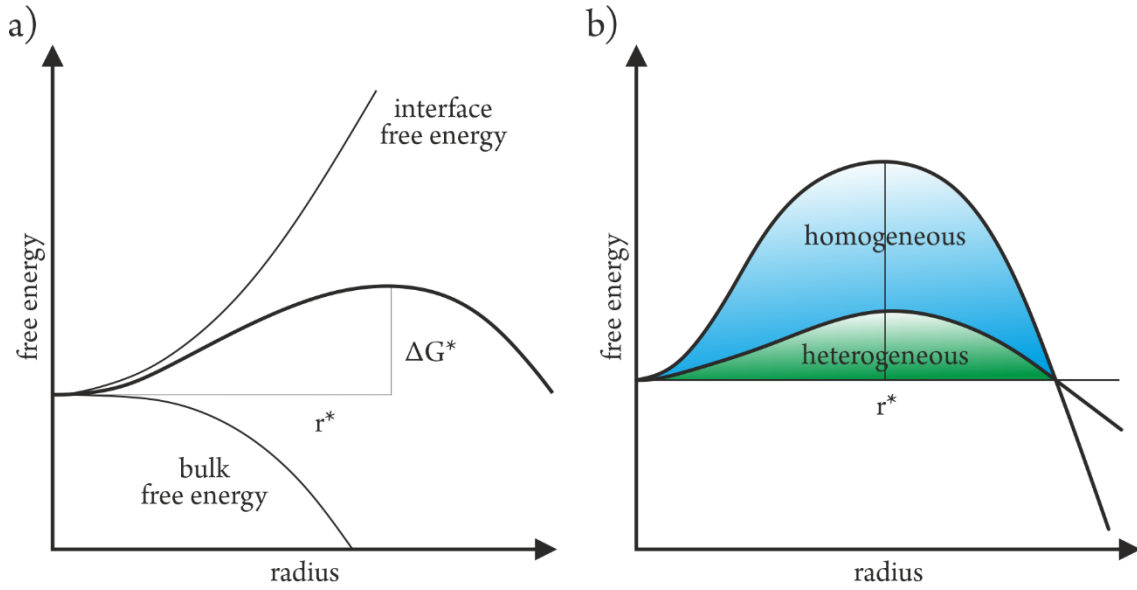


Figure 16: a) Free energy as a function of the particle's radius. The contributions to the Gibbs free energy of the surface and the bulk depends on the particles' radius. b) Heterogeneous precipitation decreases the nucleation barrier by decreasing the interface term.

While the former is proportional to the surface of the spherical particle and scales with  $r^2$ , the latter is proportional to the particles' volume and scales with  $r^3$ .

$$\Delta G = \frac{4}{3} \cdot \pi \cdot r^3 \cdot \Delta g_v + 4 \cdot \pi \cdot r^2 \cdot \sigma \quad (24)$$

$\Delta g_v$  is the difference in free energy per unit volume between the thermodynamic phase nucleation is occurring in, and the phase that is nucleating.  $\sigma$  is the energy of the interface between the nucleus and its surroundings, which is always positive. A particle is thus only stable if its radius is larger than the critical radius  $r^*$ . The associated  $\Delta G^*$  is the free energy of the particle with a radius  $r^*$  and is the turning point at which either growth or dissolution occurs predominantly.

Heterogeneous nucleation is often faster than homogeneous nucleation as the nucleation barrier is significantly decreased (Figure 16b). In heterogeneous nucleation, the surface area is small and

simply that of a sphere. In heterogeneous nucleation, the surface area is much larger as it also comprises the surface onto which it is nucleating. For the precipitation of amorphous  $\text{FePO}_4$  we made use of a polyanionic template, the genetically modified bacteriophage, as a heterogeneous template to produce nanowire-shaped precipitates.

## 2.7. Microbiological and molecular biological methods

### 2.7.1. The bacteriophage M13

This bacteriophage was found 1963 in a sample collected in a sewer in Munich (Germany).<sup>80</sup> It is a filamentous phage which almost exclusively infects *Escherichia coli* (*E. coli*). The filamentous bacteriophage has a very narrow diameter of ~9 nm and a length of almost 1  $\mu\text{m}$ . The length of the phage is quite flexible and fits, within certain limits, the length of the phage's DNA (Figure 17). Thus, if the DNA length is changed, the length of the phage changes accordingly. However, the phage was recognized by different disciplines for different reasons. While it is a useful tool in molecular biology for its efficient shuttle capabilities, it was much later recognized in materials science as biological template. For this, its filamentous shape is of utmost interest. Several groups used the phage as a template in the synthesis of nanostructures materials.

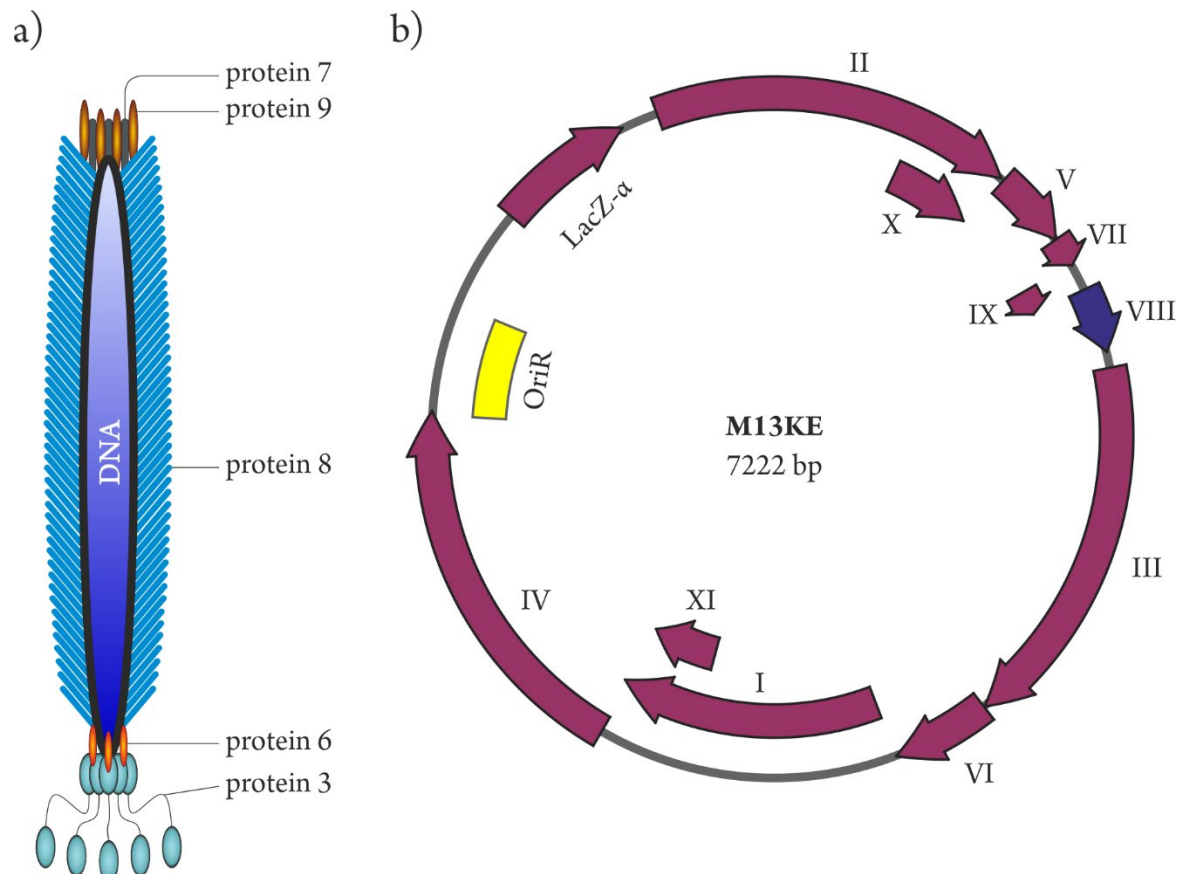


Figure 17: a) Schematic representation of the filamentous bacteriophage M13. Its compact form, shaped like a thread, is assembled around its ssDNA; protein 8 covers the hull while both ends are covered by two tip-proteins. b) Schematic representation of the circular genome of the bacteriophage M13. Arrows and roman numbers mark the open reading frames which code for the indicated proteins; OriR denotes the origin of replication.

While the name bacteriophage suggests that the phage kills the infected cell upon release, this is not the case for bacteriophage M13 which is continuously secreted from infected cells (see Figure 18). The bacteriophage can infect *E. coli* by interaction with *E. coli* outer membrane proteins (OMPs) and injects its single-stranded DNA (ssDNA) into the host cell. Having its ssDNA injected into the host cell, the host will synthesize a complementary strand complementing the ssDNA to form a double-stranded DNA (dsDNA), which is also known as replicative form.

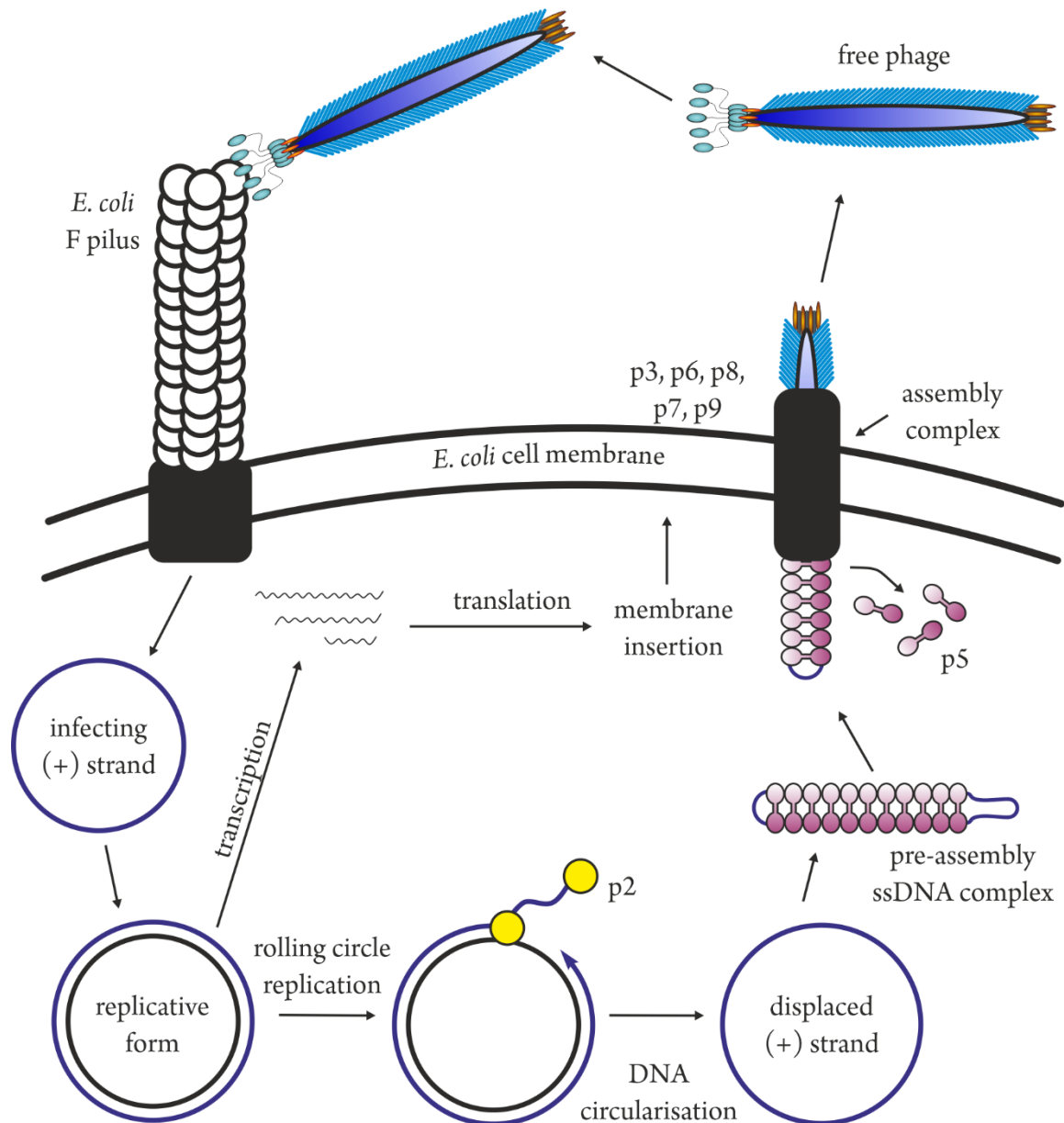


Figure 18: Overview of the lifecycle of the bacteriophage M13. After infecting an *E. coli* cell via the F pili, the ssDNA is released in the cytoplasm where its complementary strand is synthesised by the host proteins to give the replicative dsDNA form. Phage-specific proteins are expressed and initiate the rolling circle replication to produce ssDNA which is packed in a pre-assembly complex. Finally, the phage is assembled and secreted, via the assembly complex, and released into the surroundings. Inspired by<sup>81</sup>



This circular dsDNA carries all the information for the synthesis of the phage specific proteins. Some of the proteins serve only structural purposes and as such will form the proteinaceous hull of the bacteriophage. Other phage-specific proteins are involved in the replication as well as the regulation of aids in packing the ssDNA. The DNA of the bacteriophage is rather short with only 7,222 base pairs (bp). The bacteriophage can be engineered easily by means of cloning. For such an approach, the bacteriophage is amplified in *E. coli* in a liquid culture and, as the phage will be extruded into the supernatant, the phage can be isolated from the liquid phase after separation of cellular components.

#### 2.7.2. Cultivation of *E. coli* and amplification of M13

*E. coli* strains were routinely grown on LB-Lennox agar plates or in liquid media; in both cases, the media were supplemented with 50 µg / ml tetracycline (LB-Tet<sup>50</sup>). Cells were allowed to grow at 37 °C on agar plates whereas liquid cultures were aerated by shaking at 300 rpm.

Pre-cultures of *E. coli* were generated by inoculating 5 mL of LB-Tet<sup>50</sup> with a single colony of *E. coli* grown overnight at 37 °C on LB-Tet<sup>50</sup> agar plates. Sterile controls were routinely run in parallel. After incubating the pre-culture overnight, the cell density was determined by UV-Vis spectroscopy using quartz-glass cuvettes. The culture was diluted with the sterile control, which also served as a baseline (blank), to yield absorption values in the linear range in which Lambert-Beer's law holds. A culture with 10<sup>9</sup> cells / mL corresponds to an OD<sub>600</sub> of 0.5; here OD<sub>600</sub> is the optical density of the culture at a wavelength of 600 nm. The main culture was then infected to an OD<sub>600</sub> of 0.05. Cultures were grown in liquid media until reaching the early logarithmic growth-phase<sup>2</sup>, characterized by an OD<sub>600</sub> of about 0.2, and infected with bacteriophages using a multiplicity of infection (MOI) of 1. Within this phase, the *E. coli* cells are in an optimal state for infection. Using a MOI of 1 ensured that every cell is, in the mean, infected by only one bacteriophage. Infected cells were incubated for 4 h to allow high yield of bacteriophage M13 but decrease to occurrence of spontaneous mutations. To harvest the phages from the culture, cells were separated by centrifugation. The supernatant was brought to 4% w/v PEG-800 and NaCl (0.5 M) to precipitate the bacteriophages. Precipitation was enhanced by cooling (4 °C) and after over-night incubation

---

<sup>2</sup> The early log-phase is characterized by very healthy, fast-dividing cells exposed to optimal growth conditions.

the precipitates were pelleted by centrifugation. To increase the purity of the phages, the pellet was resuspended in TBS and reprecipitated before usage.

### **Extraction and quantification of M13**

Infected cell cultures were cooled to 4 °C and cells were spun down at 5,000 g for 10 min at 4 °C. The supernatant was transferred into a fresh tube and spun down again. The resulting supernatant was mixed with the PEG/NaCl-stock solution to precipitate phage particles over night at 4 °C. The cloudy solution was spun down at 12,000 g and 4 °C for 10 min and the supernatant was discarded. After resuspending the pellet in TBS, remaining cellular debris was removed by centrifugation at 4 °C and 15,000 g for 10 min. Phages within this supernatant were reprecipitated and stored at 4 °C in TBS.

The concentration of M13 in the isolates was determined by two different methods. The first method is based on the capability of the bacteriophages to infect *E. coli* cells and the concentration is deduced by the number of infected *E. coli* cells. The second method is a spectroscopic method and is based on the specific absorption of DNA at 260 nm wavelength and the absorption of aromatic amino acids at 280 nm wavelength. The former methods give concentrations as PFU / mL, Plaque forming units (PFU), and the latter concentrations as particles / mL. To identify infected *E. coli* cells, a clever trick is used.

The host strain has a deletion in the *lacZ*-gene which codes for a  $\beta$ -galactosidase and cannot produce enzymatically active galactosidase. Such strains will remain colourless if plated on agar plates containing IPTG and X-Gal. While IPTG induces the expression of genes in the *lac*-operon, in which *lacZ* is located, X-Gal is a colourless indigo dye that, if cleaved by a  $\beta$ -galactosidase turns blue. The phage carries the  $\alpha$ -complement of the  $\beta$ -galactosidase, *i.e.* the missing piece for the enzyme to become active. Now, in an infected cell, both fragments of the  $\beta$ -galactosidase will be expressed, and the enzyme will be fully functional. Cleaving of X-Gal colours the whole monoclonal *E. coli* colony which grows on the agar plate and makes these cells as infected. Given that the MOI was kept well below 1, the number of blue CFU (colony forming units) corresponds to the number of infectious phages if the dilutions are considered.

The spectroscopic method relies on the UV-Vis absorption pattern of pure M13 isolates in water. The concentration is calculated from the absorption at a wavelength of 269 nm after correction by

subtracting the absorption at 320 nm.<sup>82</sup> From the specific absorption coefficient of the bacteriophage M13, the concentration of virions per ml can be calculated according to virus particles per mL =

$$\frac{A_{269} - A_{320}}{\#bp/virion} \cdot 6 \cdot 10^{16}.$$
<sup>83</sup>

### 2.7.3. Cloning and genetic engineering

Under certain conditions, cells may take up foreign DNA from their surroundings. This capability is termed competence and can be invoked by specific treatments of the cells. Obviously, this process requires the large polyanionic DNA-molecule to pass through the semipermeable outer and inner membrane of the Gram-negative *E. coli* cells. Various methods have been developed which allow efficient uptake of the DNA and thus increase the transformation rate. In any case, the cells are mixed with a comparatively large quantity of DNA molecules and treated by e.g. an electric shock<sup>84</sup> (electroporation) or thermal shock in a specific environment<sup>85</sup> (chemical methods)<sup>86</sup>. While the exact mechanism of DNA uptake is not completely understood, it is evident that the membrane is destabilized by the heat-shock and thereby allows the uptake of the large extracellular DNA. This process was first reported by Mandel and Higa<sup>87</sup> in 1970 and is dependent on the presence of Mg<sup>2+</sup>. As the outer membrane of *E. coli* contains negatively charged lipopolysachharide (LPS), and the DNA itself is also negatively charged the addition of greater amounts of divalent cations (Mg<sup>2+</sup>, Ca<sup>2+</sup>) is important to allow tight contact between the outer membrane and the DNA.

#### **Transformation of chemically competent cells**

Cells from a mid-logarithmic growth phase culture (OD<sub>600</sub> = 0.3) were made competent following a slightly modified method after Mandel and Higa. Cells were chilled on ice, pelletized (2,220 g, 10 min, 4 °C), resuspended in a chilled CaCl<sub>2</sub>-solution (75 mM) and let stand for 30 min on ice. Consecutively, the cells were pelletized and concentrated 80-fold by resuspending in a reduced volume of a storage solution (75 mM CaCl<sub>2</sub>, 15% w/v glycerol). These cells were either used directly or stored at -80 °C.

Chemically competent cells were thawed on ice after which DNA was added to the cells. After a 30 min coincubation on ice, the cells were transformed by heat shock. The heat shock was performed for 45 sec by immersing the cell suspension containing the DNA into a water bath heated to 42 °C. The cells were chilled on ice for 5 min before 950 µL of fresh LB medium, heated to 37 °C,

was added. After 1 h of incubation at 37 °C, the cell suspension was plated in dilutions onto LB-IPTG/X-Gal agar plates and incubated over night at 37 °C. The next day, blue plaques were transferred on fresh agar plates and used to prepare ONCs of the clones.

Chemically competent *E. coli* XL-1 Blue cells were transformed with the in-situ circularized dsDNA of bacteriophage M13.

### **Isolation of M13 ssDNA from phage particles and dsDNA from infected *E. coli***

The genome of bacteriophage M13 can also be extracted in its natural ssDNA form from the phage particles. The isolation for ssDNA was mainly done for cloning purposes. A phage isolate, collected from the cell free supernatant of an infected *E. coli* culture, was used after purification twice with the PEG/NaCl-method. The precipitated phage pellet, isolated from 10 ml culture supernatant was resuspended in 400 µL NaI-buffer and mixed with 1 mL absolute EtOH. The high NaI concentration disrupts the proteinaceous hull whereas the ssDNA precipitates in the presence of EtOH and high salt concentrations. After 10 min of incubation at RT, the ssDNA is spun down at 18,000 g and 4 °C for 10 min. The ssDNA pellet is carefully overlaid with 500 µL 70% EtOH to remove excessive salt and spun again for 5 min. After removal of the supernatant, remaining EtOH is allowed to evaporate, and the pellet is carefully solubilized in 30 µL TE-buffer and used immediately or stored at -20 °C.

For cloning M13KE, dsDNA was isolated from infected *E. coli* ER2738 cultures by the method of Birnboim and Doly<sup>88</sup>. Infected cells carry copies of bacteriophage M13KE dsDNA as circular plasmids in their cytoplasm. For extraction, cells are pelletized from the culture and resuspended in lysis buffer I. Adding lysis buffer II leads to the lysis of the cell membrane due to the detergent SDS, which solubilizes parts of the membrane, and the harsh pH increase. As the cell membrane breaks, proteins and DNA are released from the cell and are denatured in the alkaline solution. To protect the DNA from irreversible damage, its exposure to this alkaline condition is kept short. The addition of the lysis buffer III neutralizes the basic solution while denatured proteins and membrane fractions precipitate along with the large genomic DNA of *E. coli*. After centrifugation (15,000 g, 4 °C, 10 min) to separate the precipitates from the suspension, the small circular dsDNA of M13KE is isolated from the supernatant by the addition of EtOH. After pelletizing the dsDNA by centrifugation (18,000 g, 4 °C, 10 min) it is carefully overlaid with 70% EtOH and finally resuspended in TE-buffer for usage or for storage at -20 °C.

## **DNA agarose gel electrophoresis**

Isolated DNA was analysed after agarose gel electrophoretic separation and staining with Midori Green (Nippon Genetics). To produce gels, 0.3 g agarose were dissolved in 30 mL 1-fold TAE-buffer by heating in a microwave oven. The gel was allowed to cool down before adding Midori Green and was cast into a mould where an 8-slot comb was inserted to generate pockets for sample injection. The solidified gels were immersed in 1xTAE-buffer and electrophoresis was conducted applying a potential difference of 70 V. Within this pH-buffered solution (pH 8), the DNA is negatively charged and thus migrates in the electric field. The negatively charged phosphate backbone results in a constant charge-to-mass ratio while the length and form of the DNA molecule influences its retention in the agarose gel. Samples were diluted appropriately, mixed with 6x gel loading dye purple (NEB) and loaded into the pockets of the gel. For crude concentration and size estimation, 1 µg of a  $\lambda$ \*BstEII standard (NEB) was applied to a separate gel pocket. After separation of DNA molecules via electrophoresis, stained DNA was visualized under UV-light. After electrophoresis, DNA molecules are focused as bands in the gel. Comparing the intensity of the unquantified DNA band with the intensity of a band of known DNA amount allows a crude quantification of DNA amounts. Most importantly, this method is very useful to qualitatively characterized the DNA isolate. By comparing the vertical position of the DNA band in the isolate with standard bands of known size allows estimation of the size. Furthermore, contaminants of foreign DNA molecules, *e.g.* genomic DNA, or degradation products are visible in developed gels.

## **Amplification and site-specific mutation of M13 DNA**

The polymerase chain reaction (PCR) was used to modify the bacteriophage M13 genome. A typical DNA-dependent DNA-polymerase can only prolong existing DNA molecules by means of using a template. In-vivo small RNA-molecules are synthesised by a primase. These primers are then elongated by the DNA-polymerase. In-vitro, synthetic single stranded DNA molecules are used as primers. These primers are designed to be complementary to a part of the region of interest in the genome (see Figure 19). In a classical PCR experiment, a DNA-dependent DNA-polymerase, dNTPs (monomers), primers and a DNA template are combined in a buffered solution.

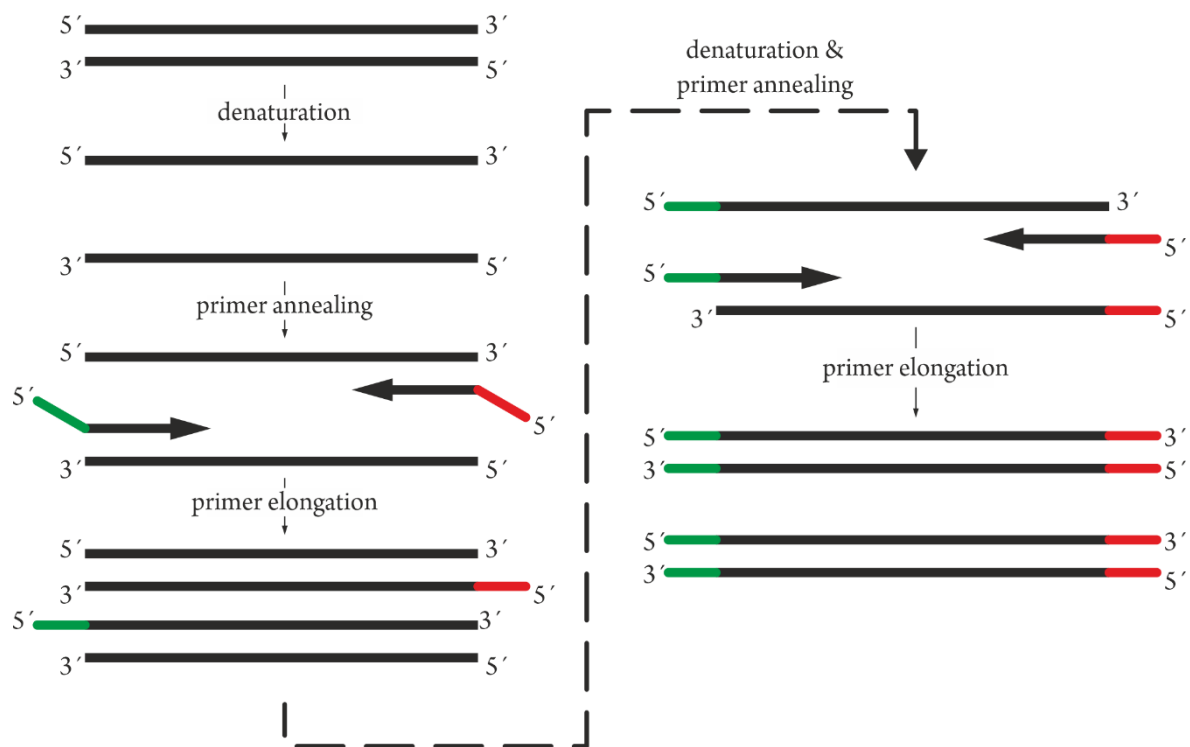


Figure 19: Exemplar representation of the individual steps of a polymerase chain reaction amplification. The double-stranded DNA template is thermally denatured to yield two single strands. The primer with 5' overhangs (red & green) can bind at lowered temperatures and are elongated by the DNA-polymerase. After the second PCR cycle, the final product is obtained, a linear fragment flanked by the overhangs.

Via defined heating and cooling cycles (see Table 1), the double-stranded template can be denatured so that the strands separate, and the single-stranded primers can bind to the complementary region. In the following step, the polymerase elongates the primers until the complete region of interest is covered. This cycle is repeated for a couple of times to produce the amplicon in sufficient quantity. Importantly, every amplicon can serve as another template in the subsequent step and thus the amplification is exponential.

Table 1: Temperature program used for PCR to amplify and modify the genome of the bacteriophage M13.

Temperature / °C	Time / s		Sequence
98	30		Initial denaturation
98	10	25 cycles	Denaturation
69	15		Primer annealing
72	180		Primer extension
72	120		Final extension
4	∞		Storage

Furthermore, the primers are part of the final products and thus, contain every sequence that is contained within the primers. Therefore, small mutations such as the insertion or the deletion of base triplets can be achieved easily.<sup>89</sup> Most importantly, also circular templates may be used and will yield linear dsDNA. After phosphorylation of the 5'-ends, the linear fragments may be circularized by a ligase to produce circular DNA molecules.

#### 2.7.4. Culture media, buffer solutions and general stock solutions

##### **LB-Lennox media (liquid, solid, soft)**

For the culture medium 5%w/v yeast extract, 5% w/v NaCl and 10% w/v bacto-tryptone were dissolved in distilled water and sterilized in an autoclave. Before sterilization of the media agar was added for solid growth media (15 % w/v) or soft overlay (7 % w/v)

##### **IPTG/X-Gal-Stock solution**

IPTG (Isopropyl  $\beta$ -D-1-thiogalactopyranoside) and X-Gal (5-Bromo-4-chloro-3-indolyl  $\beta$ -D-galactopyranoside) were dissolved in N,N-Dimethylformamide and stored at -20 °C. The 1000-fold stock solution contained 50 mg/mL IPTG and 40 mg/mL.

##### **Tetracycline-Stock solution:**

50 mg tetracycline hydrochloride was dissolved in a solution containing 50% v/v absolute EtOH and 50% v/v purified water (Millipore, > 18 M $\Omega$  cm). Sterilization of the stock solution was achieved by sterile filtration through a syringe filter with a pore size of 0.22  $\mu$ m. Aliquots were stored at -20 °C.

##### **EDTA-Stock solution**

EDTA (Ethylenediaminetetraacetic acid disodium dehydrate, FISHER Scientific) was dissolved in purified water (Millipore, > 18 M $\Omega$  cm) and a 5 M NaOH solution was used to adjust the pH to 8.0. The 0.25 M EDTA solution was sterilized in an autoclave and stored at room temperature.

##### **PEG/NaCl-Stock solution**

20 g PEG-8000 and 14,61 g NaCl were brought to 100 ml with distilled water to yield a 20% PEG/2.5 M NaCl stock solution which was heat sterilized in an autoclave.

### **TBS (pH 7.5)**

A Tris-buffered saline solution was obtained by dissolving tris(hydroxymethyl)aminomethane (Tris) and NaCl in distilled water. The pH was adjusted to 7.5 with concentrated hydrochloric acid and the final buffer solution heat sterilized. This 50 mM Tris, 150 mM NaCl solution was stored at room temperature.

### **TBS (pH 8.0)**

Same as above but the pH of the solution was adjusted to 8.0.

### **TE-buffer**

The buffered solution was obtained by mixing TBS (pH 8.0) and the EDTA-Stock solution to yield a 10 mM Tris-buffered solution containing 0.5 mM EDTA.

### **NaI-buffer**

4 M NaI, 10 mM Tris pH 8.0, 2.5 mM EDTA

### **TAE-buffer**

The pH value of the 2 M Tris, 50 mM EDTA solution was adjusted to 8 by the addition of glacial acetic solution. The solution was heat sterilized and stored at room temperature. For its usage, it was diluted 50-fold.

### **Lysis buffer I**

This buffer contains 50 mM glucose, 10 mM EDTA (pH 8.0) and 25 mM Tris-Cl (pH 8.0) and was sterilized by filtration and stored at 4 °C.

### **Lysis buffer II**

This buffer was prepared fresh just before usage by mixing a 2% (w/v) SDS (sodium dodecyl sulphate) solution with a 0.4 M NaOH solution in a 1:1 ratio.

### **Lysis buffer III**

This buffer contains 3 M KAc (potassium acetate) and 2 M acetic acid and is stored at 4 °C.

---

*Es wird ja fleißig gearbeitet und mikroskopiert, aber es  
müsst mal wieder einer einen gescheiterten Gedanken haben.  
—Rudolf Virchow*

---



### 3 Results and Discussion

---

Many of the obtained results could be published already in peer reviewed scientific journals and the corresponding publications are included. As the results have been published, there is no further discussion of the data outside of the paper, but every paper is introduced by a short summary highlighting the major finding.

The unpublished data is represented in a style similar to a paper *i.e.* a draft version of the paper. However, these draft versions are less condensed and thus contain more information than would be found in most publications.

---

*Even when all the experts agree,  
they may well be mistaken.*  
— Bertrand Russell

---

### 3.1. Glass in Two Forms: Heterogeneous Electrical Relaxation in Nanoglassy Petalite

Glasses represent an extraordinarily interesting group of ion conductors when it comes to studying microscopic effects influencing ionic conductivity. This is especially true as glasses are more flexible in their stoichiometry than ceramic ion conductors are. A glass mainly consists of a glass former such as silicate and additionally contains various amounts of network modifiers which either integrate into the network or break the network. In the case petalite, the network former is  $\text{SiO}_2$ , and the modifier is  $\text{Al}_2\text{O}_3$  which integrates into the network while  $\text{Li}_2\text{O}$  acts as a network breaker that effectively reduces the connectivity within the glass. The network breaker  $\text{Li}_2\text{O}$  is the only component introducing mobile Li ions into the system and therefore the number of charge carriers can be controlled by the amount of  $\text{Li}_2\text{O}$ . Knowing the charge carrier density permits the calculation of the charge carrier mobility from conductivity measurements. The separation of these two quantities is otherwise, by nature, fraught with difficulty.

Glasses show wider compositional flexibility than their crystalline counterparts do and per definition, lack long-range order. The lack of long-range order grants a higher degree of freedom and this is reflected in the thermodynamic properties of a glass. For example, the entropy of a glass can change during various treatments and greatly depends on its history. We must consider a glass as a metastable solid. It is usually obtained by quenching a melt, *i.e.* cooling the melt very rapidly. Via quenching, the liquid arrests so fast that most atoms freeze in their momentary positions. The short-range order resembles that of the liquid and the high entropy of the liquid state is partly preserved within the solid. The latter influences the diffusion of ions within the glass network and thus influences the ionic conductivity of the glass.

Such a glass could be called a high-entropy glass. From a thermodynamic point of view it is not stable, however, slow structural relaxation kinetics keep the glass in its high-entropy state. If such a glass is thermally annealed, its ionic conductivity decreases.<sup>23</sup> At elevated temperatures, still below the glass-transition, the kinetic is accelerated noticeable and the glass relaxes. However, such a relaxation can also be induced by mechanical treatment. High-energy ball milling also leads to a decrease of the ionic conductivity, linked to structural relaxation, and reorganization of the glassy network.<sup>90</sup> The number of bonding and non-bonding oxygen atoms as well as the coordination number is affected by ball milling. In conclusion, high-energy ball milling affects the local structure

of a quenched, high-entropy glass and finally leads to a structural relaxation analogous to thermal annealing.

This structural relaxation decreases the ionic conductivity by influencing many factors governing ionic conductivity. Detailed analysis of the Arrhenius behaviour of the ionic conductivity in the quenched glass as well as in milled samples revealed the evolution process of the relaxation and the correlated ionic conductivity. High-energy ball milling of quenched petalite causes a decrease of the mean hopping rate related to the ionic mobility. A glass that was only milled for 6 h also showed heterogeneous conduction pathways, which could be associated with different degrees of structural relaxed regions, *i.e.* slightly relaxed cores surrounded by highly relaxed shells. A glass milled for 24 h shows only one conduction process and is considered homogeneously relaxed. Albeit milled samples show equal mean hopping rates, independent of the milling time, the conductivity in the heterogeneous sample milled for 6 h is comparatively higher. The latter could be attributed to entropic terms influencing the charge carrier density actively participating in the conduction process.

**P1**

Gadermaier, B.; Stanje, B.; Wilkening, A.; Hanzu, I.; Heitjans, P. and Wilkening, H. M. R.,

**Glass in Two Forms:  
Heterogeneous Electrical Relaxation in Nanoglassy Petalite.**

The Journal of Physical Chemistry C 2019, 123, 10153-10162.

# Glass in Two Forms: Heterogeneous Electrical Relaxation in Nanoglassy Petalite

Bernhard Gadermaier,<sup>\*,†</sup> Bernhard Stanje,<sup>†,‡</sup> Alexandra Wilkening,<sup>†</sup> Ilie Hanzu,<sup>†,§</sup> Paul Heitjans,<sup>||</sup> and H. Martin R. Wilkening<sup>\*,†,§</sup>

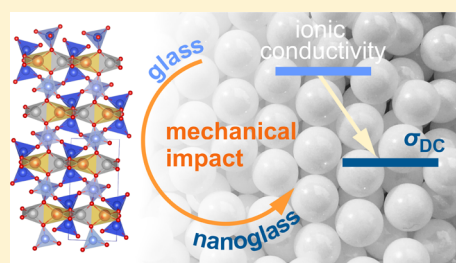
<sup>†</sup>Institute for Chemistry and Technology of Materials, Christian Doppler Laboratory for Lithium Batteries, Graz University of Technology (NAWI Graz), Stremayrgasse 9, A-8010 Graz, Austria

<sup>§</sup>Alistore – European Research Institute, CNRS FR3104, Hub de l'Énergie, Rue Baudelocque, F-80039 Amiens, France

<sup>||</sup>Institute of Physical Chemistry and Electrochemistry, Leibniz University Hannover, Callinstr. 3-3a, D-30167 Hannover, Germany

## Supporting Information

**ABSTRACT:** Glassy materials with specific functions are almost universally used in our daily life. If prepared via quenching, that is, by rapid cooling of the molten glass, a frozen liquid with a high degree of lattice disorder and stress is obtained. The release of stress through mechanical action may significantly affect the microstructure and dynamic features of the so-obtained nanoglass. Considering ion conducting glasses, it has recently been shown that mechanical treatment of glasses causes the long-range ion transport to significantly decrease. The origin of this astonishing behavior of nanoglasses is, however, far from being understood completely. Here, we show that depending on the duration of mechanical impact in a high-energy planetary ball mill, the petalite glass,  $\text{LiAlSi}_4\text{O}_{10}$ , passes through a state with two Li reservoirs distinctly differing in electrical relaxation and, thus, in ion transport. The two species, characterized by electrical relaxation rates differing by two orders of magnitude, show up clearly if we use the electric modulus representation to analyze the data. This feature is also seen in conductivity spectra revealing a two-step increase of the conductivity with frequency. Accordingly, we propose a two-phase model with nanometer-sized non-relaxed glassy particles next to or surrounded by structurally relaxed regions.



## 1. INTRODUCTION

Solid-state ionic conductors are of great interest as potential materials for all-solid-state batteries.<sup>1–3</sup> Although enormous effort has been devoted to finding electrolytes with ultrahigh ionic conductivity, focusing on fundamental phenomena is important to understand the principles behind fast conduction.<sup>4–18</sup> The latter studies also include model systems that do not necessarily show extremely high conductivities or diffusivities.<sup>19–22</sup> Such systems are useful to study, for example, the influence of structural or substitutional disorder on ion dynamics.<sup>23–25</sup> Moreover, they are also suited to investigate the effect of strain or stress on transport properties;<sup>26,27</sup> these properties may change when the glass is allowed to structurally relax upon annealing as it has been recently shown for  $\text{AgPO}_3$  glass.<sup>26</sup>

For crystalline materials, high-energy ball milling<sup>28–32</sup> is known to increase the ionic conductivity by orders of magnitude due to (i) amorphization, (ii) nanosizing, and (iii) the introduction of structural disorder in the form of zero-dimensional or higher-dimensional defects.<sup>21,23,24,33,34</sup> Ionic transport in nanocrystalline, structurally disordered ceramics is usually characterized by a lower activation energy (and, sometimes, also a higher pre-exponential factor) of the underlying Arrhenius relation when compared to the situation in the ordered, coarse-grained starting materials.<sup>7,23,24</sup> An early

example is nanocrystalline  $\text{CaF}_2$  that was prepared by inert gas condensation and studied by impedance spectroscopy<sup>35,36</sup> and  $^{19}\text{F}$  NMR measurements.<sup>37–39</sup>

For glasses,<sup>40</sup> being in an amorphous state in nature, the effect of high-energy ball milling can be quite different.<sup>21,27,41–43</sup> As has been shown recently, in this class of ionic conductors, the conductivity decreases upon high-energy ball milling.<sup>27,41–43</sup> For instance, mechanical treatment of glassy  $\text{LiAlSi}_4\text{O}_{10}$ , as has been shown by some of us recently, results in a decrease of the overall ionic conductivity,  $\sigma_g$ , by more than two orders of magnitude.<sup>43</sup> The same trend has been seen for  $\beta$ -spodumene glass.<sup>27</sup> The opposite behavior is, however, seen when crystalline  $\text{LiAlSi}_4\text{O}_{10}$  is milled; the ionic conductivity of nanocrystalline  $\text{LiAlSi}_4\text{O}_{10}$  largely exceeds that of the starting material.<sup>43</sup> At sufficiently long milling times, the ionic conductivity,  $\sigma_n$ , of nanocrystalline  $\text{LiAlSi}_4\text{O}_{10}$  coincides with that of the nanoglassy form  $\sigma_{ng} \approx \sigma_n$ . Thus, in the nanoglassy form,  $\text{Li}^+$  ion conductivity is governed by the same activation energy and the same prefactor as in the nanocrystalline one.<sup>43</sup>

Received: February 13, 2019

Revised: March 22, 2019

Published: March 25, 2019

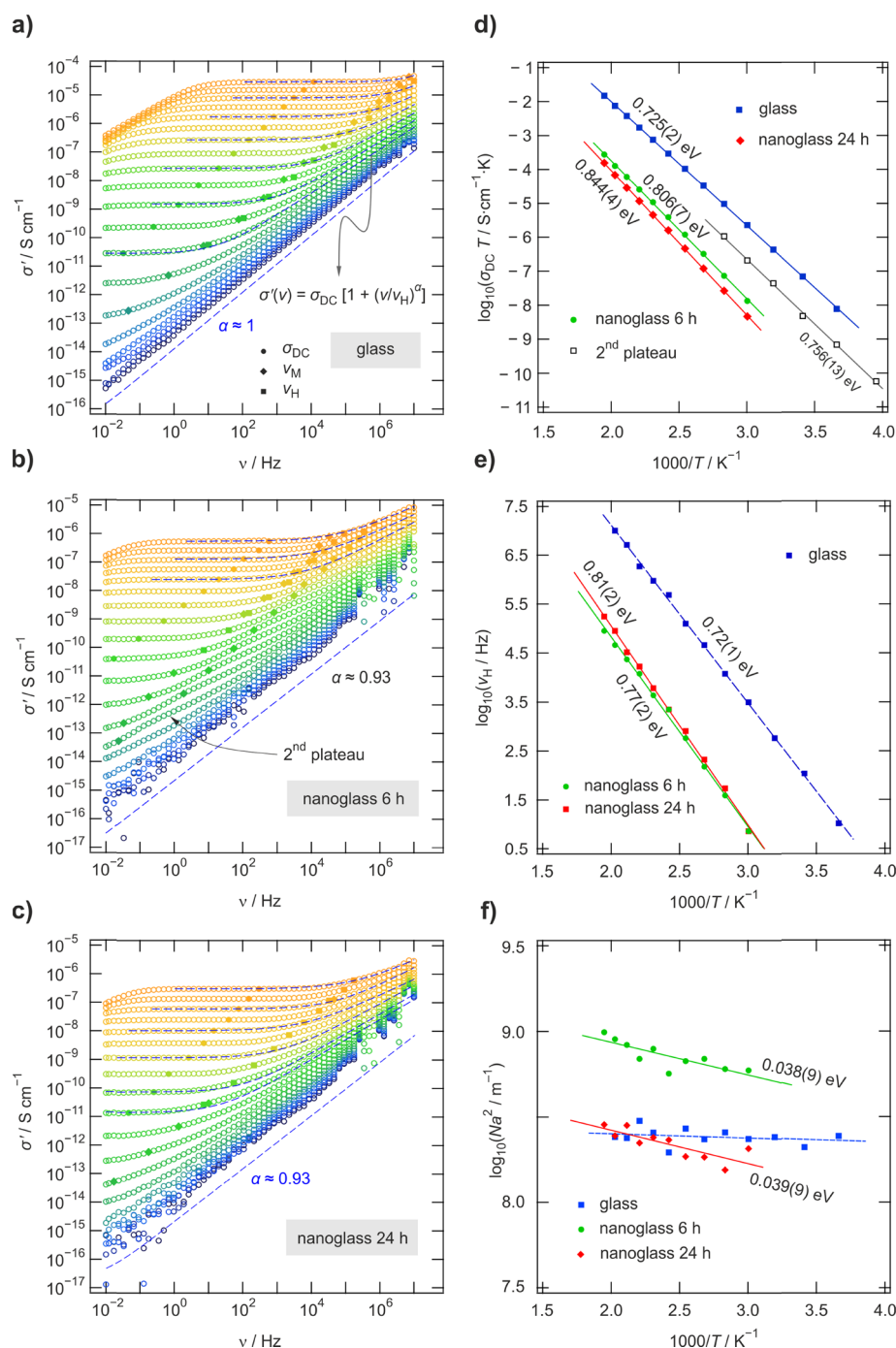


**Figure 1.** (a–c) Conductivity spectra, that is, real part  $\sigma'$  of the complex conductivity plotted versus frequency  $\nu$ , of  $\text{LiAlSi}_4\text{O}_{10}$  before and after high-energy ball milling for 6 (b) and 24 h (c). Isotherms have been recorded in steps of 20 K. Filled dots mark the DC conductivity, filled squares represent the hopping rate  $\nu_H$ , and filled rhombi indicate the frequencies where the modulus peaks show up (see text for further explanation). Dashed lines represent fits according to eq 1. For the sample milled for only 6 h, a shallow second plateau is seen, which is absent in (a) and (c). (d) Arrhenius plots of the DC conductivity of the three samples including values of the second plateau seen in (b). In (e), the temperature dependence of the hopping rate  $\nu_H$  is shown. (f) Variation of the charge carrier concentration, shown as the product of  $N$  and  $a^2$ . Solid and dashed lines in (d) to (f) show linear fits.

This behavior is not quite well understood, and to our knowledge, no detailed broad-band conductivity spectroscopy study about this phenomenon has been presented so far. It is not surprising that when coming from the crystalline form, the ionic conductivity increases for the nanocrystalline material because of the introduction of defects,<sup>21</sup> due to space charge zones<sup>44,45</sup> or the generation of free volume. Nanocrystalline  $\text{LiAlSi}_4\text{O}_{10}$ , although we can assume that it contains larger

fractions of amorphous material, still shows a lower conductivity than its quenched glassy counterpart.<sup>43</sup> The fact that we obtain  $\sigma_{\text{ng}} < \sigma_{\text{g}}$  after the glass has been milled indicates that in the nanoglassy form, new amorphous regions are generated, which resemble those in the nanocrystalline sample. This view follows the idea of Gleiter et al. who described the structure of metallic nanoglasses.<sup>46</sup> Ivanisenko and co-workers proposed a core–shell model in which the glassy particles

consists of bulk regions covered by amorphous regions with increased free volume and lower density.<sup>47</sup>

Since the glass, whose conductivity decreased upon mechanical treatment, was derived by melt quenching, we expect the rapidly frozen liquid to be characterized by a high degree of mechanical stress and a high value of entropy. We assume a close relationship between these properties and the ionic conductivity of a glassy material. Any increase in strain or stress might result in a higher diffusivity of the ions. On the other hand, ball milling is anticipated to release mechanical stress and to induce structural relaxation of the initially highly stressed glassy material. This decrease in strain might produce structurally relaxed regions whose ionic conductivity is lower than that of the non-treated quenched state. Since ball milling of crystalline materials usually leads to a heterogeneous material consisting of crystalline grains and amorphous interfacial regions, we were wondering whether something similar would take place when a glassy material is milled.

For this purpose, we studied the electrical response of nanoglassy  $\text{LiAlSi}_4\text{O}_{10}$  in more detail and thoroughly compared our results on (electrical) relaxation frequencies, activation energies, and concentration of mobile charge carriers with those from glassy and (nano)glassy petalite. Indeed, in the melt-quenched petalite glass, we were able to detect, for the first time, an electrical response pointing to two differently relaxing Li reservoirs. This response is somewhat concealed in the conductivity isotherms but is clearly visible when analyzing dielectric relaxation via the electric modulus representation.

One can envisage that the particles of the quenched glass, when hit by the balls, will mechanically and structurally relax. If we assume that this mechanically induced relaxation process will primarily affect the outer zones of the particles, at least transitory in respect to treatment time, it could indeed lead to the concept of a two-region system being similar to that established for nanocrystalline materials and, quite recently, also suggested for metallic nanoglasses.<sup>47</sup>

## 2. EXPERIMENTAL SECTION

Petalite glass specimens,  $\text{LiAlSi}_4\text{O}_{10}$ , were obtained in high purity from Schott Glaswerke; the same sample materials have been used in a previous study.<sup>43</sup> To measure ionic conductivities of the glass sample, we used a small plate (1 mm in thickness,  $5 \times 5 \text{ mm}^2$ ), that was polished on the surface on which Au electrodes (200 nm in thickness) were applied by sputtering (Leica, direct current (DC) magnetron sputtering system). Powder samples were obtained by grinding the glass plates by hand in an agate mortar. To prepare nanoglassy samples, the glass powders were milled for either 6 or 24 h under dry conditions in  $\text{ZrO}_2$  grinding beakers (45 mL) equipped with 180 balls made of  $\text{ZrO}_2$  (5 mm in diameter) using a Fritsch Planetary mill (Premium line 7); the ball-to-powder weight ratio was 4:1. The samples were analyzed by X-ray diffraction using a Bruker D8 Advance diffractometer (Bragg Brentano geometry,  $\text{Cu K}\alpha$  radiation). The original glass sample is X-ray amorphous.

To measure complex conductivities, the powders were uniaxially cold-pressed into pellets (8 mm in diameter, 0.5 to 1 mm in thickness). After applying Li ions blocking Au electrodes, a Novocontrol Concept 80 broad-band analyzer was employed to record complex impedance data from which the conductivity was calculated; the frequency  $\nu$  was varied from 10 mHz to 10 MHz ( $-140$  to  $240^\circ\text{C}$ ). In our setup, the temperature was automatically controlled by means of a

QUATRO cryosystem (Novocontrol), which uses a heating element to build up a specific pressure in a liquid nitrogen Dewar to create a  $\text{N}_2$  gas flow that is subsequently heated in order to adjust the temperature.

$^7\text{Li}$  NMR line widths were measured with an Avance III Bruker spectrometer connected to a shimmed cryomagnet (11.4 T, 194 MHz). We used a single radiofrequency pulse to nonselectively excite the spectrum. Up to 32 scans were accumulated to obtain one free induction decay. Fourier transformation yielded the  $^7\text{Li}$  NMR spectra. Prior to the NMR measurements, the samples were sealed in quartz ampoules.<sup>43</sup>  $^{27}\text{Al}$  magic angle spinning (MAS) NMR spectra (130.3 MHz, 25 kHz spinning speed, 2.5 mm  $\text{ZrO}_2$  rotors) have been recorded with a single pulse (1  $\mu\text{s}$ ) experiment; the recycle delay between each scan was 2 s, and up to 256 scans were accumulated to obtain the spectra.  $\alpha\text{-Al}_2\text{O}_3$  served as a secondary reference to determine chemical shifts; its  $\text{AlO}_6$   $^{27}\text{Al}$  NMR signal appears at 9 ppm, when referenced to aqueous  $\text{Al}(\text{NO}_3)_3$ .

## 3. RESULTS AND DISCUSSION

As has been confirmed by X-ray powder diffraction, the glassy and the nanoglassy samples are completely amorphous; no crystallization is initiated when glassy samples are treated in planetary mills. This observation also holds for nanoglassy  $\beta$ -spodumene<sup>27</sup> ( $\text{LiAlSi}_2\text{O}_6$ ) and nanoglassy eucryptite ( $\text{LiAlSiO}_4$ ) that has been studied earlier.<sup>48</sup> When using  $\text{ZrO}_2$  vials, as is the case here, abrasion is almost negligible; our samples are negligibly contaminated by  $\text{ZrO}_2$ .

Mechanical treatment of glassy  $\text{LiAlSi}_4\text{O}_{10}$  in high-energy ball mills significantly reduces its DC conductivity.<sup>43</sup> In a recent, preliminary work, this behavior (see also Figure 1d) has been shown by analyzing the frequency independent regions of conductivity isotherms.<sup>43</sup> After the glass has been milled for 24 h, its DC conductivity almost coincides with that of a heavily treated nanocrystalline  $\text{LiAlSi}_4\text{O}_{10}$  sample obtained after milling crystalline petalite.<sup>43</sup> Hence, with respect to the milling conditions applied here, an almost completely relaxed sample is obtained. This behavior is different from that of the sample milled for only 6 h, as will be discussed below.

Here, we will take a closer look at the shape of conductivity isotherms and modulus data to shed light on the underlying dynamic mechanisms leading to the significant differences in ionic conductivity and electrical relaxation of the treated and non-treated glass samples. In Figure 1a,c, the corresponding conductivity isotherms,  $\sigma'(\nu)$ , of glassy and nanoglassy  $\text{LiAlSi}_4\text{O}_{10}$  are shown. The isotherms of non-treated  $\text{LiAlSi}_4\text{O}_{10}$  are composed of distinct DC plateaus characterized by a frequency-independent conductivity value,  $\sigma_{\text{DC}}$ , that passes, with increasing frequency, into dispersive regimes. These regimes can roughly be approximated with Jonscher's power law.<sup>49,50</sup>

$$\sigma'(\nu) = \sigma_{\text{DC}} \left[ 1 + \left( \frac{\nu}{\nu_{\text{H}}} \right)^\alpha \right] \quad (1)$$

where  $\alpha$  is the power law exponent and  $\nu_{\text{H}}$  represents the so-called cross-over frequency from the  $\sigma_{\text{DC}}$  plateau to the dispersive regime.  $\nu_{\text{H}}$  is considered to be in the same order of magnitude as the hopping rate of the mobile ions. At this frequency, the conductivity is given by  $\sigma'(\nu_{\text{H}}) = 2\sigma_{\text{DC}}$ . As can be seen in Figure 1a, the exponent  $\alpha$  depends on temperature. While it adopts values of  $\sim 0.6$  at elevated temperatures, at the

**Table 1.** Pre-exponential Factors, Charge Carrier Concentration, and Hopping Frequencies of Glassy and Nanoglassy Petalite (6 and 24 h)<sup>a,b</sup>

sample	conductivity		charge carrier concentration		hopping rate	
	log <sub>10</sub> σ <sub>0</sub> <sup>c</sup>	ΔE <sub>a,DC</sub> (eV)	log <sub>10</sub> (N <sub>c</sub> ·a <sup>2</sup> ) <sup>d</sup>	ΔE <sub>c</sub> (eV)	log <sub>10</sub> ν <sub>e</sub> <sup>e</sup>	ΔE <sub>m</sub> (eV)
glass	5.31(3)	0.725(2)	8.45(7)	0.005(6)	14.38(9)	0.721(6)
nanoglass (6 h)	4.39(8)	0.806(7)	9.32(11)	0.038(9)	12.58(17)	0.769(13)
2nd plateau	4.78(22)	0.756(13)	n.d.	n.d.	n.d.	n.d.
nanoglass (24 h)	4.48(5)	0.845(4)	8.81(12)	0.039(9)	13.18(14)	0.806(11)

<sup>a</sup>Activation energies ΔE<sub>a,DC</sub>, ΔE<sub>c</sub> and ΔE<sub>m</sub> are also included. <sup>b</sup>Not determined (n.d.). <sup>c</sup>σ<sub>0</sub> in S K cm<sup>-1</sup>. <sup>d</sup>N<sub>c</sub>·a<sup>2</sup> in m<sup>-1</sup>. <sup>e</sup>ν<sub>e</sub> in s<sup>-1</sup>.

lowest temperatures, it is given by  $\alpha \approx 1$ . A linear frequency dependence results in a so-called nearly constant loss (NCL) behavior, that is, the imaginary part of the complex permittivity becomes independent of the frequency. NCL behavior<sup>49,51–54</sup> has been anticipated to be related to caged, localized motions of the mobile charge carriers.<sup>55,56</sup> This has been almost universally seen for glasses and some crystalline materials<sup>52</sup> that provide spatially confined motions. As expected, at high temperature and low frequency, our isotherms reveal a decrease of the ionic conductivity due to the charge accumulation at the blocking electrodes.<sup>57,58</sup> The higher the ionic conductivity, the more pronounced the effect is. At high temperature, polarization effects are best seen for the glassy sample that has not been mechanically treated (see Figure 1a).

The temperature dependence of σ<sub>DC</sub> of the glass and the nanoglasses is shown in Figure 1d and can be described by the well-known Arrhenius relation

$$\sigma_{\text{DC}} = \frac{\sigma_0}{T} \cdot \exp\left(-\frac{\Delta E_{\text{DC}}}{k_{\text{B}}T}\right) \quad (2)$$

where σ<sub>0</sub> is the pre-exponential factor, k<sub>B</sub> denotes Boltzmann's constant, and ΔE<sub>DC</sub> represents the activation energy of ionic conductivity. At first, we will discuss the change in σ<sub>DC</sub> and the associated hopping rate ν<sub>H</sub> of the glassy and nanoglassy samples. The unmilled glass shows the highest conductivity and the lowest activation energy (0.73 eV). By high-energy ball milling, the DC conductivity significantly decreases, and the activation energy increases to values of 0.81 and 0.84 eV for the samples milled for 6 and 24 h, respectively. Interestingly, milling also leads to a pronounced decrease of the pre-exponential factor, σ<sub>0</sub>, with a shallow minimum for the nanoglass that was obtained after 6 h of milling; see Table 1.

Given that the conductivity is related to the electrical mobility, μ, and concentration, N<sub>c</sub>, of the charge carriers by

$$\sigma_{\text{DC}} = e \cdot N_{\text{c}} \cdot \mu \quad (3)$$

where *e* is the elementary charge, it is evident that the milling process has at least affected one of these two factors. To throw light on this aspect, we need to express the relationship between σ<sub>DC</sub> and the hopping rate ν<sub>hop</sub>. The Nernst–Einstein relation<sup>59</sup> (see eq 4) correlates the ionic mobility with the diffusion coefficient, *D*, according to

$$\mu = \frac{D \cdot e}{k_{\text{B}}T} \quad (4)$$

The diffusion coefficient *D*, on the other hand, is given by the mean hopping distance squared, *a*<sup>2</sup>, a geometrical factor, γ, and ν<sub>hop</sub>

$$D = a^2 \cdot \gamma \cdot \nu_{\text{hop}} \quad (5)$$

γ contains information about the dimensionality and correlation effects of the hopping process. If we replace ν<sub>hop</sub> by ν<sub>H</sub>, as an approximation, we can rewrite eq 3 as follows:

$$\sigma_{\text{DC}} = \frac{N_{\text{c}} \cdot e^2 \cdot \gamma \cdot a^2}{k_{\text{B}}T} \cdot \nu_{\text{H}} \quad (6)$$

This equation establishes a link between the hopping rate and the charge carrier concentration with σ<sub>DC</sub>. Considering that N<sub>c</sub> and ν<sub>H</sub> may be thermally activated, these parameters can be expressed as<sup>60</sup>

$$\begin{aligned} N_{\text{c}} &= N_0 \cdot \exp\left(-\frac{\Delta G_{\text{c}}}{k_{\text{B}}T}\right) = N_0 \cdot \exp\left(\frac{\Delta S_{\text{c}}}{k_{\text{B}}}\right) \cdot \exp\left(-\frac{\Delta E_{\text{c}}}{k_{\text{B}}T}\right) \\ &= N_{\text{c}} \cdot \exp\left(-\frac{\Delta E_{\text{c}}}{k_{\text{B}}T}\right) \end{aligned} \quad (7)$$

where N<sub>0</sub>, ΔG<sub>c</sub>, ΔS<sub>c</sub>, ΔE<sub>c</sub>, and N<sub>e</sub> are the concentration of potentially mobile ions participating in conduction, the free energy of charge carrier formation, the entropy of charge carrier formation, the activation energy of charge carrier formation, and the effective charge carrier concentration at infinite temperature, respectively. For the hopping rate, this formalism leads to the following relationships

$$\begin{aligned} \nu_{\text{H}} &= \nu_0 \cdot \exp\left(-\frac{\Delta G_{\text{m}}}{k_{\text{B}}T}\right) = \nu_0 \cdot \exp\left(\frac{\Delta S_{\text{m}}}{k_{\text{B}}}\right) \cdot \exp\left(-\frac{\Delta E_{\text{m}}}{k_{\text{B}}T}\right) \\ &= \nu_{\text{e}} \cdot \exp\left(-\frac{\Delta E_{\text{m}}}{k_{\text{B}}T}\right) \end{aligned} \quad (8)$$

where ν<sub>0</sub>, ΔG<sub>m</sub>, ΔS<sub>m</sub>, and ΔE<sub>m</sub> are the vibrational frequency of the ion, the free energy of migration, the entropy of migration, and the activation energy of migration. ν<sub>e</sub> denotes the effective attempt frequency including an entropy term.<sup>60,61</sup> Substituting eqs 7 and 8 into 6 yields<sup>60</sup>

$$\begin{aligned} \sigma_{\text{DC}} &= N_{\text{c}} \nu_{\text{e}} \frac{e^2 \cdot \gamma \cdot a^2}{k_{\text{B}}T} \exp\left(-\frac{\Delta E_{\text{c}} + \Delta E_{\text{m}}}{k_{\text{B}}T}\right) \\ &= N_0 \nu_0 \exp\left(\frac{\Delta S_{\text{c}} + \Delta S_{\text{m}}}{k_{\text{B}}}\right) \frac{e^2 \cdot \gamma \cdot a^2}{k_{\text{B}}T} \exp\left(-\frac{\Delta E_{\text{c}} + \Delta E_{\text{m}}}{k_{\text{B}}T}\right) \end{aligned} \quad (9)$$

which resembles eq 2 if ΔE<sub>DC</sub> = ΔE<sub>c</sub> + ΔE<sub>m</sub>. Having ν<sub>H</sub> and σ<sub>DC</sub> extracted from the conductivity isotherms, it is possible to calculate N<sub>c</sub>·a<sup>2</sup> if we rewrite eq 6 as follows

$$N_{\text{c}} \cdot a^2 = \frac{k_{\text{B}}T}{e^2 \gamma} \cdot \frac{\sigma_{\text{DC}}}{\nu_{\text{H}}} \quad (10)$$



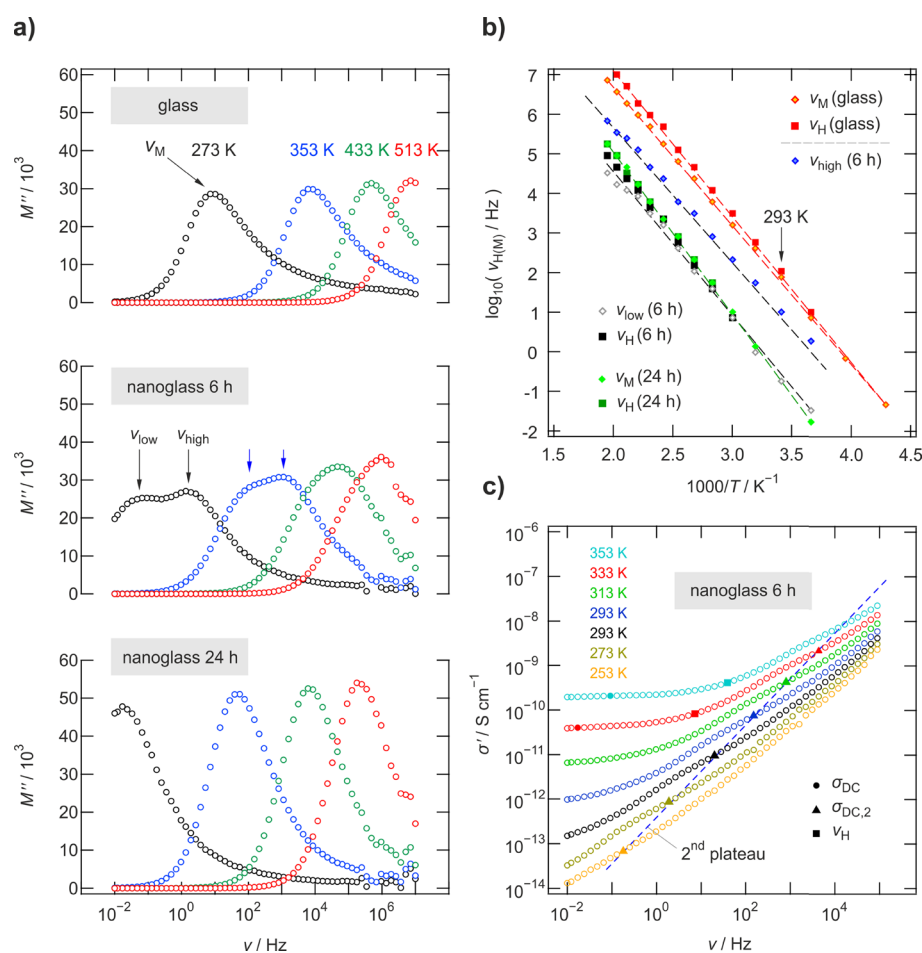


**Figure 2.** (a) Modulus spectra  $M''(\nu)$  of glassy petalite  $\text{LiAlSi}_4\text{O}_{10}$  and the nanoglass counterparts; spectra were recorded at the temperatures indicated. (b) Change of the hopping rate ( $\nu_{\text{H}}$ ) and the relaxation frequencies of the modulus spectra ( $\nu_{\text{M}}$ ) as a function of the inverse temperature. For the nanoglass (6 h), the two distinct relaxation frequencies have been included:  $\nu_{\text{low}} = \nu_{\text{H}}(24 \text{ h})$ . Dashed lines show linear fits. (c) Selected conductivity isotherms of the nanoglass (6 h); temperatures are indicated. The dashed lines are to guide the eye along the change of the conductivities associated with the second DC plateau.

thereby allowing the determination of the activation energies of creation,  $\Delta E_{\text{c}}$ , and migration,  $\Delta E_{\text{m}}$ , of the charge carriers individually; see eq 7.

Here, milling causes a continuous increase of  $\Delta E_{\text{m}}$  and furthermore a clear decrease in the effective attempt frequency,  $\nu_{\text{e}}$ , when we compare the glass with the sample treated for 24 h (Table 1). This finding shows that most likely,  $\Delta S_{\text{m}}$  is changed upon milling. The change in  $\nu_{\text{e}}$  is associated with a change of the abovementioned overall decrease of the conductivity prefactor  $\sigma_0$ ; see eqs 1 and 9 and Table 1. The change in  $\sigma_0$ , when going from the unmilled glass to the sample milled for 24 h, cannot be explained by the slight change in charge carrier concentration alone (see Table 1) as  $N_{\text{c}} \cdot a^2$  for the two samples is rather similar. Temperature effects and the subtle but important differences between the nanoglasses will be discussed below. Here, we consider attempt frequencies and entropy effects to play the most important roles in explaining the difference between  $\sigma_0(\text{glass})$  and  $\sigma_0(24 \text{ h})$ . In the context of a quenched glass where the entropy of the liquid state is at least to some extent frozen within the sample, we expect that milling leads to structural relaxation and nanosizing of particles. This mechanical impact is assumed to decrease the entropy of the system continuously with the duration of milling. Such a decrease should indeed be reflected in the prefactor of the corresponding Arrhenius relation of  $\sigma_{\text{DC}}$ . In

accordance with the literature,<sup>26,62,63</sup> we assume that the decrease of the entropy of the whole systems also directly affects the entropy of migration. Of course, we cannot exclude that besides the influence of entropy, also attempt frequencies  $\nu_0$  and mean jump distances  $a$  (see below) change upon mechanical treatment. Here, we anticipate that in the case of nanoglasses prepared by milling from their quenched counterparts, entropy effects play the crucial role in explaining the decrease in  $\sigma_0$ .

Apart from the obvious differences in the DC conductivities showing up after milling, it is important to note that there are also some fundamental differences between the nanoglasses themselves (Figure 1d–f). Surprisingly,  $\nu_{\text{e}}$  and also to a lesser extent  $\sigma_0$  are a bit higher in the nanoglass milled for 24 h than in the nanoglass obtained after milling for 6 h. Given that the conductivity is lowest in the 24 h nanoglass, we would have expected that also  $\nu_{\text{e}}$  is lowest for this sample. Compared to the unmilled glass, Figure 1d,e clearly reveals that the DC conductivity and the corresponding hopping frequencies are lower for the nanoglasses. The small difference in DC conductivities of the nanoglasses,  $\sigma_{\text{DC}}(6 \text{ h}) > \sigma_{\text{DC}}(24 \text{ h})$ , is, however, not reflected in the corresponding hopping frequencies as they are almost identical (see Figure 1d,e). Precisely speaking, at high temperatures, we even observe  $\nu_{\text{H}}(6 \text{ h}) < \nu_{\text{H}}(24 \text{ h})$ . Keeping the relation of conductivity,  $\sigma_{\text{DC}}$ ,  $N_{\text{c}}$

and hopping rate,  $\nu_H$ , in mind, it is clear that this alteration between the nanoglasses can only be explained by a slightly higher charge carrier concentration in the 6 h nanoglass as compared to that of the sample obtained after 24 h, thus compensating for the decreased electrical mobility of the charge carriers.

Although the (mean) hopping distance,  $a$ , is not precisely accessible in a (glassy) amorphous solid, the charge carrier concentration can still be deduced as a manifold of  $a^2$  and therefore used to estimate the activation energy of charge carrier creation,  $\Delta E_c$ , according to eq 7; see also Table 1.  $\Delta E_c$ , which is essentially the difference between  $\Delta E_{DC}$  and  $\Delta E_m$ , is identical in both nanoglasses (0.04 eV, see Figure 1f), and hence, the difference in charge carrier concentration can only be explained by a change of the corresponding prefactor  $N_c$  in the Arrhenius diagram shown in Figure 1f. With the help of Figure 1f, we clearly see that the charge carrier concentration and its prefactor are higher in the nanoglass obtained after 6 h compared to those of the unmilled glass as well as the sample milled for 24 h. Differences in the average hopping distance,  $a$ , between the glass and the nanoglasses cannot solely account for the differences in  $N_c \cdot a^2$ ; see Table 1.

A temperature-dependent charge carrier concentration is, in crystalline systems, if, for example, systems with a NASICON structure are considered, usually assigned to the existence of “trapped” ions.<sup>64</sup> Keeping in mind that the glass was rapidly quenched from a liquid state, one would expect that the aluminosilicate framework is disordered throughout the whole sample and constitutes one homogeneous glassy phase. High-energy ball milling is anticipated to introduce local structural changes. This effect might result in structurally relaxed regions that are characterized by a different mean electrical relaxation frequency. Such regions might host Li ions being “trapped” in contrast to those in the non-relaxed regions. One might assume that with increasing temperature, the atoms of the aluminosilicate increase their vibration amplitude in their positions allowing the “trapped” ions to escape from their sites and participate in ionic conduction. This assumption would explain the increase in charge carrier concentration with temperature for the nanoglasses obtained after milling the glass for 6 and 24 h. This feature can also be seen in the increase of the activation energy for migration,  $\Delta E_m$  (see Table 1), if we identify the value as the energy required to strain the framework and to push the ions through any bottlenecks, that is, the boundaries of the trap plus the energy difference between the sites of residence.

To find indications that the Li ions in the nanoglass sample treated for only 6 h really need to be characterized by different conductivities and electrical relaxation frequencies, we took a closer look at the conductivity isotherms and modulus spectra of this sample. Indeed, the conductivity isotherms reveal a second conductivity plateau pointing to Li ions in regions almost similar to that of the untreated glass (see Figure 1b). The same feature is even better seen if we use the complex modulus  $M^*$  to characterize the dielectric response of the samples.<sup>65</sup>  $M^*$  is related to the complex permittivity  $\epsilon^*$  by  $M^* = 1/\epsilon^*$ . If its imaginary part  $M''$  is analyzed as a function of  $\nu$  (see Figure 2) the samples obtained after milling reveal marked differences.

The characteristic frequencies,  $\nu_M$ , at which the peaks show up are proportional to  $\nu_H$ . As expected, compared to the unmilled glass, after 24 h of milling, the modulus peak has clearly been shifted, viz. by three orders of magnitude, toward

lower electrical relaxation frequencies (Figure 2a). As is shown in Figure 2b, for both the glass and the 24 h nanoglass the hopping frequencies  $\nu_H$  coincide with  $\nu_M$ . This agreement shows that we can safely assume that the extraction of  $\nu_H$  is not influenced by any artifacts, which helps us to interpret the findings seen for the sample milled for only 6 h.

Importantly, the nanoglass obtained after 6 h of milling does not exhibit a single  $M''$  curve (see Figure 2a). One could have expected a modulus peak located in between the glass and the nanoglass (24 h). This nanoglass, however, clearly shows two peaks, one almost identical with that of the nanoglass (24 h) and another one located at a frequency close to but still different from that of the unmilled glass. Thus, the 6 h nanoglass sample clearly takes an intermediate position in dielectrical relaxation behavior.

Worth mentioning is that the two modulus peaks of the 6 h nanoglass sample have a similar height. In general, the amplitude of a given  $M''$  peak is, roughly speaking, also for a non-Debye relaxation process inversely proportional to the capacitance.<sup>66</sup> If the two peaks would simply correspond to electrical relaxation in the bulk and grain boundary (g.b.) regions, they should largely differ in amplitude. While for bulk processes, capacitances in the order of some picofarads are expected, those governed by g.b. contributions should be characterized by values of  $\sim 100$  pF or higher.<sup>67</sup> Because of the similarity in  $M''(\nu)$  amplitudes of the two peaks, we conclude that they represent two different glassy regions in ball-milled  $\text{LiAlSi}_4\text{O}_{10}$ .

The abovementioned similarity between  $\nu_H$  and  $\nu_M$ , seen for the glass and the sample milled for 24 h (Figure 2b), is only valid for the  $M''$  peak that is located at lower frequencies. This low-frequency peak represents the relaxation behavior of the fully relaxed glass; thus, we have  $\nu_{M,low}(6\text{ h}) = \nu_M(24\text{ h})$ . The peak located at higher frequencies, characterized by  $\nu_{M,high}(6\text{ h})$ , is similar but not identical to that of the unmilled glass (see also Figure 2b). Compared to the non-treated glass, it is shifted to lower frequencies. Thus, it refers to a glassy form that is to a certain extent already affected by mechanically induced relaxation (Figure 2a,b). Therefore, at least for the nanoglass obtained after 6 h of milling, the two-peak structure of the corresponding modulus spectra points to a glassy material with two reservoirs characterized by distinct mean electrical relaxation frequencies. Assuming that these two reservoirs are also spatially separated from each other, we propose a core-shell model to describe its nanoglass structure. The inner nanodomains consist of partly relaxed glassy particles that remember the stressed state of the unmilled glass. These particles are surrounded by or located nearby structurally relaxed regions. The latter regions are almost fully structurally relaxed by mechanical impact.

This feature is not only revealed in the modulus representation. As mentioned above, a closer look at the conductivity isotherms shows that curvatures are seen at sufficiently high frequencies when data of the sample milled for 6 h are considered (see Figure 2c and also Figure 1b). The conductivities, which characterize these shallow plateaus, are indicated in Figure 2c by filled symbols. Importantly and in line with the modulus representation, these curvatures are absent for the homogeneous glass sample and the fully relaxed one that is obtained after 24 h of milling (Figure 1a,c). A comparison is shown in Figure S1, Supporting Information. The conductivities referring to these plateaus are also included in the Arrhenius plot of Figure 1d. As the characteristic

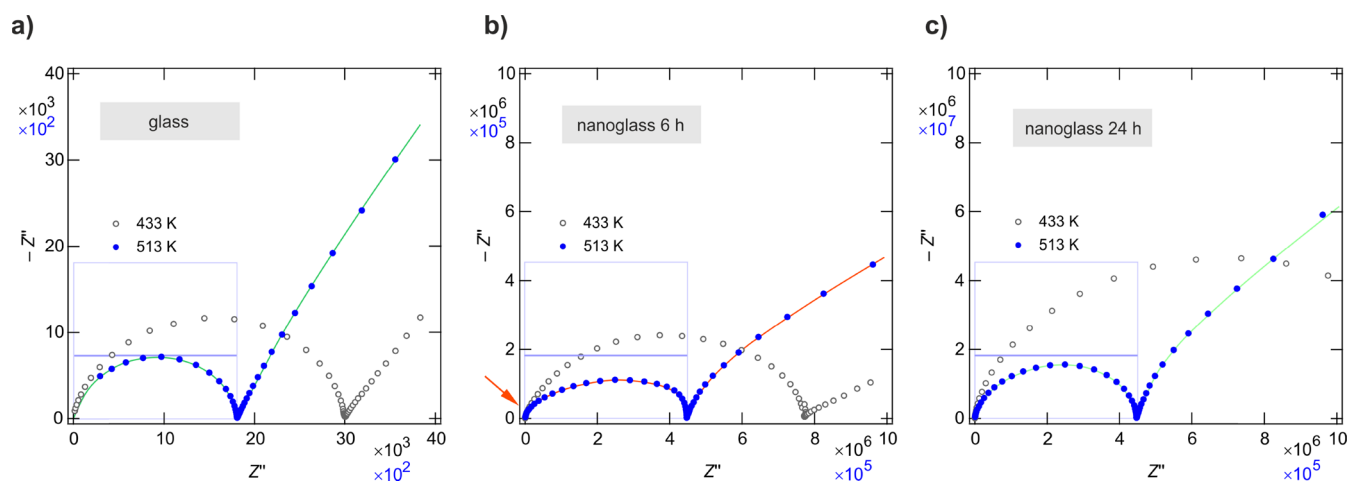


**Figure 3.** Complex plane plots of the impedance response  $Z^* = Z' - iZ''$  of glassy and nanoglassy petalite  $\text{LiAlSi}_4\text{O}_{10}$  at 433 and 513 K. The lines are to guide the eye. For the glass, at 513 K, a single depressed semicircle is seen in agreement with the homogeneous structure of this sample. Depressed semicircles point to correlated ionic motions present in the glass. A similar response is observed for the glass milled for 24 h; the resistance of this sample is, however, largely increased. The sample milled for only 6 h reveals a depressed signal that can be regarded as the superposition of many individual relaxation processes. As its total resistivity is comparable to that of the 24 h sample, the semicircle corresponding to the second plateau is hidden in the high-frequency regions marked by an arrow. It cannot be resolved with the Nyquist representation.

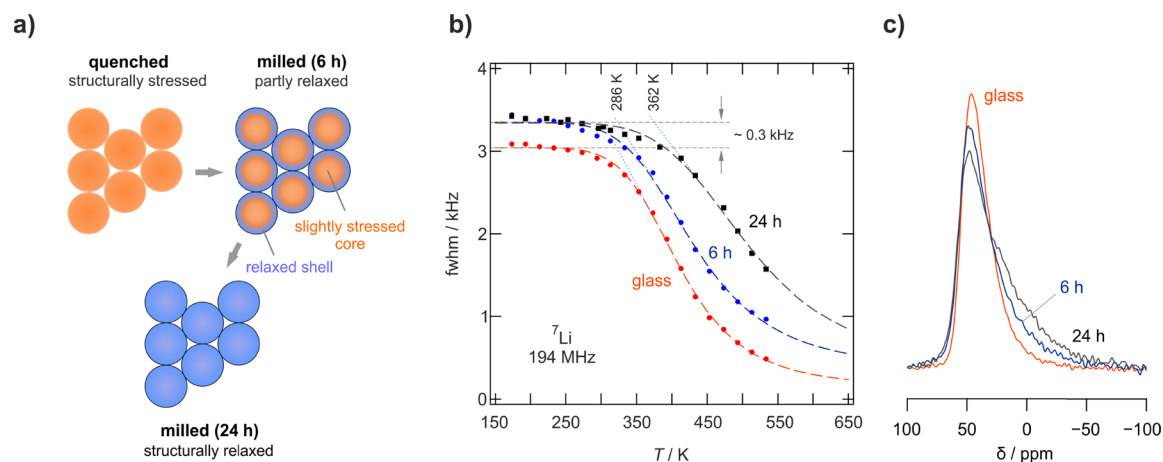


**Figure 4.** (a) Illustration of the effect of high-energy ball milling on the overall (long-range) ion dynamics in a glass. In the structurally relaxed regions, the ions are assumed to diffuse slower than in the initial morphology of the glass obtained by rapid quenching. (b) Temperature dependence of the Gaussian-shaped  ${}^7\text{Li}$  (spin quantum number  $I = 3/2$ ) NMR central line widths (fwhm = full width at half-maximum) of glassy petalite  $\text{LiAlSi}_4\text{O}_{10}$  and the corresponding milled samples. Dashed lines are drawn to guide the eye. Horizontal lines mark the rigid-lattice line width. The onset temperature of motional line narrowing is indicated by the interception of these lines with the dotted ones shown. (c)  ${}^{27}\text{Al}$  ( $I = 5/2$ ) MAS NMR spectra of nanoglassy and unmilled petalite. The increase in asymmetry and broadening are because of structural disorder introduced during the milling process.

frequencies  $\nu_M$ , they lie in between those of the glass sample and those of the sample milled for 24 h. Thus, the shallow plateau at high frequencies corresponds to the modulus peak seen at higher frequencies. Obviously, they refer to the partly relaxed regions in the interior of the nanometer-sized glassy particles.

The Nyquist representation is also helpful, here, at least in a qualitative way, to highlight the differences seen for the glassy and nanoglassy samples. Whereas in the complex plane plots of all samples, more or less a single depressed semicircle is seen, the Nyquist representation of the nanoglass (6 h) clearly reveals a superposition of several contributions and resembles the complex behavior seen in  $M''$  (see Figure 3). In contrast to the sample milled for only 6 h (Figure 3b), the impedance responses of the other two samples (Figure 3a,c), anticipated to be also more homogeneous from a structural point of view,

are rather similar; see the illustration in Figure 4a. The same similarity is seen in  $\sigma'(\nu)$ ; the corresponding isotherms are characterized by very similar Jonscher exponents  $\alpha$  (see Figure 1). Depressed semicircles are usually a sign of correlated motion; this feature becomes evident if results from (DC) conductivity spectroscopy are compared with those from NMR spin–lattice relaxation.<sup>43</sup> Here, the complex plane plot reveals that there seems to be a smooth transition when going from the almost fully relaxed regions to those only partly affected by mechanical milling; this feature is also illustrated in Figure 4a.

Further insight into (bulk) Li ion dynamics in unmilled and milled petalite glass can be deduced from the motion-induced narrowing of static  ${}^7\text{Li}$  NMR spectra recorded at different temperatures (Figure 4b).<sup>10,24</sup> At sufficiently low temperatures, that is, in the so-called rigid-lattice regime, the Li ion jump rates are too low to affect the line width, which is governed by

magnetic dipole–dipole interactions. With increasing temperature, however, the mean Li ion jump rate rapidly increases. When reaching values comparable to the rigid-lattice line width, averaging of the dipole–dipole interactions sets in, and the line starts to narrow.<sup>68</sup>

For the glass, motional narrowing (MN) begins at  $T_{\text{MN,glass}} = 286$  K. Milling the glass for 24 h shifts the onset to  $T = 362$  K (see Figure 4b); the same behavior has been seen for  $\beta$ -spodumene and nanoglassy  $\text{LiBO}_2$ .<sup>41,42</sup> Interestingly, the shorter milling time of 6 h does not influence  $T_{\text{MN,glass}}$ . Obviously, the spins in the partly relaxed regions of the 6 h nanoglass are able to cause the same MN as for the quenched glassy sample with its homogeneous structure. Also, the shapes of the curves of the non-treated glass and those milled for 6 h are similar indicating similar (local) Li ion dynamics. Similar results are obtained by impedance spectroscopy (see Figure 2b). At 293 K, that is, at a temperature very similar to  $T_{\text{MN}}$ ,  $\nu_{\text{M}}$  of the two samples differs by a factor of 7, which is 76 Hz for the unmilled glass and 10 Hz for the nanoglass (see Figure 2b).

For the fully relaxed nanoglass (24 h), on the other hand, the corresponding electrical relaxation frequency is much lower. As has been shown by  $^7\text{Li}$  NMR spin–lattice relaxation measurements, on the local length scale, however, fast  $\text{Li}^+$  diffusion processes also seem to be present in the glass milled for 24 h.<sup>43</sup> These fast processes have been anticipated to take place in regions that do not form a percolating network. Subnanometer-sized regions near the surfaces of the glass particles might host these fast diffusing spins.

Interestingly, ball milling also affects the rigid-lattice line width  $\Delta\nu_{\text{R}}$ . Compared to that of the original glassy sample, that of the nanoglasses are higher by  $\sim 0.3$  kHz. Obviously, the ions in the structurally relaxed regions sense a broader distribution of dipolar interactions and/or chemical shifts.<sup>41</sup>  $^{27}\text{Al}$  MAS NMR spectra, which are shown in Figure 4c, also show an increase in structural disorder with increasing milling time. The signal at  $\sim 47$  ppm corresponds to the  $\text{AlO}_4$  units in  $\text{LiAlSi}_4\text{O}_{10}$ .<sup>42</sup> The increase in line broadening and asymmetry reflects the increase in distributions of chemical shifts and electric field gradients sensed by the Al ions. This finding, as well as the indication of different  $^7\text{Li}$  NMR line widths in the extreme limit of MN, supports the idea of structural relaxation (Figure 4a) induced by mechanical milling of glassy samples that were obtained by quenching procedures.

#### 4. SUMMARY AND CONCLUSIONS

Mechanical treatment of quenched, glassy  $\text{LiAlSi}_4\text{O}_{10}$  in high-energy ball mills causes the overall ionic conductivity, characterizing long-range ion transport, to decrease. This astonishing effect cannot be attributed to the introduction of grain boundary regions that might block ion transport.

Here, we used results from broad-band conductivity spectroscopy and the electric modulus formalism to propose a core–shell model that tries to explain this effect.  $^7\text{Li}$  NMR line narrowing confirms that upon milling, the overall Li diffusivity in nanoglassy  $\text{LiAlSi}_4\text{O}_{10}$  decreases. Associated with this decrease and the increase in activation energy, we observe a decrease in the corresponding prefactors of the ionic conductivity and hopping rates. We attribute this change to be to a significant part caused by a decrease in migration entropy  $\Delta S_{\text{m}}$  (and/or attempt frequencies  $\nu_0$ ) upon milling. High-energy ball milling induces structural relaxation, and the corresponding nanometer-sized regions formed in the nano-

glassy structure are to be characterized by different values of  $\Delta S_{\text{m}}$  and  $\nu_0$ .

As revealed by conductivity isotherms and dielectric modulus spectra, milling the glass does not lead to homogeneous structural relaxation. Instead, heterogeneous relaxation is observed, which manifests itself in two conductivity plateaus and two distinct modulus peaks. The peaks are separated by two orders of magnitude on the frequency scale; the same difference is seen if we consider the corresponding conductivities. The two peaks of nanoglassy petalite reveal regions that are (i) fully relaxed by mechanical treatment and (ii) only partly affected by ball-milling. The latter reservoir still remembers the influence of the stressed structure of the quenched glass, at least in terms of dielectric relaxation. Complex plane plots reveal a smooth transition between these two regions.

Thus, visualizing the process of milling, it seems obvious that the impact of the balls hitting the  $\text{LiAlSi}_4\text{O}_{10}$  particles will have the strongest effect on the outer zone of the particles, thereby causing structural relaxation foremost in the surface-near region. We propose that upon milling for intermediate times, the resulting nanometer-sized particles of the corresponding nanoglass consist of a mechanically stressed core that is surrounded by a mechanically relaxed shell.

#### ■ ASSOCIATED CONTENT

##### Supporting Information

The Supporting Information is available free of charge on the ACS Publications website at DOI: 10.1021/acs.jpcc.9b01423.

Conductivity isotherms of the petalite glass and nanoglass milled for 6 and 24 h (PDF)

#### ■ AUTHOR INFORMATION

##### Corresponding Authors

\*E-mail: [bernhard.gadermaier@tugraz.at](mailto:bernhard.gadermaier@tugraz.at) (B.G.).

\*E-mail: [wilkening@tugraz.at](mailto:wilkening@tugraz.at) (H.M.R.W.).

##### ORCID

Ilie Hanzu: 0000-0002-9260-9117

Paul Heitjans: 0000-0003-1563-9176

H. Martin R. Wilkening: 0000-0001-9706-4892

##### Present Address

<sup>‡</sup>TDK Electronics, Siemensstraße 43, A-8530 Deutschlandsberg, Austria

##### Author Contributions

B.G. and M.W. designed the study and wrote the manuscript. B.G. and B.S. performed the experiments. B.G., A.W., I.H., P.H., and M.W. analyzed and interpreted the data. All authors have given approval to the final version of the manuscript.

##### Notes

The authors declare no competing financial interest.

#### ■ ACKNOWLEDGMENTS

Financial support by the Austrian Federal Ministry of Science, Research and Economy (BMWF) and the National Foundation for Research, Technology and Development (CD-Laboratory of Lithium Batteries: Ageing Effects, Technology and New Materials) is gratefully acknowledged. Moreover, we appreciate support by NAWI Graz and thank the German Research Foundation (DFG) for financial support (WI3600, 2-1/4-1; HE1574, 14-2). P.H. is grateful to the State

of Lower Saxony (Germany) for a Niedersachsen Professorship.

## REFERENCES

- (1) Thangadurai, V.; Narayanan, S.; Pinzaru, D. Garnet-Type Solid-State Fast Li Ion Conductors for Li Batteries: Critical Review. *Chem. Soc. Rev.* **2014**, *43*, 4714–4727.
- (2) Bachman, J. C.; et al. Inorganic Solid-State Electrolytes for Lithium Batteries: Mechanisms and Properties Governing Ion Conduction. *Chem. Rev.* **2016**, *116*, 140–162.
- (3) Zhang, Z.; et al. New Horizons for Inorganic Solid State Ion Conductors. *Energy Environ. Sci.* **2018**, *11*, 1945–1976.
- (4) Lunghammer, S.; Prutsch, D.; Breuer, S.; Rettenwander, D.; Hanzu, I.; Ma, Q.; Tietz, F.; Wilkening, H. M. R. Fast Na Ion Transport Triggered by Rapid Ion Exchange on Local Length Scales. *Sci. Rep.* **2018**, *8*, 11970.
- (5) Prutsch, D.; Gadermaier, B.; Brandstätter, H.; Pregartner, V.; Stanje, B.; Wohlmuth, D.; Epp, V.; Rettenwander, D.; Hanzu, I.; Wilkening, H. M. R. Nuclear Spin Relaxation in Nanocrystalline  $\beta$ - $\text{Li}_3\text{PS}_4$  Reveals Low-Dimensional Li Diffusion in an Isotropic Matrix. *Chem. Mater.* **2018**, *30*, 7575–7586.
- (6) Uitz, M.; Epp, V.; Bottke, P.; Wilkening, M. Ion Dynamics in Solid Electrolytes for Lithium Batteries. *J. Electroceram.* **2017**, *38*, 142–156.
- (7) Prutsch, D.; et al. Nanostructured Ceramics: Ionic Transport and Electrochemical Activity. *Z. Phys. Chem.* **2017**, *231*, 1361–1405.
- (8) Kuhn, A.; Gerbig, O.; Zhu, C. B.; Falkenberg, F.; Maier, J.; Lotsch, B. V. A New Ultrafast Superionic Li-Conductor: Ion Dynamics in  $\text{Li}_{11}\text{Si}_2\text{PS}_{12}$  and Comparison with other Tetragonal LGPS-Type Electrolytes. *Phys. Chem. Chem. Phys.* **2014**, *16*, 14669–14674.
- (9) Dunst, A.; Epp, V.; Hanzu, I.; Freunberger, S. A.; Wilkening, M. Short-Range Li Diffusion vs. long-range Ionic Conduction in Nanocrystalline Lithium Peroxide  $\text{Li}_2\text{O}_2$ —the Discharge Product in Lithium-Air Batteries. *Energy Environ. Sci.* **2014**, *7*, 2739–2752.
- (10) Epp, V.; Gün, Ö.; Deiseroth, H.-J.; Wilkening, M. Highly Mobile Ions: Low-Temperature NMR Directly Probes Extremely Fast  $\text{Li}^+$  Hopping in Argyrodite-Type  $\text{Li}_6\text{PS}_5\text{Br}$ . *J. Phys. Chem. Lett.* **2013**, *4*, 2118–2123.
- (11) Kuhn, A.; Duppel, V.; Lotsch, B. V. Tetragonal  $\text{Li}_{10}\text{GeP}_2\text{S}_{12}$  and  $\text{Li}_7\text{GePS}_8$  - Exploring the Li Ion Dynamics in LGPS Li Electrolytes. *Energy Environ. Sci.* **2013**, *6*, 3548–3552.
- (12) Kuhn, A.; Kunze, M.; Sreeraj, P.; Wiemhöfer, H. D.; Thangadurai, V.; Wilkening, M.; Heitjans, P. NMR Relaxometry as a Versatile Tool to Study Li Ion Dynamics in Potential Battery Materials. *Solid State Nucl. Magn. Reson.* **2012**, *42*, 2–8.
- (13) Buschmann, H.; et al. Structure and Dynamics of the Fast Lithium Ion Conductor " $\text{Li}_7\text{La}_3\text{Zr}_2\text{O}_{12}$ ". *Phys. Chem. Chem. Phys.* **2011**, *13*, 19378–19392.
- (14) Kuhn, A.; Narayanan, S.; Spencer, L.; Goward, G.; Thangadurai, V.; Wilkening, M. Li Self-Diffusion in Garnet-Type  $\text{Li}_7\text{La}_3\text{Zr}_2\text{O}_{12}$  as Probed Directly by Diffusion-Induced  $^7\text{Li}$  Spin-Lattice Relaxation NMR Spectroscopy. *Phys. Rev. B* **2011**, *83*, No. 094302.
- (15) Kuhn, A.; Sreeraj, P.; Pöttgen, R.; Wiemhöfer, H. D.; Wilkening, M.; Heitjans, P. Li Ion Diffusion in the Anode Material  $\text{Li}_{12}\text{Si}_7$ : Ultrafast Quasi-1D Diffusion and Two Distinct fast 3D Jump Processes Separately Revealed by  $^7\text{Li}$  NMR Relaxometry. *J. Am. Chem. Soc.* **2011**, *133*, 11018–11021.
- (16) Epp, V.; Wilkening, M. Fast Li Diffusion in Crystalline  $\text{LiBH}_4$  due to Reduced Dimensionality: Frequency-Dependent NMR Spectroscopy. *Phys. Rev. B* **2010**, *82*, No. 020301.
- (17) Wilkening, M.; Kuhn, A.; Heitjans, P. Atomic-Scale Measurement of Ultraslow Li Motions in Glassy  $\text{LiAlSi}_2\text{O}_6$  by Two-Time  $^6\text{Li}$  Spin-Alignment Echo NMR Correlation Spectroscopy. *Phys. Rev. B* **2008**, *78*, No. 054303.
- (18) Volgmann, K.; Epp, V.; Langer, J.; Stanje, B.; Heine, J.; Nakhil, S.; Lerch, M.; Wilkening, M.; Heitjans, P. Solid-State NMR to Study Translational Li Ion Dynamics in Solids with Low-Dimensional Diffusion Pathways. *Z. Phys. Chem.* **2017**, *231*, 1215–1241.
- (19) Bottke, P.; Freude, D.; Wilkening, M. Ultraslow Li Exchange Processes in Diamagnetic  $\text{Li}_2\text{ZrO}_3$  As Monitored by EXSY NMR. *J. Phys. Chem. C* **2013**, *117*, 8114–8119.
- (20) Brandstätter, H.; Wohlmuth, D.; Bottke, P.; Pregartner, V.; Wilkening, M. Li Ion Dynamics in Nanocrystalline and Structurally Disordered  $\text{Li}_2\text{TiO}_3$ . *Z. Phys. Chem.* **2015**, *229*, 1363–1374.
- (21) Heitjans, P.; Indris, S. Diffusion and Ionic Conduction in Nanocrystalline Ceramics. *J. Phys.: Condens. Matter* **2003**, *15*, R1257–R1289.
- (22) Uhlendorf, J.; Ruprecht, B.; Witt, E.; Chandran, C. V.; Dörrer, L.; Hüger, E.; Strauß, F.; Heitjans, P.; Schmidt, H. Slow Lithium Transport in Metal Oxides on the Nanoscale. *Z. Phys. Chem.* **2017**, *231*, 1423–1442.
- (23) Heitjans, P.; Masoud, M.; Feldhoff, A.; Wilkening, M. NMR and Impedance Studies of Nanocrystalline and Amorphous Ion Conductors: Lithium Niobate as a Model System. *Faraday Discuss.* **2007**, *134*, 67–82.
- (24) Wilkening, M.; Epp, V.; Feldhoff, A.; Heitjans, P. *J. Phys. Chem. C* **2008**, *112*, 9291–9300.
- (25) Epp, V.; Wilkening, M. Motion of  $\text{Li}^+$  in Nanoengineered  $\text{LiBH}_4$  and  $\text{LiBH}_4\text{:Al}_2\text{O}_3$  Comparison with the Microcrystalline Form. *ChemPhysChem* **2013**, *14*, 3706–3713.
- (26) Bragatto, C. B.; Cassar, D. R.; Peitl, O.; Souquet, J.-L.; Rodrigues, A. C. M. Structural Relaxation in  $\text{AgPO}_3$  Glass Followed by *in situ* Ionic Conductivity Measurements. *J. Non-Cryst. Solids* **2016**, *437*, 43–47.
- (27) Kuhn, A.; Wilkening, M.; Heitjans, P. Mechanically Induced Decrease of the Li Conductivity in an Alumosilicate Glass. *Solid State Ionics* **2009**, *180*, 302–307.
- (28) Šepelák, V.; Düvel, A.; Wilkening, M.; Becker, K. D.; Heitjans, P. Mechanochemical Reactions and Syntheses of Oxides. *Chem. Soc. Rev.* **2013**, *42*, 7507–7520.
- (29) Preishuber-Pflügl, F.; Wilkening, M. Mechanochemically Synthesized Fluorides: Local Structures and Ion Transport. *Dalton Trans.* **2016**, *45*, 8675–8687.
- (30) Wilkening, M.; Düvel, A.; Preishuber-Pflügl, F.; da Silva, K.; Breuer, S.; Šepelák, V.; Heitjans, P. Structure and Ion Dynamics of Mechanothesized Oxides and Fluorides. *Z. Kristallogr. - Cryst. Mater.* **2017**, *232*, 107–127.
- (31) Šepelák, V.; Bergmann, I.; Feldhoff, A.; Heitjans, P.; Krumeich, F.; Menzel, D.; Litterst, F. J.; Campbell, S. J.; Becker, K. D. Nanocrystalline Nickel Ferrite,  $\text{NiFe}_2\text{O}_4$ : Mechanochemical Synthesis, Non-equilibrium Cation Distribution, Canted Spin Arrangement, and Magnetic Behavior. *J. Phys. Chem. C* **2007**, *111*, 5026–5033.
- (32) Šepelák, V.; et al. Nonequilibrium Structure of  $\text{Zn}_2\text{SnO}_4$  Spinel Nanoparticles. *J. Mater. Chem.* **2012**, *22*, 3117–3126.
- (33) Wohlmuth, D.; Epp, V.; Bottke, P.; Hanzu, I.; Bitschnau, B.; Letofsky-Papst, I.; Kriechbaum, M.; Amenitsch, H.; Hofer, F.; Wilkening, M. Order vs. disorder—a Huge Increase in Ionic Conductivity of Nanocrystalline  $\text{LiAlO}_2$  Embedded in an Amorphous-Like Matrix of Lithium Aluminate. *J. Mater. Chem. A* **2014**, *2*, 20295–20306.
- (34) Wilkening, M.; Bork, D.; Indris, S.; Heitjans, P. Diffusion in Amorphous  $\text{LiNbO}_3$  studied by  $^7\text{Li}$  NMR - Comparison with the Nano- and Microcrystalline Material. *Phys. Chem. Chem. Phys.* **2002**, *4*, 3246–3251.
- (35) Puin, W.; Heitjans, P. Frequency Dependent Ionic Conductivity in Nanocrystalline  $\text{CaF}_2$  Studied by Impedance Spectroscopy. *Nanostruct. Mater.* **1995**, *6*, 885–888.
- (36) Puin, W.; Rodewald, S.; Ramlau, R.; Heitjans, P.; Maier, J. Local and Overall Ionic Conductivity in Nanocrystalline  $\text{CaF}_2$ . *Solid State Ionics* **2000**, *131*, 159–164.
- (37) Puin, W.; Heitjans, P.; Dickenscheid, W.; Gleiter, H. NMR Study of Dynamic Processes in Nanocrystalline  $\text{CaF}_2$ . In *Defects in Insulating Materials*; Kanert, O.; Spaeth, J.-M., Eds.; World Scientific: Singapore, 1993; pp 137–139.

- (38) Heitjans, P.; Schirmer, A.; Indris, S. NMR and  $\beta$ -NMR Studies of Diffusion in Interface-Dominated and Disordered Solids. In *Diffusion in Condensed Matter – Methods, Materials, Models*; Heitjans, P.; Kärger, J., Eds.; Springer: Berlin, 2005; pp 367–415.
- (39) Jain, P.; Kim, S.; Youngman, R. E.; Sen, S. Direct Observation of Defect Dynamics in Nanocrystalline  $\text{CaF}_2$ : Results from  $^{19}\text{F}$  MAS NMR Spectroscopy. *J. Phys. Chem. Lett.* **2010**, *1*, 1126–1129.
- (40) Chandra, A.; Bhatt, A.; Chandra, A. Ion Conduction in Superionic Glassy Electrolytes: An Overview. *J. Mater. Sci. Technol.* **2013**, *29*, 193–208.
- (41) Heitjans, P.; Tobschall, E.; Wilkening, M. Ion Transport and Diffusion in Nanocrystalline and Glassy Ceramics. *Eur. Phys. J.: Spec. Top.* **2008**, *161*, 97–108.
- (42) Kuhn, A.; Tobschall, E.; Heitjans, P. Li Ion Diffusion in Nanocrystalline and Nanoglassy  $\text{LiAlSi}_2\text{O}_6$  and  $\text{LiBO}_2$  - Structure-Dynamics Relations in Two Glass Forming Compounds. *Z. Phys. Chem.* **2009**, *223*, 1359–1377.
- (43) Stanje, B.; Bottke, P.; Breuer, S.; Hanzu, I.; Heitjans, P.; Wilkening, M. Ion Dynamics in a New Class of Materials: Nanoglassy Lithium Aluminosilicates. *Mater. Res. Express* **2018**, *5*, No. 035202.
- (44) Maier, J. Ionic Conduction in Space Charge Regions. *Prog. Solid State Chem.* **1995**, *23*, 171–263.
- (45) Maier, J. Nano-Ionics: Trivial and Non-Trivial Size Effects on Ion Conduction in Solids. *Z. Phys. Chem.* **2003**, *217*, 415–436.
- (46) Gleiter, H. Nanoglasses: A New Kind of Noncrystalline Material and the Way to an Age of New Technologies? *Small* **2016**, *12*, 2225–2233.
- (47) Ivanisenko, Y.; Kübel, C.; Nandam, S. H.; Wang, C.; Mu, X.; Adjaoud, O.; Albe, K.; Hahn, H. Structure and Properties of Nanoglasses. *Adv. Eng. Mater.* **2018**, *20*, 1800404.
- (48) Bottke, P. NMR-Spektroskopie an nanokristallinem, nanoglasigem und glasigem Eukryptit  $\text{LiAlSiO}_4$ . Master Thesis, Leibniz University of Hannover, 2010.
- (49) Jonscher, A. K. The ‘Universal’ Dielectric Response. *Nature* **1977**, *267*, 673–679.
- (50) Almond, D. P.; Duncan, G. K.; West, A. R. The Determination of Hopping Rates and Carrier Concentrations in Ionic Conductors by a New Analysis of AC Conductivity. *Solid State Ionics* **1983**, *8*, 159–164.
- (51) Macdonald, J. R. Nearly Constant Loss or Constant Loss in Ionically Conducting Glasses: A Physically Realizable Approach. *J. Chem. Phys.* **2001**, *115*, 6192–6199.
- (52) Ngai, K. L. *Relaxation and Diffusion in Complex Systems*; Springer: New York, 2011.
- (53) Laughman, D. M.; Banhatti, R. D.; Funke, K. Nearly Constant Loss Effects in Borate Glasses. *Phys. Chem. Chem. Phys.* **2009**, *11*, 3158–3167.
- (54) Almond, D. P.; Hunter, C. C.; West, A. R. The Extraction of Ionic Conductivities and Hopping Rates from a.c. Conductivity Data. *J. Mater. Sci.* **1984**, *19*, 3236–3248.
- (55) Laughman, D. M.; Banhatti, R. D.; Funke, K. New Nearly Constant Loss Feature Detected in Glass at Low Temperatures. *Phys. Chem. Chem. Phys.* **2010**, *12*, 14102–14108.
- (56) Banhatti, R. D.; Laughman, D.; Badr, L.; Funke, K. Nearly Constant Loss Effect in Sodium Borate and Silver Meta-phosphate Glasses: New Insights. *Solid State Ionics* **2011**, *192*, 70–75.
- (57) Ishai, P. B.; Talary, M. S.; Caduff, A.; Levy, E.; Feldman, Y. Electrode Polarization in Dielectric Measurements: A Review. *Meas. Sci. Technol.* **2013**, *24*, 102001.
- (58) Emmert, S.; Wolf, M.; Gulich, R.; Krohns, S.; Kastner, S.; Lunkenheimer, P.; Loidl, A. Electrode Polarization Effects in Broadband Dielectric Spectroscopy. *Eur. Phys. J. B* **2011**, *83*, 157–165.
- (59) Mehrer, H. *Diffusion in Solids - Fundamentals, Methods, Materials, Diffusion-Controlled Processes*; Springer: Berlin, Heidelberg, 2007.
- (60) Francisco, B. E.; Stoldt, C. R.; M’Peko, J.-C. Energetics of Ion Transport in NASICON-Type Electrolytes. *J. Phys. Chem. C* **2015**, *119*, 16432–16442.
- (61) Ahmad, M. M. Estimation of the Concentration and Mobility of Mobile  $\text{Li}^+$  in the Cubic Garnet-Type  $\text{Li}_7\text{La}_3\text{Zr}_2\text{O}_{12}$ . *RSC Adv.* **2015**, *5*, 25824–25829.
- (62) Almond, D. P.; West, A. R. Entropy Effects in Ionic Conductivity. *Solid State Ionics* **1986**, *18-19*, 1105–1109.
- (63) Metselaar, R.; Oversluizen, G. The Meyer-Neldel Rule in Semiconductors. *J. Solid State Chem.* **1984**, *55*, 320–326.
- (64) Francisco, B. E.; Stoldt, C. R.; M’Peko, J.-C. Lithium-Ion Trapping from Local Structural Distortions in Sodium Super Ionic Conductor (NASICON) Electrolytes. *Chem. Mater.* **2014**, *26*, 4741–4749.
- (65) Hodge, I. M.; Ngai, K. L.; Moynihan, C. T. Comments on the Electric Modulus Function. *J. Non-Cryst. Solids* **2005**, *351*, 104–115.
- (66) Hodge, I. M.; Ingram, M. D.; West, A. R. Impedance and Modulus Spectroscopy of Polycrystalline Solid Electrolytes. *J. Electroanal. Chem. Interfacial Electrochem.* **1976**, *74*, 125–143.
- (67) Irvine, J. T. S.; Sinclair, D. C.; West, A. R. Electroceramics: Characterization by Impedance Spectroscopy. *Adv. Mater.* **1990**, *2*, 132–138.
- (68) Stanje, B.; Rettenwander, D.; Breuer, S.; Uitz, M.; Berendts, S.; Lerch, M.; Uecker, R.; Redhammer, G.; Hanzu, I.; Wilkening, M. Solid Electrolytes: Extremely Fast Charge Carriers in Garnet-Type  $\text{Li}_6\text{La}_3\text{ZrTaO}_{12}$  Single Crystals. *Ann. Phys.* **2017**, *529*, 1700140.

# Glass in Two Forms: Heterogeneous Electrical Relaxation in Nanoglassy Petalite

B. Gadermaier,<sup>1\*</sup> B. Stanje<sup>1,2</sup>, A. Wilkening,<sup>1</sup> I. Hanzu<sup>1,2</sup>, P. Heitjans<sup>3</sup>, and H. M. R. Wilkening<sup>1,2</sup>

<sup>1</sup> Institute for Chemistry and Technology of Materials, Christian Doppler Laboratory for Lithium Batteries, Graz University of Technology (NAWI Graz), Stremayrgasse 9, A-8010 Graz, Austria

<sup>2</sup> Alistore – European Research Institute, CNRS FR3104, Hub de l’Energie, Rue Baudelocque, 80039 Amiens, France

<sup>3</sup> Institute of Physical Chemistry and Electrochemistry, Leibniz University Hannover, Callinstr. 3-3a, D-30167 Hannover, Germany

\* corresponding author: bernhard.gadermaier@tugraz.at

Figure S1 compares selected isotherms of nanoglassy and glassy petalite to highlight changes in shape that show up for the glass milled for only 6 h. In addition, in Fig. 3 c) a significant change in DC conductivity is seen when comparing the isotherm of the glass with that of the nanoglass (24 h), see vertical arrow.

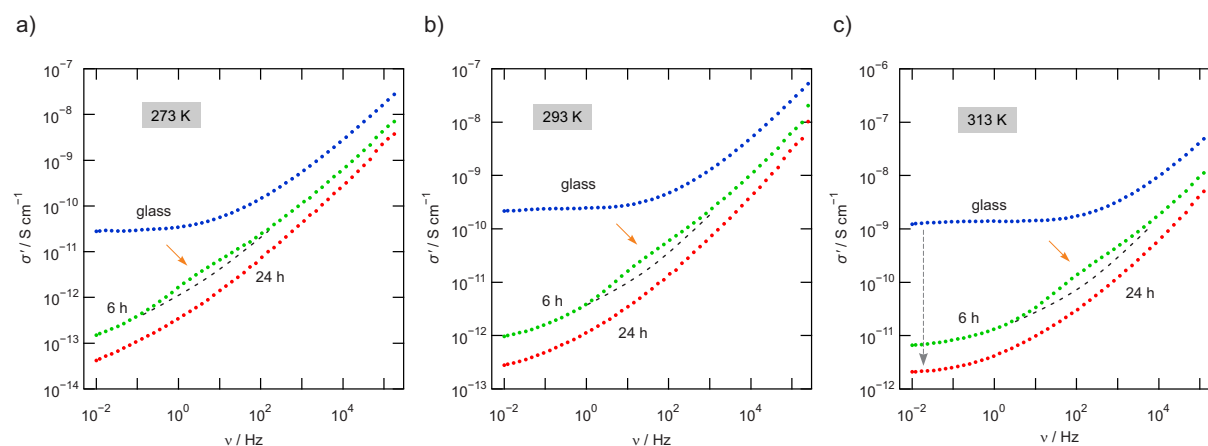


**Figure S1:** Conductivity isotherms of the petalite glass and nanoglass milled for 6 h and 24 h, respectively, at 273 K (a), 293 K (b) and 313 K (c). The glass and the nanoglass (24 h) show a smooth transition from the DC conductivity plateau to the dispersive regime at higher frequencies. The regions, which we attribute to a not fully relaxed glass, cause a small bump in this transition regime if we regard the isotherm of the nanoglass obtained after milling the glass for 6 h; the dashed lines are to guide the eye and to highlight the second plateau (see small arrows).





### 3.2. Influence of defects on ionic transport in $\text{LiTaO}_3$ – a study using EXAFS and positron annihilation lifetime spectroscopy

Ionic conductivity in solid electrolytes depends on many factors. Especially polycrystalline materials with very low ionic conductivity in their defect poor state show a huge increase of ionic conductivity after high-energy ball milling. The actual cause for this increase and to which extend individual causes affect ionic conductivity is not understood in detail. If high-energy ball milling is used to obtain such defect-rich materials, many possible origins for increased conductivity could be called to account for. High-energy ball milling does not only break microcrystalline material down to a nanocrystalline material, but also introduced many zero and higher dimensional defects. In the nanosized state, even if defect-poor, the ionic conductivity oft exceeds that of the bulk material. This is partly due to the higher surface energy, which result in increased ionic conductivity, especially if the diffusion of the ions on the surface of the particles is enhanced. Furthermore, vacancies, as well as strain and bond distortions can have an enormous impact on ionic conduction. In a crystal where the mobile ion is highly coordinated and strongly bonded in the regular structure, the ionic conductivity is rather poor. To jump from one crystallographic position to another, the ion has to break its bonds with the framework, push through an anion framework and form bonds with its new surroundings. If the bond length of the ion is modified by displacement, *i.e.* slight distortion of the anion framework, the energy required to break these bonds will change accordingly. Furthermore, the distortion of the anion framework can give rise to local connections between the crystallographic sites that can be passed easily. These connections from low-energy diffusion paths that will increase the overall ionic conductivity even if they are not percolating *i.e.* are limited to a few consecutive crystallographic sites. Apart from the distortion of the crystal structure, the generation of vacancies and defects, especially Schottky defects, strongly affects the ionic conductivity. Evidently, the ion has to jump somewhere, and a vacant crystallographic position represents a low-energy position where the ion could reside after a jump.

$\text{LiTaO}_3$  represents a material with a very low ionic conductivity in its defect poor, microcrystalline state. The conductivity enormously increases after treating this material by high-energy ball milling. The underlying mechanism responsible for this effect is not well understood. Many factors, as mentioned above, might be individually or collectively responsible. Clearly, in-detail investigations were necessary to gain more insight into the, probably multicausal, effects increasing ionic

conductivity in this material. We probed interatomic distances using Tantal EXAFS and applied PALS spectroscopy to shed light on the lower dimensional defect state of the nanocrystalline and microcrystalline samples. The study was complemented by analysis of the ionic conductivity. Especially the analysis of nanocrystalline samples annealed at different temperatures helped to draw a clearer picture of the interplay between distortion, defect structure and ionic conductivity. We found that especially distortions of the framework, reflected in a change of the mean length of the bonds in the TaO<sub>6</sub> polyhedron, substantially influence the ionic conductivity. Samples annealed at  $T \geq 500$  °C show a clear decrease in the pre-exponential factor of the Arrhenius law characterizing the ionic conductivity correlated with interatomic distances almost equal to the microcrystalline sample. Such samples, however, are still rich in vacancies and voids as indicated by high mean positron lifetimes. Therefore, we conclude that the distortions of the framework seem to have the highest impact on ionic conductivity albeit the effect of vacancies is non negligible. This is exemplified by the samples annealed at  $T = 750$  °C since these samples still show higher ionic conductivity than their microcrystalline counterpart albeit the interatomic distances are equal to those in the microcrystalline state.

## **P2**

Gadermaier, B.; Resch, L.; Pickup, D. M.; Hanghofer, I.; Hanzu, I.; Heitjans, P.; Sprengel, W.;  
Würschum, R.; Chadwick, A. V.; Wilkening, H. M. R.

### **Influence of Defects on Ionic Transport in $\text{LiTaO}_3$ – a Study Using EXAFS and Positron Annihilation Lifetime Spectroscopy**

Solid State Ionics 2020, 352, 115355.



# Influence of defects on ionic transport in LiTaO<sub>3</sub> – A study using EXAFS and positron annihilation lifetime spectroscopy

B. Gadermaier<sup>a,\*</sup>, L. Resch<sup>b</sup>, D.M. Pickup<sup>c</sup>, I. Hanghofer<sup>a</sup>, I. Hanzu<sup>a</sup>, P. Heitjans<sup>d</sup>, W. Sprengel<sup>b</sup>, R. Würschum<sup>b</sup>, A.V. Chadwick<sup>c</sup>, H.M.R. Wilkening<sup>a,e,\*\*</sup>

<sup>a</sup> Institute of Chemistry and Technology of Materials, Christian Doppler Laboratory for Lithium Batteries, Graz University of Technology (NAWI Graz), Stremayrgasse 9, A-8010 Graz, Austria

<sup>b</sup> Institute of Materials Physics, Graz University of Technology, Petersgasse 16, A-8010 Graz, Austria

<sup>c</sup> School of Physical Sciences, University of Kent, Canterbury, Kent CT2 7NH, UK.

<sup>d</sup> Institute of Physical Chemistry and Electrochemistry, Leibniz University Hannover, Callinstrasse 3-3a, D-30167 Hannover, Germany

<sup>e</sup> Alistore-ERI European Research Institute, CNRS FR3104, Hub de l'Energie, Rue Baudelocque, F-80039 Amiens, France

## ARTICLE INFO

### Keywords:

Lithium tantalate

EXAFS

Positron lifetime spectroscopy

Defects

Ionic conductivity

## ABSTRACT

Defects of various types in crystalline and nanocrystalline materials govern a range of electrical, optical and mechanical properties. In particular, they are at the heart of translational ion dynamics in solid electrolytes. One of the most prominent examples revealing a drastic increase in ionic conductivity  $\sigma_{DC}$  by several orders of magnitude when going from an ordered crystalline matrix to a structurally disordered one is lithium tantalate. Here, structurally disordered, nanocrystalline LiTaO<sub>3</sub> served as a model substance to shed light on the question to what extent the degree of disorder decreases upon annealing an originally defect-rich oxide. Disorder can be introduced by high-energy ball milling of LiTaO<sub>3</sub> crystallites with diameters in the  $\mu\text{m}$  range. Broadband conductivity spectroscopy, EXAFS and positron annihilation lifetime spectroscopy were used to correlate ion transport properties with interatomic distances, bond distortions and positron lifetimes. It turned out that milling times of only 30 min are sufficient to generate a highly defective oxide. Upon annealing at temperatures of  $T = 200\text{ }^\circ\text{C}$  the defects can almost be preserved. Annealing at  $750\text{ }^\circ\text{C}$  for 1 h is needed to induce healing of the defects. Although we observe a recovery of the original interatomic distances and an increase in activation energy  $E_a$  for ionic transport from 0.75 eV to 0.81 eV, the initial transport properties of the unmilled sample (0.97 eV) cannot be fully restored. Most interestingly, the change in  $E_a$  is accompanied by a change of the entropy-controlled Arrhenius pre-factor governing the temperature dependence of  $\sigma_{DC}T$ . Moreover, positron lifetimes remain high in the annealed samples. Hence, our results point to samples with fewer distortions but still rich in vacancy-type defects. Altogether, the combination of ball milling and annealing helps adjust ionic conductivities in LiTaO<sub>3</sub> to vary over 4 to 5 orders of magnitude.

## 1. Introduction

High-energy ball milling finds great application in the study of nanostructured solid ionic conductors, as the starting materials with  $\mu\text{m}$ -sized crystallites are readily converted to nanocrystalline ceramics being characterized by a high degree of structural disorder [1–9]. Milling of ceramic powders in high-energy planetary mills or shaker mills under dry conditions for several hours usually results in nanocrystalline materials composed of cluster-assembled nm-sized crystallites [4,8–12]. The individual nanocrystals show diameters of ca. 10 to 20 nm depending on the materials properties and exact milling

conditions [8,9,13,14].

Ball milling is also the method of choice that allows carrying out mechanochemical reactions [7–10], which, in many cases, lead to phase-pure nanostructured compounds such as oxides and fluorides [8,9]. Without any mechanochemical reaction being involved, the conversion from microcrystalline to defect-rich nanocrystalline solids is, in some cases, accompanied with an enormous increase in ionic conductivity [5,15]. In particular, such enhancements were found for materials crystallizing with structures that do not readily offer low-energy diffusion pathways for long-range ion transport [5]. According to a simple picture, in some cases the resulting nanocrystals may be

\* Corresponding author.

\*\* Correspondence to: H.M.R. Wilkening, Alistore – ERI European Research Institute, CNRS FR3104, Hub de l'Energie, Rue Baudelocque, F-80039 Amiens, France.  
E-mail addresses: [bernhard.gadermaier@tugraz.at](mailto:bernhard.gadermaier@tugraz.at) (B. Gadermaier), [wilkening@tugraz.at](mailto:wilkening@tugraz.at) (H.M.R. Wilkening).

described by a core-shell structure: the crystalline inner regions are surrounded by a structurally disordered shell with a thickness of a few nm [5,16]. However, the introduction of distortions and defects is not only restricted to the outer regions. In the case of LiTaO<sub>3</sub> the whole matrix is affected by mechanical treatment leading to a material in a non-equilibrium state with bond or polyhedra distortions and defects. The latter include also point defects, such as vacancies, interstitials and even anti-site defects, being then also present in the crystalline cores [9]. In addition, the formation of entirely amorphous (surface) regions has been documented for ball-milled samples [17]. Importantly, also point-defect related space charge effects in materials with nm-sized dimensions will play a capitol role in determining ion dynamics [18–20].

In general, for some materials structural disorder, particularly represented by strain, polyhedra distortions, changing of bond length and the formation of defects enables the Li ions to get access to (local) diffusion pathways with lower activation energies than those governing ionic transport in the ordered microcrystalline counterparts. Again, also space charge effects will contribute to this effect [18]. As an example, the poor ionic conductivity of LiTaO<sub>3</sub> can be increased by 4–5 orders of magnitude when going from microcrystalline LiTaO<sub>3</sub> to its nanocrystalline form that has been prepared by high-energy ball milling [15]. As has been shown by some of us earlier, milling times  $t_{\text{mill}}$  as short as 30 min are sufficient to greatly enhance the overall Li<sup>+</sup> ion conductivity  $\sigma_{\text{DC}}$  [15]. If planetary mills are used to prepare nanocrystalline LiTaO<sub>3</sub>, an increase of  $t_{\text{mill}}$  up to several hours does not lead to any additional increase of  $\sigma$  that significantly enhances Li<sup>+</sup> ion dynamics further. The important question, which the present study is aimed at answering, is how stable the defect-rich structures are against temperature treatment, *i.e.*, soft annealing of the powders. A previous NMR investigation and conductivity study on nanocrystalline LiTaO<sub>3</sub> indicated that samples, which had been shortly milled for only 30 min, can easier be transformed back to a structural state resembling that of the starting material [15]. Of course, this transformation sensitively depends on the exact annealing conditions.

Here, we used broadband conductivity measurements, EXAFS (extended X-ray absorption fine structure) [12,21–24] measurements and positron annihilation lifetime spectroscopy (PALS) [25–27] to correlate ionic transport parameters of nanocrystalline LiTaO<sub>3</sub> with the degree of structural disorder remaining after annealing. Specifically, we probed activation energies of ionic transport and extracted Arrhenius prefactors, estimated interatomic distances and positron lifetimes to qualitatively characterize the extent of disorder and defects remaining after different annealing steps. Most importantly, structural disorder is almost untouched when the samples are subjected to soft annealing carried out at temperatures as low as 200 °C. The conservation of disorder ensures a high ionic conductivity, which still exceeds that of microcrystalline LiTaO<sub>3</sub> by 4 orders of magnitude. This finding is important for all-solid-state battery research as thin films of nanocrystalline or amorphous LiTaO<sub>3</sub> are increasingly used to protect Li metal anodes [28] from being covered with insulating decomposition products of electrochemically instable ceramic electrolytes [29]. Moreover, the combination of milling and annealing allows us to tailor ionic conductivities in nanocrystalline LiTaO<sub>3</sub> over several orders of magnitude.

## 2. Experimental

Microcrystalline LiTaO<sub>3</sub> (99.99% purity, metals basis) was obtained from Alfa Aesar. To prepare nanocrystalline LiTaO<sub>3</sub>, the powder was milled for either 30 min or 10 h under dry conditions in ZrO<sub>2</sub> grinding beakers (45 ml) equipped with 180 balls made of ZrO<sub>2</sub> (5 mm in diameter) using a Fritsch Planetary mill (Premium line 7). According to our experience, the abrasion of ZrO<sub>2</sub> is low when LiTaO<sub>3</sub> (or fluorides such as BaF<sub>2</sub> [30,31]) is milled. Especially for short milling times of only 30 min we assume a negligible effect of ZrO<sub>2</sub> abrasion or even

Zr<sup>4+</sup> incorporation. Thus, ZrO<sub>2</sub> abrasion cannot be the reason for the large increase in conductivity already seen after 30 min of milling. The effect is also intended of the material of the vials used as it is also seen with Al<sub>2</sub>O<sub>3</sub> vials [15]. Moreover, because of the very low amount of abraded ZrO<sub>2</sub>, any Li<sup>+</sup> transport along possible LiTaO<sub>3</sub>|ZrO<sub>2</sub> interfaces is more than negligible. After mechanical treatment the milled samples were annealed at 250 °C, 500 °C and 750 °C, respectively, for 1 h ( $t_{\text{mill}} = 30$  min) and 6 h ( $t_{\text{mill}} = 10$  h) at a heating rate of 5 K/min.

For X-ray powder diffraction, the samples were either analysed using a Bruker D8 Advance diffractometer or a Rigaku Miniflex 600 (Bragg Brentano geometry, CuK<sub>α</sub> radiation). The patterns were recorded with a step size of 0.02° (waiting time 2 s) in the 2 $\theta$ -range 20° to 100°. Rietveld refinement was carried out by using X'PertHighScorePlus (Panalytical).

For our impedance measurements, the powders were uniaxially pressed into pellets (5 mm in diameter, 1 to 1.5 mm in thickness). After applying Au electrodes *via* sputtering (Leica sputter device), a Novocontrol Concept 80 broadband analyser was employed to record complex impedance data from which conductivity values were calculated. We varied the frequency  $\nu$  from 10 mHz to 10 MHz (20 °C to 140 °C, in steps of 20 °C). In our setup the temperature was automatically controlled by means of a QUATRO cryosystem (Novocontrol), which uses a heating element to build up a specific pressure in a liquid nitrogen Dewar to create an N<sub>2</sub> gas flow that is subsequently heated in order to adjust the temperature. For the *in situ* measurements to probe healing of the defects, the samples were heated to 200 °C and held at that temperature for 9 h in the impedance measurement setup; each hour impedance measurements were carried out to record the change in conductivity over time.

For the positron lifetime measurements of the present study, a <sup>22</sup>Na source (encapsulated in Al foil) was sandwiched between two identical samples; pellets of 5 mm diameter and 2 mm thickness. The positron lifetime spectra were recorded using an analogue positron lifetime spectrometer obtaining a full width at half maximum of the resolution function of 220 ps. Each lifetime spectrum contained > 10<sup>6</sup> counts and was analysed after background and source correction by means of the program PALSfit [32]. All spectra were fitted to two lifetime components and their intensities.

X-ray absorption spectroscopy scans were collected for the appropriate edge (Ta L3-edge) at room temperature on beam line B18 at the Diamond Light Source (Didcot, UK). Data collection used transmission mode with ion chamber detectors. Continuous scanning (QEXAFS) was employed; an individual scan required 180 s and several scans were performed to improve the signal-to-noise ratio. The synchrotron energy and current were 3 GeV and 300 mA, respectively. The beam size at the sample was 700 × 700 μm. Powdered samples were mixed with cellulose as a diluent and pressed into 13 mm diameter pellets. The spectra were normalized in Athena and analysed in the frame of scattering models in *R*-space produced by FEFF in Artemis [33].

## 3. Results and discussion

As has been shown in an earlier study by some of us, high-energy ball milling drastically increases the conductivity of otherwise poorly conducting LiTaO<sub>3</sub> [15]. The crystal structure of LiTaO<sub>3</sub> is shown in Fig. 1c (for XRPD patterns see Fig. S1). The same behaviour [5] has previously been found for LiNbO<sub>3</sub> and resembles the giant increase in ionic conductivity described by Glass et al. [34] for glassy LiNbO<sub>3</sub> when compared with its crystalline or even monocrystalline counterpart [35]. Comparing the microcrystalline starting material with nanocrystalline LiTaO<sub>3</sub>, which is obtained after several hours of mechanical treatment in high-energy ball mills, clearly reveals that the increase in conductivity is a result of both i) a strong decrease of the activation energy  $E_a$  of the underlying Arrhenius relation and ii) an increase of the corresponding prefactor  $\sigma_0$  (see Fig. 1a) [11]. Here, we measured conductivity isotherms, that is, the variation of the real part  $\sigma'$  of the

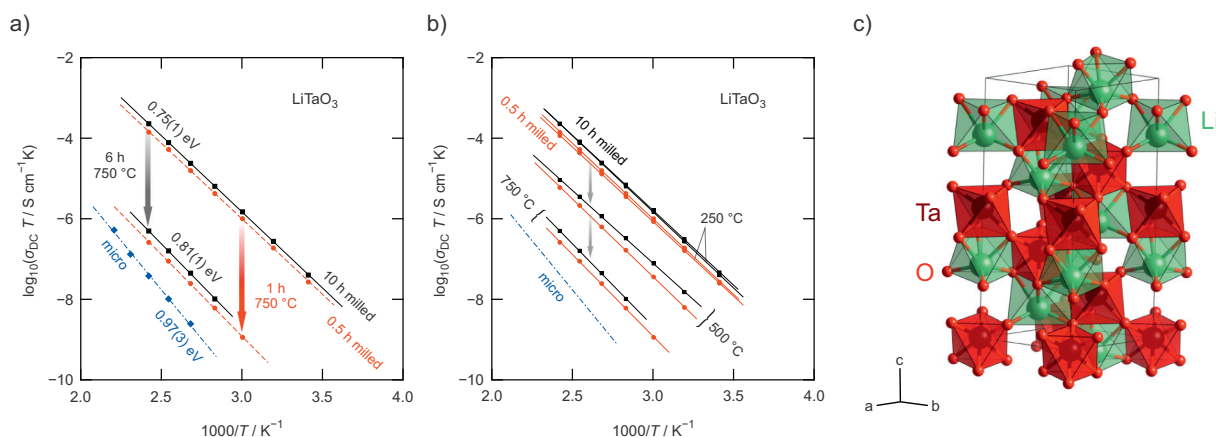


**Fig. 1.** a) Arrhenius diagram showing the conductivities of the microcrystalline and the milled samples ( $t_{\text{mill}} = 30 \text{ min}$ ,  $10 \text{ h}$ ) before and after annealing at  $750 \text{ }^\circ\text{C}$  (for  $1 \text{ h}$  and  $6 \text{ h}$ , respectively). Solid lines represent fits to the Arrhenius equation; activation energies are indicated, these change from  $0.97(3) \text{ eV}$  to  $0.75(1) \text{ eV}$ . Error bars are smaller than the size of the symbols used. b) Change of ionic conductivity after annealing the samples milled for  $30 \text{ min}$  ( $\bullet$ ) and  $10 \text{ h}$  ( $\blacksquare$ ), respectively, upon annealing at  $250 \text{ }^\circ\text{C}$ ,  $500 \text{ }^\circ\text{C}$  and  $750 \text{ }^\circ\text{C}$  for  $1 \text{ h}$  ( $t_{\text{mill}} = 30 \text{ min}$ ) and  $6 \text{ h}$  ( $t_{\text{mill}} = 10 \text{ h}$ ); the corresponding activation energies are shown in Fig. 2. For comparison, the temperature dependence of the ionic conductivity of unmilled  $\text{LiTaO}_3$  is indicated by a dashed-dotted line. c) Crystal structure of  $\text{LiTaO}_3$ ;  $\text{LiO}_6$  octahedra are connected in a corner-sharing manner and do not build fast  $\text{Li}^+$  diffusion pathways. Consequently, in microcrystalline  $\text{LiTaO}_3$  the ionic conductivity is rather poor.

complex conductivity as a function of a broad frequency range [36–38]. These isotherms are composed of a typical frequency-independent plateau, which corresponds to the so-called DC ionic conductivity  $\sigma_{\text{DC}}$  being a measure for long-range ionic transport [9,39,40].

Interestingly, milling a sample of microcrystalline  $\text{LiTaO}_3$  for only  $30 \text{ min}$  increases the room-temperature conductivity  $\sigma_{\text{DC}}$  by almost 5 orders of magnitude, i.e., it increases from approximately  $2 \times 10^{-15} \text{ S cm}^{-1}$  to ca.  $9.2 \times 10^{-11} \text{ S cm}^{-1}$ . Prolonged milling for  $t_{\text{mill}} = 10 \text{ h}$  increases the conductivity only slightly, at room temperature a value of  $1.4 \times 10^{-10} \text{ S cm}^{-1}$  is reached that is highly comparable to that of the sample milled for only  $30 \text{ min}$  (see Fig. 1a).

Analysing the temperature dependence of the ionic conductivity with the Arrhenius equation  $\sigma_{\text{DC}} = \sigma_0/T \exp(-E_a/(k_B T))$  shows that milling leads to an increase of the pre-exponential factor from  $\log_{10}(\sigma_0/S \text{ K cm}^{-1}) = 4.40$  for the microcrystalline sample to  $5.25$  and further to  $5.52$  when going to samples milled for  $30 \text{ min}$  and for  $10 \text{ h}$ , respectively. This increase of  $\sigma_0$  is accompanied by a marked decrease of the corresponding activation energy  $E_a$  from  $0.97 \text{ eV}$  to approximately  $0.75$  for the two samples (see Fig. 1b). These values are comparable to trends seen in earlier studies [11,15] that report on activation energies ranging from  $0.63 \text{ eV}$  to  $0.69 \text{ eV}$  for nanocrystalline  $\text{LiTaO}_3$  and  $0.85 \text{ eV}$  to  $0.90 \text{ eV}$  for microcrystalline lithium tantalate. Here, to further analyse the relationship between ionic conductivity and structural disorder, the milled samples have been annealed at different temperatures to follow the change in  $\sigma_{\text{DC}}$ ,  $E_a$  and  $\sigma_0$ , see Figs. 1b and 2.

For both samples, either milled for  $30 \text{ min}$  or  $10 \text{ h}$ , annealing leads to a decrease of the overall conductivity (see Fig. 1). After the annealing step at  $250 \text{ }^\circ\text{C}$  the change in conductivity is rather small as indicated by the barely changed prefactors and activation energies (see Figs. 1b and 2a). A stronger change is caused when the samples are annealed at  $500 \text{ }^\circ\text{C}$ . While the prefactor decreases distinctively, the activation energy, however, changes only slightly. Interestingly, the change in prefactor of the  $10\text{-h}$  sample is at maximum after this annealing step; simultaneously, this drop in  $\sigma_0$  is even accompanied by a further, very small decrease in  $E_a$ , which resembles the behaviour predicted by the so-called Meyer-Neldel rule [41,42] connecting low prefactors with low activation energies. Annealing at  $750 \text{ }^\circ\text{C}$  causes a marked increase in  $E_a$  which reaches values of ca.  $0.8 \text{ eV}$  for both samples. The slightly higher prefactor characterizing the  $10\text{-h}$  sample finally results in a somewhat higher ionic conductivity after this annealing step, see Fig. 1b.

A more direct comparison of the change in conductivity upon annealing is shown in Fig. 2b which illustrates the evolution of ionic conductivities  $\sigma_{\text{DC}}$  of the two samples ( $t_{\text{mill}} = 30 \text{ min}$  and  $10 \text{ h}$ ) as a

function of annealing time,  $t_{\text{anneal}}$ . The samples were kept inside the impedance sample holder for several hours at  $200 \text{ }^\circ\text{C}$  and under  $\text{N}_2$  atmosphere. It can be clearly seen that after the initial decrease in conductivity,  $\sigma_{\text{DC}}$  of the  $30\text{-min}$  sample rapidly reaches a saturation value. The change in  $\sigma_{\text{DC}}$  can be parameterized with a stretched exponential. Instead, the sample treated for  $10 \text{ h}$  reveals a decay curve that is best described by a double-exponential function, pointing to structural changes that need longer annealing times to be restored as compared to the sample milled only shortly.

Before putting the data acquired by impedance spectroscopy into context with the structural data obtained by PALS and EXAFS the overall picture of the changes in conductivity evoked by milling and subsequent annealing shall be shortly discussed. In line with earlier reports [11,15], milling of the microcrystalline educt greatly improves  $\text{Li}^+$  long-range ionic transport even after very short milling times of only  $30 \text{ min}$ . Longer milling times of  $10 \text{ h}$  do only slightly improve  $\sigma_{\text{DC}}$ . In the case of  $\text{LiTaO}_3$ ,  $\text{Li}^+$  is the main mobile charge carrier. Fielitz et al. showed by  $^{18}\text{O}$  tracer diffusion experiments that the diffusivity of oxygen is, compared to Li ion diffusivity, very low and characterized by a very high activation energy ( $> 4 \text{ eV}$ ) [43]. Thus, in the investigated temperature regime oxygen diffusion is very likely negligible. In addition, we expect that loss of oxygen upon ball-milling, and thus affecting ionic conductivity, plays a marginal role if at all.

Upon annealing of the samples, we see both similarities and differences between the two samples. Only after annealing at temperatures of  $500 \text{ }^\circ\text{C}$  and above,  $\sigma_{\text{DC}}$  is significantly changed. Of course, this change depends on the duration of annealing  $t_{\text{anneal}}$ , which we varied from  $1 \text{ h}$  to  $6 \text{ h}$ . The decrease seen for  $\sigma_{\text{DC}}$  is foremost caused by a decrease of the prefactor of the underlying Arrhenius equation (see Fig. 1a). Nevertheless, even after annealing the samples at  $750 \text{ }^\circ\text{C}$  for several hours, the conductivity of the milled samples surpasses that of the structurally ordered microcrystalline counterpart consisting of  $\mu\text{m}$ -sized crystallites. With the soft annealing conditions chosen here, the original state of the starting material cannot be fully recovered. We show that the ionic conductivity of the milled samples, if exposed to temperatures of  $250 \text{ }^\circ\text{C}$  and below, is remarkably robust against heat treatment.

Generally, the introduction of defects, site disorder and distortions during ball milling is responsible for the large increase in conductivity. This increase originates from a decrease of  $E_a$  and an increase of the prefactor  $\sigma_0$ . The latter is, besides other factors such as jump lengths, also influenced by an entropy term [44–46]. During the annealing steps, we expect both distortions and point defects, such as vacancies and interstitials, to be healed. Importantly, healing of defects turned out

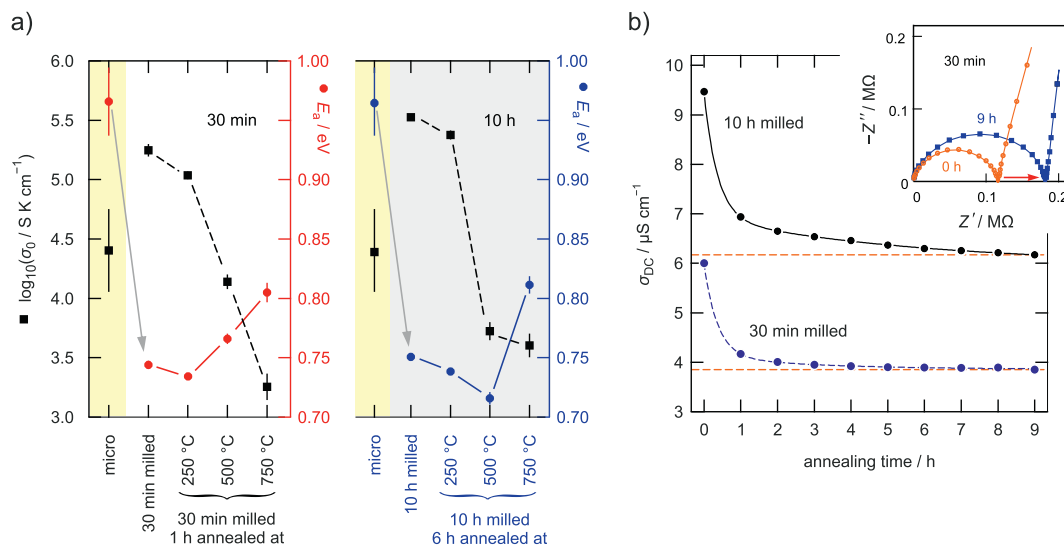


**Fig. 2.** a) Change of the prefactors  $\sigma_0$  and activation energies  $E_a$  characterizing the ionic conductivities of the various samples investigated (see horizontal axis); the values have been determined by least square fitting, see the data shown in Fig. 1. The lower the ionic conductivity of the samples, the larger the error bars. Samples with high activation energies, *i.e.*, steep slopes in the corresponding Arrhenius diagram result, of course, in pre-factors with a larger error margin. Importantly, even after the annealing step at 750 °C (6 h,  $t_{\text{mill}} = 10$  h) the original activation energy of 0.97 eV cannot be recovered, see text for further details. b) Change of the DC ionic conductivity during annealing the sample milled for 30 min and 10 h, respectively, at  $T = 200$  °C. At this temperature the ionic conductivity drops by a factor of 2 reaching for the 30-min sample a saturation value after 6 to 7 h. This behaviour is in contrast to the sample heavily treated mechanically for 10 h. After the initial drop during the first 1 to 2 h,  $\sigma_{\text{DC}}$  decays slower than it is the case for the 30-min sample. This two-step decay behaviour has been visualized with a double-exponential function (solid line) to guide the eye. For comparison, the change seen for the sample milled for only 30 min can be parameterized with a single exponential (dashed line). The inset shows the complex plane plot (Nyquist plot) of the impedance for the sample milled for 30 min;  $Z'$  represents the real part of the complex impedance and  $Z''$  denotes the imaginary part. The semicircle seen reflects electrical relaxation in the bulk, the spikes indicate electrode polarization.

to be much easier for the sample milled for 30 min as annealing steps with a duration of only  $t_{\text{anneal}} = 1$  h are sufficient to recover conductivities that are very similar to those obtained for the 10-h sample that needs to be annealed for a longer period of time *viz.*  $t_{\text{anneal}} = 6$  h. Hence, we conclude that structural disorder introduced after 30 min of mechanical treatment is readily “healed” by annealing for short durations as is reflected in the change of  $\sigma_{\text{DC}}$  (see Figs. 1 and 2). This conclusion is also supported by the annealing curves recorded at 200 °C shown in Fig. 2b. The sample milled for 10 h, however, does not only contain these “fast healing” defects, but, as seen in the steady decrease of its ionic conductivity, is also equipped with defects with a much slower healing rate. The latter, which manifests in a two-step decay of the annealing curve (see Fig. 2c), is absent for the sample milled for  $t_{\text{mill}} = 30$  min (see also Fig. 2b). Again, as we see qualitatively the same change in conductivity when the samples are annealed in air or in  $\text{N}_2$  atmosphere, we conclude that there is no loss of oxygen occurring under the annealing conditions chosen, see above. If present, annealing in air or  $\text{N}_2$  would result in markedly different results. Furthermore, if we compare the conductivities of the 10 h milled sample before and after annealing at 250 °C for 6 h we see that there is hardly any change, *cf.* Fig. 1b.

In general, we assume that in milled  $\text{LiTaO}_3$ , crystallizing in the antiperovskite-type structure, the  $\text{Li}^+$  ionic conductivity is not only controlled by the amount of structurally disordered interfacial regions but also by the number and type of point defects [15] in the grains. The latter include both Schottky and Frenkel defects introduced during mechanical treatment. Therefore, we analysed the milled samples by PALS, which is, in particular, sensitive to free volume type defects, voids and vacancies [25].

For two microcrystalline  $\text{LiTaO}_3$  samples, within experimental uncertainty the same set of positron ( $e^+$ ) lifetime components of 209 ps ( $\tau_1$ ) and 324 ps ( $\tau_2$ ) were obtained. This finding indicates a well-defined as-received state (see Table 1), serving here as a reference for the ball-milled samples. From the two components and their relative intensities, we calculated the respective mean positron lifetime  $\tau_{\text{mean}}$  according to

**Table 1**

Positron lifetime components  $\tau_i$  with relative intensities  $I_i$  ( $i = 1, 2$  (in %)) and mean positron lifetimes  $\tau_{\text{mean}}$  for  $\text{LiTaO}_3$  in the as-received microcrystalline state, after ball-milling, and after subsequent annealing. The numerical uncertainty for  $\tau_i$  is  $\pm 4$  ps.

Sample	$\tau_1/\text{ps}$	$I_1$	$\tau_2/\text{ps}$	$I_2$	$\tau_{\text{mean}}/\text{ps}$
Microcrystalline	209	77	324	23	235
30 min	230	82	411	18	262
+ 1 h@750 °C	240	92	452	8	256
10 h	234	83	428	17	268
+ 6 h@750 °C	243	90	428	10	261

$$\tau_{\text{mean}} = \tau_1 I_1 + \tau_2 / I_2 \text{ (Table 1).}$$

For materials with similar valence electron densities, such as  $\text{LiTaO}_3$ ,  $\text{BaTiO}_3$ ,  $\text{SrTiO}_3$ , or  $\text{PbTiO}_3$ , typical bulk lifetimes  $\tau_{\text{bulk}}$  range from 150 to 160 ps [47,48]. These values clearly show that the  $e^+$  lifetime component  $\tau_1 = 209$  ps in as-received  $\text{LiTaO}_3$  cannot be attributed to annihilation in the free state. In fact, a value for the bulk lifetime of  $\tau_{\text{bulk}} = (I_1/\tau_1 + I_2/\tau_2)^{-1} = 227$  ps would follow from a simple two-state trapping model [49]. Therefore, considering also the  $\tau_1$  values after ball-milling, the component  $\tau_1 = 209$  ps in the as-received state, most likely, reflects an effective value arising from  $e^+$  annihilation in both the free state and a vacancy-trapped state. The lifetime component  $\tau_2 = 324$  ps is, on the other hand, characteristic of free volumes of the size of several missing atoms, *i.e.*, vacancy agglomerates or nanovoids.

High-energy ball milling gives rise to a significant increase of the mean positron lifetime  $\tau_{\text{mean}}$  by 27 ps (30 min of milling) and by 33 ps for a milling period of 10 h (see Table 1). This increase clearly indicates that mechanical treatment leads to the formation of defects. The only minor increase upon prolonged milling compared to 30 min is in line with the change in ionic conductivity observed where ball milling for 30 min causes a marked increase whereas prolonged milling for 10 h increases the conductivity only slightly (see Fig. 1a).

The increase of  $\tau_{\text{mean}}$  upon milling primarily arises from the increase of the component  $\tau_1$ . The value of 230/234 ps (10 min/10 h) is attributed to  $e^+$ -annihilation in Ta-vacancies, taking into account similar lifetime values which have been reported for LiNbO<sub>3</sub> single crystals (230 to 250 ps) [50] and which have been considered to arise from Nb-vacancies [51]. This finding implies that after ball-milling all positrons are trapped at defects whereas in microcrystalline LiTaO<sub>3</sub> the lifetime  $\tau_1$  reflects partial annihilation in the free state (see above). The increase of  $\tau_2$  upon ball-milling shows that mechanical treatment leads to a growth of the size of the vacancy agglomerates or nanovoids.

Annealing the ball-milled samples gives rise to a decrease of the mean positron lifetime  $\tau_{\text{mean}}$  by 6 to 7 ps for the two milling times studied (Table 1). As the spectra analyses shows, the decrease in  $\tau_{\text{mean}}$  is caused by a decrease of the ratio  $I_2/I_1$  of the intensities of  $\tau_2$  and  $\tau_1$ . The ratio  $I_2/I_1$  corresponds to the ratio of the respective trapping rates, which is proportional to the concentration ratio of nanovoids (corresponding to  $\tau_2$ ) and vacancies (corresponding to  $\tau_1$ ). Since an increase of the vacancy concentration upon annealing appears rather unlikely, the decrease of  $I_2/I_1$  obviously reflects an annealing-induced decrease of the concentration of nanovoids.

To collect information on the microstructural changes introduced upon ball milling and how these changes are affected by annealing, we analysed the milled and annealed samples by EXAFS; the corresponding data are shown in Fig. 3a and b. In particular, EXAFS is suited to probe local structural disorder as it does not rely on long-range order [17,52,53]. For ball-milled LiTaO<sub>3</sub> it points to structurally amorphous regions that are produced during the milling process. In a recent study we have shown that milling for as little as 30 min already increases the amount of amorphous material to values of ca. 25%; increasing  $t_{\text{mill}}$  to 8 h yields samples with 55% of amorphous material [17]. Here, the mean radial distances Ta-Ta, Ta-O<sub>1</sub> (first O shell) and Ta-O<sub>2</sub> (second O shell) of the samples milled for 30 min and 10 h are shown in Fig. 3. Upon milling the distance Ta-O<sub>1</sub> increases. This change in Ta-O<sub>1</sub> distance is fully reversible as the initial value is reached after the samples

have been annealed at  $t_{\text{anneal}} = 500$  °C. In agreement with the crystal structure of LiTaO<sub>3</sub>, the Ta-O<sub>2</sub> distance is decreased for the ball milled samples. Interestingly, it decreases even further at prolonged milling times  $t_{\text{mill}}$ . Again, the initial values can be fully restored if the 30-min sample if annealed at or above 500 °C; the same behaviour is seen for the 10-h milled sample, initial values are re-obtained after annealing at 750 °C. The average Ta-Ta distance also decreases continuously with milling time  $t_{\text{mill}}$ . The original distance is recovered at or above 500 °C for the 30-min sample; a similar behaviour is seen for the nanocrystalline LiTaO<sub>3</sub> sample obtained after 10 h of milling. In the latter, however, the Ta-Ta distance remains smaller than that in the microcrystalline educt.

Our DC conductivity measurements probe an activation energy that is the sum of the migration activation energy  $E_{a,m}$  and the formation activation energy  $E_{a,f}$ , referring to the formation of a local defect. Assuming that in both the ball milled and annealed samples the defect concentration is far above its thermodynamic equilibrium value,  $E_a$  is mainly given by the change in  $E_{a,m}$ . Thus, in a lattice with heavy polyhedra distortions,  $E_{a,m}$  for Li<sup>+</sup> migration is obviously lower than in a perfectly ordered LiTaO<sub>3</sub> crystal.

Besides interatomic distances, the Debye-Waller factor contains further information of the extent of structural disorder introduced during milling. Debye-Waller factors are shown for all samples in Fig. 4. For the microcrystalline sample, being poor in defects and amorphous regions, a comparatively small disorder parameter is obtained. After mechanical treatment, however, the extent of structural disorder is significantly increased for all three radial distances, i.e., Ta-Ta, Ta-O<sub>1</sub> and Ta-O<sub>2</sub>; the dependency on milling time is depicted in Fig. 4.

Local changes in interatomic distances as seen by EXAFS can also be visualized by nuclear magnetic resonance (NMR) spectroscopy [11,15] being sensitive to local electric field gradients produced in the direct neighbourhood of the spin-3/2 nucleus <sup>7</sup>Li. Recently, we have shown that the quadrupole powder patterns of <sup>7</sup>Li NMR spectra from samples milled for only 30 min do not reveal sharp quadrupolar singularities any longer [11]. Distinct singularities are, however, seen in the <sup>7</sup>Li NMR powder pattern of microcrystalline LiTaO<sub>3</sub>. Instead, for the 30-min sample a broadened pattern is obtained resembling that of a sample milled for 10 h. As pointed out recently [11], the changes introduced during milling sensitively depend on the milling conditions and the type of mill chosen. Whereas planetary mills seem to produce amorphous material, shaker mills are able to effectively decrease the crystallite size while keeping the amount of amorphous material in a tolerable range. The two kinds of mills also lead to differences in morphologies of metallic alloys [54].

Our EXAFS analysis reveals further that annealing the nanocrystalline powders at and above 500 °C has the highest impact on local structures and interatomic distances. After the annealing step at 750 °C, for 1 h and 6 h, respectively, the properties of the microcrystalline material can almost be recovered. We assume that bulk regions can be restored best, while we suppose that grain-boundary regions still conserve structural disorder. Comparing our results from EXAFS with those from PALS we see that while annealing is able to restore interatomic distances and to remove bond distortions as well as to relieve strain, i.e., to reduce the amount of disordered or stressed regions with bond distortions, point defects seem to be almost conserved. Here, we anticipate that point defects in the crystalline interior of the nanocrystallites survive during heat treatment at 750 °C. Although it is still under debate what the prevailing kinds of defects in LiTaO<sub>3</sub> are [55–57], they control Li<sup>+</sup> ionic transport properties in the annealed samples.

On the other hand, amorphous material and structurally disordered interfacial regions, seem to be highly responsible for the increase in ionic conductivity directly seen after high-energy ball milling. Hence, both a large concentration of defects in the crystalline grains and the disordered interfacial regions contribute to the overall conductivity seen after high-energy ball milling. For ball-milled LiTaO<sub>3</sub> a separation of these two contributions can neither be seen in conductivity isotherms

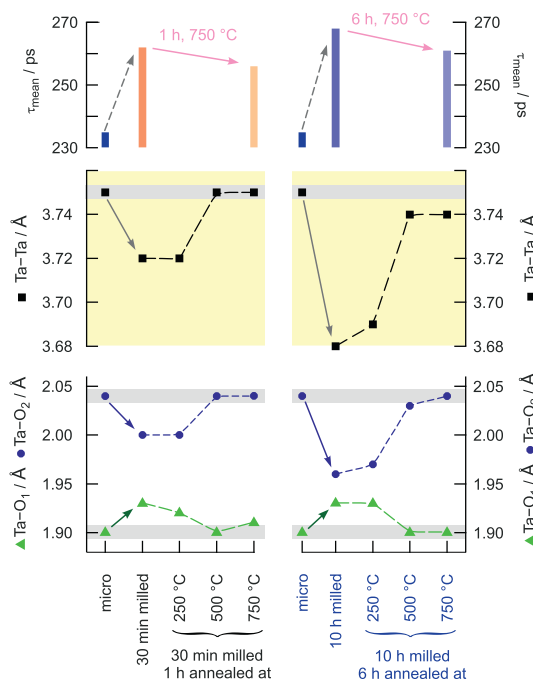


**Fig. 3.** Mean positron lifetimes in microcrystalline and nanocrystalline LiTaO<sub>3</sub> before and after annealing at 750 °C for 1 h and 6 h, respectively (see upper part). Mean radial distances between Ta-Ta, Ta-O<sub>1</sub> and Ta-O<sub>2</sub> in the milled and annealed samples as obtained from EXAFS analysis of the Ta L<sub>3</sub>-edge. The horizontal bars in grey color mark the respective values of the microcrystalline sample (see lower part).



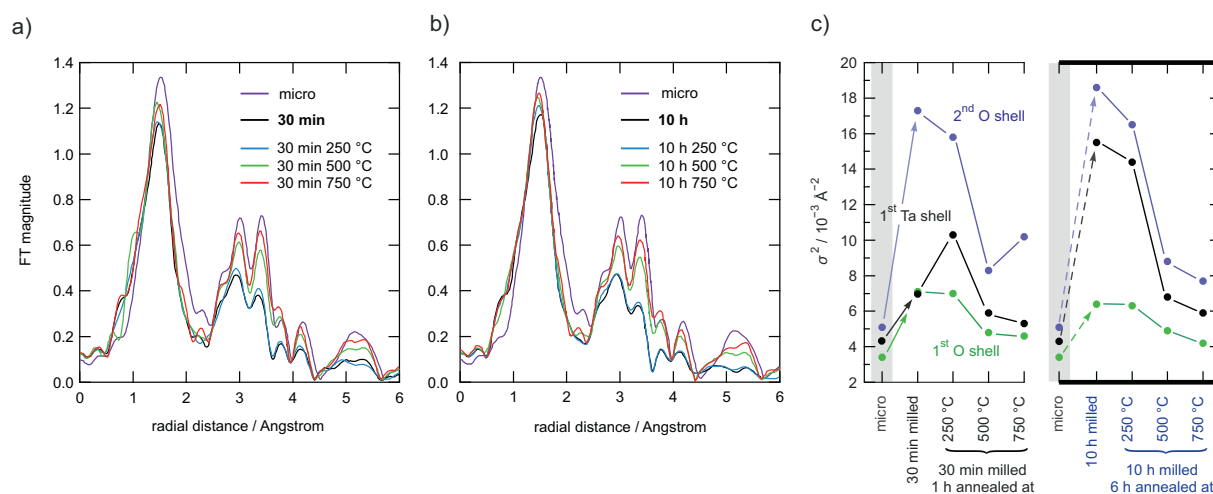


**Fig. 4.** Fourier transform of the Ta  $L_3$ -edge EXAFS of  $\text{LiTaO}_3$  milled for 30 min (a) and 10 h (b). c) The Ta  $L_3$ -edge EXAFS Debye-Waller factors for  $\text{LiTaO}_3$  as a function of milling and subsequent annealing. Structural disorder induced by ball milling gradually decreases by annealing but remains to some degree for samples annealed 750 °C.

nor in  $^7\text{Li}$  NMR measurements. Nanocrystalline  $\text{LiTaO}_3$ , in contrast to what has been observed for  $\text{LiNbO}_3$  [5], behaves, from a dynamic point of view, like a uniform phase [15]. We conclude that defects and stress introduced in the nanocrystalline grains greatly help the ions to diffuse through the material; these pathways seem to be very similar to those in the outer interfacial regions, for which an amorphous-like structure is expected.

#### 4. Conclusion

Nanocrystalline  $\text{LiTaO}_3$ , which was prepared by high-energy ball milling, served as a suitable model substance to study the extent of structural disorder on ionic transport. Milling times of only 30 min are sufficient to reach a critical level of disorder generating a network of fast migration pathways. The resulting highly defective oxide has to be characterized by a reduced activation energy of 0.75 eV for ionic transport as compared to the starting material (0.97 eV). Increasing the milling time from 30 min to 10 h does not significantly enhance ionic transport. EXAFS supports this result and points to a pronounced change of interatomic distances and a large increase in the overall distortion of bond lengths. These structural changes are accompanied by the introduction of vacancy type defects that are clearly detected by PALS revealing increased lifetimes of positrons. While the two samples are similar in ionic transport properties they differ, however, in their ability to withstand high temperatures which causes healing of defects. It turned out that soft annealing at only 200 °C retains the structural disorder and that the defects are almost preserved. Thus these samples are nanocrystalline ionic conductors whose ionic conductivities are stable at elevated temperatures.

While EXAFS showed that the original interatomic distances can be recovered upon annealing, PALS revealed that point defects, such as  $\text{Li}^+$  and  $\text{Ta}^{5+}$  vacancies that are introduced during 10 h of milling, survive the annealing process. Hence, the final samples obtained after annealing at 750 °C for 6 h have to be characterized by only small amounts of structurally disordered (amorphous) regions, however, they are still rich in vacancy-type defects that need higher temperatures to be removed. Altogether, annealing steps at different temperatures help to fine-tune the ionic conductivity in nanocrystalline  $\text{LiTaO}_3$ . In ideal cases the combination of milling and annealing allows us to adjust transport properties over a dynamic range of 4 to 5 orders of magnitude.

#### Notes

The authors declare no competing financial interest.

#### Author statement

B. Gadermaier: Conceptualization, Investigation, Formal analysis, Visualization, Writing – original Draft, Methodology. L. Resch: Investigation, Formal analysis, Writing – Review & Editing. D. M. Pickup: Investigation, Formal analysis. I. Hanghofer: Investigation, Formal analysis. I. Hanzu: Writing – Review & Editing. P. Heitjans: Conceptualization, Writing – Review & Editing. W. Sprengel: Supervision, Formal analysis, Writing – Review & Editing. R. Würschum: Supervision, Writing – review & editing. A. V. Chadwick: Formal analysis, Writing – Review & Editing. H. M. R. Wilkening: Conceptualization, Supervision, Writing - review& editing, Funding acquisition.

#### Declaration of competing interest

The authors declare that they have no known competing financial interests or personal relationships that could have appeared to influence the work reported in this paper.

#### Acknowledgement

Financial support by the Deutsche Forschungsgemeinschaft (DFG) in the frame of the Research Unit 1277, grant no. WI3600/2-1(4-1) (FOR1277)) as well as by the Austrian Federal Ministry of Science, Research and Economy, and the Austrian National Foundation for Research, Technology and Development (Christian Doppler Laboratory of Lithium Batteries: Ageing Effects, Technology and New Materials) is greatly appreciated. Furthermore, we thank the Österreichische Forschungs-Förderungsgesellschaft (FFG) in the frame of the K project safe battery.

#### Appendix A. Supplementary data

Rietveld refinement for X-ray powder diffraction patterns of ball-milled and annealed  $\text{LiTaO}_3$ . Supplementary data to this article can be found online at <https://doi.org/10.1016/j.ssi.2020.115355>.

## References

- [1] P. Heitjans, S. Indris, Diffusion and ionic conduction in nanocrystalline ceramics, *J. Phys.: Condes. Matter* 15 (2003) R1257–R1289.
- [2] M. Wilkening, D. Bork, S. Indris, P. Heitjans, Diffusion in amorphous  $\text{LiNbO}_3$  studied by  $^7\text{Li}$  NMR: comparison with the nano- and microcrystalline material, *Phys. Chem. Chem. Phys.* 4 (2002) 3246–3251.
- [3] V. Šepelák, A. Feldhoff, P. Heitjans, F. Krumeich, D. Menzel, F.J. Litterst, I. Bergmann, K.D. Becker, Nonequilibrium cation distribution, canted spin arrangement, and enhanced magnetization in nanosized  $\text{MgFe}_2\text{O}_4$  prepared by a one-step mechanochemical route, *Chem. Mater.* 18 (2006) 3057–3067.
- [4] A. Chadwick, S. Savin, Structure and dynamics in nanoionic materials, *Solid State Ionics* 177 (2006) 3001–3008.
- [5] P. Heitjans, M. Masoud, A. Feldhoff, M. Wilkening, NMR and impedance studies of nanocrystalline and amorphous ion conductors: lithium niobate as a model system, *Faraday Discuss.* 134 (2007) 67–82.
- [6] P. Heitjans, S. Indris, Diffusion and ionic conduction in nanocrystalline ceramics, *MRS Proc.* 676 (2011) Y6.6.
- [7] A. Düvel, A. Kuhn, L. Robben, M. Wilkening, P. Heitjans, Mechanochemical synthesis of solid electrolytes: preparation, characterization, and Li ion transport properties of garnet-type Al-doped  $\text{Li}_7\text{La}_3\text{Zr}_2\text{O}_{12}$  crystallizing with cubic symmetry, *J. Phys. Chem. C* 116 (2012) 15192–15202.
- [8] V. Šepelák, A. Düvel, M. Wilkening, K.-D. Becker, P. Heitjans, Mechanochemical reactions and syntheses of oxides, *Chem. Soc. Rev.* 42 (2013) 7507–7520.
- [9] F. Preishuber-Pflügl, M. Wilkening, Mechanochemically synthesized fluorides: local structures and ion transport, *Dalton Trans.* 45 (2016) 8675–8687.
- [10] M. Wilkening, A. Düvel, F. Preishuber-Pflügl, K. da Silva, S. Breuer, V. Šepelák, P. Heitjans, Structure and ion dynamics of mechanochemically synthesized oxides and fluorides, *Z. Krist. - Cryst. Mater.* 232 (2017) 107–127.
- [11] D. Prutsch, S. Breuer, M. Uitz, P. Bottke, J. Langer, S. Lunghammer, M. Philipp, P. Posch, V. Pregartner, B. Stanje, A. Dunst, D. Wohlmuth, H. Brandstätter, W. Schmidt, V. Epp, A. Chadwick, I. Hanzu, M. Wilkening, Nanostructured ceramics: ionic transport and electrochemical activity a short journey across various families of materials, *Z. Phys. Chem.* 231 (2017) 1361–1405.
- [12] S.L.P. Savin, A.V. Chadwick, L.A. O'Dell, M.E. Smith, Structural studies of nanocrystalline oxides, *Solid State Ionics* 177 (2006) 2519–2526.
- [13] M. Heise, G. Scholz, E. Kemnitz, Mechanochemical synthesis of  $\text{PbF}_2$  by high-energy ball milling, *Solid State Sci.* 72 (2017) 41–46.
- [14] G. Scholz, I. Dörfel, D. Heidemann, M. Feist, R. Stösser, Nanocrystalline  $\text{CaF}_2$  particles obtained by high-energy ball milling, *J. Solid State Chem.* 179 (2006) 1119–1128.
- [15] M. Wilkening, V. Epp, A. Feldhoff, P. Heitjans, Tuning the Li diffusivity of poor ionic conductors by mechanical treatment: high Li conductivity of strongly defective  $\text{LiTaO}_3$  nanoparticles, *J. Phys. Chem. C* 112 (2008) 9291–9300.
- [16] P. Heitjans, E. Tobschall, M. Wilkening, Ion transport and diffusion in nanocrystalline and glassy ceramics, *Eur. Phys. J. - Spec. Top.* 161 (2008) 97–108.
- [17] A.V. Chadwick, D.M. Pickup, S. Ramos, G. Gibin, N. Tapia-Ruiz, S. Breuer, D. Wohlmuth, M. Wilkening, An X-ray absorption spectroscopy study of ball-milled lithium tantalate and lithium titanate nanocrystals, *Inst. Phys.: IOP Conf. Series: Mat. Sci. Engin.* 169 (2017) 12015.
- [18] J. Maier, Ionic conduction in space charge regions, *Prog Solid State Ch* 23 (1995) 171–263.
- [19] J. Maier, Nanoionics: ionic charge carriers in small systems, *Phys. Chem. Chem. Phys.* 11 (2009) 3011–3022.
- [20] J. Maier, Nano-ionics: trivial and non-trivial size effects on ion conduction in solids, *Z. Phys. Chem.* 217 (2003) 415–436.
- [21] A.V. Chadwick, S.L.P. Savin, EXAFS study of nanocrystalline  $\text{CeO}_2$  samples prepared by sol-gel and ball-milling routes, *J. Alloys Comp.* 488 (2009) 1–4.
- [22] G.E. Rush, A.V. Chadwick, I. Kosacki, H.U. Anderson, An EXAFS study of nanocrystalline yttrium stabilized cubic zirconia films and pure zirconia powders, *J. Phys. Chem. B* 104 (2000) 9597–9606.
- [23] P.D. Battle, C.R.A. Catlow, A.V. Chadwick, G.N. Greaves, L.M. Moroney, EXAFS studies of fluoride oxides, *J. de Phys.* 47 (1986) 669–673.
- [24] C.R.A. Catlow, A.V. Chadwick, G.N. Greaves, L.M. Moroney, EXAFS studies of disorder in crystalline ionic solids, *Cryst. Latt. Def. and Amorph. Mat.* 12 (1985) 193–211.
- [25] M. Eldrup, B.N. Singh, Studies of defects and defect agglomerates by positron annihilation spectroscopy, *J. Nucl. Mater.* 251 (1997) 132–138.
- [26] M. Eldrup, Positron methods for the study of defects in bulk materials, *J. de Phys.* 5 (4) (1995) 93–109.
- [27] Y.C. Wu, F. Ye, V. Barbe, W. Sprengel, K. Reimann, K.J. Reichle, D. Goll, R. Würschum, H.E. Schaefer, Characterization of free volumes in amorphous and nanostructured  $\text{Pr}_2\text{Fe}_{14}\text{B}$  using positron lifetime spectroscopy, *Phys. Status Sol. A* 198 (2003) 204–209.
- [28] Y. Zhao, K. Zheng, X.L. Sun, Addressing interfacial issues in liquid-based and solid-state batteries by atomic and molecular layer deposition, *Joule* 2 (2018) 2583–2604.
- [29] C.P. Yang, K. Fu, Y. Zhang, E. Hitz, L.B. Hu, Protected lithium-metal anodes in batteries: from liquid to solid, *Adv. Mater.* 29 (2017) 1701169.
- [30] B. Ruprecht, M. Wilkening, A. Feldhoff, S. Steuernagel, P. Heitjans, High anion conductivity in a ternary non-equilibrium phase of  $\text{BaF}_2$  and  $\text{CaF}_2$  with mixed cations, *Phys. Chem. Chem. Phys.* 11 (2009) 3071–3081.
- [31] B. Ruprecht, M. Wilkening, S. Steuernagel, P. Heitjans, Anion diffusivity in highly conductive nanocrystalline  $\text{BaF}_2\text{:CaF}_2$  composites prepared by high-energy ball milling, *J. Mater. Chem.* 18 (2008) 5412–5416.
- [32] J.V. Olsen, P. Kirkegaard, N.J. Pedersen, M. Eldrup, PALSfit: a new program for the evaluation of positron lifetime spectra, *Phys. Status Sol. C* 4 (2007) 4004–4006.
- [33] B. Ravel, M. Newville, ATHENA, ARTEMIS, HEPHAESTUS: data analysis for X-ray absorption spectroscopy using IFEFFIT, *J. Synchrotron Radiat.* 12 (2005) 537–541.
- [34] A.M. Glass, M.E. Lines, K. Nassau, J.W. Shiever, Anomalous dielectric behavior and reversible Pyroelectricity in roller-quenched  $\text{LiNbO}_3$  and  $\text{LiTaO}_3$  Glass, *Appl. Phys. Lett.* 31 (1977) 249–251.
- [35] M. Masoud, P. Heitjans, Impedance spectroscopy study of Li ion dynamics in single crystal, microcrystalline, nanocrystalline, and amorphous  $\text{LiNbO}_3$ , *Diff. Mater. (DIMAT)* 237–240 (2005) 1016–1021.
- [36] K. Funke, R.D. Banhatti, L.G. Badr, D.M. Laughman, H. Jain, Toward understanding the second universality - a journey inspired by Arthur Stanley Nowick, *J. Electroceram.* 34 (2015) 4–14.
- [37] F. Preishuber-Pflügl, P. Bottke, V. Pregartner, B. Bitschnau, M. Wilkening, Correlated fluoride diffusion and ionic conduction in the nanocrystalline  $\text{F}^-$  solid electrolyte  $\text{Ba}_{0.6}\text{La}_{0.4}\text{F}_{2.4} - ^{19}\text{F}$   $T_{1\rho}$  NMR relaxation vs. conductivity measurements, *Phys. Chem. Chem. Phys.* 16 (2014) 9580–9590.
- [38] K. Funke, Jump relaxation in solid electrolytes, *Prog. Solid State Chem.* 22 (1993) 111–195.
- [39] A. Düvel, B. Ruprecht, P. Heitjans, M. Wilkening, Mixed alkaline-earth effect in the metastable anion conductor  $\text{Ba}_{1-x}\text{Ca}_x\text{F}_2$  ( $0 \leq x \leq 1$ ): correlating long-range ion transport with local structures revealed by ultrafast  $^{19}\text{F}$  MAS NMR, *J. Phys. Chem. C* 115 (2011) 23784–23789.
- [40] J.C. Dyre, P. Maass, B. Roling, D.L. Sidebottom, Fundamental questions relating to ion conduction in disordered solids, *Rep. Prog. Phys.* 72 (2009) 046501.
- [41] R. Metselaar, G. Oversluizen, The Meyer-Neldel rule in semiconductors, *J. Solid State Chem.* 55 (1984) 320–326.
- [42] S. Breuer, M. Wilkening, Mismatch in cation size causes rapid anion dynamics in solid electrolytes: the role of the Arrhenius pre-factor, *Dalton Trans.* 47 (2018) 4105–4117.
- [43] P. Fielitz, O. Schneider, G. Borchardt, A. Weidenfelder, H. Fritze, J. Shi, K.D. Becker, S. Ganschow, R. Bertram, Oxygen-18 tracer diffusion in nearly stoichiometric single crystalline lithium niobate, *Solid State Ionics* 189 (2011) 1–6.
- [44] D.P. Almond, G.K. Duncan, A.R. West, Analysis of conductivity prefactors and ion hopping rates in  $\text{AgI-Ag}_2\text{MoO}_4$  glass, *J. Non-Cryst. Solids* 74 (1985) 285–301.
- [45] D.P. Almond, A.R. West, Entropy effects in ionic conductivity, *Solid State Ionics* 18–19 (1986) 1105–1109.
- [46] N.B. Desai, K. Byrappa, G.S. Gopalakrishna, S. Srikantaswamy, A.B. Kulkarni, Conductivity pre-exponential factors for some new superionic conductors, *Bull. Mater. Sci.* 9 (1987) 317–321.
- [47] V.J. Ghosh, B. Nielsen, T. Friessnegg, Identifying open-volume defects in doped and undoped perovskite-type  $\text{LaCoO}_3$ ,  $\text{PbTiO}_3$  and  $\text{BaTiO}_3$ , *Phys. Rev. B* 61 (2000) 207–212.
- [48] D.J. Keeble, S. Wicklein, R. Dittmann, L. Ravelli, R.A. Mackie, W. Egger, Identification of A- and B-site cation vacancy defects in perovskite oxide thin films, *Phys. Rev. Lett.* 105 (2010) 226102.
- [49] R. Krause-Rehberg, H.S. Leipner, Positron Annihilation in Semiconductors: Defect Studies, Springer, Berlin, 1999.
- [50] R. Pareja, R. González, M.A. Pedrosa, Study of thermochemically reduced and electron-irradiated  $\text{LiNbO}_3$  single crystals by positron annihilation and optical absorption measurements, *Phys. Status Sol. A* 84 (1984) 179–183.
- [51] A. García-Cabaes, J.A. Sanz-García, J.M. Cabrera, F. Agulló-López, C. Zaldo, R. Pareja, K. Polgár, K. Raksányi, I. Fölvár, Influence of stoichiometry on defect-related phenomena in  $\text{LiNbO}_3$ , *Phys. Rev. B* 37 (1988) 6085–6091.
- [52] A.V. Chadwick, EXAFS studies of dopant sites in metal oxides, *Solid State Ionics* 63–65 (1993) 721–727.
- [53] G. Cheng, J.D. Carter, T. Guo, Investigation of co nanoparticles with EXAFS and XANES, *Chem. Phys. Lett.* 400 (2004) 122–127.
- [54] A. Zolriasatein, A. Shokuhfar, F. Safari, N. Abdi, Comparative study of SPEX and planetary milling methods for the fabrication of complex metallic alloy nanoparticles, *Micro Nano Lett.* 13 (2017) 448–451.
- [55] W. He, X. Gao, L. Pang, D. Wang, N. Gao, Z. Wang, First-principles investigation of vacancies in  $\text{LiTaO}_3$ , *J. Phys.: Condes. Matter* 28 (2016) 315501.
- [56] X. Kang, L. Liang, W. Song, F. Wang, Y. Sang, H. Liu, Formation mechanism and elimination methods for anti-site defects in  $\text{LiNbO}_3/\text{LiTaO}_3$  crystals, *Cryst. Eng. Commun.* 18 (2016) 8136–8146.
- [57] A. Vyalikh, M. Zschornak, T. Köhler, M. Nentwich, T. Weigel, J. Hanzig, R. Zaripov, E. Vavilova, S. Gemming, E. Brendler, D.C. Meyer, Analysis of the defect clusters in congruent lithium tantalate, *Phys. Rev. Mater.* 2 (2018) 013804.



### 3.3. The Electronic Conductivity of Single Crystalline Ga-Stabilized Cubic $\text{Li}_7\text{La}_3\text{Zr}_2\text{O}_{12}$ — A Technologically Relevant Parameter for All-Solid-State Batteries

In an electrochemical cell, it is of utmost importance to have separate paths for electrons and ionic charge carriers. Only if the electronic path, *i.e.*, the electronic resistance, is adjustable, the battery can work at its full potential. Considering the fact that a charged battery is always thermodynamically unstable, otherwise, it could not supply power, it is obvious that at least one of the charge transport mechanisms must be controllable at will, *i.e.*, externally. Due to its assembly and the fact that electrons drive any electronic device, from motors to microprocessors, it is obvious that the electronic path is used to control the electrochemical reaction rate in a battery. Now, every battery has two electrodes which are electronically insulated but contacted by an electrolyte that permits charges to pass only in the form of ions. However, even the best (electronic) insulator poses a finite resistance. Self-explanatory, the electrolyte needs to be an electronic insulator in order to have a system that is kinetically stable by controlling the flow of electrons. Ideally, the specific ionic conductivity of an electrolyte is well above  $1 \text{ mS cm}^{-1}$  and its electronic conductivity as low as possible, *i.e.*, below  $1 \text{ nS cm}^{-1}$ . Liquid electrolytes show truly insignificant specific electronic conductivities in the order  $10^{-12}$  to  $10^{-9} \text{ S cm}^{-1}$ . Solid electrolytes on the other hand, have not been as thoroughly investigated in terms of specific electronic conductivity as liquid electrolytes have been. In the last decades, research devoted to solid electrolytes has primarily been concerned with finding solid electrolytes with high, liquid-like, ionic conductivity and large electrochemical stability windows. Furthermore, considering the inhomogeneity often present in solid electrolytes, *i.e.*, grain boundaries, impurities, and their rigid nature, the investigation of the electronic conductivity is fraught with difficulty.

Apart from the chemical and mechanical nature of solid electrolytes, also the techniques to study their respective electronic conductivity are far from being unequivocally accepted. Not every method might be applicable to a specific solid electrolyte due to e.g. electrochemical instabilities and decomposition at interfaces<sup>91,92</sup>. The method of Tubandt<sup>93</sup> and the well-known Hebb-Wagner polarisation method<sup>94-96</sup>, both require intimate contact as well as the absence of any electrochemical reaction at the electrolyte-electrode interface, a requirement fulfilled by only very few solid electrolytes if metallic lithium is used. However, if only very small potentials are used for the DC

polarisation of solid electrolytes with ion-blocking electrodes, the steady-state current is of pure electronic origin and the specific electronic conductivity can be determined. Furthermore, applying very small potentials in combination with inert electrodes (Au) suppresses the formation of thin interlayer, *i.e.* interphases, which would be in series with the electronic resistance of the solid electrolyte and would thus lead to an underestimating the specific electronic conductivity. Similarly, any phase impurity in the sample may change the electronic conductivity. A single crystal undoubtedly represents a specimen with outstanding phase-purity. Furthermore, there are no discontinuities within a single crystal, *i.e.*, grain boundaries, foreign phases and the concentration of defects and disorder is far below that of a polycrystalline sample. Therefore, the specific electronic conductivity measured at such a sample, taking that the sample is directly in contact with the electrodes, *i.e.*, no interlayer is present, represents a materials specific property. Such investigations on a single Ga-stabilized LLZO single crystal are reported in the following publication.

## **P3**

Philipp, M.; Gadermaier, B.; Posch, P.; Hanzu, I.; Ganschow, S.; Meven, M.; Rettenwander, D.;  
Redhammer, G. J.; Wilkening, H. M. R.

### **The Electronic Conductivity of Single Crystalline Ga-Stabilized Cubic $\text{Li}_7\text{La}_3\text{Zr}_2\text{O}_{12}$ : A Technologically Relevant Parameter for All- Solid-State Batteries**

Advanced Materials Interfaces 2020, 7, 2000450.

# The Electronic Conductivity of Single Crystalline Ga-Stabilized Cubic $\text{Li}_7\text{La}_3\text{Zr}_2\text{O}_{12}$ : A Technologically Relevant Parameter for All-Solid-State Batteries

Martin Philipp, Bernhard Gadermaier, Patrick Posch, Ilie Hanzu, Steffen Ganschow, Martin Meven, Daniel Rettenwander, Günther J. Redhammer, and H. Martin R. Wilkening\*

The next-generation of all-solid-state lithium batteries need ceramic electrolytes with very high ionic conductivities. At the same time a negligible electronic conductivity  $\sigma_{\text{eon}}$  is required to eliminate self-discharge in such systems. A non-negligible electronic conductivity may also promote the unintentional formation of Li dendrites, being currently one of the key issues hindering the development of long-lasting all-solid-state batteries. This interplay is suggested recently for garnet-type  $\text{Li}_7\text{La}_3\text{Zr}_2\text{O}_{12}$  (LLZO). It is, however, well known that the overall macroscopic electronic conductivity may be governed by a range of extrinsic factors such as impurities, chemical inhomogeneities, grain boundaries, morphology, and size effects. Here, advantage of Czochralski-grown single crystals, which offer the unique opportunity to evaluate intrinsic properties of a chemically homogeneous matrix, is taken to measure the electronic conductivity  $\sigma_{\text{eon}}$ . Via long-time, high-precision potentiostatic polarization experiments an upper limit of  $\sigma_{\text{eon}}$  in the order of  $5 \times 10^{-10} \text{ S cm}^{-1}$  (293 K) is estimated. This value is by six orders of magnitude lower than the corresponding total conductivity  $\sigma_{\text{total}} = 10^{-3} \text{ S cm}^{-1}$  of Ga-LLZO. Thus, it is concluded that the high values of  $\sigma_{\text{eon}}$  recently reported for similar systems do not necessarily mirror intragrain bulk properties of chemically homogeneous systems but may originate from chemically inhomogeneous interfacial areas.

but intermittent energy sources such as solar, wind or tidal.<sup>[1]</sup> Lithium-ion batteries with insertion hosts<sup>[2]</sup> are currently the most powerful electrochemical storage systems used in portable electronics and in the transportation sector.<sup>[2c,3]</sup> To increase both their energy and power density, the use of Li metal as anode material is re-envisaged since a couple of years.<sup>[4]</sup> The replacement of flammable liquid electrolytes used in conventional systems by ceramic ones is expected to enable the safe use of Li metal and to widen the thermal stability window of such systems. For practical reasons, the ionic conductivity  $\sigma_{\text{ion}}$  of suitable ceramic electrolytes, acting as electronic insulators, should, however, be in the order of  $1 \text{ mS cm}^{-1}$  or higher to ensure proper battery operation at ambient and lower temperatures. The garnet-type solid electrolyte  $\text{Li}_7\text{La}_3\text{Zr}_2\text{O}_{12}$  (LLZO)<sup>[5]</sup> crystallizing with cubic symmetry definitely represent one of the frontrunners in the group of the most promising oxidic solid electrolytes.<sup>[6]</sup> With their outstanding ionic conductivity,<sup>[7]</sup> and their wide electrochemical stability window, they are envisaged to play an important role in both the development of volume-type<sup>[8]</sup> and thin-film batteries.<sup>[9]</sup> Of course, sulfide-based electrolytes or thiophosphates show even


## 1. Introduction

Cutting our dependency on fossil fuels requires powerful systems that can efficiently store electricity from so-called renewable

ionic conductivity,<sup>[7]</sup> and their wide electrochemical stability window, they are envisaged to play an important role in both the development of volume-type<sup>[8]</sup> and thin-film batteries.<sup>[9]</sup> Of course, sulfide-based electrolytes or thiophosphates show even

M. Philipp, B. Gadermaier, Dr. P. Posch, Dr. I. Hanzu, Dr. D. Rettenwander, Prof. H. M. R. Wilkening  
 Institute for Chemistry and Technology of Materials, Christian Doppler Laboratory for Lithium Batteries  
 Graz University of Technology (NAWI Graz)  
 Stremayrgasse 9, Graz 8010, Austria  
 E-mail: wilkening@tugraz.at

Dr. I. Hanzu, Prof. H. M. R. Wilkening  
 Alistore-ERI European Research Institute  
 CNRS FR3104  
 Hub de l'Energie, Rue Baudelocque, Amiens 80039, France

 The ORCID identification number(s) for the author(s) of this article can be found under <https://doi.org/10.1002/admi.202000450>.

© 2020 The Authors. Published by WILEY-VCH Verlag GmbH & Co. KGaA, Weinheim. This is an open access article under the terms of the Creative Commons Attribution License, which permits use, distribution and reproduction in any medium, provided the original work is properly cited.

DOI: 10.1002/admi.202000450

Dr. S. Ganschow  
 Leibniz-Institut für Kristallzüchtung  
 Max-Born-Str. 2, Berlin 12489, Germany

Dr. M. Meven  
 Institute of Crystallography  
 RWTH Aachen University  
 Aachen 52056, Germany

Dr. M. Meven  
 Jülich Centre for Neutron Science (JCNS)  
 Forschungszentrum Jülich GmbH at Heinz  
 Maier-Leibnitz Zentrum (MLZ)  
 Garching 85748, Germany

Prof. G. J. Redhammer  
 Department of Chemistry and Physics of Materials  
 Jakob-Haringer-Strasse 2a  
 University of Salzburg  
 Salzburg 5020, Austria

higher conductivity values<sup>[10]</sup> but suffer from their air-sensitivity and electrochemical instability.<sup>[11]</sup>

To circumvent unwanted self-discharge and the occurrence of internal short circuits evoked by Li dendrites,<sup>[12]</sup> which is, in general, one of the main safety risks of batteries,<sup>[13]</sup> the ceramic electrolyte has to exhibit negligible electronic conductivity  $\sigma_{\text{eon}}$ . The suppression of Li dendrite formation by suitable interface engineering thus belongs to the key tasks in battery research.<sup>[13]</sup> Very recently, Han et al. suggested that a very low but non-negligible value of  $\sigma_{\text{eon}}$  ( $10^{-8}$  S cm<sup>-1</sup>) can provoke the formation of Li dendrites in LLZO-type garnets.<sup>[14]</sup>

Han et al., however, used polycrystalline samples and the same holds for the other very few studies, which appeared in literature so far. In all cases polycrystalline samples were studied that had been stabilized in their cubic modification by supervalent doping. Depending on the exact stoichiometry, including the defect chemistry in the bulk and in surface regions, as well as the measurement conditions  $\sigma_{\text{eon}}$  values presented in literature differ, however, by more than four orders of magnitude.<sup>[14,15]</sup> This finding shows that the influence of (local) chemical inhomogeneities, surface morphologies and particularly that of the grain boundaries regions<sup>[12]</sup> on  $\sigma_{\text{eon}}$  is still not clear. One might expect that these regions in LLZO show slightly different compositions and defect structures as compared to the situation in the grains. Thus, surface areas and grain boundary (g. b.) regions, inevitably forming a percolating network in any pelletized sample, could show a higher electronic conductivity than that present in the crystalline grains, as also suggested by Tian et al.<sup>[16]</sup> In other words, these regions, as also seen in other ceramics,<sup>[17]</sup> might act as fast pathways for electrons or polarons causing the relatively high electronic conductivities seen in some of the samples studied so far.<sup>[12]</sup> Such extrinsic, interfacial effects will, however, mask intragrain properties.

Here, we took advantage of chemically homogeneous Czochralski-grown LLZO-type crystals of the nominal composition  $\text{Li}_{6.4}\text{Ga}_{0.2}\text{La}_3\text{Zr}_2\text{O}_{12}$  to study both bulk electronic conductivities  $\sigma_{\text{eon}}$  and total conductivities  $\sigma_{\text{total}}$ . The acentric crystal structure of Ga-LLZO is shown in **Figure 1**. While the general structure of the cubic garnet is depicted in **Figure 1a**,

highlighting the densely packed structure, the complex distribution of Li ions among three different crystallographic sites is presented in **Figure 1b**. Jumping between these sites enables the Li ions to move easily over long distances. The structure has in detail been described by Wagner et al.,<sup>[18]</sup> see also the Supporting Information for further structural details.

Having single crystals at hand, we used high-precision potentiostatic polarization measurements to reveal the upper limit of  $\sigma_{\text{eon}}$  that refers to the intragrain regions in cubic Ga-stabilized LLZO. As yet, only few studies<sup>[14,15]</sup> focused, however, on the estimation or measurement of the electronic conductivity that contributes to the total conductivity in LLZO. In general, a clear separation of ionic and electronic contributions is by far not trivial<sup>[19]</sup> and has been documented for few other materials.<sup>[20]</sup>

## 2. Results and Discussion

LLZO, if present in its tetragonal modification (space group  $I4_1/acd$ ), exhibits a low ionic conductivity of  $\approx 10^{-6}$  S cm<sup>-1</sup> at room temperature.<sup>[21]</sup> Upon heating, the crystal structure changes to a cubic modification ( $Ia\bar{3}d$ ) and the ionic conductivity increases by almost three orders of magnitude.<sup>[22]</sup> Using supervalent dopants such as Ga, Ta or Al, cubic, or in the case of Ga, acentric modifications, crystallizing with the space group  $I\bar{4}3d$ , can be stabilized at much lower temperatures. These samples yield, in the ideal case, room-temperature (total) conductivities reaching values of 1 mS cm<sup>-1</sup> or conductivities (slightly) above this value;<sup>[23]</sup> as an example Qin et al. reached 2 mS cm<sup>-1</sup> if Ga-LLZO is present in a self-textured form.<sup>[24]</sup> Here, we studied Czochralski-grown Ga-stabilized LLZO single crystals with total room-temperature conductivities in this order of magnitude, 1 mS cm<sup>-1</sup> (293 K).

In **Figure 2a** the real part of the complex conductivity  $\sigma'$ , measured at 293 K, is plotted as a function of the period, which is the inverse of the frequency  $\nu$ . The corresponding conductivity isotherms are shown in **Figure 3a**. They are composed of three regimes I to III, as also indicated in **Figure 3b**. At low frequencies a frequency-dependent polarization regime I is seen that passes into the so-called frequency independent direct current (DC) conductivity plateau (regime II). A stepwise decay of  $\sigma'$  in regime I is, most likely, due to the formation of space charge zones in front of the ion-blocking electrode<sup>[25]</sup> that also slow down ion transport farther away from the electrode. Due to the high total conductivity  $\sigma_{\text{DC}} (\equiv \sigma_{\text{total}})$ , the dispersive regime III, characterized by an increase of  $\sigma'$  at high frequencies according to Jonscher's power law, is only seen at the lowest temperatures (see **Figure 3a**). The isotherm recorded at 293 K reveals that  $\sigma_{\text{DC}}$ , being the total conductivity, turned out to be 1 mS cm<sup>-1</sup>. At this temperature,  $\sigma'$  steadily decreases if we go to frequencies lower than  $10^4$  Hz. This strong polarization effect already indicates that  $\sigma_{\text{eon}}$  is at least lower than  $10^{-7}$  S cm<sup>-1</sup>. Note that the electrodes applied are nonblocking for e<sup>-</sup>; thus,  $\sigma_{\text{eon}}$  is expected to show a plateau at sufficiently low  $\nu$ , i.e., at values being considerably lower than  $10^{-2}$  Hz.

The electronic conductivity of the Ga-LLZO single crystal was probed by using potentiostatic polarization measurements using symmetric Au|Ga-LLZO|Au cells; polarization curves were recorded at various temperatures and potentials. Thereby,

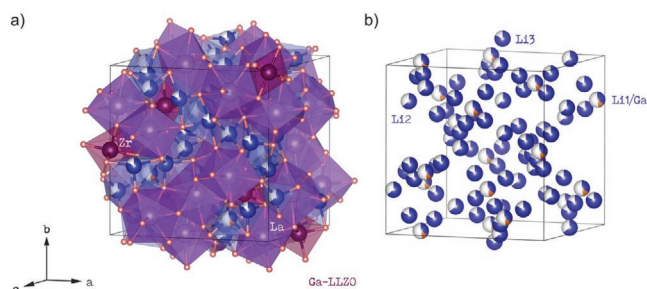


**Figure 1.** a,b) Crystal structure of Ga-containing  $\text{Li}_{6.4}\text{Ga}_{0.2}\text{La}_3\text{Zr}_2\text{O}_{12}$  (space group  $I\bar{4}3d$  (No. 220)) as determined by a combined, simultaneous refinement of both data from X-ray diffraction and neutron diffraction, see Tables S1 and S2 of the Supporting Information for further details. The Li ions are distributed over three different crystallographic sites (12a (Li1), 12b (Li2), 48e (Li3)) in the acentric space group.  $\text{Ga}^{3+}$  ions share sites with  $\text{Li}^+$  located at the Li1 site, being the Wyckoff position 12a. The  $\text{Li}^+$  ions form a 3D network enabling them to quickly diffuse through the crystal structure.



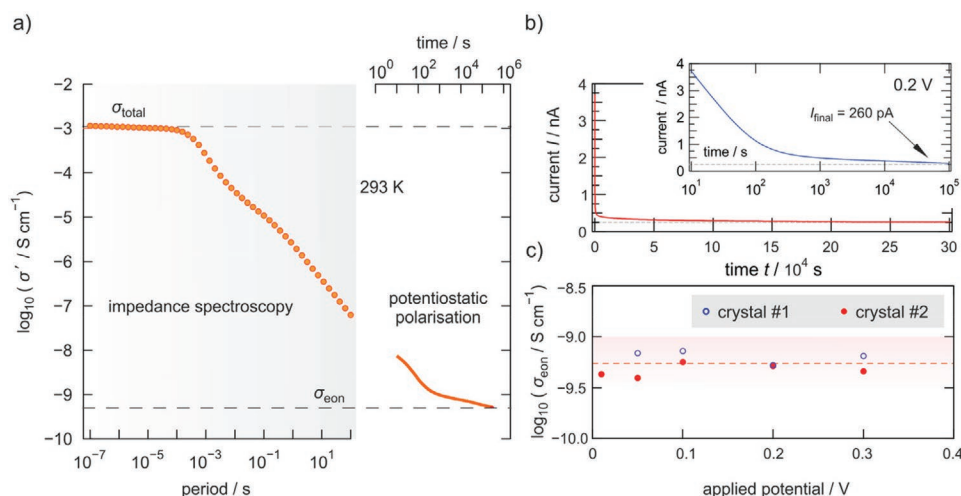


**Figure 2.** a) Conductivity isotherm of a Ga-stabilized LLZO single crystal as obtained by broadband impedance spectroscopy using ion-blocking Au electrodes.  $\sigma'$  is shown as a function of the period, being the inverse frequency. On the right hand side of the result of our potentiostatic (0.2 V) polarization measurement is shown. It already indicates that  $\sigma'$  will reach a plateau pointing to an electronic conductivity lower than  $10^{-9} \text{ S cm}^{-1}$ . b) Evolution of the current  $I$  with increasing time during potentiostatic polarization at 0.2 V and 293 K. The residual current is expected to be purely electronic (same data as shown in (a)). The inset shows the same curve, however, with the time axis plotted logarithmically. c) Specific electronic conductivity  $\sigma_{\text{eon}}$  of two different single crystals with the same composition at potentials ranging from 10 to 300 mV.

we measured the evolution of the current  $I$  over an extended time window of up to  $3 \times 10^5 \text{ s}$ , i.e., for a period of >83 h. At room temperature, we found that the final (or steady-state) current  $I_{\text{final}} = 260 \text{ pA}$ , which we assume to be electronic in origin, corresponds to  $\sigma_{\text{eon}}$  that is at least six orders of magnitude lower than  $\sigma_{\text{total}}$  (see also Figure 2b). Specific electronic conductivities, taking the area and thickness of the sample and the applied potential into account, are shown in Figure 2c. The electronic conductivity was measured for two different single crystals and at different potentials ranging from 10 to 300 mV (see Figure 2c). As the values are identical within a factor of 2, we assume that the potential applied was chosen to be well below the decomposition potential for Ga-LLZO.<sup>[26]</sup>

In Figure 3b the total conductivity of Ga-LLZO is plotted as a function of the inverse temperature  $1/T$  in an Arrhenius graph; data were read off from the isotherms shown in Figure 3a, see above. Considering the negligible electronic contribution to the total conductivity, which amounts in our case to be less than 1 ppm, we can safely assume that  $\sigma_{\text{ion}} = \sigma_{\text{total}}$  and, thus, expect a classical Arrhenius relation between  $\sigma$  and  $1/T$ . Analyzing our data according to  $\sigma T = \sigma_0 \exp(-E_a/(k_B T))$  we obtain an activation energy  $E_a$  of 0.30(1) eV (see Figure 3a);  $\sigma_0$  denotes the pre-exponential factor and  $k_B$  is Boltzmann's constant. Such a low activation energy is a typical value for fast ion conductors and has been found for a row of solid electrolytes such as Li-bearing argyrodites,<sup>[27]</sup> NaSICON-type electrolytes,<sup>[28]</sup> and

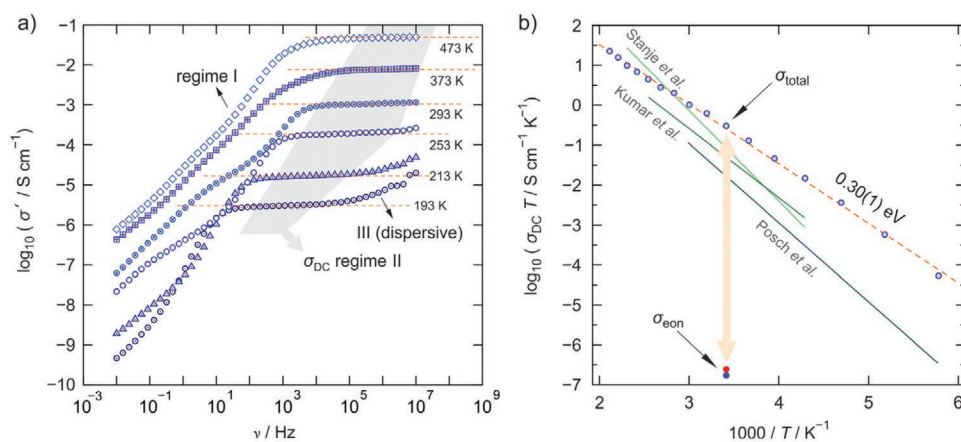


**Figure 3.** a) Conductivity isotherms of a Ga-LLZO single crystal showing the real part of the complex conductivity versus the applied frequencies. Temperatures are indicated; the isotherms are composed of three regimes labeled I, II, and III, see text for further explanation. The broad frequency-independent DC plateau (regime II) is followed by electrode polarization effects appearing at lower frequencies. Only at very low temperatures  $T$  the Jonscher-type dispersive regime III is accessible in the frequency range used to record the isotherms. b) Arrhenius plot of the total conductivity  $\sigma_{\text{total}}$  read off from regime II yielding an activation energy as low as 0.3 eV. The mean electronic conductivity  $\sigma_{\text{eon}}$  of two single crystals investigated at room temperature is also shown. For comparison, the total conductivity for Al-stabilized single crystalline LLZO (Posch et al.<sup>[32a]</sup>), Ta-stabilized single crystalline LLZO (Stanje et al.<sup>[22]</sup>), and Al-stabilized polycrystalline LLZO (Kumar et al.<sup>[32b]</sup>) are included as well.

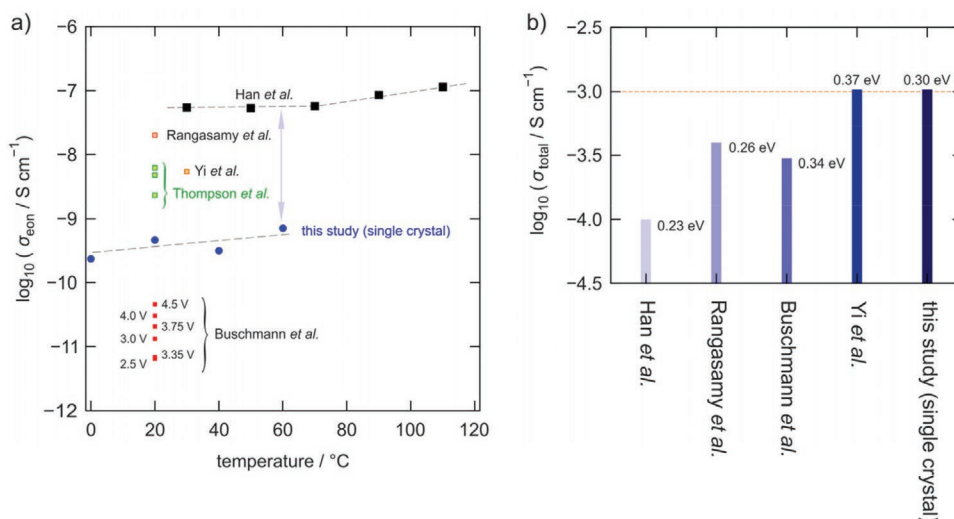


**Figure 4.** a) Change of the electronic conductivity of single crystalline Ga-LLZO as measured in this study as a function of temperature. For comparison,  $\sigma_{\text{eon}}$  values of other studies of cubic LLZO stabilized by the incorporation of either  $\text{Al}^{3+}$ ,  $\text{Ta}^{3+}$ , or  $\text{Ga}^{3+}$  ions are also included; of course, these studies focus on charge carrier transport in LLZO-type garnets with different compositions. b) Total conductivities  $\sigma_{\text{total}}$  (and corresponding activation energies) that refer to the results on polycrystalline samples shown in (a).

the Ti- and Ge-containing thiophosphates such as lithium titanium phosphate<sup>[29]</sup> and lithium germanium thiophosphate.<sup>[30]</sup> Importantly, the value is well in line with that obtained from total conductivity measurements in highly dense polycrystalline Ga-LLZO samples with negligible g. b. contributions.<sup>[31]</sup> For comparison, in Figure 3b results from other LLZO samples are included as well.<sup>[22,32]</sup>

The temperature dependence of  $\sigma_{\text{eon}}$  is shown in **Figure 4a**. It revealed a weak thermal activation pointing to an activation energy of 0.14(7) eV. For comparison, the values of Han et al.<sup>[14]</sup> yield an activation energy of 0.23(2) eV for polycrystalline  $\text{Li}_{6.4}\text{La}_3\text{Zr}_{1.4}\text{Ta}_{0.6}\text{O}_{12}$ . Note, however, that the polarization time in their study was only 1 h at 100 mV (200 nm thick Cu electrodes). Values of their study are included in Figure 4a; compared to this work  $\sigma_{\text{eon}}$  is higher by two orders of magnitude and might play a role in Li dendrite formation as assumed by the authors. Rangasamy et al.<sup>[15b]</sup> investigated the ionic and electronic conductivity of Al-doped polycrystalline garnets with the composition  $\text{Li}_{6.24}\text{Al}_{0.24}\text{La}_3\text{Zr}_2\text{O}_{11.98}$ ; they found  $\sigma_{\text{total}} = 4 \times 10^{-4} \text{ S cm}^{-1}$  with an activation energy of  $E_a = 0.26 \text{ eV}$  and an electronic conductivity  $\sigma_{\text{eon}}$  of  $2 \times 10^{-8} \text{ S cm}^{-1}$  at room temperature. Again, this value is by approximately two orders of magnitude higher than that probed in this study. A very similar value of  $3.59 \times 10^{-8} \text{ S cm}^{-1}$  has been reported by Song et al. for polycrystalline  $\text{Li}_7\text{La}_{2.75}\text{Ca}_{0.25}\text{Zr}_{1.75}\text{Nb}_{0.25}\text{O}_{12}$ ;<sup>[12]</sup> the authors point out the importance of grain boundary regions to be responsible for enhanced electronic conduction.<sup>[16,17]</sup> As has been shown in the elegant study of Song et al.<sup>[26]</sup> the electronic conductivity in polycrystalline LLZO samples, if high potentials are applied, is best described by the behavior of a varistor, exhibiting a potential-dependent electronic resistance. If the applied electric voltage exceeds a certain limit, electric breakdown at the grain boundaries will occur and significantly increase the electronic conductivity; below this threshold, LLZO shows ohmic behavior. Obviously, the electric field the grain boundaries can

withstand depends on the local composition including, for example, impurities, segregated phases, and vacancies. A general discussion of this effect and the influence of even small variations of the dopant concentration is given in Zhao et al.<sup>[33]</sup>

In an earlier work Buschmann et al.<sup>[15a]</sup> presented a total conductivity of  $3 \times 10^{-4} \text{ S cm}^{-1}$  for Al-stabilized (0.9% wt) polycrystalline garnets, which is very similar to that of Rangasamy et al.<sup>[15b]</sup> The corresponding activation energy turned out to be 0.34 eV.<sup>[15a]</sup> The specific electronic conductivity was measured by the Hebb–Wagner technique at potentials ranging from 2.5 to 4.5 V; very low values of  $6.4 \times 10^{-12} \text{ S cm}^{-1}$  (2.5 V) and  $4.6 \times 10^{-11} \text{ S cm}^{-1}$  (4.5 V) were reported. Yi et al.<sup>[15d]</sup> investigated the ionic and electronic conductivity of polycrystalline Al-free but Ta-stabilized LLZO ( $\text{Li}_{6.7}\text{La}_3\text{Zr}_{1.7}\text{Ta}_{0.3}\text{O}_{12}$ ). By using Ag electrodes and a constant potential of 100 mV they found that the specific electronic conductivity  $\sigma_{\text{eon}}$  takes values in the order of  $5.4 \times 10^{-9} \text{ S cm}^{-1}$ . This value was obtained after 8 min of polarization; for comparison, the total conductivity was  $10^{-3} \text{ S cm}^{-1}$  at 303 K (0.37 eV). Thompson et al.<sup>[15c]</sup> studied the electronic conductivity of Ta-bearing as well as Al-stabilized polycrystalline cubic LLZO samples in a semiblocking cell configuration (Li|LLZO|Au) at various potentials. The corresponding values are also included in Figure 4a. Figure 4b summarizes the total conductivities at room temperature that refer to the results for the samples included in Figure 4a.

We notice that even for similar polycrystalline samples the specific electronic conductivity may differ by some orders of magnitude. Although different methods have been employed to measure  $\sigma_{\text{eon}}$ , we can group the data that has been derived by applying low potentials. In this group, the electronic conductivity measured in Ga-LLZO single crystals turns out to be the lowest one and cannot be affected by any g. b. contributions,<sup>[26]</sup> thus representing a pure bulk value. This observation is in line with the general finding that the electronic conductivity of garnets is higher in polycrystalline than in single crystalline samples.<sup>[34]</sup>

Single crystalline Ga-LLZO studied here has to be characterized by a relatively high ionic conductivity, its electronic conductivity, on the other hand, turned out to be rather low.<sup>[35]</sup> Hence, also by considering results in literature presented so far, it is very likely that electron transport is not coupled with ion transport, as it may happen in some other materials with poor ion conducting properties.<sup>[36]</sup> The low activation energy associated with electronic conductivity is very likely the key reason for this decoupling. Having a low activation energy, the electron mobility is significantly less influenced by the temperature than the ionic mobility. While electrons are mobile at all times, the concentration of electron defects is most likely extremely low, thus accounting for the low electronic conductivity seen in polarization experiments.

We should consider the value for  $\sigma_{\text{eon}}$  as an upper limit for the electronic conductivity. We assume that the sandwich pellet equipped with the two ion-blocking electrodes reaches a stationary state after a certain time under polarization. This state should be seen as a dynamic equilibrium in which the flux of ions moving from or toward the interfaces under the applied electric field equals the flux of ions that move in the opposite direction due to the formation of ion concentration gradients. We anticipate that in addition to the flux of  $\text{Li}^+$  ions, oxygen ion transport<sup>[37]</sup> is by several orders of magnitude lower than that associated with  $I_{\text{final}}$ . Also, it is assumed that local electric fields and those forming in front of the metal electrodes (the induced space charge fields) are negligible and do not lead to any breakdown phenomena and/or electrochemical reaction. This assumption also includes that no leakage currents contribute to the steady-state values obtained after a sufficiently long period of polarization. In our opinion, taking into account such effects, which are extremely hard to quantify separately, would yield even lower values for  $\sigma_{\text{eon}}$ . Nevertheless, the value of the electronic part of conductivity determined by the simple polarization method used here, while certainly affected by some errors, represents a technologically relevant parameter. In a real solid-state battery, the electrodes will always be good electron conductors and the solid electrolyte will continuously face a certain polarization voltage, depending on the operational potential of the electrodes and state of charge. Thus, for any practical application, it would be important to know what is the apparent electronic conductivity to estimate the self-discharge current caused by i) overall electron transport through the solid electrolyte and by ii) electron transport through the crystal lattice.

### 3. Conclusion

Here, we probed the electronic and ionic conductivity of single crystalline, Czochralski-grown Ga-stabilized  $\text{Li}_{6.4}\text{Ga}_{0.2}\text{La}_3\text{Zr}_2\text{O}_{12}$  by means of broadband impedance spectroscopy and potentiostatic polarization. To stay well below the decomposition potential of LLZO we chose very low potentials to polarize a symmetric Au|Ga-LLZO|Au cell. We found that the electronic conductivity, as estimated from polarization curves, is at least six orders of magnitude lower than the total conductivity to which impedance spectroscopy is, at sufficiently high frequencies, sensitive. In contrast to earlier speculations we think that in the present case a residual electric conductivity in the order of  $10^{-10} \text{ S cm}^{-1}$  does not trigger the formation of Li dendrites.

In the present case,  $\text{Li}^+$  transport in Ga-LLZO turned out to be independent and, thus, not coupled with the residual electronic bulk conductivity.

### 4. Experimental Section

Single crystals with the composition  $\text{Li}_{6.4}\text{Ga}_{0.2}\text{La}_3\text{Zr}_2\text{O}_{12}$  were directly grown from the melt by the Czochralski method. The advantages of this method over many other methods of producing crystalline materials are that it yields large single crystals. Furthermore, the elemental distribution of dopants in a single crystal is homogeneous compared to polycrystalline samples.<sup>[38]</sup> In the context of this study, the advantage lies foremost in the fact that a large single crystal could be produced. The starting materials  $\text{Li}_2\text{CO}_3$  (Alfa Aesar, 99.999%),  $\text{La}_2\text{O}_3$  (Fox Chemicals, 99.999%),  $\text{Ga}_2\text{O}_3$  (Fox Chemicals, 99.999%), and  $\text{ZrO}_2$  (Merck, Optipur) were dried and then mixed with an excess of 10 wt% of  $\text{Li}_2\text{CO}_3$ . The mixture was isostatically pressed and calcined at a maximum temperature of 1230 °C following the procedure commonly used for the preparation of LLZO ceramic samples.<sup>[18]</sup> Afterward, the material was melted in an inductively heated iridium crucible in  $\text{N}_2$  atmosphere. Crystallization was initiated by dipping an iridium wire into the supercooled melt; this wire was slowly pulled upward at a constant rate of 0.4 mm  $\text{h}^{-1}$  under rotation of 10  $\text{min}^{-1}$ . After growth, the crystal was cooled down to room temperature within 15 h. The obtained crystal was 14 mm in diameter and about 50 mm long, it is of yellow color with white opaque adhesions and some cracks. However, the interior was mainly transparent and allowed for the preparation of several smaller measurement specimens. The single crystals were characterized by X-ray diffraction and neutron diffraction (Tables S1 and S2, Supporting Information).

For the measurement of total and electronic conductivity the crystals were cut into square specimens (5 mm) and a thickness of 1 mm. To remove any newly formed surface contaminations, such as thin layers of  $\text{Li}_2\text{CO}_3$ , they were transferred into an Ar-filled glovebox ( $\text{H}_2\text{O}$  and  $\text{O}_2 < 1$  ppm) and thoroughly polished with sanding paper (SiC, 4000 grit). Then, ion blocking electrodes were applied (100 nm, Au) by means of sputtering, again under inert gas atmosphere. The total conductivity, that is the sum of the ionic and the electronic conductivity, was measured on symmetric Au|Ga-LLZO|Au pellets with a Concept80 broadband impedance spectrometer (Novocontrol) applying a root-mean-square (rms) sinusoidal voltage amplitude of 0.1  $\text{V}_{\text{rms}}$ . Conductivity isotherms were recorded over a broad frequency range ( $10^{-2}$  and  $10^7$  Hz) and at different temperatures ranging from 173 to 373 K. For potentiostatic polarization, the samples in sandwich configuration were kept in an airtight Swagelock-type cell and subjected to a constant potential (Parstat MC potentiostat); the current  $I$  was recorded as a function of time  $t$ . Polarization measurements using ion-blocking Au electrodes were performed at 273, 293, 313, and at 333 K. The steady state current  $I_{\text{final}}$  corresponds to the residual electronic current, which can be converted into the specific electronic conductivity  $\sigma_{\text{eon}}$ . Here, the well-known Hebb–Wagner method is not used to assess  $\sigma_{\text{eon}}$  as LLZO is not thermodynamically stable in contact with metallic lithium.<sup>[39]</sup>

### Supporting Information

Supporting Information is available from the Wiley Online Library or from the author.

### Acknowledgements

Financial support by the Austrian Federal Ministry of Science, Research and Economy (BMWF), and the National Foundation for Research, Technology and Development (CD-Laboratory of Lithium Batteries: Ageing Effects, Technology and New Materials) is gratefully

acknowledged. Moreover, financial support by the Austrian Science Fund (FWF) in the frame of InterBatt (P 31437) and the FFG (Austrian Research promotion Agency) K-project “safe battery” is gratefully acknowledged. In addition, the study received funding from the European Union’s Horizon 2020 research and innovation program under Grant Agreement No. 769929. The neutron measurements were performed on the single-crystal diffraction beamline HEiDi operated jointly by RWTH Aachen (Institute of Crystallography) and Forschungszentrum Jülich GmbH (JCNS) within the JARA cooperation.

## Conflict of Interest

The authors declare no conflict of interest.

## Keywords

direct current-polarization, electronic conductivity, ionic conductivity, LLZO, single crystals

Received: March 12, 2020  
Revised: April 20, 2020  
Published online: June 11, 2020

- [1] D. Larcher, J. M. Tarascon, *Nat. Chem.* **2015**, *7*, 19.
- [2] a) M. S. Whittingham, *Chem. Rev.* **2014**, *114*, 11414; b) M. S. Whittingham, *Chem. Rev.* **2004**, *104*, 4271; c) J. B. Goodenough, Y. Kim, *Chem. Mater.* **2010**, *22*, 587.
- [3] a) M. Li, J. Lu, Z. W. Chen, K. Amine, *Adv. Mater.* **2018**, *30*, e1800561; b) J. W. Choi, D. Aurbach, *Nat. Rev. Mater.* **2016**, *1*, 16013; c) B. Scrosati, J. Hassoun, Y. K. Sun, *Energy Environ. Sci.* **2011**, *4*, 3287.
- [4] J. B. Goodenough, *Energy Storage Mater.* **2015**, *1*, 158.
- [5] R. Murugan, V. Thangadurai, W. Weppner, *Angew. Chem., Int. Ed.* **2007**, *46*, 7778.
- [6] a) X. Huang, Y. Lu, Z. Song, T. Xiu, M. E. Badding, Z. Wen, *J. Energy Chem.* **2019**, *39*, 8; b) F. Flatscher, M. Philipp, S. Ganschow, H. M. R. Wilkening, D. Rettenwander, *J. Mater. Chem. A* **2020**, <https://doi.org/10.1039/C9TA14177D>.
- [7] a) V. Thangadurai, S. Narayanan, D. Pinzaru, *Chem. Soc. Rev.* **2014**, *43*, 4714; b) J. C. Bachman, S. Muy, A. Grimaud, H. H. Chang, N. Pour, S. F. Lux, O. Paschos, F. Maglia, S. Lupart, P. Lamp, L. Giordano, Y. Shao-Horn, *Chem. Rev.* **2016**, *116*, 140; c) A. Manthiram, X. Yu, S. Wang, *Nat. Rev. Mater.* **2017**, *2*, 16103; d) F. Zheng, M. Kotobuki, S. Song, M. O. Lai, L. Lu, *J. Power Sources* **2018**, *389*, 198; e) J. Schnell, T. Günther, T. Knoche, C. Vieider, L. Köhler, A. Just, M. Keller, S. Passerini, G. Reinhart, *J. Power Sources* **2018**, *382*, 160.
- [8] S. Afyon, K. V. Kravchik, S. Wang, J. van den Broek, C. Hänsel, M. V. Kovalenko, J. L. M. Rupp, *J. Mater. Chem. A* **2019**, *7*, 21299.
- [9] a) J. van den Broek, S. Afyon, J. L. M. Rupp, *Adv. Energy Mater.* **2016**, *6*, 1600736; b) I. Garbayo, M. Struzik, W. J. Bowman, R. Pfenninger, E. Stimp, J. L. M. Rupp, *Adv. Energy Mater.* **2018**, *8*, 1702265.
- [10] Z. Z. Zhang, Y. J. Shao, B. Lotsch, Y. S. Hu, H. Li, J. Janek, L. F. Nazar, C. W. Nan, J. Maier, M. Armand, L. Q. Chen, *Energy Environ. Sci.* **2018**, *11*, 1945.
- [11] a) S. Wenzel, S. Randau, T. Leichtweiß, D. A. Weber, J. Sann, W. G. Zeier, J. Janek, *Chem. Mater.* **2016**, *28*, 2400; b) W. Zhang, F. H. Richter, S. P. Culver, T. Leichtweiss, J. G. Lozano, C. Dietrich, P. G. Bruce, W. G. Zeier, J. Janek, *ACS Appl. Mater. Interfaces* **2018**, *10*, 22226.
- [12] Y. L. Song, L. Y. Yang, W. G. Zhao, Z. J. Wang, Y. Zhao, Z. Q. Wang, Q. H. Zhao, H. Liu, F. Pan, *Adv. Energy Mater.* **2019**, *9*, 1900671.
- [13] T. Swamy, R. Park, B. W. Sheldon, D. Rettenwander, L. Porz, S. Berendts, R. Uecker, W. C. Carter, Y.-M. Chiang, *J. Electrochem. Soc.* **2018**, *165*, A3648.
- [14] F. Han, A. S. Westover, J. Yue, X. Fan, F. Wang, M. Chi, D. N. Leonard, N. J. Dudney, H. Wang, C. Wang, *Nat. Energy* **2019**, *4*, 187.
- [15] a) H. Buschmann, J. Dölle, S. Berendts, A. Kuhn, P. Bottke, M. Wilkening, P. Heitjans, A. Senyshyn, H. Ehrenberg, A. Lotnyk, V. Duppel, L. Kienle, J. Janek, *Phys. Chem. Chem. Phys.* **2011**, *13*, 19378; b) E. Rangasamy, J. Wolfenstine, J. Sakamoto, *Solid State Ionics* **2012**, *206*, 28; c) T. Thompson, S. Yu, L. Williams, R. D. Schmidt, R. Garcia-Mendez, J. Wolfenstine, J. L. Allen, E. Kioupakis, D. J. Siegel, J. Sakamoto, *ACS Energy Lett.* **2017**, *2*, 462; d) M. Yi, T. Liu, X. Wang, J. Li, C. Wang, Y. Mo, *Ceram. Int.* **2019**, *45*, 786.
- [16] H. K. Tian, B. Xu, Y. Qi, *J. Power Sources* **2018**, *392*, 79.
- [17] a) X. Guo, J. Fleig, J. Maier, *J. Electrochem. Soc.* **2001**, *148*, J50; b) M. J. Verkerk, B. J. Middelhuis, A. J. Burggraaf, *Solid State Ionics* **1982**, *6*, 159.
- [18] R. Wagner, G. J. Redhammer, D. Rettenwander, A. Senyshyn, W. Schmidt, M. Wilkening, G. Amthauer, *Chem. Mater.* **2016**, *28*, 1861.
- [19] a) I. Riess, *Solid State Ionics* **2003**, *157*, 1; b) I. Riess, *Solid State Ionics* **1992**, *51*, 219.
- [20] a) R. Amin, P. Balaya, J. Maier, *Electrochem. Solid-State Lett.* **2007**, *10*, A13; b) S. Wang, M. Yan, Y. Li, C. Vinado, J. Yang, *J. Power Sources* **2018**, *393*, 75.
- [21] a) J. Awaka, N. Kijima, H. Hayakawa, J. Akimoto, *J. Solid State Chem.* **2009**, *182*, 2046; b) A. Kuhn, S. Narayanan, L. Spencer, G. Goward, V. Thangadurai, M. Wilkening, *Phys. Rev. B* **2011**, *83*, 094302; c) G. Menzer, *Z. Kristallogr. - Cryst. Mater.* **1929**, *69*, 300.
- [22] B. Stanje, D. Rettenwander, S. Breuer, M. Uitz, S. Berendts, M. Lerch, R. Uecker, G. Redhammer, I. Hanzu, M. Wilkening, *Ann. Phys.* **2017**, *529*, 1700140.
- [23] a) N. Zhao, W. Khokhar, Z. J. Bi, C. Shi, X. X. Guo, L. Z. Fan, C. W. Nan, *Joule* **2019**, *3*, 1190; b) J. Su, X. Huang, Z. Song, T. Xiu, M. E. Badding, J. Jin, Z. Wen, *Ceram. Int.* **2019**, *45*, 14991; c) A. J. Samson, K. Hofstetter, S. Bag, V. Thangadurai, *Energy Environ. Sci.* **2019**, *12*, 2957.
- [24] S. Qin, X. Zhu, Y. Jiang, M. e. Ling, Z. Hu, J. Zhu, *Appl. Phys. Lett.* **2018**, *112*, 113901.
- [25] S. Emmert, M. Wolf, R. Gulich, S. Krohns, S. Kastner, P. Lunkenheimer, A. Loidl, *Eur. Phys. J. B* **2011**, *83*, 157.
- [26] Y. Song, L. Yang, L. Tao, Q. Zhao, Z. Wang, Y. Cui, H. Liu, Y. Lin, F. Pan, *J. Mater. Chem. A* **2019**, *7*, 22898.
- [27] a) I. Hanghofer, M. Brinek, S. L. Eisbacher, B. Bitschnau, M. Volck, V. Hennige, I. Hanzu, D. Rettenwander, H. M. R. Wilkening, *Phys. Chem. Chem. Phys.* **2019**, *21*, 8489; b) M. A. Kraft, S. P. Culver, M. Calderon, F. Bocher, T. Krauskopf, A. Senyshyn, C. Dietrich, A. Zevalkin, J. Janek, W. G. Zeier, *J. Am. Chem. Soc.* **2017**, *139*, 10909; c) I. Hanghofer, B. Gadermaier, H. M. R. Wilkening, *Chem. Mater.* **2019**, *31*, 4591.
- [28] a) S. Lunghammer, D. Prutsch, S. Breuer, D. Rettenwander, I. Hanzu, Q. Ma, F. Tietz, H. M. R. Wilkening, *Sci. Rep.* **2018**, *8*, 11970; b) S. Lunghammer, Q. Ma, D. Rettenwander, I. Hanzu, F. Tietz, H. M. R. Wilkening, *Chem. Phys. Lett.* **2018**, *701*, 147.
- [29] D. Di Stefano, A. Miglio, K. Robeyns, Y. Filinchuk, M. Lechartier, A. Senyshyn, H. Ishida, S. Spinnenberger, D. Prutsch, S. Lunghammer, D. Rettenwander, M. Wilkening, B. Roling, Y. Kato, G. Hautier, *Chem* **2019**, *5*, 2450.
- [30] N. Kamaya, K. Homma, Y. Yamakawa, M. Hirayama, R. Kanno, M. Yonemura, T. Kamiyama, Y. Kato, S. Hama, K. Kawamoto, A. Mitsui, *Nat. Mater.* **2011**, *10*, 682.

- [31] L. Buannic, B. Orayech, J.-M. López Del Amo, J. Carrasco, N. A. Katcho, F. Aguesse, W. Manalastas, W. Zhang, J. Kilner, A. Llordés, *Chem. Mater.* **2017**, *29*, 1769.
- [32] a) P. Posch, S. Lunghammer, S. Berendts, S. Ganschow, G. J. Redhammer, A. Wilkening, M. Lerch, B. Gadermaier, D. Rettenwander, H. M. R. Wilkening, *Energy Storage Mater.* **2020**, *24*, 220; b) P. J. Kumar, K. Nishimura, M. Senna, A. Düvel, P. Heitjans, T. Kawaguchi, N. Sakamoto, N. Wakiya, H. Suzuki, *RSC Adv.* **2016**, *6*, 62656.
- [33] J. Zhao, B. Wang, K. Lu, *Ceram. Int.* **2014**, *40*, 14229.
- [34] A. J. Samson, K. Hofstetter, E. Wachsmann, V. Thangadurai, *J. Electrochem. Soc.* **2018**, *165*, A2303.
- [35] J. Wolfenstine, J. Ratchford, E. Rangasamy, J. Sakamoto, J. L. Allen, *Mater. Chem. Phys.* **2012**, *134*, 571.
- [36] M. Philipp, S. Lunghammer, I. Hanzu, M. Wilkening, *Mater. Res. Express* **2017**, *4*, 075508.
- [37] M. Kubicek, A. Wachter-Welzl, D. Rettenwander, R. Wagner, S. Berendts, R. Uecker, G. Amthauer, H. Hutter, J. Fleig, *Chem. Mater.* **2017**, *29*, 7189.
- [38] a) S. Smetaczek, M. Bonta, A. Wachter-Welzl, S. Taibl, R. Wagner, D. Rettenwander, J. Fleig, A. Limbeck, *J. Anal. At. Spectrom.* **2020**, *35*, 972; b) A. Wachter-Welzl, J. Kirowitz, R. Wagner, S. Smetaczek, G. C. Brunauer, M. Bonta, D. Rettenwander, S. Taibl, A. Limbeck, G. Amthauer, J. Fleig, *Solid State Ionics* **2018**, *319*, 203.
- [39] Y. Zhu, J. G. Connell, S. Tepavcevic, P. Zapol, R. Garcia-Mendez, N. J. Taylor, J. Sakamoto, B. J. Ingram, L. A. Curtiss, J. W. Freeland, D. D. Fong, N. M. Markovic, *Adv. Energy Mater.* **2019**, *9*, 1803440.

# ADVANCED MATERIALS INTERFACES

## Supporting Information

for *Adv. Mater. Interfaces*, DOI: 10.1002/admi.202000450

The Electronic Conductivity of Single Crystalline  
Ga-Stabilized Cubic  $\text{Li}_7\text{La}_3\text{Zr}_2\text{O}_{12}$ : A Technologically  
Relevant Parameter for All-Solid-State Batteries

*Martin Philipp, Bernhard Gadermaier, Patrick Posch,  
Ilie Hanzu, Steffen Ganschow, Martin Meven, Daniel  
Rettenwander, Günther J. Redhammer, and H. Martin R.  
Wilkening\**

**The Electronic Conductivity of Single Crystalline  
Ga-Stabilized Cubic  $\text{Li}_7\text{La}_3\text{Zr}_2\text{O}_{12}$  —  
A Technologically Relevant Parameter for All-Solid-State Batteries**

*M. Philipp<sup>1</sup>, B. Gadermaier<sup>1</sup>, P. Posch<sup>1</sup>, I. Hanzu<sup>1,2</sup>, S. Ganschow<sup>3</sup>, M. Meven,<sup>4</sup> D. Rettenwander<sup>1</sup>, G. J. Redhammer,<sup>5</sup>  
and H. M. R. Wilkening<sup>1,2\*</sup>*

<sup>1</sup> Institute for Chemistry and Technology of Materials, Christian Doppler Laboratory for Lithium Batteries, Graz University of Technology (NAWI Graz), Stremayrgasse 9, 8010 Graz, Austria

<sup>2</sup> Alistore-ERI European Research Institute, CNRS FR3104, Hub de l'Energie, Rue Baudelocque, 80039 Amiens, France

<sup>3</sup> Leibniz-Institut für Kristallzüchtung, Max-Born-Str. 2, 12489 Berlin, Germany

<sup>4</sup> Institut für Kristallographie, RWTH Aachen, Außenstelle Heinz Maier-Leibnitz Zentrum (TU München), Lichtenbergstraße 1, 85747 Garching, Deutschland

<sup>5</sup> Department of Chemistry and Physics of Materials, Jakob-Haringer-Strasse 2a, University of Salzburg, 5020 Salzburg, Austria

## Experimental

Single crystal X-ray diffraction data were collected on a Bruker SMART APEX CCD diffractometer (graphite-monochromatized  $\text{Mo K}\alpha$  X-ray radiation (50 kV, 20 mA)). The single crystals were selected according to their optical properties, *i.e.*, with regard to homogeneity and colour. They were glued on top of a glass capillary (0.1 mm in diameter). The crystal-to-detector distance was 30 mm and the detector has been positioned at  $-28^\circ 2\theta$  and  $-40^\circ 2\theta$  using an  $\omega$ -scan mode strategy at four different positions ( $0^\circ$ ,  $90^\circ$ ,  $180^\circ$  and  $270^\circ$ ) each. 666 frames with  $\Delta\omega = 0.3^\circ$  were acquired for each run. Three-dimensional data were integrated and corrected for Lorentz effects, polarization effects and the influence of background effects using the APEX3 software (Bruker, 2015).

Single crystal neutron diffraction has been carried out at the HEiDi diffractometer at a temperature of 298 K with  $\lambda = 0.793 \text{ \AA}$  (Ge-(420) monochromator). HEiDi is a four circle single crystal diffractometer with an acentric Eulerian cradle using the high flux of hot neutrons of the beam tube SR9A of the FRM II reactor (Meven & Sazonov, 2015). For a full structural characterization, data was acquired up to  $\sin(\theta/\lambda) = 0.806$  with 608 independent Bragg reflections ( $R_{\text{int}} = 4.31 \%$ ). In a combined and simultaneous approach both X-ray diffraction and neutron diffraction data were used for full structure analysis employing the WinGX software package (Farrugia, 2012), SHELXL-2014 (Sheldrick, 2015) and the FULLPROF software suite.

## Results

Analysis of intensity data from single crystal X-ray and neutron diffraction experiments reveals the presence of a weak superstructure reflection which violates the  $Ia\bar{3}d$  symmetry and points to an acentric space group  $I\bar{4}3d$  (No. 220) as has been found recently for Ga-doped LLZO by Wagner (Wagner *et al.*, 2016). In general, the structural topology of

the Czochralski-grown Ga-doped LLZO single crystal resembles the one obtained by Wagner *et al.* (Wagner *et al.*, 2016); La<sup>3+</sup> resides on the 8-fold coordinated 24*d* position, Zr<sup>4+</sup> is located at the 6-fold coordinated 16*c* position and the two independent oxygen atoms are positioned at 48*e*.

Single crystal X-ray diffraction revealed the presence of three possible sites for Li<sup>+</sup>, namely special positions Li1 at 12*a*, Li2 at 12*b*, both tetrahedrally coordinated, and Li3 at a general position called 48*e*.<sup>a</sup> Inspection of residual electron density maps from X-ray diffraction did not reveal any significant and reliable hints to further Li sites. Assuming that only Li<sup>+</sup> contributes to scattering, the occupation factor of the Li1 site is larger (0.42) than the allowed values for this 12*a* Wyckoff position (0.25); the occupation factor corresponding to Li2 is approximately 0.16. Strong evidence is found that Ga<sup>3+</sup> occupies the Li1 site and that the sites Li2 and Li3 are only partly occupied by Li<sup>+</sup>.

**Table S1: Details on data collection and structure refinement for cubic Ga-doped LLZO with  $a = 12.9689(2)$  Å, space group  $I\bar{4}3d$  (Nr. 220),  $Z = 8$**

Identification code	Neutron data	X-ray data
Data collection device	HEiDi	Smart APEX
Temperature (K)	298(2)	300(2)
Wavelength (Å)	0.793	0.71073
Crystal size (mm <sup>3</sup> )	2.1 × 1.8 × 1.7	0.16 × 0.14 × 0.08
Theta range for data collection (°)	4.295 to 39.672	3.846 to 36.602
Index ranges:		
<i>h</i>	− 20 ... 20	− 21 ... 21
<i>k</i>	0 ... 20	− 21 ... 21
<i>l</i>	0 ... 20	− 21 ... 21
Reflections collected	2662	33921
Independent reflections	608 [R(int) = 0.0431]	903 [R(int) = 0.0274]
Goodness of fit, F <sup>2</sup>	1.153	1.425
Final R indices [ $I > 2\sigma(I)$ ]	R <sub>1</sub> = 0.0228, wR <sub>2</sub> = 0.0391	R <sub>1</sub> = 0.0181, wR <sub>2</sub> = 0.0394
R indices (all data)	R <sub>1</sub> = 0.0271, wR <sub>2</sub> = 0.0401	R <sub>1</sub> = 0.0183, wR <sub>2</sub> = 0.0394
Extinction coefficient	0.0010(3)	0.0002(2)
Largest diff. peak and hole	0.414 and − 0.547 e Å <sup>−3</sup>	0.837 and − 0.559 e Å <sup>−3</sup>

This view is strongly supported by neutron diffraction; localization of Li2 and Li3 sites is straightforward due to the negative scattering cross section of Li. It is, however, quite difficult to allocate the Li1 site. This difficulty does not arise because of the fact that the site is unoccupied but rather stems from the circumstance that at this site the negative coherent scattering cross section of Li (− 1.9 fm)<sup>b</sup> overlaps with the strongly positive resonant cross section of Ga (7.288 fm). Hence, in total only a small positive nuclear density is observed at the 12*a* site in neutron diffraction data and refinement of this position turned out to be difficult. As on 12*a* also vacancies are assumed to be present, the content of Ga was constrained to the amount detected by inductively coupled plasma mass spectrometry (ICP-MS) used to analyse the chemical composition of the Ga-LLZO single crystal.

To obtain more reliable results, particularly regarding the 12*a* position, we performed a combined refinement of both X-ray and neutron diffraction data, analysing the data in equal terms. The result of this final refinement with full anisotropic description of all atoms using the FULLPROF suite of programs is listed in the Tables S1 and S2. It turned out that the 12*a* site is occupied by 0.50(3) Li<sup>+</sup> atoms per formula unit (apfu) and by 0.2 apfu Ga<sup>3+</sup>, as determined also experimentally by ICP-MS. This finding shows that the site occupation factor of this site is less than 1/2. The 12*b* site is occupied by a distinctly higher amount of Li<sup>+</sup> ions, namely 0.96(3) apfu, while the general position 48*e* reveals a high

<sup>a</sup> This position must not be mixed with a special 48*g* position in LLZO compounds crystallizing with the space group  $Ia\bar{3}d$ , which is, considering literature, sometimes proposed to be occupied.

<sup>b</sup> <https://www.nist.gov/ncnr/planning-your-experiment/scattering-length-periodic-table>



Li<sup>+</sup> population of 82 %, or 4.93(5) Li<sup>+</sup> apfu. In contrast to earlier findings of Wagner *et al.* (see Wagner *et al.*, 2016), the Czochralski-grown single crystal of the present study has no La<sup>3+</sup> deficiencies on the 24d site. In summary, the site occupation refinements give a balanced formula with regard to the valances of the cations and anions in Ga-LLZO.

**Table S2: Fractional atomic coordinates, equivalent isotropic and anisotropic atomic displacement parameters for the Ga-doped LLZO single crystal as determined from a joint analysis of both single crystal neutron diffraction data and X-ray diffraction data**

Name	<i>x</i>	<i>y</i>	<i>z</i>	<i>U</i> <sub>eq</sub>	occ.	Wykoff mult.
Zr1	− 0.00019(10)	− 0.00019(10)	− 0.00019(10)	0.00566(15)	1	16
La1	0.12147(8)	0.00000	0.25000	0.0070(3)	1.005(5)	24
O1	0.0979(2)	0.1963(2)	0.2800(2)	0.0088(10)	1.000(5)	48
O2	0.0338(2)	0.4451(2)	0.1476(2)	0.0105(11)	1.000(5)	48
Li1	0.37500	0.00000	0.25000	0.009(4)	0.336(8)	12 <sub>a</sub>
Ga1	0.37500	0.00000	0.25000	0.009(4)	0.133(8)	12 <sub>a</sub>
Li2	0.87500	0.00000	0.25000	0.027(7)	0.640(8)	12 <sub>b</sub>
Li3	0.0954(5)	0.1872(6)	0.4240(4)	0.023(3)	0.822(3)	48 <sub>e</sub>
Name	<i>U</i> <sub>11</sub>	<i>U</i> <sub>22</sub>	<i>U</i> <sub>33</sub>	<i>U</i> <sub>12</sub>	<i>U</i> <sub>13</sub>	<i>U</i> <sub>23</sub>
Zr1	0.00566(15)	0.00566(15)	0.00566(15)	− 0.00003(18)	− 0.00003(18)	− 0.00003(18)
La1	0.0083(3)	0.0064(4)	0.0064(4)	0	0	0.00098(19)
O1	0.0070(11)	0.0091(10)	0.0103(10)	− 0.0004(8)	0.0002(7)	0.0011(8)
O2	0.0125(11)	0.0119(12)	0.0071(11)	0.0010(9)	− 0.0011(7)	0.0007(9)
Li1/Ga1	0.009(4)	0.009(4)	0.009(4)	0	0	0
Li2	0.010(5)	0.036(7)	0.036(7)	0	0	0
Li3	0.035(3)	0.021(3)	0.014(2)	− 0.009(3)	0.005(2)	− 0.004(2)

## References

- Bruker. (2015). APEX3 (Version 2015. 10-0), Bruker AXS Inc, Madison, Wisconsin, USA.
- Farrugia, L. (2012). WinGX and ORTEP for Windows: an update. *Journal of Applied Crystallography*, 45(4), 849-854.
- Katcho, N. A., Carrete, J., Reynaud, M., Rousse, G., Casas-Cabanas, M., Mingo, N., . . . Carrasco, J. (2019). An investigation of the structural properties of Li and Na fast ion conductors using high-throughput bond-valence calculations and machine learning. *Journal of Applied Crystallography*, 52(1), 148-157.
- Meven, M., & Sazonov, A. (2015). HEiDi: Single crystal diffractometer at hot source. *Journal of large-scale research facilities*, 1(A7), 1-4.
- Sheldrick, G. (2015). Crystal structure refinement with SHELXL. *Acta Crystallographica Section C*, 71(1), 3-8.
- Wagner, R., Redhammer, G. J., Rettenwander, D., Senyshyn, A., Schmidt, W., Wilkening, M., & Amthauer, G. (2016). Crystal Structure of Garnet-Related Li-Ion Conductor Li<sub>7-3x</sub>Ga<sub>x</sub>La<sub>3</sub>Zr<sub>2</sub>O<sub>12</sub>: Fast Li-Ion Conduction Caused by a Different Cubic Modification? *Chemistry of Materials*, 28(6), 1861-1871.
- Wong, L. L., Chen, H., & Adams, S. (2017). Design of fast ion conducting cathode materials for grid-scale sodium-ion batteries. *Physical Chemistry Chemical Physics*, 19(11), 7506-7523.



### 3.4. Fast Li<sup>+</sup> transport in Li<sub>4</sub>Ti<sub>5</sub>O<sub>12</sub> — Conductivity spectroscopy reveals two distinct

#### Li ion dynamic processes in lithium pentatitanate

Li<sub>4</sub>Ti<sub>5</sub>O<sub>12</sub> is well-known and astonishing active material used in Li ion batteries. As its electrochemical potential of 1.5 V<sup>1</sup> vs. Li/Li<sup>+</sup> is comparatively high for an anode material, chances for Li-plating during fast charging are significantly reduced. Albeit it has a high molecular weight, it has a decent specific capacity of ~170 mAh/g as it can reversibly accommodate up to three Li<sup>+</sup> ions. Astonishingly, the integration of these three excessive Li<sup>+</sup> ions in the crystal structure leads to almost no expansion of the unit cell. Therefore, this material is known as a zero-strain anode material.<sup>2</sup>

Similar to LiFePO<sub>4</sub>, a cathode active material, it exhibits very low ionic and electronic conductivity. However, lithiated and concomitantly, reduced, the ionic as well as the electronic conductivity significantly increases for Li<sub>4+x</sub>Ti<sub>5</sub>O<sub>12</sub> (0 < x < 3). As some Ti<sup>4+</sup> centres are reduced to Ti<sup>3+</sup>, the presence of this Ti<sup>4+</sup>/Ti<sup>3+</sup> couple enables fast polaronic conduction. The ionic conduction on the other hand is increased due to a different reason. As Li<sup>+</sup> ions are inserted in the structure, they occupy a formerly empty sublattice constituted by the empty 16c octahedral sites. These octahedra share faces with the Li<sup>+</sup> containing 8a tetrahedra; they constitute a filled sublattice in Li<sub>4</sub>Ti<sub>5</sub>O<sub>12</sub>. Due to steric restrictions and Coulomb interactions, occupation of adjacent 16c and 8a sites is energetically unfavourable and this leads to a depletion of the 8a sublattice as the 16c sublattice is filled; the Li<sup>+</sup> ions on 8a sites change their site preference to 16c sites. In the intermediate state, both sublattices are partially filled and this situation is known to enable very fast ion diffusion.

It is well-known that LTO offers fast reaction kinetics in batteries, and this is well in line with the high ionic and electronic conductivity in its intermediate state. However, given its highly insulating nature it is rather puzzling how this material may be lithiated and reduced starting from the pristine state.

Here, we focused on this pristine state, that is LTO in the oxidized form Li<sub>4</sub>Ti<sub>5</sub>O<sub>12</sub> and used impedance spectroscopy as well as <sup>6</sup>Li MAS NMR spectroscopy to characterize the Li ion conduction. Using impedance spectroscopy and soft in situ annealing we could reveal a fast short-ranged Li<sup>+</sup> conduction mechanism which is associated with, if not enabled by, the oxygen vacancies we identified by EPR spectroscopy.

## Draft 1

# Fast Li<sup>+</sup> transport in Li<sub>4</sub>Ti<sub>5</sub>O<sub>12</sub> — Conductivity spectroscopy reveals two distinct Li ion dynamic processes in lithium pentatitanate

B. Gadermaier<sup>1</sup>, K. Hogrefe<sup>1</sup>, P. Frühwirt<sup>2</sup>, G. Gescheidt<sup>2</sup>, I. Hanzu<sup>1</sup>, H. M. R. Wilkening<sup>1</sup>

<sup>1</sup> Institute of Chemistry and Technology of Materials, Graz University of Technology (NAWI Graz), Stremayrgasse 9, A-8010 Graz, Austria

<sup>2</sup> Institute of Physical and Theoretical Chemistry, Graz University of Technology (NAWI Graz), Stremayrgasse 9, A-8010 Graz, Austria

### *Abstract*

During insertion, the Li ions change their preference for crystallographic positions, a process giving rise to a large increase in conductivity. Many studies have focused on the change in Li-ion conductivity during the insertion process however, there is still some debate on the ion dynamics in the fully de-lithiated form, Li<sub>4</sub>Ti<sub>5</sub>O<sub>12</sub>. In this impedance study, we found that the parent compound shows different, distinct conduction mechanisms on different time and length scales. We found two conduction processes, one comparatively fast process associated with highly correlated motion, the other associated with ion-range Li-ion conductivity in LTO. However, both conduction mechanisms likely correspond to bulk processes and do not just represent a process in the bulk that is slowed by resistive grain boundaries.

KEYWORDS: ionic conductors, active material, fast diffusion, oxygen vacancies, NMR, EPR

## Introduction

$\text{Li}_4\text{Ti}_5\text{O}_{12}$  is a well-known anode material for reversible storage of up to 3 Li ions per formula unit. LTO crystallizes in the spinel-like structure and is a peculiar material which shows zero-strain during insertion of  $\text{Li}^+$  ions. During lithiation, the large octahedra vacancies (16c) are occupied by  $\text{Li}^+$  ions and hence the volume remains virtually constant. In a publication by Schmidt *et al.* it was shown that Li ion dynamics in LTO is strongly influenced by the insertion level of  $\text{Li}^+$ .<sup>3</sup> Although the material is well characterized especially in terms of electrochemical performance, only few studies focused on the ion dynamics in the non-intercalated host material  $\text{Li}_4\text{Ti}_5\text{O}_{12}$ .

In the non-intercalated spinel structure, the 32e site is fully occupied by oxygen anions and the 8a site is fully occupied by Li cations. The 16d site, however, is shared between  $\text{Ti}^{4+}$  and  $\text{Li}^+$  whereas the former occupies 5/6 and the latter 1/6.

For  $\text{Li}_4\text{Ti}_5\text{O}_{12}$  many studies on Li-ion dynamics have been performed with different techniques (NMR, Impedance spectroscopy and electrochemical methods). Nevertheless, the picture of the diffusion mechanism is far from being complete, even for its end member  $\text{Li}_4\text{Ti}_5\text{O}_{12}$ . Extensive NMR studies by Schmidt *et al.* have shed some light on the change of the occupational disorder of the Li-ions during intercalation. It was shown that in  $\text{Li}_{4+x}\text{Ti}_5\text{O}_{12}$  the Li-ions which for  $x=0$  reside on the 8a-site are shifted to the 16c site upon intercalation due to steric repulsion of Li ions on 8a and 16c sites.<sup>4</sup> This shift is of course associated with a change in the diffusion dynamics. For  $x=0$  it is anticipated that the diffusion of Li from one 8a-site to another ( $8a \rightarrow 8a$ ) is mediated through an empty 16c site or vice versa, thus forming an 8a-16c-8a-pathway throughout the crystal structure.<sup>5</sup>

6

## Experimental

$\text{Li}_4\text{Ti}_5\text{O}_{12}$  was obtained from Süd Chemie (EXM1037) in high purity and dried in vacuum (1  $\mu\text{Bar}$ ) at 60 °C for 24 h. For X-ray powder diffraction, the sample was analysed using a Rigaku Miniflex 600 diffractometer (Bragg Brentano geometry,  $\text{CuK}_\alpha$  radiation). The pattern was recorded with a step size of 0.01 ° (10 °/min) in the  $2\theta$ -range 10 ° to 90 °. Rietveld refinement was carried out by using X'PertHighScorePlus (Panalytical). To analyse complex conductivities, the powder was uniaxial cold pressed to pellets (5 mm in diameter, 0.5 to 1 mm in thickness). After applying 100 nm thick Au electrodes by means of sputtering, a Novocontrol Concept 80 broadband analyser was employed to record conductivity isotherms; the frequency was varied from 10 mHz to 10 MHz. We

measured impedance data at temperatures from 20 °C to 200 °C cycling between these temperatures for 5 times. To exclude the influence of moisture, the sample was heated up to 180 °C and cooled down to 20 °C before isotherms were measured. In our setup, the temperature is automatically controlled by means of a QUATRO cryosystem (Novocontrol), which uses a heating element to build up a specific pressure in a liquid nitrogen Dewar to create a N<sub>2</sub> gas flow. Infrared spectra of samples dried in vacuum at different temperatures and durations were obtained by a FT-IR spectrometer (Bruker) – 10 scans were accumulated. <sup>6</sup>Li Magic angle spinning (MAS) NMR measurements were performed on a Bruker AVANCE III spectrometer in a nominal magnetic field of 11.7 T. The samples were loaded into MAS rotors (ZrO<sub>2</sub>, 2.5 mm) under argon and spun at 25 kHz in a Bruker MAS probe head. <sup>6</sup>Li Free induction decays (FID) were acquired at room temperature and the corresponding spectra were obtained via Fourier transformation. FIDs for the spectra were acquired using a single 90° excitation pulse followed by the FID acquisition. Using recycling delays of up to 10 min we collected up to 512 scans for a single spectrum. The spin-lattice relaxation rate (SLR) was recorded using a saturation recovery pulse sequence. This sequence consists of the destruction of the longitudinal magnetization via 10 closely spaced 90°-pulses, a variable recovery-time,  $t_R$ , and a 90°-pulse followed by the acquisition of the FID. The recovery of magnetization as a function of  $t_R$  can be analysed by a stretched exponential function and yields the overall relaxation rate. However, to assess the site-specific relaxation rates, we used the integral of the signal intensity for the individual <sup>6</sup>Li signals in the spectra. Continuous wave-electron paramagnetic resonance (CW-EPR) measurements were performed with a Bruker EMX X-band EPR spectrometer (100 kHz field modulation) equipped with a variable-temperature unit (Eurotherm B-VT 2000). EPR spectra were acquired at RT and 180 K using 2 mW microwave power and 0.1 mT field modulation. The g factor was calculated using 2,2-diphenyl-1-picrylhydrazyl (DPPH;  $g = 2.0036$ ) as an internal reference.

## Results and Discussion

The cubic spinel oxide  $\text{Li}_4\text{Ti}_5\text{O}_{12}$  (LTO,  $\text{Li}[\text{Li}_{1/3}\text{Ti}_{5/3}]\text{O}_4$ ) belongs to the space group  $Fd-3m$  with all atoms residing on the crystallographic positions 8a, 16d and 32e (Figure 1 and Figure S1). Whereas the 8a and the 32e positions are fully occupied by  $\text{Li}^+$  and  $\text{O}^{2-}$  respectively, the 16d position is co-occupied by  $\text{Li}^+$  (1/6) and  $\text{Ti}^{4+}$  (5/6). Worthwhile to note is that only 1/8 of tetrahedral sites and 1/2 of the octahedral sites are occupied. Thus,  $\text{Li}_4\text{Ti}_5\text{O}_{12}$  can accommodate up to 3 extra  $\text{Li}^+$  ions without appreciable change of the cell volume as the additional ions occupy vacant 16c octahedra (see Figure 1 b, c). Coulombic repulsion between Li ions on 8a and 16c sites modify the energy landscape and induces a depopulation of the 8a sites. This phenomenon leads to a significant increase of the ionic conduction in  $\text{Li}_{4+x}\text{Ti}_5\text{O}_{12}$  even for low insertion levels  $x < 0.3$ .

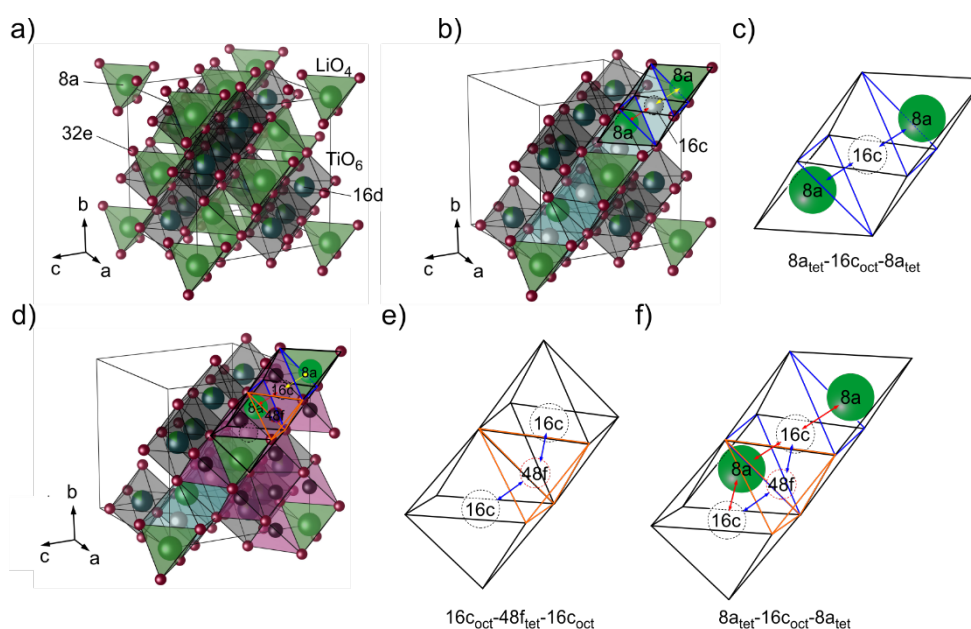


Figure 1: Crystal structure of  $\text{Li}_4\text{Ti}_5\text{O}_{12}$  and possible diffusion pathways of  $\text{Li}^+$ . a)  $\text{LiO}_4$  tetrahedra (8a), mixed occupied  $\text{Li}/\text{TiO}_6$  octahedra (16d) and oxygen atoms (32e) are shown. b) Partial unit cell highlighting the face-sharing connection of the 8a-tetrahedra with the 16c-octahedra. c) A possible diffusion pathway. d) Same as a) but in addition, the 48f tetrahedra are shown. e) 16c octahedra are also connected by common faces with the 48f tetrahedra. f) representation of the diffusion network comprising the  $8a_{\text{Oct}}$ ,  $16c_{\text{Tet}}$  and  $48f_{\text{Oct}}$ , all connected by common faces.

Changing the oxidation state of  $\text{Ti}^{4+}$  to  $\text{Ti}^{3+}$  along with  $\text{Li}^+$  insertion also increases the electronic conductivity of the material, however, it is expected that the  $\text{Ti}^{3+}$  centres are non-percolating at the early stages of insertion ( $x < 0.3$ ) *i.e.* before phase separation into a Li-rich and Li-poor phase occurs.<sup>7</sup> Obviously, the conduction mechanism in  $\text{Li}_{4+x}\text{Ti}_5\text{O}_{12}$  is rather complex as it involves, possibly, various diffusion pathways and changes from predominantly ionic to mixed ionic

electronic during insertion. The diffusion paths lead through face-sharing polyhedron and compromise 8a, 16c and 16d sites. Furthermore, reports additionally suggest involvements of the 48f tetrahedra as well as 32e sites (see Figure 1 d-f).<sup>8,9</sup> In any case, the Li<sup>+</sup> diffusion in Li<sub>4</sub>Ti<sub>5</sub>O<sub>12</sub> is mediated via a (direct) interstitial mechanism as neither 16c nor 48f are occupied. The defect chemistry as well as the Li:Ti-ratio substantially influence the conductivity process in such a material. Even for Li<sub>4</sub>Ti<sub>5</sub>O<sub>12</sub> the picture is not well resolved, and few studies report on the electronic as well as the ionic conductivity of this material. Chen *et al.* measured the specific electronic conductivity at room temperature and found a remarkably low value ( $<10^{13} \text{ S}\cdot\text{cm}^{-1}$ ) by using a four-point DC measurement method<sup>10</sup>. However, only an upper limit was reported and the few other studies reporting on electric properties of Li<sub>4</sub>Ti<sub>5</sub>O<sub>12</sub> show a rather controversial picture.<sup>11</sup>

Here, the conductivity of Li<sub>4</sub>Ti<sub>5</sub>O<sub>12</sub> was measured by broadband impedance spectroscopy covering frequencies from 10 mHz to the MHz region at temperatures ranging from 20 °C to 200 °C. The measurements were repeated for several times to monitor changes during the heat treatment of the sample (see Figure S3a). Conductivity isotherms of the last heating cycle are exemplarily shown in Figure 2a. The isotherm at the highest temperature shows three distinct features: the electrode polarisation at the lowest frequencies (EP), a broad conductivity plateau (1) followed by a dispersive regime at higher frequencies. We made use of Jonscher's power law<sup>12</sup>  $\sigma'(\nu) = \sigma_{DC} \cdot (1 + (\nu/\nu_H)^\alpha)^{-1}$  and extracted, by fitting it to our data, a dispersion parameter  $\alpha$  of 0.77(1) typical for a 3D ionic conductor.<sup>13,14</sup> The temperature dependent crossover frequency,  $\nu_H$ , is according to the formalism introduced by Almond and West interpretable as the mean hopping frequency.<sup>15</sup> At lower temperatures a second DC-plateau (2) at respectively higher frequencies emerges and is followed by the nearly constant loss (NCL) regime. This plateau shows a small frequency dependency and is attributed to a fast but short-ranged, *i.e.* localized, conduction process.<sup>16</sup> The narrow size and slight frequency dependence might be attributed to a large variation of the small, non-percolating, volume involved in this conduction process.<sup>16-18</sup> These two plateaus are often associated with the conduction in the crystallites (2) and the conduction throughout the whole sample (1), *i.e.* reduced conductivity due to resistive grain boundaries (g.b.).<sup>19</sup> While the conduction within the regular crystal structure is high, the discontinuity imposed by the grain boundaries results in areas of reduced ion mobility, and thus reduced long-range conductivity. However, the resistance imposed by the spatially confined grain boundaries leads to profound



charge accumulation reflected in capacitances in the order of a few nF. In contrast, the bulk conduction process has a capacitance in the order of a few pF, *i.e.* two to three orders of magnitude lower values.<sup>20-22</sup> There are several ways to estimate the capacitance associated with a particular conduction process. One way is to analyse the real part of the complex permittivity ( $\epsilon'$ ), assuming plate-like capacitor geometry. Here, we find very similar capacitances, in the order of 10-100 nF for both processes. This is in accordance with the similar height of the  $M''$  peaks (Figure 2b); the peak value is inversely proportional to the associated capacitance. As the conductivity of the two processes differs by at least 3 orders of magnitude, a considerable accumulation of charges, *i.e.* a higher capacitance would be expected. We expect that the picture in  $\text{Li}_4\text{Ti}_5\text{O}_{12}$  is not as trivial as it is in typical ionic conductors and thus refrain from ascribing these two processes to bulk and g.b. effects. Fehr *et al.* found a similar situation in one  $\text{Li}_4\text{Ti}_5\text{O}_{12}$  sample while another sample exhibited the classical capacitances for g.b..<sup>11</sup> However, synthesis conditions largely affect the effect of grain boundaries. Additionally, even unintended soft-annealing may exhibit a strong affect on ionic conductivity (see Figure S2 and S3). For solid electrolytes the effect of grain boundaries range from detrimental (cubic LLZO, LATP)<sup>21</sup> to negligible (LPSC)<sup>23</sup> while for many battery active materials the effect of the grain boundaries is indiscernible from the bulk response ( $\text{LiCoO}_2$ , NMC)<sup>24</sup>.

For further analysis, we extracted the DC conductivities,  $\sigma_{\text{DC}}$ , from the conductivity plateaus.  $\sigma_{\text{DC}}$  exhibits a thermal activation following the well-known Arrhenius relation  $\sigma_{\text{DC}} = \frac{\sigma_0}{T} \exp\left(\frac{-E_{\text{DC}}}{k_{\text{B}} \cdot T}\right)$  where  $k_{\text{B}}$  is Boltzmann's constant and  $E_{\text{DC}}$  is the activation energy of conduction.<sup>25</sup> It is important to note that  $\sigma_{\text{DC}}$  is proportional to the mobile charge carrier concentration,  $N$ , and their mobility, *i.e.* hopping rates,  $\nu_{\text{H}}$ . Likewise, the activation energy of conduction,  $E_{\text{DC}}$ , is the sum of the activation energy needed to mobilize charge carriers,  $E_{\text{N}}$ , and the activation energy of hopping,  $E_{\text{H}}$ . The Arrhenius plot (Figure 2c) shows the temperature dependent DC conductivities *vs.* the inverse temperature as well as the apex frequencies of the  $M''$  peaks,  $\nu_{\text{low}}$  and  $\nu_{\text{high}}$  (Figure 2b). The slow long-range conduction process (1) shows an activation energy of 0.83 eV identical to the activation energy of the associated electric relaxation derived from  $M''$  *vs.*  $1/T$  (see Figure 2c).  $^7\text{Li}$  NMR SAE measurements, sensitive to long range  $\text{Li}^+$  self-diffusion,<sup>26</sup> showed an almost identical activation energy  $E_{\text{m}}$  of 0.86 eV.<sup>5</sup> Furthermore,  $^7\text{Li}$  NMR SAE relaxation and dielectric relaxation are characterized by almost identical pre-exponential factors of  $4.9 \cdot 10^{13} \text{ s}^{-1}$  and  $1.9 \cdot 10^{13} \text{ s}^{-1}$ , respectively.

This suggests that the same diffusion process is analysed by both techniques and, furthermore, indicates that the diffusion process is associated with the bulk. This is also in line with the bulk-like capacitance values associated with this conduction process.

The fast short-range conduction process (2) shows a much smaller activation energy of 0.54 eV and interestingly, the activation energy of the peak frequencies of  $M''$  is even lower (0.48 eV). A value

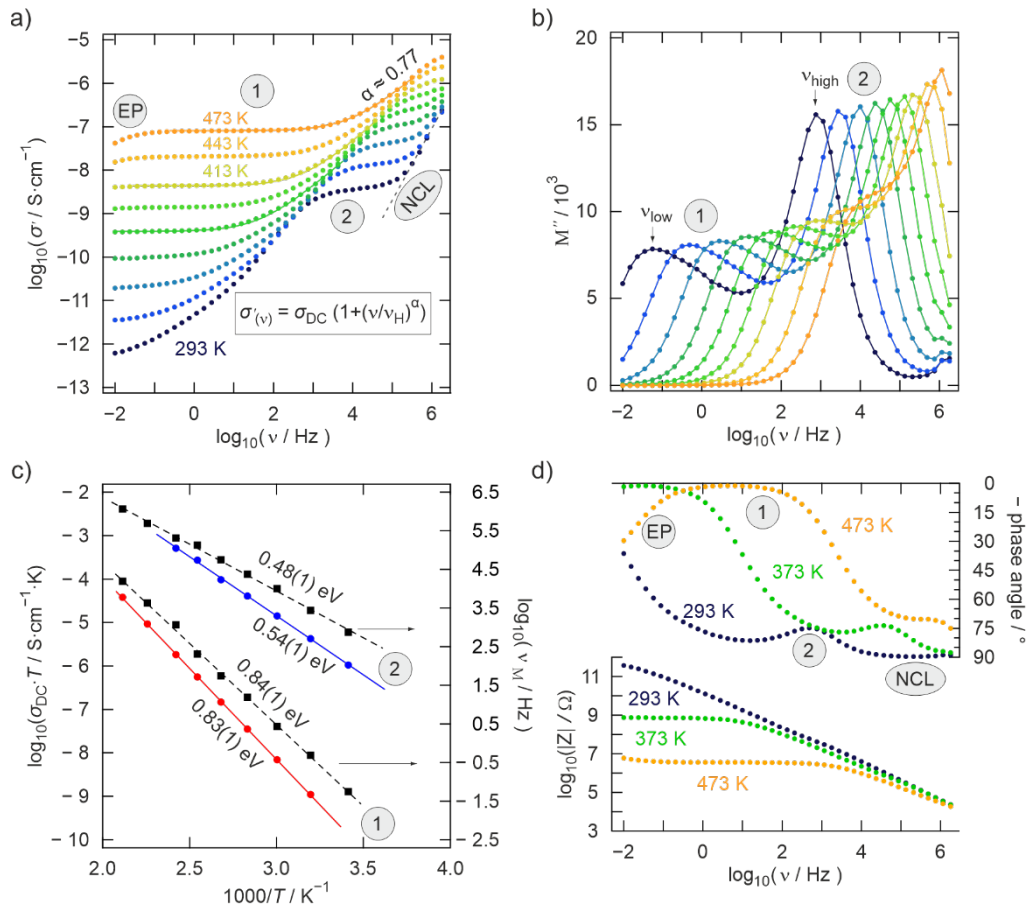


Figure 2: **a)** Conductivity isotherms of  $\text{Li}_4\text{Ti}_5\text{O}_{12}$  showing the real part of the complex conductivity ( $\sigma'$ ) vs. the frequency. From low to high frequencies, the isotherms show electrode polarization (EP), two conductivity plateaus, (1) and (2), followed by a dispersive regime (NCL). Jonscher's power law approximates the dispersive regime well with a dispersion parameter of 0.77. **b)** Isotherms of the imaginary part of the Modulus,  $M''$ , vs. frequency. At its maximum,  $M''$  is proportional to the inverse of the capacitance of the undelaying transport process. Both processes are associated with very similar capacities, *i.e.* only differing by a factor of 2. Arrows at high (2) and low frequencies (1) indicate characteristic peak frequencies. **c)** Change of the DC conductivities and peak frequencies  $M''$  as a function of the inverse temperature. Conductivity and dielectric relaxation are equally activated in the slow diffusion process (1) by  $E_{\text{DC}} = E_{\text{M}} = 0.83$  eV. The fast diffusion process is characterized by an activation energy of  $E_{\text{M}} = 0.48$  eV and  $E_{\text{DC}} = 0.54$  eV. Lines represent fit to the Arrhenius equation. **d)** Bode plot showing the magnitude of the impedance and the phase angle of selected isotherms. At high frequencies, a small "bump" in the phase angle (2) indicates the small plateau seen in (a).

of 0.48 eV was also found by Ren *et al.*<sup>27</sup> for the dielectric relaxation and DFT calculations<sup>28</sup> also identify this to be the energy barrier for a Li-ion to jump from one 8a to another 8a site. On the other hand, Monte carlo simulations indicated that isolated Ti anti-site defects could permit fast local diffusion of Li-ions.<sup>29</sup> Considering the low abundance of anti-site defects, very few charge carriers could participate in such a fast process before being subjected to the energy landscape of the regular crystal structure. Therefore, it is unexpected that such a process could be monitored by <sup>7</sup>Li NMR spectroscopic relaxation measurements, as these techniques are population biased.<sup>30, 31</sup> Surprisingly, the pre-exponential factor of the dielectric relaxation frequency characterizing this fast short-range process is rather low,  $1.7 \cdot 10^{11} \text{ s}^{-1}$ ; 2 orders of magnitude lower than the long-range process. Nevertheless, at ambient temperatures it is much faster due to its low activation energy. To gain further insight into the conduction processes we made use of the Almond and West formalism based on Jonscher's power law, *i.e.* we extracted mean hopping rates of the mobile charge carriers. For the slow conduction process at low frequencies ((1) in Figure 2c) the hopping rates show exactly the same activation energy,  $E_H$ , as the dielectric relaxation,  $E_M$  and the conduction process,  $E_{DC}$  (see Figure 3a). Therefore, the change in conductivity can be perfectly explained by the change of the charge carrier's mobility. The hopping rate characterizing the fast short-range process ((2) in Figure 2c) is thermally activated only by  $E_H = 0.31 \text{ eV}$  while  $E_{DC}$  and  $E_M$  equal 0.54 eV and

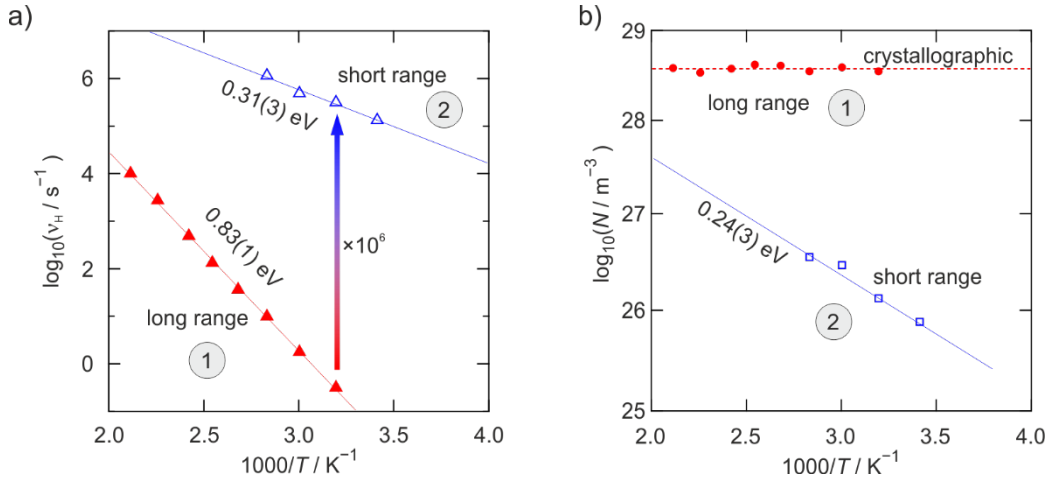


Figure 3: a) The mean hopping rates of the mobile charge carriers, *i.e.* their mobility, are temperature dependent. The associated activation energy for the long-range conduction process is 0.83 eV and reproduces the temperature dependence of the conduction. The activation energy of the hopping in the short-range conduction process is much lower, 0.31 eV. b) The charge carrier density (red circles) involved in the slow long-range process (1) perfectly match the theoretical charge carrier density (dashed line). The number of charge carriers in the short-range conduction process is much lower and temperature dependent. The activation energy associated with the increase of mobile charge carriers is 0.24 eV.

0.48 eV, respectively. Noteworthy is that Fehr *et al.* found the electronic conductivity at elevated temperatures, *i.e.* above 500 K to be characterized by an activation energy of 0.31 eV.

For a comparison of activation energies and pre-exponential factors, see *Table 1*. Considering that the conductivity is proportional to the charge carrier density and their hopping rate,  $\sigma_{DC} \propto N \cdot \nu_H$ , one would expect a similar activation energy for conductivity and the hopping rate, as is the case for the long-range conduction process. However, if the fraction of charge carriers which has access to the fast conduction process increases with temperature, conductivity raises faster than the overall mobility does. Following this line of thought we made use of the Almond-West model and calculated the charge carrier density involved in the conduction processes. Assuming a jump distance equal to the Li-Li nearest neighbour distance of 0.18 nm, a correlation factor and Haven-ratio of unity, and 3D isotropic diffusion, we calculated the charge carrier density for both processes according to:  $N = \frac{k_B \cdot T \cdot \sigma_{DC}}{\langle a \rangle^2 \cdot e^2 \cdot \gamma \cdot \nu_H}$  where  $\langle a \rangle^2$ ,  $e$  and  $\gamma$  are the mean-square displacement, the elementary charge and a correction factor that equals 1/6 and accounting for the Haven-ratio, the correlation factor.<sup>32</sup>  $\nu_H$  denotes the mean hopping rate. Indeed, we found that only a fraction of all  $\text{Li}^+$  ions in  $\text{Li}_4\text{Ti}_5\text{O}_{12}$  have access to this fast conduction process (see Figure 3b). As temperature increases, the conductivity increases with a rate equal to the increase of mobility and charge carriers, *i.e.*  $E_{DC} = E_N + E_\nu$ . For comparison, also the theoretical charge carrier density, derived from the density of  $\text{Li}^+$  ions in the crystal structure, is shown (Figure 3b). The long-range conduction process, however, shows similar activation energies,  $E_{DC} = E_H$  and a constant, temperature independent charge carrier density in the same order as the theoretical one. However, only a fraction of the charge carriers has access to the fast conduction process and this fraction increases with temperature (see Figure 3b).

*Table 1: Activation energies and pre-exponential factors of the Arrhenius equation governing conductivity, dielectric relaxation, hopping rates and charge carrier density.*

Quantity	Long-range (1)	Short-range (2)
$E_{DC} / \text{eV}$	0.83(1)	0.54(1)
$E_M / \text{eV}$	0.84(1)	0.48(1)
$E_H / \text{eV}$	0.83(1)	0.31(3)
$E_N / \text{eV}$	-	0.24(3)
$\log_{10}(\sigma_0 / \text{S cm}^{-1} \text{K})$	4.42(4)	2.5(3)
$\log_{10}(\nu_{0,M} / \text{S cm}^{-1} \text{K})$	13.3(3)	11.0(2)
$\log_{10}(\nu_{0,hop} / \text{S cm}^{-1} \text{K})$	12.9(2)	10.4(5)

We have to note that impedance spectroscopy is as such not sensitive to the nature of the charge carrier. Therefore, the hopping of ions or polarons and even a combination thereof may cause these DC plateaus. This is for example the case in the poor ionic conductor  $\text{Na}_2\text{O}_2$  for which the low overall conductivity at room temperature ( $\sim 10^{-13} \text{ S cm}^{-1}$ ) is caused by ionic and electronic conduction.<sup>33</sup> However, it has to be mentioned that the capacitance at the lowest frequencies is much higher in LTO than in  $\text{Na}_2\text{O}_2$  even at temperatures where to conductivity is similar<sup>34</sup>. Albeit different values for the electronic conductivity in  $\text{Li}_4\text{Ti}_5\text{O}_{12}$  were reported, most of those obtained from pristine samples, lie in the order of  $10^{-13} \text{ S cm}^{-1}$  *i.e.* comparable to the total conductivity at 20 °C. Therefore, it is important to note that at 200 °C the conductivity plateau is terminated due to the blocking electrodes, *i.e.* electrodes blocking ions but not electrons (see Figure 2a). Furthermore, the capacitances found at these frequencies are in the order of  $\mu\text{F}$ , a clear indication for electrode polarisation. Furthermore, the activation energy for the slow process also matches that found by  $^7\text{Li}$  SAE NMR experiments sensitive to self-diffusion of  $^7\text{Li}$ . Clearly, the ionic conductivity is the root cause of the plateau seen at low frequencies.

For the sake of completeness, we also must mention that one may also assume that the high frequency plateau is caused by hopping of polarons in a confined non-percolating space. However, the charge carrier density we extracted seems too high for polaronic conduction. Song *et al.*<sup>35</sup>, performed Hall Effect measurements on in  $\text{Li}_{4-y/3}\text{Ti}_{5-2y/3}\text{Cr}_y\text{O}_{12}$  to determine the charge carrier density  $n_{el}$  and electric mobility  $\mu_{el}$ . While doping of up to  $y = 3$  raised the electronic conductivity up to  $10^{-6} \text{ S cm}^{-1}$ , the charge carrier density remained well below  $10^{12} \text{ m}^{-3}$ . The extremely low electronic conductivity in the undoped sample ( $< 10^{-13} \text{ S cm}^{-1}$ ), however, prevented the quantification of both. The presence of mixed valent  $\text{Ti}^{4+}$  and  $\text{Cr}^{3+}$  in the spinel offers significantly increased electronic conductivity at a low charge carrier density but high mobility. Similarly, a reduction of  $\text{Ti}^{4+}$  to  $\text{Ti}^{3+}$  could give rise to significantly increased the electronic conductivity.<sup>36-38</sup> We performed EPR measurements but found no indication for the presences of  $\text{Ti}^{3+}$  while a strong signal with a g-factor of 2.003 was observed in a sample dried at 300 °C in vacuum for 60 h (see SI Figure S4a). We attribute this signal to single electrons trapped in oxygen vacancies,  $[\text{V}_\text{O}^\cdot]$ , which were generated during the annealing process. The vacant oxygen sites offer a new diffusion pathway for Li in the defective LTO structure.<sup>39</sup>

In any case, the possible Li-diffusion pathways as depicted in Figure 1c, e, f relay on the hopping of lithium through an oxygen-triangle and thus the Li-diffusion is significantly affected by oxygen-vacancies. To gain further insight into the changes in Li-ion dynamics as seen by impedance spectroscopy, we performed  ${}^6\text{Li}$  MAS spectroscopy. While no difference in the overall powder pattern was observed for the samples annealed at 105 °C and 300 °C respectively, the line corresponding to 8a is significantly narrowed (see SI Figure S4b). The narrowing of the line may be attributed to increase Li ion dynamics in the sample which is in line with our hypothesis that a fraction of the Li ions is exposed to localized but fast diffusion pathways. To quantify the exact relaxation rates, which reflect the Li-diffusivity, we performed spin-lattice relaxation rate measurements under MAS conditions at 303 K and spinning speeds of 25 kHz (Figure 4).

The overall magnetization transients were only double exponential at sufficiently large delay times due to the onset of appreciable 16d relaxation. To extract the site-specific relaxation rates, we integrated fractions of the corresponding peaks for every delay time. These delay-time dependent

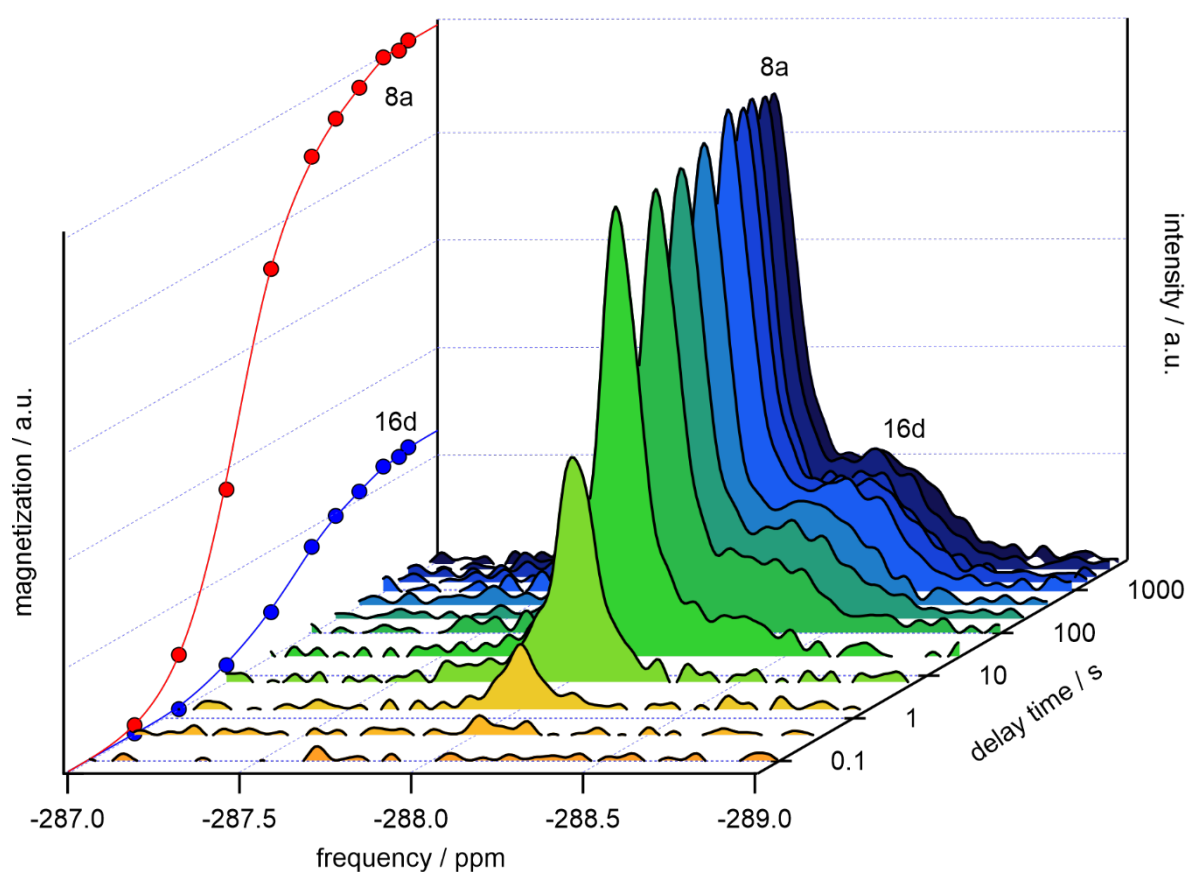


Figure 4:  ${}^6\text{Li}$  MAS NMR spin lattice relaxation magnetization transients and the corresponding spectra of LTO annealed at 300 °C. We recorded the FIDs at 303 K with delay times of up to 4000 s to ensure full relaxation of all  ${}^6\text{Li}$  spins.

integrals were parametrized with single stretched exponentials to yield the site-specific spin lattice relaxation times. The Li-ions residing on the 8a position show a relaxation rate as short as  $T_1(8a) = 10.2(3)$  s while those residing on 16d exhibit a relaxation time of  $T_1(16d) = 33(3)$  s. As only 25% of the Li ions reside on the 16d position and the corresponding low relaxation rate  $R_1 = 1/T_1$ , the overall magnetization transients are almost exclusively governed by the dynamic behaviour of the Li ions residing on 8a. Albeit  ${}^6\text{Li}$  relaxation rates are scarcely measured, and reported, we can, at least qualitatively compare our results with those obtained from  ${}^7\text{Li}$  SLR measurements. Here, especially those reported by Schmidt et al.<sup>3</sup>, using the same spectrometer and sample, reveal that we are indeed facing significantly increased SLR rates in the sample annealed at 300 °C. While they found  $\log_{10}(1/T_1) \approx -1.7$  at 303 K, for  ${}^7\text{Li}$ , we are facing much higher relaxation rates of  $\log_{10}(1/T_1) \approx -1.0$  for  ${}^6\text{Li}$ . This shows significantly increased diffusivity as  $R_1$  of  ${}^6\text{Li}$  is usually much lower than that of  ${}^7\text{Li}$ . Not only is the  ${}^7\text{Li}$  isotope more abundant (~92%) than  ${}^6\text{Li}$  and thus permits more efficient homonuclear dipolar coupling, but it is also characterized by a much stronger quadrupolar momentum sensing and coupling with electric field gradients. Nevertheless, the  ${}^6\text{Li}$  relaxation rate in the sample annealed at 300 °C is much higher than that of  ${}^7\text{Li}$  in the native sample and indicates highly increased diffusivity.

In light of our results, we hypothesize that fast localized Li diffusion in  $\text{Li}_4\text{Ti}_5\text{O}_{12}$  is present even in the pristine material. However, only very few charge carriers have access to these fast conduction pathways as they are associated with slight distortions of the anion-lattice as evoked by oxygen vacancies. This fast diffusion process is characterized by a low activation energy of 0.54 eV but is only accessible by few  $\text{Li}^+$  ions. Another pathway, seldom considered due to the often highly resistant grain boundaries, is a surface conduction mechanism along the grain boundaries.<sup>40</sup> However, the conductivity along grain boundaries, a undoubtedly percolating network, would not result in similar activation energies as deduced from NMR<sup>5</sup> and impedance spectroscopy (this study).

### Conclusion

Revisiting the conduction mechanism in the well-known anode material LTO in its parent state,  $\text{Li}_4\text{Ti}_5\text{O}_{12}$ , revealed the existence of two conduction mechanisms. Annealing experiments in combination with TGA, IR and impedance spectroscopy suggest that both processes are associated

with the bulk of the crystallites. Oxygen vacancies, formed via soft annealing, were identified via EPR while significantly reduced  ${}^6\text{Li}$  relaxation SLR times were detected by NMR spectroscopy. These fast conduction pathways, apparently enhanced by oxygen vacancies, could serve as an efficient doorway for the lithiation of  $\text{Li}_4\text{Ti}_5\text{O}_{12}$  and may explain the fast kinetics in the beginning of lithiation.

## References

1. Zachau-Christiansen, B.; West, K.; Jacobsen, T.; Atlung, S. *Solid State Ionics* **1990**, 40-41, 580-584.
2. Ohzuku, T.; Ueda, A.; Yamamoto, N. *Journal of The Electrochemical Society* **1995**, 142, (5), 1431-1435.
3. Schmidt, W.; Bottke, P.; Sternad, M.; Gollob, P.; Hennige, V.; Wilkening, M. *Chemistry of Materials* **2015**, 27, (5), 1740-1750.
4. Wagemaker, M.; Simon, D. R.; Kelder, E. M.; Schoonman, J.; Ringpfeil, C.; Haake, U.; Lützenkirchen-Hecht, D.; Frahm, R.; Mulder, F. M. *Advanced Materials* **2006**, 18, (23), 3169-3173.
5. Wilkening, M.; Amade, R.; Iwaniak, W.; Heitjans, P. *Physical Chemistry Chemical Physics* **2007**, 9, (10), 1239-1246.
6. Wilkening, M.; Iwaniak, W.; Heine, J.; Epp, V.; Kleinert, A.; Behrens, M.; Nuspl, G.; Bensch, W.; Heitjans, P. *Physical Chemistry Chemical Physics* **2007**, 9, (47), 6199-6202.
7. Schmidt, W.; Wilkening, M. *The Journal of Physical Chemistry C* **2016**, 120, (21), 11372-11381.
8. Dolotko, O.; Senyshyn, A.; Mühlbauer, M. J.; Boysen, H.; Monchak, M.; Ehrenberg, H. *Solid State Sciences* **2014**, 36, 101-106.
9. Pang, W. K.; Peterson, V. K.; Sharma, N.; Shiu, J.-J.; Wu, S.-h. *Chemistry of Materials* **2014**, 26, (7), 2318-2326.
10. Chen, C. H.; Vaughey, J. T.; Jansen, A. N.; Dees, D. W.; Kahaian, A. J.; Goacher, T.; Thackeray, M. M. *Journal of The Electrochemical Society* **2001**, 148, (1), A102-A104.
11. Fehr, K. T.; Holzapfel, M.; Laumann, A.; Schmidbauer, E. *Solid State Ionics* **2010**, 181, (23), 1111-1118.
12. Jonscher, A. K. *Nature* **1977**, 267, 673.
13. Sidebottom, D. L. *Physical Review Letters* **1999**, 83, (5), 983-986.
14. Almond, D. P.; Hunter, C. C.; West, A. R. *Journal of Materials Science* **1984**, 19, (10), 3236-3248.
15. Hairetdinov, E. F.; Uvarov, N. F.; Patel, H. K.; Martin, S. W. *Physical review. B, Condensed matter* **1994**, 50, (18), 13259-13266.



16. Funke, K.; Banhatti, R. D.; Grabowski, P.; Nowinski, J.; Wrobel, W.; Dinnebier, R.; Magdysyuk, O.; Funke, K.; Banhatti, R. D.; Grabowski, P.; Nowinski, J.; Wrobel, W.; Dinnebier, R.; Magdysyuk, O. *Solid State Ionics* **2015**, 271, (Complete), 2-9.
17. Kidner, N. J.; Homrighaus, Z. J.; Ingram, B. J.; Mason, T. O.; Garboczi, E. J. *Journal of Electroceramics* **2005**, 14, (3), 283-291.
18. Kidner, N. J.; Homrighaus, Z. J.; Ingram, B. J.; Mason, T. O.; Garboczi, E. J. *Journal of Electroceramics* **2005**, 14, (3), 293-301.
19. Lunghammer, S.; Ma, Q.; Rettenwander, D.; Hanzu, I.; Tietz, F.; Wilkening, H. M. R. *Chemical Physics Letters* **2018**, 701, 147-150.
20. Irvine, J. T. S.; Sinclair, D. C.; West, A. R. *Advanced Materials* **1990**, 2, (3), 132-138.
21. Breuer, S.; Prutsch, D.; Ma, Q.; Epp, V.; Preishuber-Pflügl, F.; Tietz, F.; Wilkening, M. *Journal of Materials Chemistry A* **2015**, 3, (42), 21343-21350.
22. Wang, H.; Yu, C.; Ganapathy, S.; van Eck, E. R. H.; van Eijck, L.; Wagemaker, M. *Journal of Power Sources* **2019**, 412, 29-36.
23. Hanghofer, I.; Brinek, M.; Eisbacher, S. L.; Bitschnau, B.; Volck, M.; Hennige, V.; Hanzu, I.; Rettenwander, D.; Wilkening, H. M. R. *Physical Chemistry Chemical Physics* **2019**, 21, (16), 8489-8507.
24. Wang, S.; Yan, M.; Li, Y.; Vinado, C.; Yang, J. *Journal of Power Sources* **2018**, 393, 75-82.
25. Wang, Y.; Richards, W. D.; Ong, S. P.; Miara, L. J.; Kim, J. C.; Mo, Y.; Ceder, G. *Nature Materials* **2015**, 14, 1026.
26. Wilkening, M.; Heitjans, P. *ChemPhysChem* **2012**, 13, (1), 53-65.
27. Ren, S.; Liu, J.; Wang, D.; Zhang, J.; Ma, X.; Knapp, M.; Liu, L.; Ehrenberg, H. *Journal of Alloys and Compounds* **2019**, 793, 678-685.
28. Ziebarth, B.; Klinsmann, M.; Eckl, T.; Elsässer, C. *Physical Review B* **2014**, 89, (17), 174301.
29. Heenen, H. H.; Scheurer, C.; Reuter, K. *Nano letters* **2017**, 17, (6), 3884-3888.
30. Verkuijlen, M. H. W.; Ngene, P.; de Kort, D. W.; Barré, C.; Nale, A.; van Eck, E. R. H.; van Benthum, P. J. M.; de Jongh, P. E.; Kentgens, A. P. M. *The Journal of Physical Chemistry C* **2012**, 116, (42), 22169-22178.
31. Breuer, S.; Uitz, M.; Wilkening, H. M. R. *The Journal of Physical Chemistry Letters* **2018**, 9, (8), 2093-2097.
32. Gadermaier, B.; Stanje, B.; Wilkening, A.; Hanzu, I.; Heitjans, P.; Wilkening, H. M. R. *The Journal of Physical Chemistry C* **2019**, 123, (15), 10153-10162.
33. Philipp, M.; Lunghammer, S.; Hanzu, I.; Wilkening, M. *Materials Research Express* **2017**, 4, (7), 075508.
34. Dunst, A.; Sternad, M.; Wilkening, M. *Materials Science and Engineering: B* **2016**, 211, 85-93.

35. Song, H.; Jeong, T.-G.; Yun, S.-W.; Lee, E.-K.; Park, S.-A.; Kim, Y.-T. *Scientific Reports* **2017**, 7, (1), 43335.
36. Pickup, P. G. *Journal of The Electrochemical Society* **1984**, 131, (4), 833.
37. Bhargava, A.; Chen, C. Y.; Dhaka, K.; Yao, Y.; Nelson, A.; Finkelstein, K. D.; Pollock, C. J.; Caspary Toroker, M.; Robinson, R. D. *Chemistry of Materials* **2019**, 31, (11), 4228-4233.
38. Bhargava, A.; Eppstein, R.; Sun, J.; Smeaton, M. A.; Paik, H.; Kourkoutis, L. F.; Schlom, D. G.; Caspary Toroker, M.; Robinson, R. D. *Advanced Materials* **2020**, n/a, (n/a), 2004490.
39. Guo, Q.; Cheng, X.; Shi, Y.; Sheng, Z.; Chang, C. *Journal of Alloys and Compounds* **2017**, 710, 383-392.
40. Kim, S.; Avila-Paredes, H. J.; Wang, S.; Chen, C.-T.; De Souza, R. A.; Martin, M.; Munir, Z. A. *Physical Chemistry Chemical Physics* **2009**, 11, (17), 3035-3038.

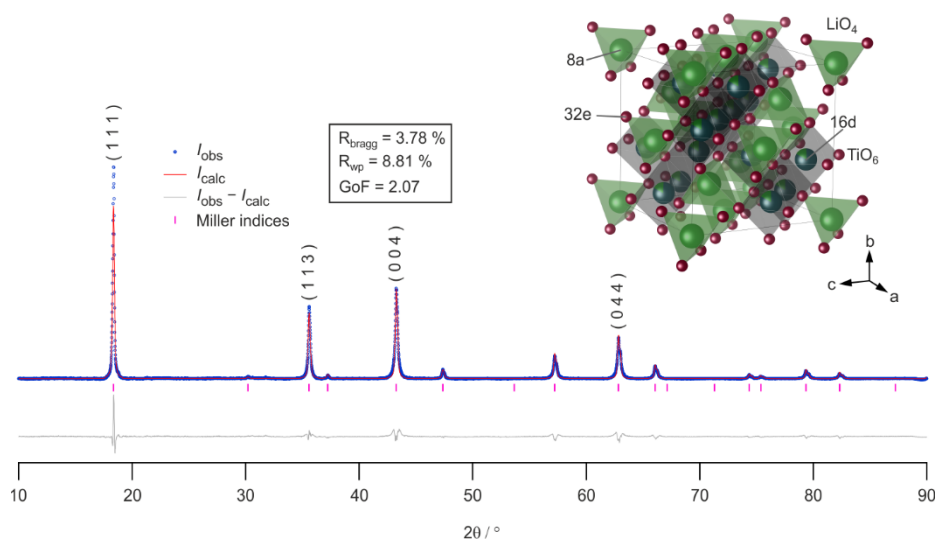


Figure S1: Rietveld refinement of the X-ray powder diffraction (XRPD) pattern of  $\text{Li}_4\text{Ti}_5\text{O}_{12}$ . The observed and calculated intensities as well as their residuals are depicted. Bragg positions are indicated, and the most prominent reflexes are labelled with their corresponding hkl-indices. The inset shows the crystal structure of LTO ( $Fd-3m$ , origin choice 1). The crystallographic positions for O (32e, red), Li (8a, green) and Ti (16d, blue) are labelled. The 16d site is occupied by Ti (5/3) and Li (1/3).

The XRPD pattern of  $\text{Li}_4\text{Ti}_5\text{O}_{12}$  (Figure S1) was analysed via the Rietveld refinement method making use of single crystal reference pattern (ICSD: 160655). By using a single reference pattern, the measured XRPD pattern of our sample was well refined by the Rietveld method after subtraction of the background. A possible impurity phase,  $\beta\text{-Li}_2\text{TiO}_3$  (ICSD: 57017), might be present but is hard to distinguish from LTO by XRPD as its pseudocubic structure yields reflexes almost identical to those of LTO<sup>1</sup>.  $^6\text{Li}$  NMR line shape measurements under MAS conditions at this exact same material did show the presence of a negligible amount of  $\beta\text{-Li}_2\text{TiO}_3$  (<3%) thus we excluded it from our Rietveld refinement.<sup>2</sup> Also others found this phase in small amount as impurity in  $\text{Li}_4\text{Ti}_5\text{O}_{12}$ .<sup>3</sup>

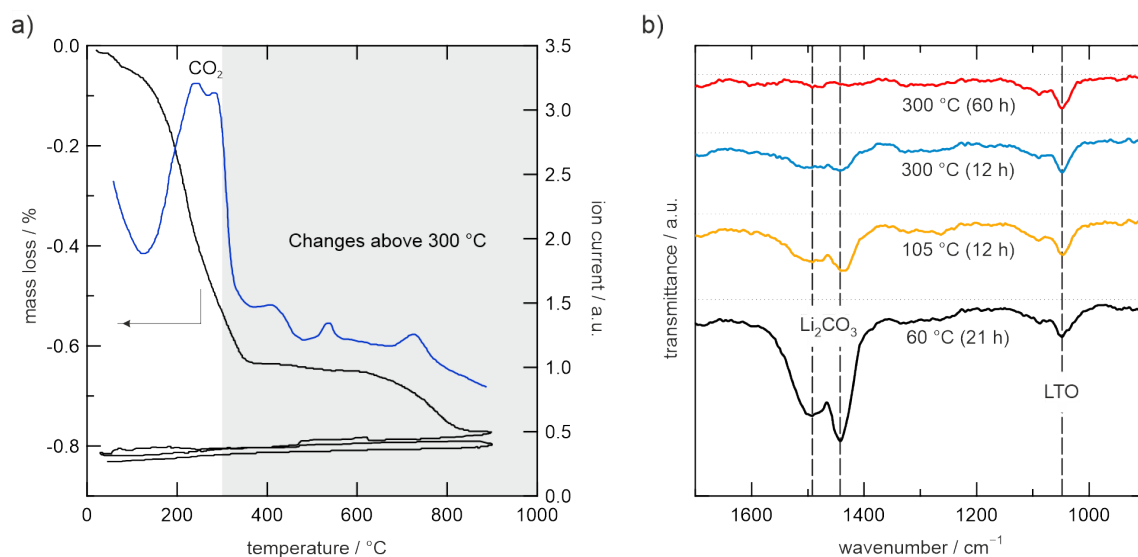


Figure S2: a) Thermogravimetric analysis of  $\text{Li}_4\text{Ti}_5\text{O}_{12}$  after drying at  $60\text{ }^\circ\text{C}$ . The decomposition of surface near  $\text{Li}_2\text{CO}_3$  is monitored via the evolution of  $\text{CO}_2$  (reproduced from ref. <sup>4</sup>) b) FT-IR spectra of  $\text{Li}_4\text{Ti}_5\text{O}_{12}$  dried in vacuum under indicated conditions.

In many active materials as well as solid electrolytes, the exposure to air leads to degradation of the material.<sup>5-7</sup> However, the reaction with moisture and  $\text{CO}_2$  is often limited to the surface of the grains and is, for some materials, reversible. The reaction of LTO with atmospheric  $\text{CO}_2$  leads to the formation of a thin  $\text{Li}_2\text{CO}_3$  coating<sup>8</sup>. To estimate the extent of  $\text{Li}_2\text{CO}_3$  present in our sample a thermogravimetric analysis was performed and the release of  $\text{CO}_2$  was monitored by means of mass spectrometry. After drying the air-exposed sample at  $60\text{ }^\circ\text{C}$  it was heated to  $900\text{ }^\circ\text{C}$  while the release of  $\text{CO}_2$  was monitored (see Figure S2a). While a total mass loss of  $\sim 0.78\%$  is observed at  $900\text{ }^\circ\text{C}$ , most of the mass is lost already at temperatures as low as  $350\text{ }^\circ\text{C}$  ( $\sim 0.63\%$ ). We expect that drying at  $300\text{ }^\circ\text{C}$  in vacuum is even more efficient in removing the sub-nm thick  $\text{Li}_2\text{CO}_3$  layer covering the grains. Indeed, FT-IR spectra clearly show how the  $\text{Li}_2\text{CO}_3$  vanishes with vacuum annealing (see Figure S2b). Importantly, such a layer will foremost influence the long-range ionic conductivity.

To test to which extent the thin  $\text{Li}_2\text{CO}_3$  layer affects conductivity, we monitored the change of pre-exponential factors and activation energies characterizing the conduction processes over many heating and cooling cycles between 20 °C and 200 °C. These changes are shown for a sample previously dried in vacuum at 60 °C (Figure S3a) and 300 °C (Figure S3b), respectively.

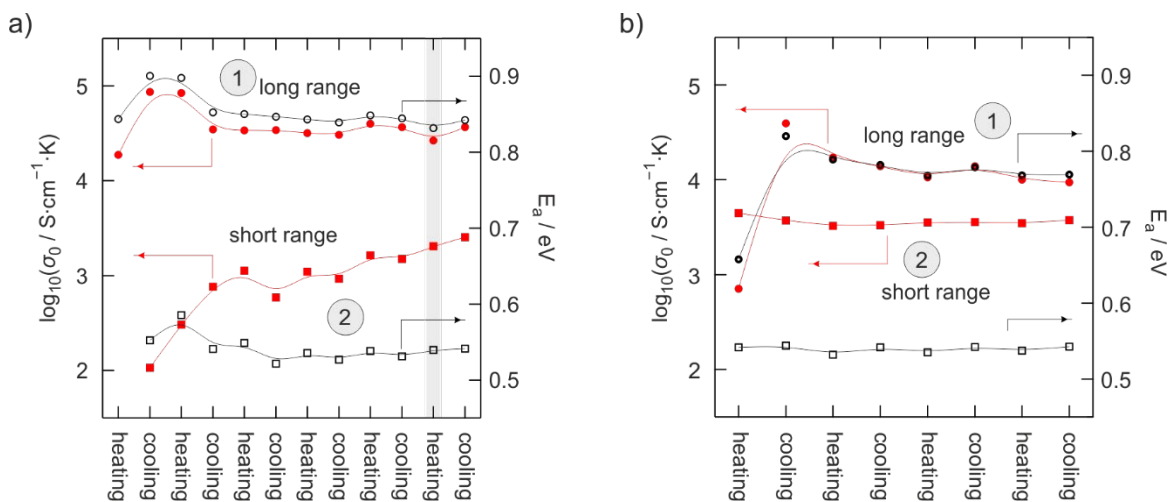


Figure S3: Evolution of the conductivities during consecutive heating and cooling cycles, i.e. soft annealing for a sample dried in vacuum at 60 °C (a) and 300 °C (b) prior to the measurement.

The short-range, high frequency process, shows, even after the first three cycles, a small but steady increase of  $\sigma_0$  whereas  $E_a$  remains constant. Considering that  $\sigma_0$  is a complex quantity<sup>9-11</sup> that also contains an entropy term<sup>12</sup>, the root cause for changes in this quantity remains elusive. However, especially after a few temperature cycles we can exclude the presence of water as the cause and want to remind the reader that the sample is subjected to high temperatures (up to 200 °C) in a reducing atmosphere ( $\text{N}_2$ ). Under these circumstances a slight reduction of the sample might occur accompanied by the generation of oxygen vacancies<sup>13</sup> and thereby increasing the ionic conductivity;<sup>14</sup> reflected in an increase of the corresponding pre-exponential factor. We have to note that the white samples turned slightly gray after drying at 300 °C for 60 h without any bluish colour which would indicate the presence of  $\text{Ti}^{3+}$ . The sample annealed at 300 °C shows a slightly reduced activation energy for long-range conduction but, at the same time, a reduced pre-exponential factor. The short-range process remains unchanged during the heating and cooling cycle with values approached by the sample annealed at 60 °C; if the latter would have been subjected to even more heating and cooling cycles, its short-range process would be characterized by similar values. In other words, the short-range conduction process in the *in-situ* annealed sample approaches that of the *ex-situ* annealed sample.

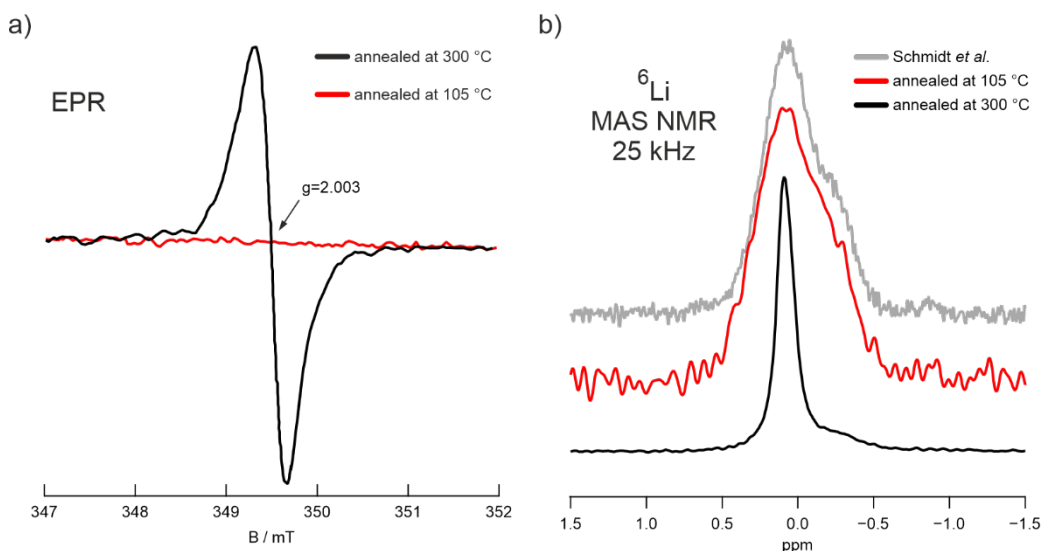


Figure S4: a) EPR spectra of LTO annealed at 105 °C and 300 °C. The signal in the latter is attributed to oxygen vacancies containing a single trapped electron. b) <sup>6</sup>Li MAS NMR spectra of the same samples. The central line is significantly narrowed in the annealed sample.

Trying to find the root cause for the observed changes in conductivity during in-situ annealing we analysed a sample dried in vacuum at 300 °C by electron paramagnetic resonance (EPR) spectroscopy as well as by <sup>6</sup>Li spin-lattice relaxation (SLR) rates under magic angle-spinning (MAS) conditions. Considering the slightly reducing heat treatment, we assumed that reduction of Ti<sup>4+</sup> to Ti<sup>3+</sup>, in minute amounts as well as oxygen vacancies might affect the conductivity. Indeed, we found that in vacuo annealing generates a strong resonance signal with a Landé factor of 2.003 pointing to free electrons that are most likely trapped in oxygen vacancies (see Figure S4a). Most importantly, EPR gave no evidence for Ti<sup>3+</sup>, neither at room temperature, nor at 180 K, which could give rise to polaronic conductivity. However, charge neutrality demands compensation which is usually achieved by the formal reduction of Ti<sup>4+</sup> to Ti<sup>3+</sup> such that  $[\text{Ti}'_{\text{Ti}}] + [\text{V}_{\text{O}}] \rightarrow \text{Nil}$  fulfils electroneutrality.

For comparison, we reproduced the spectrum reported by Schmidt *et al.*<sup>15</sup> obtained under almost exactly the same conditions. The spectrum of Schmidt *et al.* was recorded at a MAS spinning rate of 30 kHz using a recycled delay of 600 s. The spectra of the samples annealed at 105 °C and 300 °C were recorded at a MAS spinning rate of 25 kHz (see Figure S4b). For the sample annealed at 105 °C a recycle delay of 600 s was necessary to ensure complete relaxation. The pattern of the sample annealed at 300 °C, however, gave a fully developed pattern at a recycle delay of only 5 s.

## References

1. Laumann, A.; Boysen, H.; Bremholm, M.; Fehr, K. T.; Hoelzel, M.; Holzapfel, M. *Chemistry of Materials* **2011**, 23, (11), 2753-2759.
2. Schmidt, W.; Wilkening, M. *The Journal of Physical Chemistry C* **2016**, 120, (21), 11372-11381.
3. Becker, D.; Haberkorn, R.; Kickelbick, G. *Inorganics* **2018**, 6, (4), 117.
4. Schmidt, W. Zur Li-Ionendynamik in batterie relevanten Festkörpern: Li(4)Ti(5)O(12) und Li-haltige Granate Graz University of Technology, 2015.
5. Xia, X.; Wang, Z.; Chen, L. *Electrochemistry Communications* **2008**, 10, (10), 1442-1444.
6. Muramatsu, H.; Hayashi, A.; Ohtomo, T.; Hama, S.; Tatsumisago, M. *Solid State Ionics* **2011**, 182, (1), 116-119.
7. Xia, W.; Xu, B.; Duan, H.; Tang, X.; Guo, Y.; Kang, H.; Li, H.; Liu, H. *Journal of the American Ceramic Society* **2017**, 100, (7), 2832-2839.
8. Gao, Y.; Wang, Z.; Chen, L. *Journal of Power Sources* **2014**, 245, 684-690.
9. Gadermaier, B.; Stanje, B.; Wilkening, A.; Hanzu, I.; Heitjans, P.; Wilkening, H. M. R. *The Journal of Physical Chemistry C* **2019**, 123, (15), 10153-10162.
10. Almond, D. P.; West, A. R. *Solid State Ionics* **1983**, 11, (1), 57-64.
11. Hodge, I. M.; Ngai, K. L.; Moynihan, C. T. *Journal of Non-Crystalline Solids* **2005**, 351, (2), 104-115.
12. Almond, D. P.; West, A. R. *Solid State Ionics* **1986**, 18-19, 1105-1109.
13. Kröger, F. A.; Vink, H. J., Relations between the Concentrations of Imperfections in Crystalline Solids. In *Solid State Physics*, Seitz, F.; Turnbull, D., Eds. Academic Press: 1956; Vol. 3, pp 307-435.
14. Pang, W. K.; Peterson, V. K.; Sharma, N.; Shiu, J.-J.; Wu, S.-h. *Chemistry of Materials* **2014**, 26, (7), 2318-2326.
15. Schmidt, W.; Bottke, P.; Sternad, M.; Gollob, P.; Hennige, V.; Wilkening, M. *Chemistry of Materials* **2015**, 27, (5), 1740-1750.





### 3.5. NMR spectroscopic investigations into the Li<sup>+</sup> dynamics of Li<sub>4</sub>C<sub>60</sub>

Lithiated Buckminster fullerene were identified as a new class of fast ion conductor for possible application in all-solid-state batteries. The lithiation of the monomeric C<sub>60</sub> molecules was shown to induced polymerization. In the case of Li<sub>4</sub>C<sub>60</sub>, the resulting monoclinic crystal consists of C<sub>60</sub> molecules that are covalently linked and form a 2D polymer.<sup>98-100</sup> Above and below the covalent bonds between the C<sub>60</sub> units, the Li ions reside in pseudo-tetrahedral and pseudo-octahedral polyhedra.<sup>100</sup>

While the average Li-Li distance in Li<sub>4</sub>C<sub>60</sub> is much larger than the average Li jump-length, the open structure offers many possible metastable interstitial positions via which diffusion could be possible. Nevertheless, the 2D sheet-like polymers could suppress Li diffusion in one dimension and thus impose foremost 2D-diffusion upon the system.

To shed some light on the Li<sup>+</sup> dynamics in Li<sub>4</sub>C<sub>60</sub> we performed a series of <sup>7</sup>Li NMR spectroscopic measurements employing different pulse sequences, that is, different techniques. Static <sup>7</sup>Li line shape measurements revealed a temperature-independent linewidth while spin-alignment echoes indicated the lack of significant electric field gradients in the direct <sup>7</sup>Li-neighborhood. However, classic spin-lattice relaxation rate (SLR) rate measurements,  $R_1$ , revealed a diffusion-induced maximum of the relaxation rates. Additional SLR measurements in the rotating frame of reference,  $R_{1\rho}$ , known to be sensitive to slower diffusion processes<sup>101</sup>, produce a rate peak which seems to characterize a different process as the one seen in  $R_1$  measurements. However, at temperatures higher than the temperature at which the  $R_{1\rho}$  peak is obtained,  $R_{1\rho}$  shows another increase. Given that this increase shows the same activation energy as the  $R_1$  peak, it is likely that the same process is monitored. Additionally, performed spin-spin relaxation rate measurements,  $R_2$ , reveal temperature-independent rates.

Comparing <sup>7</sup>Li NMR  $R_1$  rates measured at different Larmor frequencies by us, and others indicates that the Li<sup>+</sup> dynamics in Li<sub>4</sub>C<sub>60</sub> are governed by low dimensional, correlated and highly localized <sup>7</sup>Li jump processes.

## Draft 2

# NMR spectroscopic investigations into the $\text{Li}^+$ dynamics of $\text{Li}_4\text{C}_{60}$

B. Gadermaier<sup>†</sup> and H. Martin R. Wilkening<sup>†,§</sup>

<sup>†</sup>Institute for Chemistry and Technology of Materials, Christian Doppler Laboratory for Lithium Batteries, Graz University of Technology (NAWI Graz), Stremayrgasse 9, A-8010 Graz, Austria

<sup>§</sup>Alistore – European Research Institute, CNRS FR3104, Hub de l’Energie, Rue Baudelocque, F-80039 Amiens, France

### *Abstract*

Lithiated Buckminster fullerene,  $\text{Li}_4\text{C}_{60}$ , was recently identified by Riccò *et al.*<sup>1</sup> as a potential solid electrolyte due to its extraordinarily high ionic conductivity. However, some doubt was raised about the nature of the high conductivity as Sundqvist *et al.*<sup>3</sup> showed that the electronic (polaronic) conductivity succeeded the ionic conductivity in this material. Here we present our multiple technique NMR-based analysis of  $^7\text{Li}$  dynamics in  $\text{Li}_4\text{C}_{60}$ . Our results point to strictly localized Li hopping which does not necessarily give rise to high long-range ionic conductivity. We hope to stimulate further investigations of conductivity in  $\text{Li}_4\text{C}_{60}$  and raise awareness that spin-lattice relaxation maxima neither require nor necessarily characterize long-range diffusion processes.

KEYWORDS: ionic conductor, high conductivity, NMR relaxation, lower dimensional diffusion

## Introduction

Future technologies such as all-solid-state batteries demand the development of new solid electrolytes with high ionic conductivities. Thus, much effort is dedicated to finding and characterizing new solid electrolytes and many new solid electrolytes with high ionic conductivity have been reported in the last decades in literature. One example of such a rather new material is represented by the lithiated Buckminster fullerenes  $\text{Li}_4\text{C}_{60}$ . Lithiation of the  $\text{C}_{60}$  molecules induces a peculiar polymerization of the otherwise monomeric  $\text{C}_{60}$  balls. Albeit polymerization is also achieved by high intensity illumination<sup>4</sup>, or application of high pressure and temperature<sup>5</sup>, only the reaction with alkali metals yields these potential new “superionic” conductors. Due to their unique electronic properties, the alkali metal, A, derived  $\text{C}_{60}$  polymers  $\text{A}_x\text{C}_{60}$  have been studied extensively. Their properties strongly depend on the ratio alkali metal: $\text{C}_{60}$  as well as on the alkali metal itself. The latter affects the distances between the  $\text{C}_{60}$  balls, *i.e.* the bond length and modifies the electronic properties.<sup>6</sup> The stoichiometric coefficient, x, of  $\text{A}_x\text{C}_{60}$  largely affects the polymerization and dictates the formation of 1D chains<sup>7</sup> or 2D sheets<sup>8</sup>. For example,  $\text{AC}_{60}$  (A= Rb, K) is a 1D polymer with single C-C bonds.<sup>9</sup> If  $\text{C}_{60}$  is doped by four metal atoms,  $\text{A}_4\text{C}_{60}$  (A= Na, Li), the resulting structure is a 2D network of covalently linked  $\text{C}_{60}$  molecules. For  $\text{Li}_4\text{C}_{60}$  this 2D polymer is formed by single covalent C-C bonds in one crystallographic direction and two single C-C bonds in the orthogonal direction (see Figure 1).<sup>8</sup> In these low-level intercalated fullerites, the partial charge transfer<sup>10</sup> from Li to the  $\text{C}_{60}$  molecules induces the formation of a polyanionic 2D sheet structured framework. Many of such layer-structured materials also show (foremost) low-dimensional diffusion; the diffusion is restricted to two dimensions by the layer structure. This is for example the case in layer structured materials such as  $\text{Li}_3\text{N}$ <sup>11</sup>,  $\text{Li}_{0.7}\text{TiS}_2$ <sup>12</sup>,  $\text{Li}_{0.5}[\text{Mg}_{2.5}\text{Li}_{0.5}]\text{Si}_4\text{O}_{10}\text{F}_2$ <sup>13</sup>, and  $\text{RbSn}_2\text{F}_5$ <sup>14</sup>. Restriction of diffusion to two dimensions may significantly increase the diffusion coefficient and result in very high ionic conductivity.

While  $\text{Li}_4\text{C}_{60}$  has been studied by various groups and various techniques, there is still debate about the origin of the high conductivity reported in literature.<sup>15-19</sup> The problem is also aggravated by the fact that various lithiation levels of  $\text{Li}_{4\pm\delta}\text{C}_{60}$  are stable and show considerably differing properties. Particularly, there is some debate about the charge carrier responsible for the high conductivity reported.<sup>3</sup> To study the ionic conductivity in  $\text{Li}_4\text{C}_{60}$  we made use of  $^7\text{Li}$  NMR relaxation measurements which is a rather useful method to study ionic conductivity, especially in samples with mixed ionic-electronic conductivity. This method does not rely on any post-synthesis

preparation, is contact-free and non-destructive. The method is furthermore charge carriers sensitive, even down to the isotope level, *i. e.*  ${}^6\text{Li}$  and  ${}^7\text{Li}$  diffusion may be measured separately. Here we made use of  ${}^7\text{Li}$  NMR spectroscopy to study the Li-diffusion in  $\text{Li}_4\text{C}_{60}$  samples obtained from Riccò *et al.*

### *Experimental*

Here we studied a sample of lithiated buckminsterfullerene a.k.a. bucky-balls with the nominal formula  $\text{Li}_4\text{C}_{60}$  synthesized via the reaction of a stoichiometric amount of lithium azide,  $\text{LiN}_3$ , with  $\text{C}_{60}$ . To protect the sample from atmosphere it was fire sealed under vacuum in a glass ampoule of 5 mm in diameter.

We analysed the sample by solid state NMR spectroscopy using a Bruker AVANCE III spectrometer and a shielded magnet with a magnetic flux density of 7 T (300 MHz  ${}^1\text{H}$ ) corresponding to a  ${}^7\text{Li}$  Larmor frequency of 116 MHz. NMR measurements at temperatures ranging from 393 K to 193 K were performed using a high-temperature ceramic NMR probe-head (Bruker Biospin). We monitored the sample temperature via a T-type thermocouple in close proximity to the sample. A Bruker Variable Temperature unit (BVT3000) adjusted the sample temperature by a stream of temperature-controlled nitrogen. For measurements at temperatures down to 113 K we used an NMR cryoprobe-head (Bruker). Using two Cernox-sensors, the temperature of the sample was monitored and controlled via a LakeShore 331 unit.

We acquired  ${}^7\text{Li}$  NMR spin lattice relaxation (SLR) rates,  $R_1$ , using a saturation-recovery pulse sequence.<sup>20</sup> First, the magnetization of the sample is destroyed by a pulse sequence consisting of ten closely spaced  $\pi/2$  pulses. After variable delay times, a  $\pi/2$  pulse is used as a reading pulse and the following free induction decay (FID) is recorded. Keeping the recycle delay larger than 5 times the relaxation time ensured complete relaxation between every single scan. We accumulated up to 32 scans to increase the signal-to-noise ratio (SNR). Resultant magnetization transients were parameterized using stretched exponential functions to extract the relaxation rates  $R_1$  ( $= 1/T_1$ ).

Relaxation rates in the rotating frame of reference ( $R_{1\rho}$ ) were recorded using the spin-lock pulse sequence.<sup>20-27</sup> The pulse sequence consists of a  $\pi/2$  pulse immediately followed by a locking pulse of variable duration,  $t_{\text{lock}}$ , after which the FID is recorded. We used a locking frequency,  $\omega_1/2\pi$ , of 12.5 kHz. The locking pulse generates a comparatively small magnetic field  $B_1$  and allows observing the SLR in the rotating frame of reference. Within the rotating field of reference, the resonance

frequency  $\omega_0$  (MHz) is formally replaced by the much smaller frequency  $\omega_1$  (kHz). This formal replacement of a frequency in the order of MHz with a frequency in the order of kHz enables the detection of much slower diffusion processes.

The temperature dependent relaxation rates  $R_1$  and  $R_{1\rho}$  pass through a maximum at the temperature where the jump-rate,  $\tau^{-1}$ , is comparable to the respective resonance frequency  $\omega_0$  and  $\omega_1$ . The jump-rate  $\tau^{-1}$  increases with temperature and is well described by the Arrhenius relation:  $\tau^{-1} = \tau_0^{-1} \cdot \exp(\Delta E_a / (k_B \cdot T))$ .  $\Delta E_a$  denotes the activation energy,  $k_B$  the Boltzmann constant and  $T$  the absolute temperature;  $\tau_0^{-1}$  is a pre-exponential factor. With increasing temperature,  $\tau^{-1}$  increases and leads to relaxation maxima in  $R_{1\rho}$  when  $\tau^{-1} \approx \omega_1$  and  $R_1$  when  $\tau^{-1} \approx \omega_0$ . Since  $\omega_1 \ll \omega_0$ , much lower jump rates result in a maximum in  $R_{1\rho}$  and thus much slower diffusion processes are probed.

We recorded transverse relaxation rates ( $R_2$ ) by using a solid-echo two-pulse sequence optimized for spin-3/2 nuclei.<sup>28</sup> The used pulse sequence consists of a  $\pi/2$  ( $90^\circ$ ) pulse followed by a variable delay,  $t_{\text{echo}}$ , before a second pulse ( $64^\circ$ ) is applied and the FID is recorded. Immediately after the  $90^\circ$  pulse, the spins are in phase but rapidly dephase. Different local fields and concomitantly slightly different Larmor frequencies predominantly cause this dephasing. After a defined time,  $t_{\text{echo}}$ , a  $64^\circ$  pulse effectively causes the spins to invert. This inversion leads to a refocusing of the magnetization and gives the solid echo. As the spins refocus, magnetization increases until reaching a maximum, which is followed by a decrease of the magnetization. The decrease of the echo and the respective decay times are parameterized by single exponential functions to extract  $T_2$  times.

To specifically probe electric field-gradients affecting the  $^7\text{Li}$  nuclei we made use of a two-time spin-alignment echo (SAE) technique. We employed the three-pulse sequence introduced by Jeener and Broekaert<sup>29</sup>. The three pulses are separated by a mixing time,  $t_m$ , and an evolution time  $t_p$  in the following order:  $\pi/2$  pulse –  $t_m$  –  $\pi/4$  pulse –  $t_p$  –  $\pi/4$  pulse –  $t_{\text{acq}}$  where  $t_{\text{acq}}$  denotes the acquisition time. We acquired the echo at  $-20^\circ\text{C}$  using a mixing time  $t_m = 40 \mu\text{s}$ , an evolution time,  $t_p = 20 \mu\text{s}$  and an acquisition time  $t_{\text{acq}} = 2048 \mu\text{s}$ . The respective  $^7\text{Li}$  SAE NMR spectrum, obtained by means of Fourier transformation of the magnetization transient, is shown in Figure S1.

## Results and Discussion

The lithiation of  $C_{60}$  to  $Li_4C_{60}$  yields a sheet-like 2D polymeric structure. The crystal structure of  $Li_4C_{60}$  is somewhat subjected to a controversy. Reports of tetragonal<sup>16</sup>, face-centred cubic<sup>30</sup> and monoclinic<sup>8,10</sup> structure have been published. According to Margadonna *et al.*<sup>8</sup>, the crystal structure of 2-dimensional layer-structured  $Li_4C_{60}$  is monoclinic (space group:  $I2/m$ ). The  $C_{60}$  molecules are connected by a single C-C bond along the crystallographic a-axis and two C-C bonds along the crystallographic b-axis forming a 2D network (see Figure 1a). Within this anisotropic network, the Li ions reside on the crystallographic  $4i$  positions (blue and green spheres in Figure 1a). Their position is located slightly off-centred in pseudo-tetrahedral and -octahedral holes. Wågberg *et al.* confirmed by  $^7Li$  MAS NMR measurements that there are at least two Li-position which correlates well with the crystallographic positions in pseudo-tetrahedral and -octahedral vicinities.<sup>31</sup> These Li ions are separated by comparatively large distances of 3.6 Å, 4.5 Å and 5.0 Å (see Figure 1b) and suggest very low  $^7Li$  homonuclear coupling. These distances are much larger than those found in other fast ion conductors such as  $Li_6PS_5Cl$  (2.3 Å)<sup>32</sup>, LLZO (2 Å)<sup>33</sup>,  $\beta$ - $Li_3PS_4$  (2.5 Å)<sup>34</sup>. Nevertheless, assuming nearest-neighbour jumps, a possible Li-diffusion pathway could lead along a 2D-plane. This plane is indicated in Figure 1b and consists of Li positions separated by distance between 3.6 Å and 5 Å. Such large distances are unlikely overcome by a single jump process but exchange between the positions might be mediated via metastable interstitial sites. Albeit

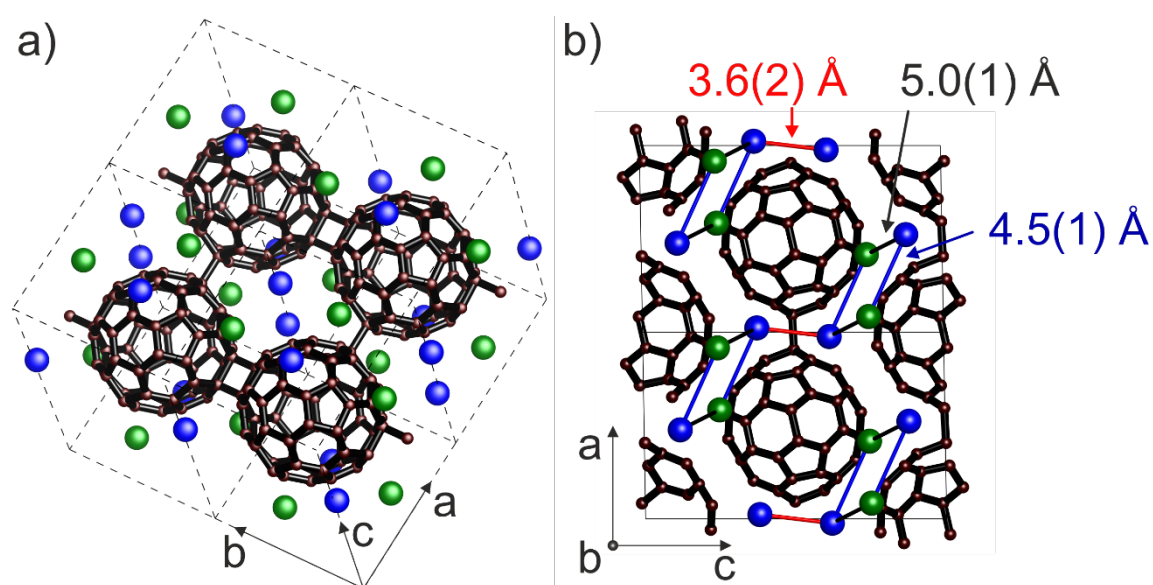


Figure 1: a) Crystal structure of 2D polymerized  $Li_4C_{60}$  (space group:  $I2/m$ ). The lithium ions (blue and green) reside on two different positions with the Wyckoff position,  $4i$ , whereas the carbon atoms of the  $C_{60}$ -fullerene reside on  $8j$ ; the  $C_{60}$ -fullerene are centered at  $2a$ . b) View along the b-axis. The nearest neighbor Li-Li distances are indicated.

speculative, comparison with the very similar structure of  $\text{Li}_{12}\text{C}_{60}$  ( $P2_1/n$ )<sup>35</sup> highlights the 4e position as possible metastable sites in  $\text{Li}_4\text{C}_{60}$  via which diffusion may occur.

A first glance at the Li-ion dynamics in  $\text{Li}_4\text{C}_{60}$  is given by the NMR spectra recorded at temperatures ranging from 115 K to 393 K (Figure 2). The patterns show single central transition lines and are rather featureless; no quadrupolar satellites are present. Considering that Cattaneo *et al.* reported that the quadrupolar coupling constant of  $^7\text{Li}$  in  $\text{Li}_4\text{C}_{60}$  is in the order of 80-200 kHz<sup>36</sup>, non-vanishing electric field gradients (EFGs) are expected to modulate these spectra. The absence of quadrupolar satellites, however, indicates that the electric field gradients (EFGs) are either vanishingly small or not present at all. To specifically probe EFGs, we performed  $^7\text{Li}$  SAE NMR measurements at 253 K. The resultant spectrum lacks the undistinguishably footprint of EFG and indicates that these are negligibly small (see Figure 2a).

The linewidth of the central line, FWHM, remains constant over the whole temperature range. Usually, the temperature-dependent linewidth is large at low temperature (i) and decreases with raising temperature (ii) until reaching a constant linewidth (iii). These three regions referred to as

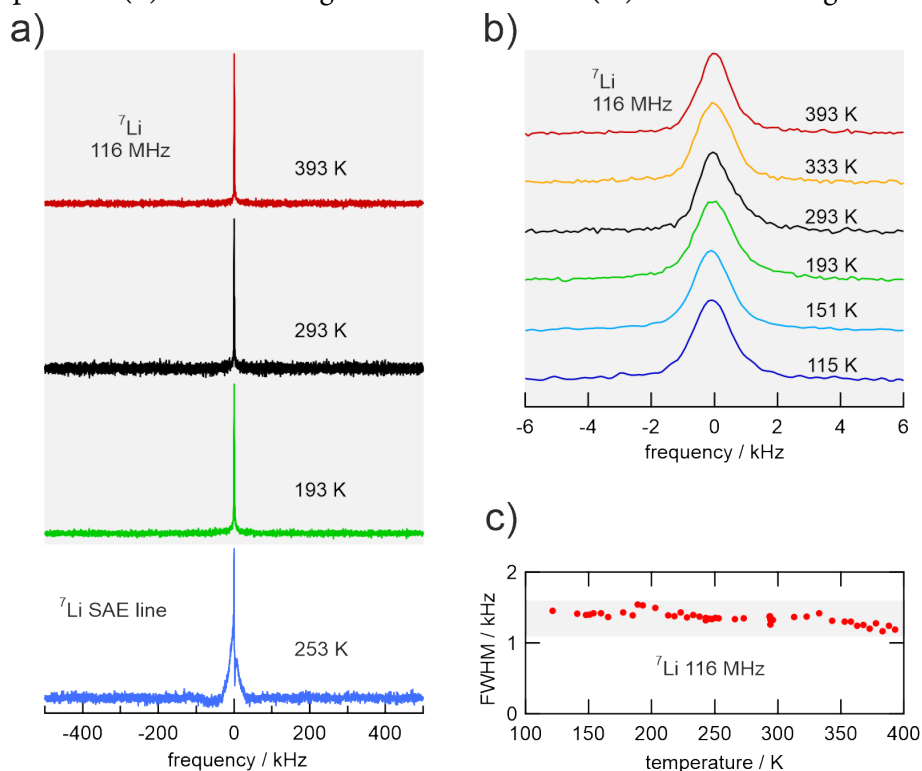


Figure 2: (a)  $^7\text{Li}$  NMR spectra of  $\text{Li}_4\text{C}_{60}$  recorded in single pulse experiments at 116 MHz (gray area) and the  $^7\text{Li}$  SAE spectrum (bottom); temperatures are indicated. The spectra consist of only one single transition line. (b) Close-up of the central transition lines at indicated temperatures. (c) Linewidth (FWHM) of the central transition line as a function of temperature; the linewidth remains almost constant.

rigid lattice linewidth (i), motional narrowing (ii) and extreme line narrowing (iii) are located at low temperatures, intermediate temperatures, and high temperatures, respectively. At very low temperatures the ions are immobile and only sense the local magnetic and electric field at their specific site. These fields also contain the contribution of dipolar coupling and modulate the resonance frequency of the nuclei. A distribution of local fields results in a distribution of resonance frequencies and thus a broad linewidth. Raising the temperatures increases the jump-rate of the mobile ions. These mobile ions jump from site to site and are exposed to different local fields. If the jump-rate is high enough, the ions will no longer sense their local field but an averaged field. This effect sets in when the jump rate is in the order of the rigid lattice linewidth and effectively narrows the linewidth; thus, motional narrowing. Even higher jump rates will narrow the line until the local fields are completely averaged and the linewidth remains constant even if temperature increases further. In this extreme line narrowing regime, the remaining linewidth is foremost determined by the inhomogeneity of the magnetic field of the magnet. The temperature independent  ${}^7\text{Li}$  linewidth shown by  $\text{Li}_4\text{C}_{60}$  might be explained by the following argumentation. Usually, homonuclear dipolar coupling is one of the major factors influencing the linewidth. Very similar local fields, that is (homonuclear) dipolar coupling is negligible, result in a very narrow line. Some models use this correlation to extract jump-rates and activation energies from the motional narrowing.<sup>37-39</sup> However, dipolar coupling is proportional to  $1/r^3$  where  $r$  is the distance between two adjacent  ${}^7\text{Li}$  nuclei. Recalling that the shortest Li-Li distance in the  $\text{Li}_4\text{C}_{60}$  structure as proposed by Margadonna *et al.*<sup>8</sup> is 3.6 Å, a very weak heteronuclear coupling is expected and in line with our observations. As dipolar coupling effects are insignificant, we can only extract little information about  $\text{Li}^+$  dynamics in  $\text{Li}_4\text{C}_{60}$  from the linewidths.

To gain further insight into  $\text{Li}^+$  dynamics we performed  ${}^7\text{Li}$  NMR spin-lattice relaxation (SLR) rate measurements in a temperature dependent manner. The relaxation rates,  $R_1$ , recorded at a  ${}^7\text{Li}$  resonance frequency of 116 MHz are shown in Figure 2a. We kept the temperature restricted to  $T < 400$  K to prevent decomposition of the 2D fullerene network.<sup>1, 40, 41</sup> The relaxation rates show a typical increase with temperature. At low temperatures, the relaxation rates are low,  $R_1 < 0.1$ , but steeply increase between 165 K and 193 K. According to Arčon *et al.*<sup>41</sup> the  $\text{Li}^+$  ions are frozen below 200 K (grey region in Figure 3a and b). Above 200 K, two rate maxima emerge. The first maximum is located at 255 K but is only visible as a shoulder of the second maximum located at 378 K. To gain information about the  $\text{Li}^+$  dynamics from the rate peaks it is important to note that the



motional correlation time  $\tau_c$  is related to  $\omega_0$ . At the rate maxima the condition  $\omega_0\tau_c \approx 0.7$  is fulfilled.<sup>42</sup> For diffusion induced  $R_1$  maxima, the motional correlation rate  $1/\tau_c$  is identical, within a factor of two, with the  $\text{Li}^+$  jump rate  $1/\tau$ .<sup>43</sup>

Relaxation rate-peaks were extracted by fitting a sum of two BPP-relaxation processes. In the simplest case, the relaxation peaks can be approximated by a Lorentzian-shaped spectral density function  $J(\omega_0, T) \propto \tau_c / (1 + (\omega_0\tau_c)^\beta)$  which is proportional to  $R_1$ . The spectral density function  $J(\omega_0, T)$  is the Fourier transform of the underlying microscopic motional correlation function  $G(t')$ .<sup>20</sup> With these BPP-type<sup>42</sup> fits, we separated the two rate peaks into the individual processes and obtained activation energies and symmetry parameters,  $\beta$  (Figure 3a).

The symmetry parameter  $\beta$  is affected by many factors such as correlated motion, motion in lower dimensions and disorder. For isotropic 3D diffusion the rate peaks are symmetric and  $\beta = 2$ . The first rate-peak, however, with its maximum located at 255 K is slightly asymmetric and fitting yields an asymmetry-parameter of 1.7. The activation energy of asymmetric peaks is slightly different for the high-T and low-T flank and is related to the symmetry-parameter by  $E_{a,LT} = (\beta - 1)E_{a,HT}$ . Therefore, the activation energy of this peak is 0.14 eV at the high-T flank but 0.1 eV at the low-T flank. The second process with its maximum located at 378 K is characterized by an activation energy of 0.3 eV and is symmetric in shape. We first compare this rate peak located at 378 K with results obtained by others. Riccò *et al.* measured  $^7\text{Li}$  SLR rates in  $\text{Li}_4\text{C}_{60}$  at magnets with nominal fields of 2 T and 5 T corresponding to resonance frequencies of 33 MHz and 83 MHz.<sup>1</sup> We digitized their data and show it along with our results in Figure 3b. All three datasets show the same symmetric peak. The maxima of the peaks shift to lower temperatures with decreasing  $^7\text{Li}$  Larmor frequencies, *i.e.*, decreasing external magnetic fields. This is well in line with that fact that a maximum is located at  $\omega_0\tau_c \approx 0.7$ . This condition is fulfilled at lower temperatures if the  $^7\text{Li}$  Larmor frequency is lower. Before discussing this rate-peak in more detail, we will have a look at the second relaxation peak. As mentioned, this peak shows a maximum located at 255 K and is asymmetric in shape. Maniwa *et al.* reported an  $R_1$  peak, also asymmetric, at circa 227 K at a higher  $^7\text{Li}$  resonance frequency of 155 MHz.<sup>2</sup> Considering that this  $R_1$  peak is just shoulder, that is, the full peak is not accessible, the determination of the peak maximum is not very accurate. However, judging by

activation energy it is likely that they probed the same process as we did in this temperature regime. Interestingly, their rate maximum is slightly higher which could be caused by faster relaxation due to increased coupling of the  ${}^7\text{Li}$  nuclei. Arčon *et al.*<sup>41</sup> reported  ${}^7\text{Li}$  SLR rates measured at a  ${}^7\text{Li}$  resonance frequency of 105 MHz (6.34 T). They found an abrupt change in the  $\text{Li}^+$  dynamics in  $\text{Li}_4\text{C}_{60}$  between 200 K and 220 K, close to the temperature where an  $R_1$  peak was observed by Maniwa *et al.* Above 220 K their magnetization transients of the  ${}^7\text{Li}$  SLR show a single exponential behaviour but below 200 K the transients exhibit a bi-exponential recovery. The magnetization

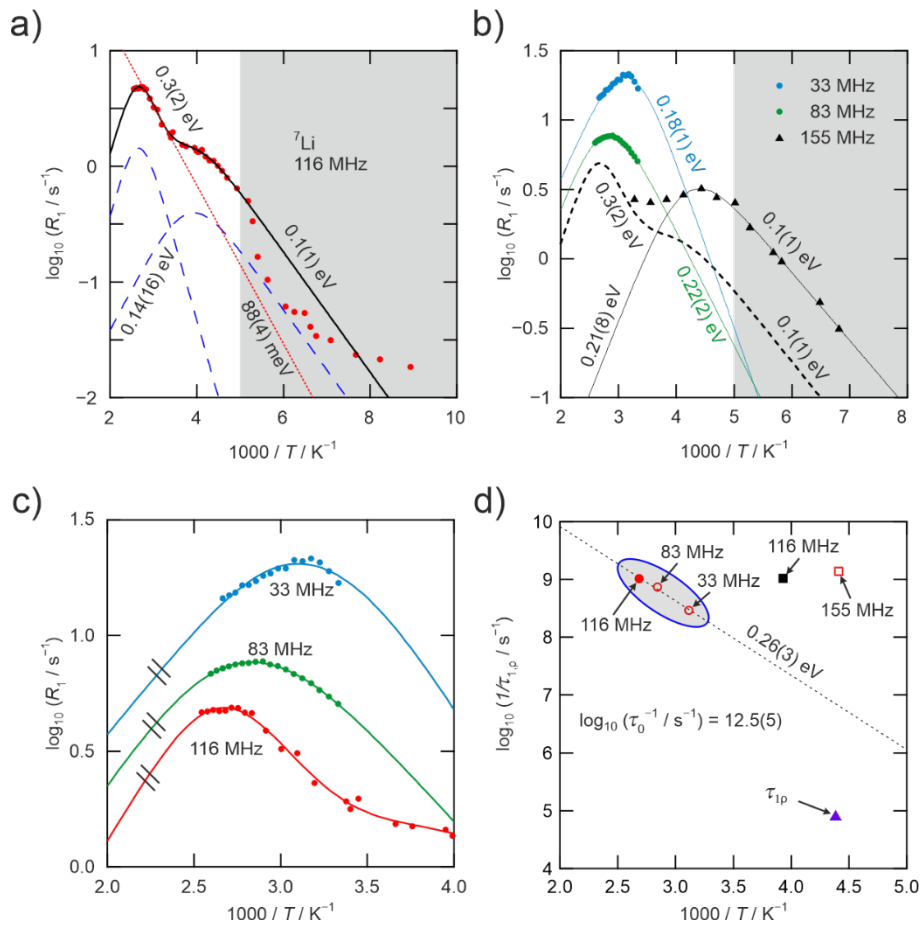


Figure 3: **a)**  ${}^7\text{Li}$  SLR NMR rates recorded at a Larmor frequency of 116 MHz (red dots). The rates  $R_1$  show maxima at 378 K and 255 K and a steep decrease beginning at  $\sim 200$  K (grey region). Above 200 K, the rates are well fitted by two BPP-fits (black line); dashed lines represent these individual fits. Using a straight line as model-free fit of the low-T flank yields considerably lower activation energies (0.088 eV). **b)** Comparison of  $R_1$  rates measured at 116 MHz (dashed line, this study) and  $R_1$  rates measured at 33 MHz, 83 MHz (Ricco *et al.*<sup>1</sup>) and 155 MHz (Maniwa *et al.*<sup>2</sup>); full lines represent BPP-fits with given activation energies. **c)** zoom-in of (b) highlighting the parallelism of the high-T flanks of the BPP-fits indicating lower dimensional diffusion ( $< 3\text{D}$ ). **d)** Rate peaks of  $R_1$  and  $R_{1p}$  measured in this study (filled symbols) and other studies (empty symbols). The high-T  $R_1$  maximum (grey region) observed by us (116 MHz) and others (33 and 83 MHz) for a straight line following the Arrhenius relation expected for  $\tau_c$ . The activation energy of 0.26 eV is comparable to the activation energy deduced from the BPP-fit (0.3 eV). The low-T maxima found at 116 MHz and 155 MHz almost coincide.

transients we obtained showed no discontinuity and followed simple exponential behaviour in the whole temperature range. Evidently there are some changes in the  $\text{Li}^+$  dynamics around 200 K. We observe a steep increase of  $R_1$ , Arçon *et al.* observed a change of relaxation behaviour and Maniwa *et al.* shows a rate peak close to this temperature. Considering that we are comparing different samples, albeit produced by the same method, we assume that these differences might be caused by small variations in stoichiometry and defect concentrations.

Now, coming back to the  $R_1$  peak at higher temperatures which was also observed by Riccò *et al.*<sup>1</sup>. As mentioned above, this peak is symmetric in shape and this is usually associated with 3D isotropic motion in the framework of the BPP-relaxation model. In Figure 3c we show a close-up of the  $R_1$  peaks along with the BPP-fits. Now, for 3D isotropic motion, high- $T$  flanks would coincide at high temperatures. However, the high- $T$  flanks do not coincide but run in parallel which indicates that the  $\text{Li}^+$  motion is not anisotropic but limited to less than three dimensions. Lower dimensional diffusion, however, should yield asymmetric rate peaks with  $\beta < 2$ , which is not the case. This apparent discrepancy is resolved if the  $\text{Li}^+$  motion is correlated. Correlated motion decreases only the slope of the low- $T$  flank, whereas lower dimension diffusion decreases the slope of the high- $T$  flank. Thus, ionic diffusion restrained to less than three dimensions and influenced by correlation will yield  $R_1$  NMR peaks resembling those of 3D anisotropic diffusion processes, *i.e.*, symmetric rate-peaks.<sup>44</sup> Only by assessing the same diffusion process by means of SLR rate measurements at different Larmor frequencies reveals the subtle difference indicating low dimensional diffusion in  $\text{Li}_4\text{C}_{60}$ .

We extracted the temperatures and relaxation rates at the  $R_1$  and  $R_{1p}$  maxima and show them in Figure 3d. The  $R_1$  maxima at 378 K and those reported by Riccò *et al.* form a straight line in the Arrhenius representation indicating that the same diffusion process is probed. The activation energy of this process is 0.26 eV and similar to the activation energy we obtained by fitting the high- $T$ , symmetric rate peak (0.3 eV). Intriguingly, the  $R_1$  peak reported by Maniwa *et al.* and the  $R_{1p}$  peak are located at almost identical temperatures (227 K and 228 K, respectively).

To further clarify the puzzling  $\text{Li}^+$  dynamics in  $\text{Li}_4\text{C}_{60}$  we measured  $^7\text{Li}$  relaxation rates in the rotating frame of reference ( $R_{1\rho}$ ) and transversal relaxation rates ( $R_2$ ). We obtained  $R_{1\rho}$  relaxation rates employing a locking frequency of 12.5 kHz.  $R_{1\rho}$  shows a minimum around 260 K (see Figure 4a).

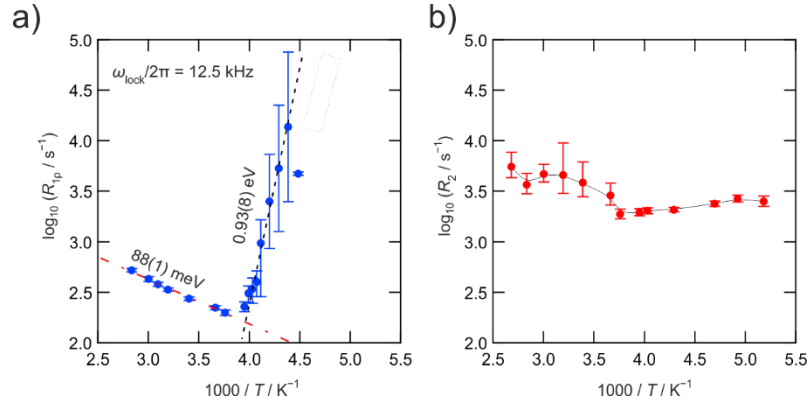


Figure 4: a)  ${}^7\text{Li}$  SLR relaxation rates in the rotating frame of reference ( $R_{1p}$ ) obtained using a locking frequency of  $\omega/2\pi = 12.5 \text{ kHz}$ . The dashed and dash-dotted lines are Arrhenius fits to the data points; activation energies are shown. b) Transverse relaxation rates ( $R_2$ ) of  ${}^7\text{Li}$  extracted from solid-echo transients.  $R_2$  rates slightly increase above 260 K; the black line is a guide to the eye. Error bars represent single standard deviations.

At higher temperatures, the rates increase linearly with a small activation energy of 0.088 eV. Note that this activation energy is identical with the activation energy found for the low- $T$  flank of the maximum almost equal to that of the low- $T$  flank of the rate peak at lower temperatures (see Figure 3a).

At lower temperatures, the relaxation rates steeply increase with an activation energy of almost 1 eV until reaching a maximum at 228 K. Between 243 K and 228 K the standard deviations of  $R_{1p}$  increase until the rates peak. The magnetization transients in this temperature range can be parameterized equally well using single- or double-exponential functions.  $R_{1p}$  rates are usually sensitive to slower diffusion processes compared to  $R_1$  rates since  $R_{1p}$  shows a maximum if the jump rate is in the order of the locking frequency. For 3D uncorrelated diffusion, however, the peak in  $R_{1p}$  should be located at an extension of the high temperature flank of the  $R_1$  peak. If we look at Figure 3a, we see that the  $R_1$  peak at high temperatures, if a straight line fits its low-temperature flank, yields an activation energy of 0.088 eV. This is exactly the same activation energy seen in  $R_{1p}$  above 250 K. Interestingly, also the minimum in  $R_{1p}$  coincides with the onset of the second rate peak in  $R_1$ . Therefore, in this temperature range  $R_1$  and  $R_{1p}$  measurements probe the same diffusion process. Restricted by the thermal stability of the sample, we only have access to the low temperature flank of this peak in  $R_{1p}$ .

The transversal relaxation rates ( $R_2$ ) do not significantly change within the investigated temperature regime.  $R_2$  usually decreases in ionic conductors as temperature increases. With increasing temperature, the jump rates increase, and the ions screen a larger ensemble of

inequivalent magnetic sites.  $R_2$  is expected to decrease with increasing temperature and should, at temperatures where  $\omega_0\tau_c \ll 1$  holds, coincide with the high-T flank of  $R_1$ .<sup>45</sup> However, here  $R_2$  remains almost constant over a large temperature range (193 K – 373 K). A constant  $R_2$  value might be expected for a sample with magnetically equivalent Li positions. We must stress that constant  $R_2$  values are well in line with the constant linewidth (Figure 3c bottom). Nevertheless, the peculiar behaviour between 200 K and 260 K seen in our measurements are currently not fully understood. These phenomena might be related to changes in correlation or ionic motion, changes in the dynamics of the anion framework and are linked to the diffusive properties of  $\text{Li}^+$  in  $\text{Li}_4\text{C}_{60}$ . For the sake of completeness, the Korringa relation<sup>46</sup> in the independent electron limit, which states that  $T_1 \cdot T = \text{const}$ , is not fulfilled. Thus, the observations are not caused by coupling of the  $^7\text{Li}$  nuclear spins to electrons (spin-orbit coupling).

### Conclusion

We analysed  $\text{Li}^+$  motion in  $\text{Li}_4\text{C}_{60}$  by means of various  $^7\text{Li}$  NMR measurements covering a broad dynamic range. While SLR rates,  $R_1$ , show a diffusion induced maximum, the linewidth and the transversal relaxation rates,  $R_2$ , do not indicate significant long-range diffusion.  $^7\text{Li}$  NMR  $R_1$  rates measured at different Larmor frequencies, by us and others, do not coincide at high temperatures although the rate peaks are highly symmetric. Low dimensional, correlated and highly localized  $^7\text{Li}$  jump processes perfectly explain our findings. As the reports on  $\text{Li}^+$  dynamics in  $\text{Li}_4\text{C}_{60}$  are quite differing, we have to assume that the route of preparation has a large influence on the final product. Apart from obvious defects caused by deviations from stoichiometry, also defects in the 2D polymeric network might have a large influence on the local  $\text{Li}^+$  dynamics probed by NMR spectroscopic techniques. Considering the lack of motional narrowing and the comparatively broad line, even at elevated temperatures, combined with the relatively low activation energies, we consider the Li ion motion in  $\text{Li}_4\text{C}_{60}$  to be strictly localized. Such localized jump processes are sufficient to produce a peak in  $^7\text{Li}$  NMR SLR rates.<sup>32</sup>

### References

1. Ricco, M.; Belli, M.; Mazzani, M.; Pontiroli, D.; Quintavalle, D.; Janossy, A.; Csanyi, G. *Phys Rev Lett* **2009**, 102, (14), 145901.

2. Maniwa, Y.; Ikejiri, H.; Tou, H.; Yasukawa, M.; Yamanaka, S. *Synthetic Metals* **2001**, 121, (1), 1105-1106.
3. Bertil, S.; Ove, A.; Chen, G.; Bingbing, L.; Bounphanh, T.; Junchun, Y.; Mingguang, Y. *New Journal of Physics* **2015**, 17, (2), 023010.
4. Rao, A. M.; Zhou, P.; Wang, K.-A.; Hager, G. T.; Holden, J. M.; Wang, Y.; Lee, W.-T.; Bi, X.-X.; Eklund, P. C.; Cornett, D. S.; Duncan, M. A.; Amster, I. J. *Science* **1993**, 259, (5097), 955-957.
5. Núñez-Regueiro, M.; Marques, L.; Hodeau, J. L.; Béthoux, O.; Perroux, M. *Physical Review Letters* **1995**, 74, (2), 278-281.
6. Sundqvist, B.; Wågberg, T.; Yao, M. *Diamond and Related Materials* **2011**, 20, (4), 600-603.
7. Poloni, R.; Miguel, A. S.; Fernandez-Serra, M. V. *Journal of Physics: Condensed Matter* **2012**, 24, (9), 095501.
8. Margadonna, S.; Pontiroli, D.; Belli, M.; Shiroka, T.; Riccò, M.; Brunelli, M. *Journal of the American Chemical Society* **2004**, 126, (46), 15032-15033.
9. Röding, R.; Stenmark, P.; Wågberg, T.; Johnels, D.; Sundqvist, B. *Fullerenes, Nanotubes and Carbon Nanostructures* **2005**, 12, (1-2), 319-325.
10. Rols, S.; Pontiroli, D.; Cavallari, C.; Gaboardi, M.; Aramini, M.; Richard, D.; Johnson, M. R.; Zanotti, J. M.; Suard, E.; Maccarini, M.; Riccò, M. *Physical Review B* **2015**, 92, (1), 014305.
11. Alpen, U. v. *Journal of Solid State Chemistry* **1979**, 29, (3), 379-392.
12. Wilkening, M.; Heitjans, P. *Physical Review B* **2008**, 77, (2), 024311.
13. Hiebl, C.; Loch, P.; Brinek, M.; Gombotz, M.; Gadermaier, B.; Heitjans, P.; Breu, J.; Wilkening, H. M. R. *Chemistry of Materials* **2020**, 32, (17), 7445-7457.
14. Gombotz, M.; Lunghammer, S.; Breuer, S.; Hanzu, I.; Preishuber-Pflügl, F.; Wilkening, H. M. R. *Physical Chemistry Chemical Physics* **2019**, 21, (4), 1872-1883.
15. Yasukawa, M.; Yamanaka, S. *Chemical Physics Letters* **2001**, 341, (5), 467-475.
16. Wågberg, T.; Stenmark, P.; Sundqvist, B. *Journal of Physics and Chemistry of Solids* **2004**, 65, (2), 317-320.
17. Riccò, M.; Belli, M.; Pontiroli, D.; Mazzani, M.; Shiroka, T.; Arçon, D.; Zorko, A.; Margadonna, S.; Ruani, G. *Physical Review B* **2007**, 75, (8), 081401.
18. Sundqvist, B.; Yao, M.; Wågberg, T. *High Pressure Research* **2008**, 28, (4), 597-600.
19. Yao, M.; Pischedda, V.; Wågberg, T.; Sundqvist, B.; Floch, S. L.; Miguel, A. S. *Chemical Physics Letters* **2010**, 489, (1), 64-68.
20. Uitz, M.; Epp, V.; Bottke, P.; Wilkening, M. *Journal of Electroceramics* **2017**.
21. Ailion, D.; Slichter, C. P. *Physical Review Letters* **1964**, 12, (7), 168-171.

22. Ailion, D. C.; Slichter, C. P. *Physical Review* **1965**, 137, (1A), A235-A245.
23. Slichter, C. P.; Ailion, D. *Physical Review* **1964**, 135, (4A), A1099-A1110.
24. Slichter, C. P.; Holton, W. C. *Physical Review* **1961**, 122, (6), 1701-1708.
25. Look, D. C.; Lowe, I. J. *The Journal of Chemical Physics* **1966**, 44, (8), 2995-3000.
26. Redfield, A. G. *Physical Review* **1955**, 98, (6), 1787-1809.
27. Anderson, A. G.; Hartmann, S. R. *Physical Review* **1962**, 128, (5), 2023-2041.
28. Langer, J.; Epp, V.; Heitjans, P.; Mautner, F. A.; Wilkening, M. *Physical Review B* **2013**, 88, (9), 094304.
29. Jeener, J.; Broekaert, P. *Physical Review* **1967**, 157, (2), 232-240.
30. Imaeda, K.; Yakushi, K.; Inokuchi, H. *Fullerene Science and Technology* **1995**, 3, (5), 545-552.
31. Wågberg, T.; Johnels, D. *Journal of Physics and Chemistry of Solids* **2006**, 67, (5), 1091-1094.
32. Hanghofer, I.; Brinek, M.; Eisbacher, S. L.; Bitschnau, B.; Volck, M.; Hennige, V.; Hanzu, I.; Rettenwander, D.; Wilkening, H. M. R. *Physical Chemistry Chemical Physics* **2019**, 21, (16), 8489-8507.
33. Buschmann, H.; Dölle, J.; Berendts, S.; Kuhn, A.; Bottke, P.; Wilkening, M.; Heitjans, P.; Senyshyn, A.; Ehrenberg, H.; Lotnyk, A.; Duppel, V.; Kienle, L.; Janek, J. *Physical Chemistry Chemical Physics* **2011**, 13, (43), 19378-19392.
34. Prutsch, D.; Gadermaier, B.; Brandstätter, H.; Pregartner, V.; Stanje, B.; Wohlmuth, D.; Epp, V.; Rettenwander, D.; Hanzu, I.; Wilkening, H. M. R. *Chemistry of Materials* **2018**, 30, (21), 7575-7586.
35. Giglio, F.; Pontiroli, D.; Gaboardi, M.; Aramini, M.; Cavallari, C.; Brunelli, M.; Galinetto, P.; Milanese, C.; Riccò, M. *Chemical Physics Letters* **2014**, 609, 155-160.
36. Cattaneo, A. S.; Dall'Asta, V.; Pontiroli, D.; Riccò, M.; Magnani, G.; Milanese, C.; Tealdi, C.; Quartarone, E.; Mustarelli, P. *Carbon* **2016**, 100, 196-200.
37. Hendrickson, J. R.; Bray, P. J. *Journal of Magnetic Resonance (1969)* **1973**, 9, (3), 341-357.
38. Waugh, J. S.; Fedin, E. I. *Sov. Phys. Solid State* **1963**, 4, (8), 1633-1636.
39. Abragam, A., *The principles of nuclear magnetism*. Oxford university press: 1961.
40. Quintavalle, D.; Márkus, B. G.; Jánossy, A.; Simon, F.; Klupp, G.; Györi, M. A.; Kamarás, K.; Magnani, G.; Pontiroli, D.; Riccò, M. *Physical Review B* **2016**, 93, (20), 205103.
41. Arčon, D.; Zorko, A.; Mazzani, M.; Belli, M.; Pontiroli, D.; Riccò, M.; Margadonna, S. *New Journal of Physics* **2008**, 10, (3), 033021.
42. Bloembergen, N.; Purcell, E. M.; Pound, R. V. *Physical Review* **1948**, 73, (7), 679-712.
43. Wilkening, M.; Epp, V.; Feldhoff, A.; Heitjans, P. *The Journal of Physical Chemistry C* **2008**, 112, (25), 9291-9300.

44. Wilkening, M.; Heitjans, P. *ChemPhysChem* **2012**, 13, (1), 53-65.
45. Wilkening, M.; Heitjans, P. *Defect Diffus. Forum* **2005**, 237-240, 1182-1187.
46. Clausen, D.; Burmester, I.; Heitjans, P.; Schirmer, A. *Solid State Ionics* **1994**, 70-71, 482-487.





### 3.6. Nanostructured M13 bio templated amorphous $\text{FePO}_4$ as green cathode for Li-ion batteries

The electrochemical performance of an electrodes in a Li ion battery depends on many factors. The contact area between the electrolyte and the active material as well as the active materials electron conducting connection to the current collector are such factors. Optimized active material are thus often nanosized and coated by a thin carbon layer to promote efficient electron transport. However, also disorder or even the complete lack of long-range order, as in an amorphous system, may influence these factors.

Here we modified the filamentous bacteriophage M13 in a way to use it as a template for the synthesis of amorphous  $\text{FePO}_4$  nanowires. These nanowires are obtained from the liquid phase by precipitation and can be used directly in Li ion batteries after drying. Residual water in the material is stable during electrochemical cycling and modulates the redox potential by decreasing the inductive effect of the  $\text{PO}_4$  group.

Chemical lithiation of the amorphous educt produces a metastable material with elevated ionic conductivity. This amorphous  $\text{LiFePO}_4$  exhibits a lower activation energy than its crystalline counterpart and seems to allow  $\text{Li}^+$  ions to diffuse in three dimensions; crystalline  $\text{LiFePO}_4$  is reported to be a 1D ion conductor.

## Draft 3

# Nanostructured M13 bio templated amorphous FePO<sub>4</sub> as green cathode for Li-ion batteries

B. Gadermaier<sup>1</sup>, I. Hanzu<sup>1,2</sup> and H.M.R. Wilkening<sup>1,2</sup>

<sup>1</sup>Institute for Chemistry and Technology of Materials, Christian Doppler Laboratory for Lithium Batteries,  
Graz University of Technology (NAWI Graz), Stremayrgasse 9,  
A-8010 Graz, Austria

<sup>2</sup>Alistore - European Research Institute, CNRS FR3104, Hub de l'Energie, Rue Baudelocque, 80039  
Amiens, France

### *Abstract*

One of the major challenges of the 21st century is the need for sustainable energy conversion and energy storage devices. Therefore, we need not only to identify novel materials for energy storage but also find new, low-energy consuming ways to produce them. The use of biological templates represents an elegant way to prepare highly anisotropic cathode materials for Li ion batteries. Such cathode materials are amorphous in nature and do not suffer from the limitations imposed by their crystal structure. In the case of amorphous (Li)FePO<sub>4</sub> which adopted the filamentous shape of the bio template, this yields a low-cost and well-performing active material. While not outperforming its optimized crystalline counterpart, in its nanosized and carbon-coated form, it shows encouraging performance. This performance may be associated with the increased conductivity in these bio templated amorphous (Li)FePO<sub>4</sub> nanowires.

**Keywords:** amorphous, nanostructured, biotemplated, green synthesis, ionic conduction, active material

## Introduction

For the use of green energy, we need not only to find ways to convert these energies efficiently, but we also need to find ways of storing it. Especially for stationary electrical energy storage systems, the gravimetric as well as volumetric capacities are not of utmost importance. More importantly, the electrochemical energy storage systems must be adapted in terms of electrochemical potential to fit to the energy converters, *i.e.*, solar panels, wind turbines and so on. Furthermore, for a sustainable long-term strategy, we need not only to think of the characteristics of the active materials themselves, but we also must focus on the production process of those materials. These materials for future energy storage do not necessarily need to have outstanding properties in terms of capacity, charge rate and electrochemical potential. They need to consist of abundant elements that can be sourced eco-friendly. Furthermore, the synthesis of the active materials as well as the production of the storage system must be of low cost, financially as well as environmentally. As has been shown in a game changing work by Belcher and her group, the bacteriophage M13, a biological template, can be used for the synthesis of amorphous eco-friendly iron phosphate with very interesting properties.<sup>1</sup> With the aid of the template, it is possible to synthesize this cathode material in an aqueous process at room temperature. This is done without the use of toxic materials and the only side product is sodium chloride, one of the most abundant salts on earth. Here we present the synthesis of amorphous bio templated FePO<sub>4</sub> provide data about the synthesis process and a thorough analysis of the product itself. Transmission electron microscopy, in combination with XRPD and STA-MS as well as elemental analysis of the amorphous FePO<sub>4</sub> gives detailed information about the morphology, composition as well as nature of the as obtained product, amorphous FePO<sub>4</sub>. Chemically lithiated  $\alpha$ -LiFePO<sub>4</sub> is furthermore characterized by impedance spectroscopy to gain insight into the ionic conduction in this material. The cathode material is further characterized by electrochemical methods such as CVA and GCPL to study the thermodynamics as well as kinetics of this green cathode material.

## Experimental

### Sample preparation

Synthesis of bio templated amorphous iron-phosphate nanowires was achieved by using a modified bacteriophage M13KE as a structural template (Figure 1d). The modified bacteriophage displaying

an E3D-motif on every protein 8 was used in an aqueous precipitation procedure (Figure 1e). We employed a strategy similar to that used by Lee *et al.*<sup>1</sup> In brief,  $4 \cdot 10^{13}$  plaque forming units (PFU) were dialyzed for 24 h against a tenfold volume of pure water (Millipore Milli-Q, 18.2 M $\Omega$ ) and brought to 20 ml with pure water. The dialyzed phage suspension was mixed with 100 mL of a 120 mM ferric chloride solution (Fluka Chemika, anhydrous  $\geq 97\%$ ) and incubated for various durations at 4 °C. The precipitation of amorphous bio templated iron phosphate was achieved by the addition of 120 mL of a 100 mM sodium phosphate solution (Sigma-Aldrich, 96%). After 4 hours the precipitates were collected by vacuum filtration and washed thrice with pure water and finally with acetone. As collected samples were dried at 60 °C for at least 36 h with intermitting grinding.

### **Microbiological and molecular biological methods**

*E. coli* XL1-Blue and ER2738 were routinely grown in LB-Lennox medium (10 g tryptone, 5 g yeast extract and 5 g NaCl per litre supplemented with 20 mg/L tetracycline) at 37°C under aeration (250 rpm). For cloning *E. coli* XL1-Blue was used and for phage amplification ER2738 was infected in its early logarithmic growth phase (log-phase) and phages were allowed to grow for 4.5 h at 37°C under aeration.

Bacteriophage M13KE was harvested by a standard method employing a polyethylene glycol (PEG)-based precipitation. In brief, bacteria were pelleted twice (5,000 g, 4 °C, 10 min) and the phages in the supernatant were precipitated by the addition of 5%(w/v) PEG 8,000 and 0.5 M NaCl. After 24 h of precipitation in the cold, phages were pelleted (12,000 g, 4 °C, 10 min) and suspended in 10 mM Tris-buffered saline (TBS, pH 7.4). Pure phage isolates were obtained after removal of remaining cell debris by centrifugation (15,000 g, 4 °C, 10 min) and a second precipitation step. Phage concentrations were estimated by UV-VIS absorption spectroscopy and by a plaque-assay. For photometric quantification, phage isolates were diluted, and the absorbance measured at 269 nm and 320 nm. After background subtraction, the concentration of virus particles was calculated according to:<sup>2</sup> 
$$\text{virus particles per mL} = \frac{A_{269} - A_{320}}{\#bp/virion} \cdot 6 \cdot 10^{16}$$
.  $A_{269}$  and  $A_{320}$  are the absorption at 269 nm and 320 nm respectively whereas #bp/virion represents the number of nucleobase pairs per virion. Phage concentrations were confirmed by plaque forming assay. In brief, phage isolates were serially diluted and used to infect *E. coli* ER2738 in its early logarithmic growth phase. After a short infection time (5 min) of ER2738, the cells were spread in a soft agar overlay

onto LB-IPTG<sup>50</sup>-XGal<sup>40</sup> agar plates and incubated at 37 °C overnight. Colour plaques were counted.

For cloning M13KE, dsDNA was isolated from infected *E. coli* ER2738 cultures by the method of Birnboim and Doly<sup>3</sup>. For sequencing, ssDNA was isolated from purified phages. To disrupt their proteinaceous hull, phages were suspended in NaI-buffer (4 M NaI, 10 mM Tris, pH 8.0, 2.5 mM EDTA) and ssDNA was precipitated by addition of 70% ethanol. After 10 min of standing at RT the ssDNA was pelletized by centrifugation (18,000 g, 4 °C, 10 min) and washed with 70% ethanol. Concentrated, ethanol-free ssDNA was stored at -20 °C in TE-buffer (10 mM Tris, pH 8.0, 0.5 mM EDTA). Integrity and concentration of DNA was assessed by comparing intensity of the band with λ\*BstEII standard (NEB) after DNA gel electrophoresis and staining with Midori Green Advance (Nippon Genetics EUROPE) according to manufacturer recommendations.

For cloning an inverse polymerase chain reaction (PCR) using the Q5<sup>®</sup> Site-Directed Mutagenesis Kit (NEB) was employed according to the recommendations of the manufacturer. To insert a tag encoding for four glutamate residues between the first and the second codon of the native major *protein 8* dsDNA was used as a template using the primers listed in Table 1.

Linear PCR products were separated according to their size by gel electrophoresis and analysed after staining. The product, a single linear PCR Fragment of about 7.3 kbp was used without further purification for phosphorylation and ligation to form circular plasmids. Circularized plasmids were successfully transformed into freshly prepared competent *E. coli* XL1-Blue cells using the method of Mandel and Higa<sup>4</sup>.

Table 1: Primers used for modification of protein 8.

<b>name</b>	<b>primer sequence (5'-3')<sup>a</sup></b>	<b>T<sub>m</sub></b>
Fw_M13KEp8E4	<u>GAG GAG</u> GAT CCC GCA AAA GCG GCC	70 °C
Rv_M13KEp8E4	<u>CTC CTC</u> AGC AGC GAA AGA CAG CAT CG	68 °C

<sup>a</sup> underlined nucleotides refer to the insert

Transformants were grown on LB-IPTG<sup>50</sup>-XGal<sup>40</sup> agar plates overnight at 37°C. Modifications were checked by Sanger sequencing (NEB) using a standard sequencing primer (-96gIII).

### **Structural and compositional analysis**

For X-ray powder diffraction, bio templated amorphous  $\text{FePO}_4$  was annealed at 200 °C, 480 °C and 680 °C for 5 h in air (heating rate 10 °C/min). Biotemplated amorphous  $\text{LiFePO}_4$  was crystallized at 700 °C for 5 h in a quartz glass ampoule. These samples were analysed by X-ray powder diffraction using a Bruker D8 Advance diffractometer (Bragg Brentano geometry,  $\text{Cu K}_\alpha$  radiation). The Patterns shown in Figure 4 were recorded with a step size of 0.02° (waiting time 2 s) in the  $2\theta$ -range 20° to 100°. Rietveld refinement was carried out by using X'PertHighScorePlus (Panalytical).

The purity of amorphous  $\text{FePO}_4$  was also confirmed by inductively-coupled plasma optical emission spectroscopy (ICP OES). The sample analysed was dried at 60 °C in vacuum overnight and dissolved in concentrated hydrochloric acid.

For simultaneous thermal analysis (STA), a Netzsch STA Model STA-449F1 coupled with a QMS-403C mass spectrometer was employed. Measurements were performed from RT to 800 °C under protective atmosphere ( $\text{N}_2$ ) and a heating rate of 10 °C/min. Samples were pressed into tablets (5 mm diameter) and the sample chamber was evacuated thrice to remove surface bound water before the measurement was started. The coupled MS allowed the online monitoring of the evolving volatile species during mass loss in TGA and to ascribe the mass losses to removal of structural water and decomposition of the biotemplate.

Structural investigations regarding the particle's morphology were conducted by means of transmission electron microscopy. For investigation of the particle formation kinetics, various incubation times of the phages in the respective  $\text{FeCl}_3$  and  $\text{Na}_3\text{PO}_4$  solutions were investigated. For TEM analysis, suspended samples were dropped onto a Cu-grid coated by a C-film and washed with distilled water. Dried samples were investigated in the TEM.

### **Impedance analysis**

M13 a- $\text{FePO}_4$  samples were dried for 48 h at 60 °C followed by vacuum drying for 6 h at 60 °C, 6 h at 105 °C and 20 h at 250 °C and transferred into a argon-filled glovebox ( $\text{O}_2$  &  $\text{H}_2\text{O}$  < 1 ppm). For chemical lithiation, samples were grinded with the aid of an agate mortar and pestle and suspended in hexane. To ensure full lithiation, a 40% excess of n-Butyllithium (2.5 M in hexane) was added and the suspension was stirred for 2 days. Lithiated a- $\text{FePO}_4$  was washed thrice with hexane and dried for 24 h at ambient temperature in the glovebox followed by 6 h at 60 °C in vacuum.

For impedance measurements, the dried samples were uniaxial cold pressed into tablets and Li ion blocking Au electrodes (100 nm) were applied on both sides by means of sputtering (DC Magnetron sputtering, Leica). Impedance spectra were recorded with a Novocontrol Alpha analyser using  $0.1 V_{\text{RMS}}$  as excitation amplitude. Data were recorded at frequencies ranging from 10 mHz to 10 MHz at temperatures ranging from  $-100\text{ }^{\circ}\text{C}$  to  $200\text{ }^{\circ}\text{C}$ . Measurements were performed in a stream of freshly evaporated nitrogen that was heated to the specified temperature employing a Novocontrol Quattro System.

### **Electrode preparation and cell assembly**

For cathode production a wet slurry mixing, and casting process was employed achieving a final active material loading of  $0.4\text{ mg cm}^{-2}$  with a final film thickness of  $\sim 67\text{ }\mu\text{m}$ . In brief, active material was mixed with carbon black (C-65) and PVDF-binder (Kynar Flex 2801) in a ratio of 70:25:5. The slurry was prepared by soft ball-milling in NMP to produce homogeneous mixtures. Slurries were cast with a thin film applicator ( $100\text{ }\mu\text{m}$  film thickness) onto etch-cleaned aluminium foils and dried at  $60\text{ }^{\circ}\text{C}$  to evaporate the solvent. Disc electrodes were punched, dried in vacuum, weighed and dried again before storage in an argon filled glovebox ( $\text{O}_2$  &  $\text{H}_2\text{O} < 1\text{ ppm}$ ).

For electrochemical testing, electrodes were assembled in a three-electrode configuration using T-type Swagelok-cells. Metallic lithium foil was used as anode and reference electrode and LP30 (1 M  $\text{LiPF}_6$  in EC-DMC (50/50)) was used as electrolyte. Glass microfiber filter (GF/F Whatman) was used as separator.

### **Electrochemical characterisation**

After assembly in an argon filled glovebox ( $\text{O}_2$  &  $\text{H}_2\text{O} < 1\text{ ppm}$ ), cells were monitored for at least 12 h and the open circuit potential (OCV) was recorded. Cyclic voltammetry (CV) was performed between 2 V and 4 V.2 vs  $\text{Li/Li}^+$  at different scanning rates ranging from  $0.05\text{ mV/s}$  to  $10\text{ mV/s}$ . The rate capability, capacity and cycling performance was analysed by means of galvanostatic cycling with potential limitation (GCPL) with an upper and lower potential limit of 4.2 V and 2 V vs  $\text{Li/Li}^+$  respectively. All techniques were performed with the aid of an MPG-2 multichannel potentiostat/galvanostat (BioLogic).



## Genetic Engineering

Genetic engineering of the major coat protein 8, covering the bacteriophage M13KE (see Figure 1a & b), was performed to enable the phage to electrostatically interact with cations. Introducing four acidic glutamate amino acids (Glu, E) at the surface exposed N-terminus of protein 8 results in a phage covered by carboxylic acids that can bind cations (Figure 1c). However, like others<sup>5,6</sup>, we found that the E4-mutant, displaying the sequence AEEEE at the N-terminus of the major protein 8 is genetically unstable. We found that the sequence AEEED (Ala-Glu-Glu-Glu-Asp) that most probably arose from replication misalignment is genetically stable. Given that the chemical properties of Glu and Asp are very similar since both have a carboxylic acid terminating their side chain, the chemical properties of that mutant are as desired. As the hull of the bacteriophage consists of ~2,700 copies of the protein 8, each being modified to carry the E3D sequence, the surface displays about 10,800 carboxylic acids. Synthesis of bio templated amorphous iron-phosphate nanowires was achieved by using this modified bacteriophage M13KE as a structural template (Figure 1d). The modified bacteriophage displaying an E3D-motif on every protein 8 was used in an aqueous precipitation procedure as outlined in Figure 1e.

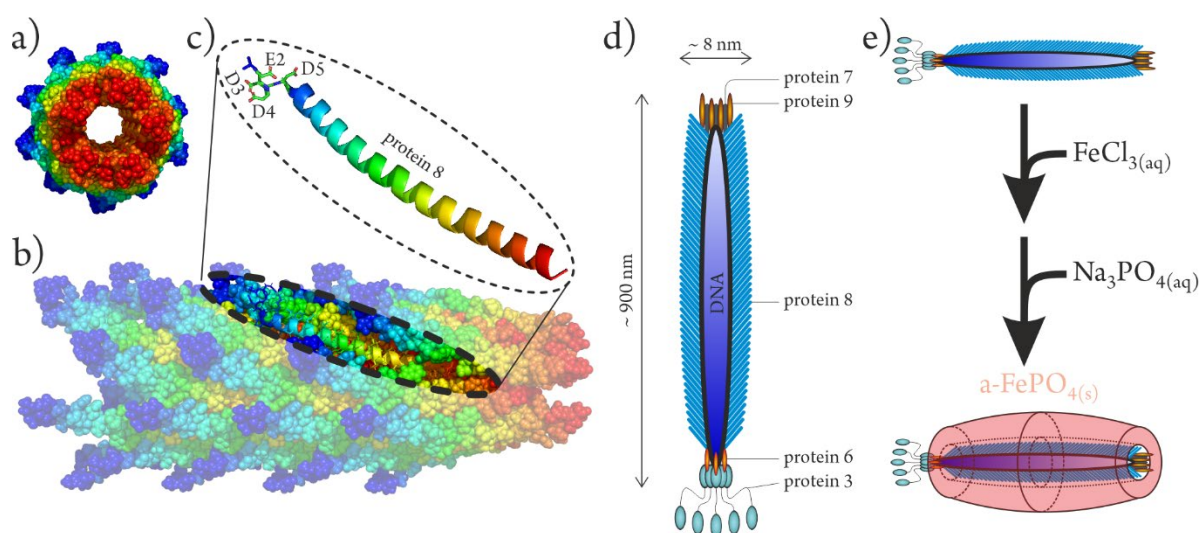


Figure 1: a) Capsid model of the bacteriophage M13KE from the top and side (b). c) Cartoon representation of the  $\alpha$ -helical protein 8 with its modified, acidic N-terminus is shown. d) Schematic representation of the bacteriophage M13. The shell consists of modified protein 8 and is primed for electrostatic interactions with cations. e) Diagram of the biotemplated precipitation process.

## Kinetics of Precipitation

Aliquots of bacteriophage M13KE E3D were investigated by means of transmission electron microscopy (TEM) after defined incubation periods in  $\text{FeCl}_3$  solutions and after addition of  $\text{Na}_3\text{PO}_4$ . The bacteriophage itself, consisting of only light elements, exhibits very low contrast in TEM and staining with heavier elements such as uranium or tungsten is usually a prerequisite for TEM analysis of bacteriophages.<sup>7</sup> As a result of the modification of protein 8, the bacteriophage is capable of coating itself with  $\text{Fe}^{3+}$  cations and is therefore clearly visible in TEM after incubation in  $\text{FeCl}_3$  solutions (Figure 2). Coating of the phage E3D with  $\text{Fe}^{3+}$  was examined by TEM imaging after an incubation period of 4 h, 8 h and 24 h at  $4^\circ\text{C}$  in a 100 mM  $\text{FeCl}_3$  solution at  $4^\circ\text{C}$  ( $1.6 \cdot 10^{14}$  PFU/l).

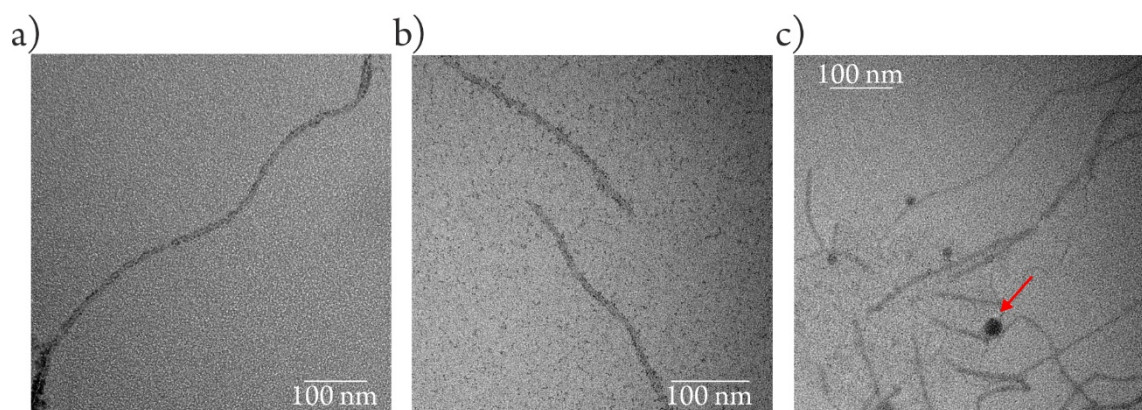


Figure 2: Transmission electron microscopy images of E3D after incubation in a 100 mM  $\text{FeCl}_3$  solution at  $4^\circ\text{C}$  for 4 h (a), 8 h (b) or 24 h (c). E3D shows uniform coating with  $\text{Fe}^{3+}$  already after 4 h of incubation indicated by the high contrast of the phage (a). After 8 h of incubation, small nanoparticles form and appear as black dots in the image (b). For prolonged incubation periods (c) these iron hydroxide nanoparticles grow to larger particles (red arrow).

We found that the phage E3D is already coated by  $\text{Fe}^{3+}$  after the shortest incubation period of 4 h (Figure 2a) whereas a prolonged incubation period leads to spontaneous formation of iron oxide/hydroxide nanoparticles (Figure 2b & c). After an incubation period of 24 h these nanoparticles are already in the size range of 10-30 nm; indicated by the red arrow in Figure 2c. These results clearly show that an incubation period of 4 h is sufficient for coating of the phage with  $\text{Fe}^{3+}$  cations. coated E3D phages after 4 h of incubation. Upon addition of  $\text{Na}_3\text{PO}_4$ ,  $\text{FePO}_4$  is formed within a few seconds due to the very low solubility product of  $\text{FePO}_4$ .<sup>8-10</sup> Bio templated  $\text{FePO}_4$  was collected 2 h, 22 h and 24 h after addition of the  $\text{Na}_3\text{PO}_4$  solution and the morphology was visualized by TEM (Figure 3)

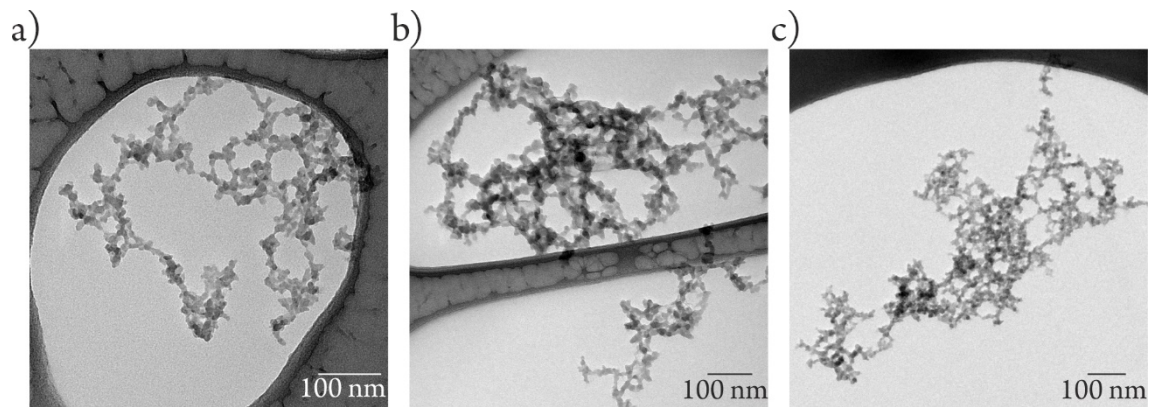


Figure 3: Transmission electron microscopy images of  $\text{FePO}_4$ -coated E3D 2 h (a), 22 h (b) and 24 h (c) after addition of a 100 mM  $\text{Na}_3\text{PO}_4$  solution at  $4^\circ\text{C}$ . A network of intertwined  $\text{FePO}_4$  nanowires can be observed already 2 h after addition of  $\text{Na}_3\text{PO}_4$  (a). At longer incubation times, 22 h (b) and 24 h (c), the thickness of the wires is not changes indicating that the precipitation is already complete after 2 h.

To precipitate bio templated  $\text{FePO}_4$ , a solution of  $\text{Na}_3\text{PO}_4$  (100 mM,  $4^\circ\text{C}$ ) was added to the  $\text{Fe}^{3+}$ -. Already after an incubation period of 2 h bio templated  $\text{FePO}_4$  nanowires, agglomerated in the form of a network, are obtained (Figure 3a). No changes can be observed after prolonged incubation periods (Figure 3b and c) indicating that the precipitation is already complete after an incubation period of 2 h at  $4^\circ\text{C}$ .

### Materials characterization

To analyse the prepared bio templated amorphous  $\text{FePO}_4$  samples X-ray powder diffraction (XRPD) was performed on samples annealed below the crystallisation temperature of  $\text{FePO}_4$  and at a sample crystallized by annealing at  $680^\circ\text{C}$ . Complementary, also the lithiated samples were analysed before and after crystallization. After annealing the bio templated amorphous  $\text{FePO}_4$  at  $200^\circ\text{C}$  and  $480^\circ\text{C}$  the XRPD pattern is rather featureless, being only characterized by two broad peaks located around  $12^\circ 2\theta$  and  $25^\circ 2\theta$  indicative for amorphous materials (see Figure 4a). Evidently, there is a small change in the shape of the peaks and in the location of the peak that is located at higher  $2\theta$  values. We suspect that this might be caused by structural relaxation of the amorphous  $\text{FePO}_4$ . After crystallisation of the bio templated amorphous  $\text{FePO}_4$  the diffraction pattern exhibits reflexes perfectly matching those of triclinic  $\text{FePO}_4$ . Rietveld refinement indicates that the diffraction pattern shows phase pure triclinic  $\text{FePO}_4$  (space group:  $\text{P3}_121$ ) lacking any impurities (Figure 4b). After lithiation we obtained amorphous  $\text{LiFePO}_4$  as indicated by the lack of reflexes in the XRPD pattern (Figure 4c). This material crystallizes in the well-known olivine structure (space group:  $\text{Pnma}$ ) after annealing at  $700^\circ\text{C}$  for 5 h. The XRPD pattern shows sharp

reflexes perfectly matching the reference pattern. Rietveld refinement indicates pure crystalline  $\text{LiFePO}_4$  (see Figure 4c).

It has been reported that different iron-phosphate species with various compositions can be obtained by precipitation from aqueous  $\text{Fe}^{3+}$  and  $\text{PO}_4^{3-}$  solutions. Scaccia *et al.* reported that  $\text{Fe}_2(\text{HPO}_4)_3$  crystallizes as  $\text{FePO}_4$  during annealing, whereby the nonstoichiometric phosphorous

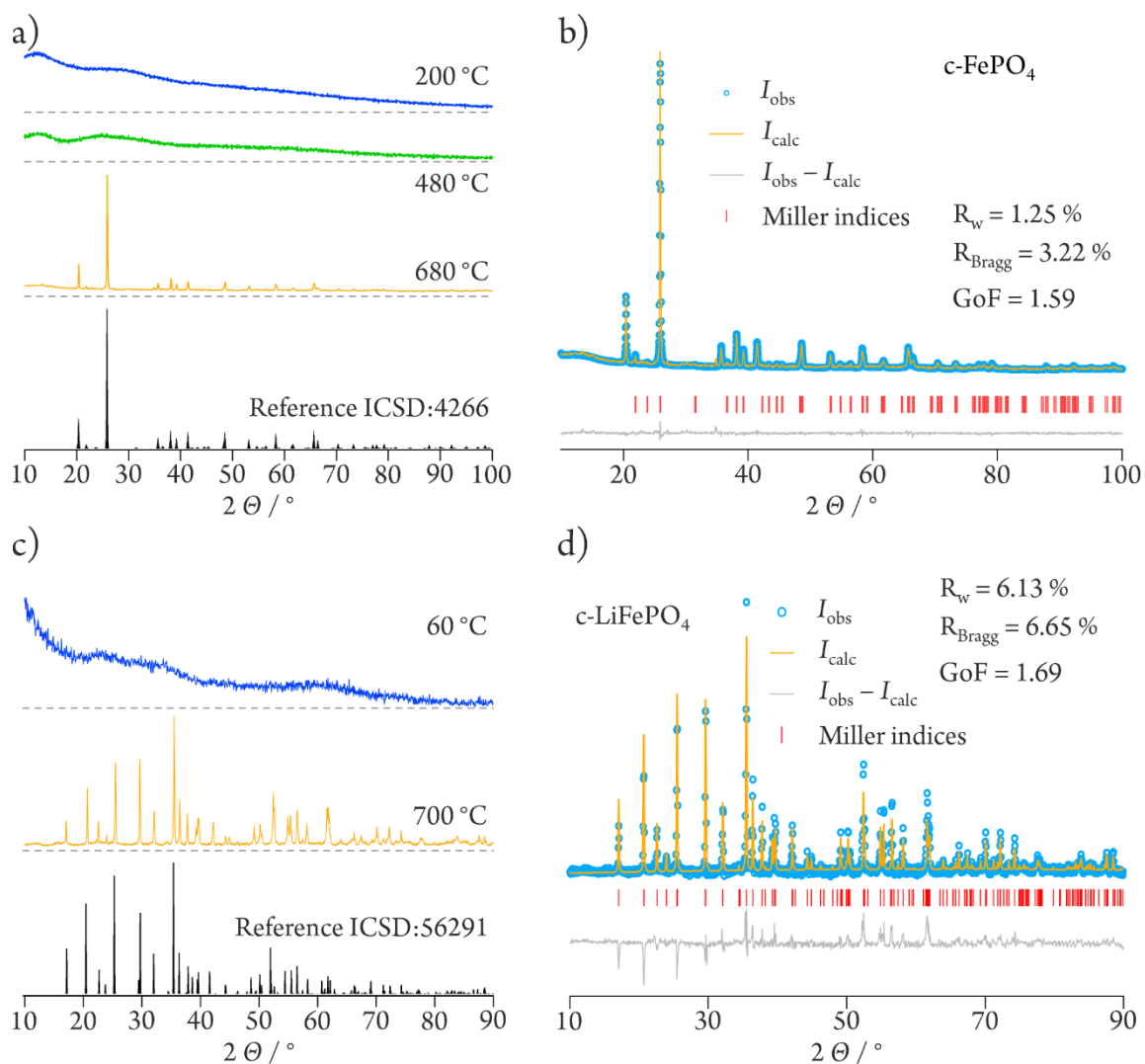


Figure 4: X-ray powder diffraction patterns obtained using  $\text{Cu K}\alpha$  radiation including Rietveld refinement of the respective crystalline phases. a) XRPD patterns obtained from biotemplated  $\text{FePO}_4$  after heating to indicated temperatures. The lack of reflexed and the broad halo around  $25^\circ 2\theta$  indicated that the material amorphous until heated at  $680^\circ\text{C}$ . b) The pattern obtained from the  $\text{FePO}_4$  samples after crystallization. The reflexes perfectly match those of the reference and the single-phase Rietveld refinement yielded excellent agreement parameters. c) XRPD patterns of lithiated  $\text{FePO}_4$  obtained after heating to indicated temperatures. d) XRPD pattern obtained after crystallizing the lithiated  $\text{FePO}_4$ . All reflexes match those of the reference pattern and the Rietveld refinement indicates phase pure  $\text{c-LiFePO}_4$ . In b) and d) the miller indices for the respective phases are shown along with the calculated and observed intensities and the residuals. See text for further information.

species evaporates as  $\text{H}_3\text{PO}_4$ .<sup>11</sup> However, the chemical analysis of bio templated amorphous  $\text{FePO}_4$  by ICP-OES revealed an atomic Fe to P ratio of 1:0.98(1). This clearly confirms that the bio templated precipitate is  $\text{FePO}_4$  in its amorphous form.

Simultaneous thermal analysis (STA) coupled with a mass spectrometer was used to analyse bio templated  $\text{FePO}_4$  that has been dried in vacuum at  $60^\circ\text{C}$  for 72 h (Figure 5a) and additionally for 20 h at either  $105^\circ\text{C}$  (Figure 5b) or at  $180^\circ\text{C}$  (Figure 5c). Neglecting the very small mass loss caused by the decomposition of the bio template, and therefore ascribing the mass loss to the evaporation of adsorbed and structurally bound water, we can estimate the water content of the samples. For the sample dried in vacuum at  $60^\circ\text{C}$ , at  $105^\circ\text{C}$  and, at  $180^\circ\text{C}$  this corresponds to  $\text{FePO}_4 \cdot 1.1 \text{H}_2\text{O}$ ,  $\text{FePO}_4 \cdot 0.5 \text{H}_2\text{O}$  and  $\text{FePO}_4 \cdot 0.3 \text{H}_2\text{O}$  respectively.

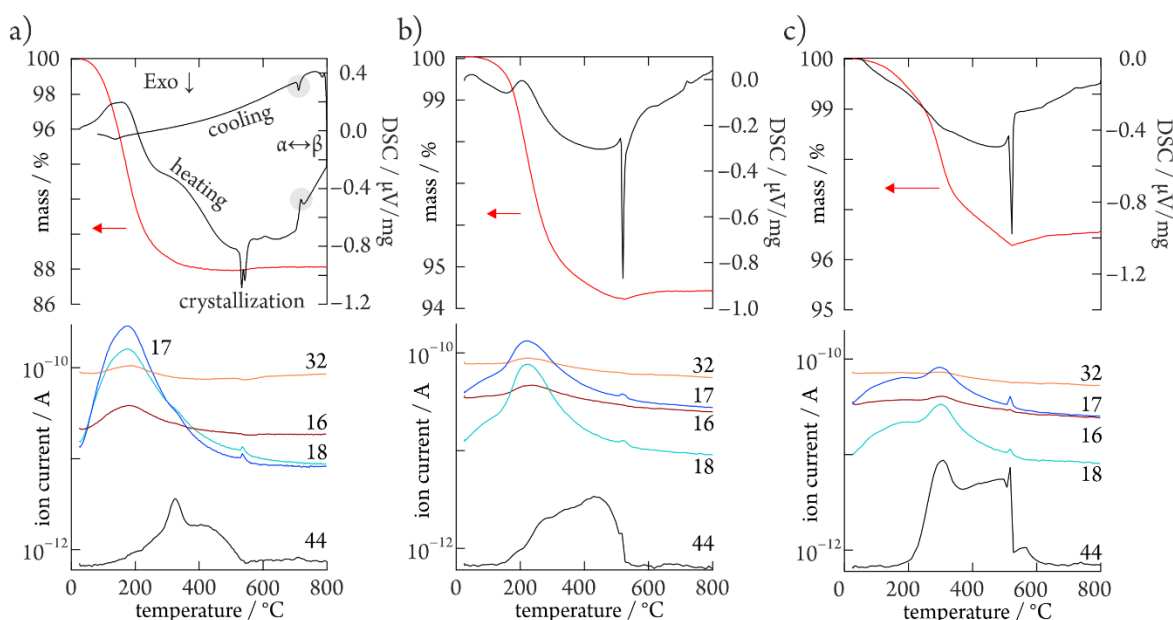


Figure 5: Simultaneous thermal analysis and mass spectrometry of bio templated  $\text{FePO}_4$  after drying in vacuum at  $60^\circ\text{C}$  for 72 h (a) followed by drying at  $105^\circ\text{C}$  (b) and  $180^\circ\text{C}$  (c) for another 20 h. a) A pronounced mass-loss is accompanied by the release of water ( $m/z$  17 & 18) followed by the decomposition of the bio template ( $m/z$  44) starting at  $\sim 200^\circ\text{C}$ . Crystallization of the amorphous material is accompanied by an exothermic peak. The reversible phase transition between the  $\alpha$ - and the  $\beta$ -quartz phase is marked by the small peaks (gray circles). b) Dried at  $105^\circ\text{C}$ , the loss of water is less pronounced and shifted to higher temperatures. c) If dried at  $180^\circ\text{C}$ , a two-step mass loss is observed which may be attributed to adsorbed water and finally, the decomposition of the bio template.

## Impedance spectroscopy

Ionic conductivity was measured in bio templated amorphous  $\text{LiFePO}_4$  as well as in crystalline  $\text{LiFePO}_4$  (Sigma-Aldrich,  $5\ \mu\text{m}$ ). Conductivity isotherms were recorded from  $-100\ ^\circ\text{C}$  to  $200\ ^\circ\text{C}$  after holding the sample at  $120\ ^\circ\text{C}$  for 30 min in a stream of freshly evaporated nitrogen gas. The conductivity isotherms shown in Figure 6 reveal a DC plateau at low frequencies which is followed by the dispersive regime at higher frequencies. This DC plateau and the dispersive regime may be approximated by Jonscher's power law fit,  $\sigma'_{(\nu)} = \sigma_{DC}(1 + (\nu/\nu_H)^\alpha)$ , where  $\nu_H$  and  $\alpha$  are the transition frequency from DC to dispersive response and the dispersion parameter, respectively. Interestingly, the bio templated amorphous  $\text{LiFePO}_4$  exhibits a second plateau most likely representing the bulk conductivity (see Figure 6a).

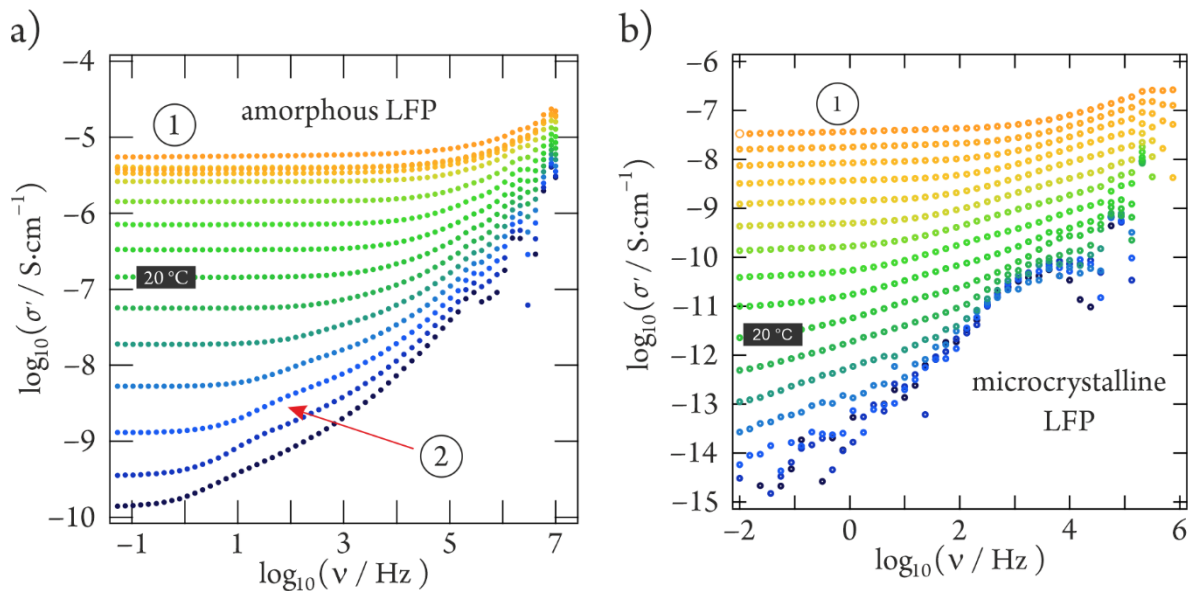


Figure 6: Conductivity isotherms recorded from  $-100\ ^\circ\text{C}$  to  $200\ ^\circ\text{C}$  at a) biotemplated amorphous  $\text{LiFePO}_4$  and b) microcrystalline  $\text{LiFePO}_4$ . a) A typical DC-plateau (1) is shown by both samples. A narrow 2<sup>nd</sup> plateau (2) is discernable (red arrow) at low temperatures.

Interestingly, the conductivity of bio templated amorphous LFP is about 5 orders of magnitude higher than in its microcrystalline counterpart. Note that the conductivity increases with temperature in a manner well described by the Arrhenius law. For bio templated amorphous LFP however, the conductivity decreases if the temperature is raised above  $120\ ^\circ\text{C}$ , the temperature at which it was in-situ annealed. This nonlinearity may be caused by structural relaxation of the sample and is accompanied by an increased activation energy of conduction in the following cooling cycle (see Figure 7a). Considering that the activation energy is tightly linked to structural aspects in

amorphous and glassy material, any structural relaxation due to thermal treatment will affect the ionic conductivity and its activation energy.<sup>12-14</sup> Compared to the crystalline LFP, the conductivity in the bio templated amorphous LFP is significantly increased, especially at technologically relevant, *i.e.* ambient, temperatures. However, conductivity decreases if the sample is heated above 120 °C and we assume that this decrease is associated with a structural relaxation of the FePO<sub>4</sub>-framework. Interestingly, at elevated temperatures, the conductivity approaches that of the nanocrystalline sample (see Figure 7b). The conductivities for crystalline LFP were obtained by digitizing the data from Zaghbi et al.<sup>15</sup> (15 μm) and Shahid et al.<sup>16</sup> (1 μm, 50 nm).

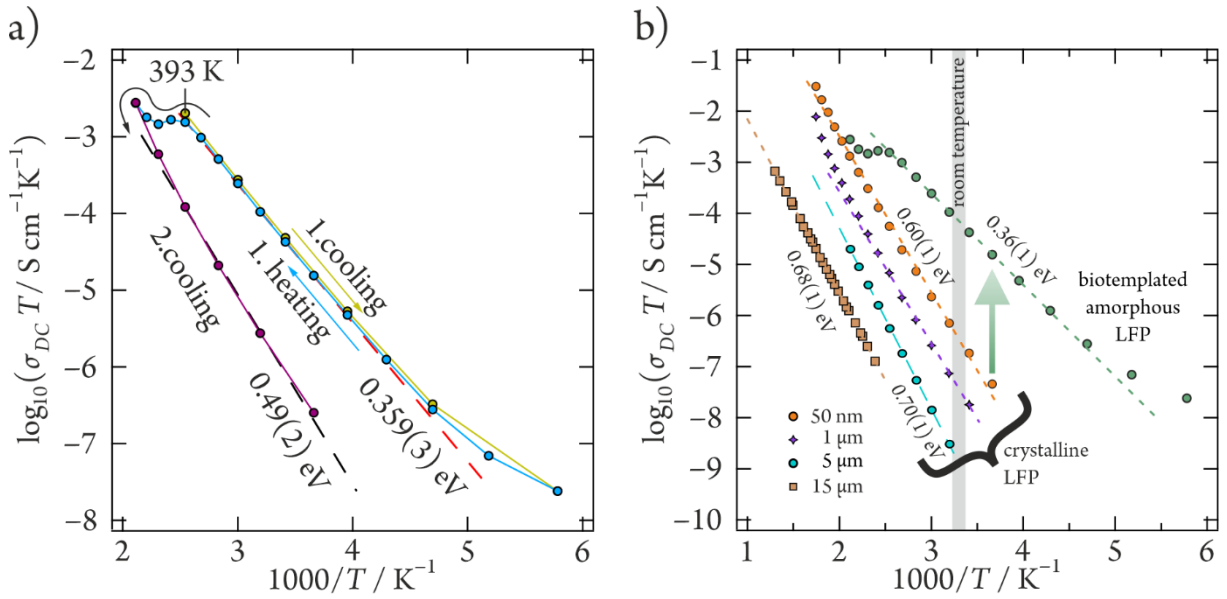


Figure 7: Arrhenius plot showing the temperature dependent conductivity of bio templated amorphous LFP a) during the heating and cooling cycles and b) in comparison to micro- and nanocrystalline samples.

Interestingly, we also find a second plateau, best seen at lower temperatures, that is located at higher frequencies (see Figure 6a). In the Nyquist plots of the impedance measured at —100 °C and —20 °C two convoluted semi circles can be discerned (see Figure 8). A simple equivalent circuit using only two R-CPE-units perfectly models the complete response of the sample and allows separating it into two distinct processes. Typical for a heterogeneous system, the separate semi-circles are depressed which is associated with a large distribution of relaxation times.

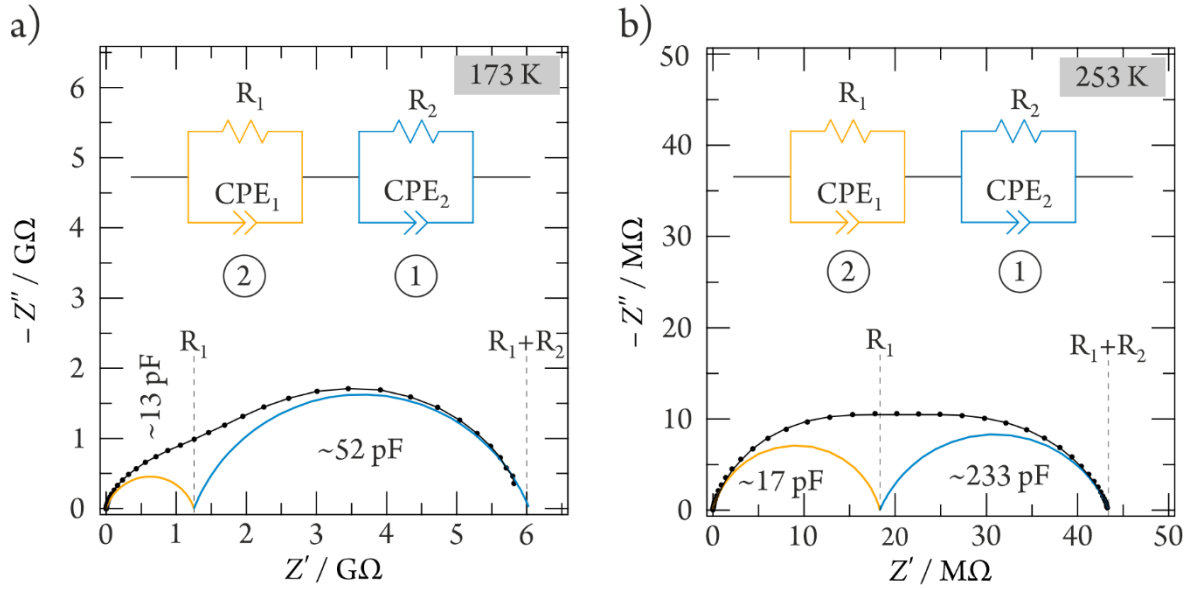


Figure 8: Nyquist plots showing the impedance of biotemplated amorphous  $\text{LiFePO}_4$  at a)  $-100^\circ\text{C}$  and b)  $-20^\circ\text{C}$  respectively.

Based on the capacitances of the processes we ascribe these responses to bulk and grain boundary processes. However, we must note that already at temperature as low as  $-20^\circ\text{C}$  the resistance of these processes is almost identical, at higher temperatures they converge to one conduction process as the resistance of the grain boundaries becomes negligible and the conductivity is dominated by the bulk response.

To analyse the conductivity further, we have to take a closer look at dispersive regime at high frequencies of the conductivity isotherms shown in Figure 6. As stated above, this regime and the DC-plateau can be approximated by Jonschers' power law and gives excess to the dispersion parameter  $\alpha$  (see Figure 9a). According to Sidebottom<sup>17</sup>, this parameter reflects the dimensionality of diffusion. This indeed yields dispersion parameters, or exponents, in the order of 0.6 for the amorphous sample while the microcrystalline sample, at similar temperatures, yields values of 0.4. Such values correspond to 3 D and 1 D diffusion, respectively (see Figure 9b).



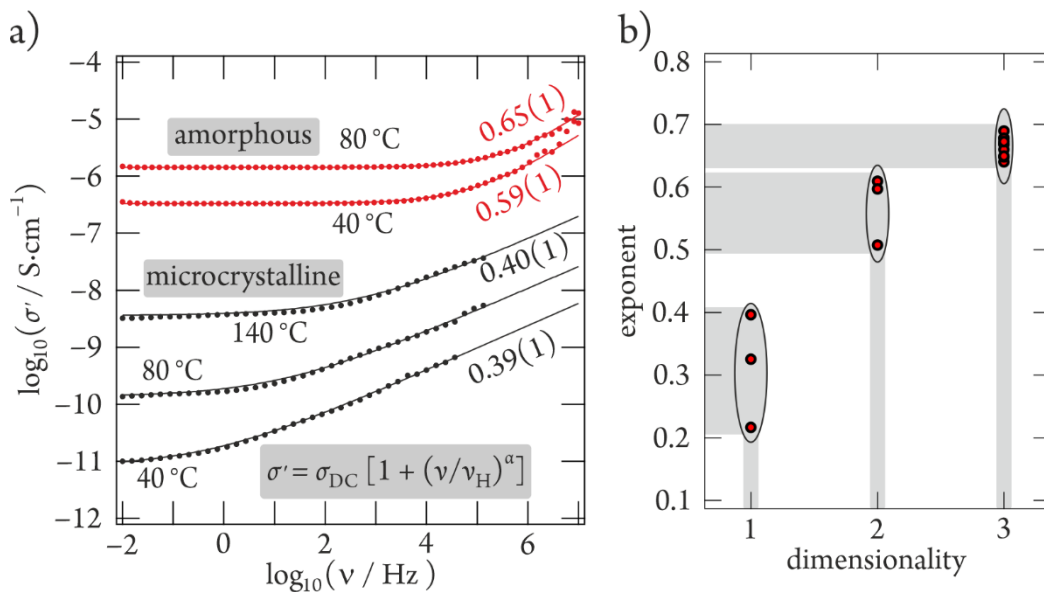


Figure 9: a) Isotherms of amorphous bio templated  $\text{LiFePO}_4$  at 80 °C and 40 °C (red) and of microcrystalline LFP at 140 °C, 80 °C and 40 °C. Fits using Jonschers power law reveal lower exponents for the crystalline sample. b) Digitalized data from Sidebottom showing the correlation between exponent and dimensionality of diffusion.

### Electrochemical tests

For the electrochemical characterisation of the bio templated  $\text{FePO}_4$ , materials with different amount of residual, coordinated water have been used for electrode preparation. For comparison also commercially available carbon-coated  $\text{LiFePO}_4$  was assembled into half-cells and analysed by cyclic voltammetry (CV) as well as galvanostatic cycling with potential limitation (GCPL), see Figure S1. The first sample analyzed, was only dried in air at 60 °C and the active material is, as determined by thermogravimetric analysis,  $\text{FePO}_4 \cdot 2.3 \text{H}_2\text{O}$ . During OCV, the cell shows an initial steep decrease in potential within the first 2 h after which the potential stabilizes at about 3.25 V vs  $\text{Li}/\text{Li}^+$  (Figure 10a). Information about the kinetics and thermodynamics, that is, the potential at which oxidation and reduction of the active material occurs and the corresponding currents were obtained by cyclic voltammetry using different scan rates (see Figure 10b & c). Starting with lowest scan rate (0.05 mV/s) the active material is reduced at 3.05 V and oxidized at 3.23 V. At the highest scan rate (10 mV/s) this reduction-peak is shifted to 2.88 V and the oxidation-peak is shifted to 3.42 V vs  $\text{Li}/\text{Li}^+$ .

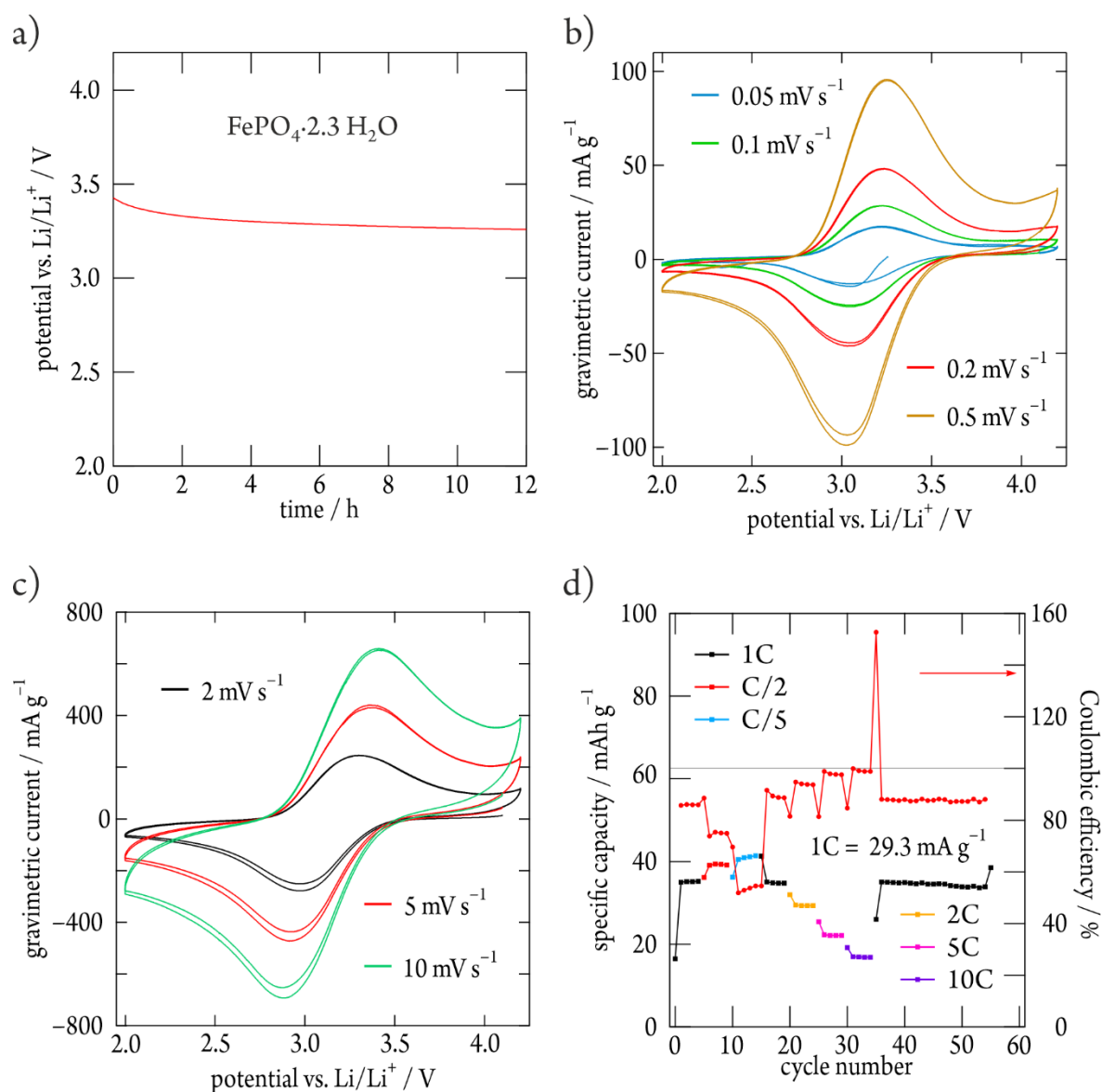


Figure 10: a) Open circuit voltage (OCV) of bio templated  $\text{FePO}_4 \cdot 2.3 \text{H}_2\text{O}$  vs. the  $\text{Li}/\text{Li}^+$  redox couple. b) and c) cyclic voltammograms at different scan rates and d) galvanostatic cycling at different C-rates between 2 V and 4.2 V vs  $\text{Li}/\text{Li}^+$ .

Another oxidation peak is visible at potentials above 4 V which is probably caused by the decomposition of the electrolyte due to instability with the cathode at elevated potentials. At a much higher scan-rate (10  $\text{mV/s}$ ), the reduction and oxidation peaks are only shifted by 200 mV if compared to those observed at a scan rate of 0.05  $\text{mV/s}$ . The capacity was estimated via one GCPL cycle using a current of 59  $\text{mA/g}$  which translates to a C-rate of 0.4 based on the theoretical capacity of  $\text{FePO}_4 \cdot 2.3 \text{H}_2\text{O}$ . Cycling at this current rate allowed reversible storage of only 29.3  $\text{mAh/g}$ . The C-rates for further GCPL measurements were based on this gravimetric capacity. At a cycling rate of 1C a specific capacity of about 35  $\text{mAh/g}$  were achieved at, however, low Coulombic efficiency

of 85% (see Figure 10d). Cycling at lower C-rates gave, as expected higher discharge capacities, albeit at lower Coulombic efficiencies which might be attribute to the electrolyte decomposition above 4 V. At higher C-rates, the capacity decreases while the Coulombic efficiency increases. However, even at currents as high as 10C, the Coulombic efficiency is almost 100% while the capacity equals ~16 mAh/g. Albeit, in absolute figures, this value is far from being of practical relevance, it important to note that this corresponds to about 50% of the achievable capacity if this cell is cycled at 1C. The material as such seems to be remarkable stable; after the C-rate capability tests the capacitance and Coulombic efficiency is constant at 1C (see Figure 10d). This indicates that the water content within the active material is structurally bound and is not involved in electrochemical (side) reactions. Zaghbi et al.<sup>18</sup> showed that crystalline  $\text{FePO}_4 \cdot 2 \text{H}_2\text{O}$  could be cycled vs. lithium in a stable manner and found that 0.74 Li ions could reversibly be stored per formula unit.

By further drying, especially in vacuum, the water content could be drastically reduced to give  $\text{FePO}_4 \cdot 1.1 \text{H}_2\text{O}$ . Cathodes made from this material showed a significantly increased specific capacity. Again, after equilibrating the cell to allow for stabilization (see Figure 11a), the cell was subjected to CV for a first analysis (see Figure 11b & c). This material behaves very similar to the above shown sample, but the currents are higher at similar scan-rates. Comparing the oxidation peaks at different scan rates reveals that the oxidation peak is shifted by only 100 mV between a scan rate of 0.05 mV/s and 10 mV/s. The reduction peak, however, is shifted by almost 300 mV. GCPL indicates that this material shows a much higher specific capacity of about 140 mAh/g if cycled at 0.1C (see Figure 11d). At a higher C-rate of 0.2 (C/5), the capacity drops to slightly below 100 mAh/g. To improve the electrochemical behaviour of the cathode, which does not only depend on the active material alone, porosity and other factors also play important roles, we compacted electrodes by short isostatic pressing at room temperature (0.64 to/cm<sup>2</sup> for 1 min). This compacted electrode showed decreased capacity at C/10 but delivered more power at a higher C-rate of C/5 (see Figure 11d).

Comparing these two samples shows that the reduction potential is lowered by the residual water content ( $\text{FePO}_4 \cdot 2.3 \text{H}_2\text{O}$  vs.  $\text{FePO}_4 \cdot 1.1 \text{H}_2\text{O}$ ). Hydrated samples are expected to show lower reduction and oxidation potentials as the OH groups coordinating the  $\text{Fe}^{3+}$  are expected to destabilize the Fe-O-P inductive effect, thus rendering it less effective.<sup>18</sup>

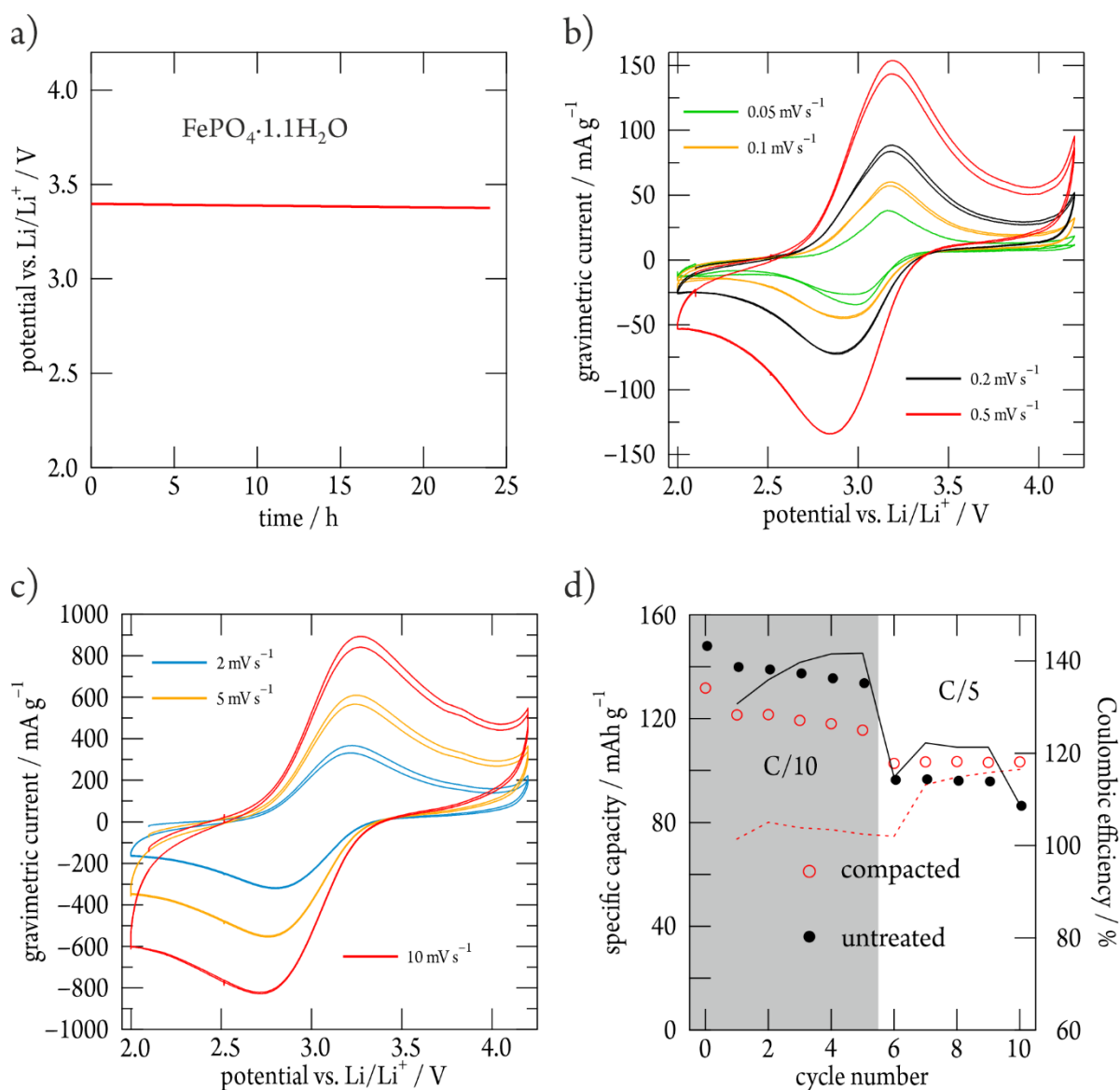


Figure 11: Open circuit voltage (OCV) of bio templated  $\text{FePO}_4 \cdot 1.1\text{H}_2\text{O}$  vs. the  $\text{Li}/\text{Li}^+$  redox couple. b) and c) cyclic voltammograms at different scan rates and d) galvanostatic cycling at different C-rates between 2 V and 4.2 V vs  $\text{Li}/\text{Li}^+$ .

Therefore, a sample containing less structural water is expected to exhibit a stronger Fe-O-P inductive effect and therefore a higher reduction potential. Here, however, this is not the case which might be caused by the fact that the hydrated  $\text{FePO}_4$  is completely amorphous and could exhibit different coordination of the  $\text{Fe}^{3+}$ , that is tetrahedral or octahedral coordination. During drying, a change of coordination number could take place and thus would changing the respective redox potentials. Although the redox potentials are lower, the relative currents are significantly higher in the less hydrated sample compared to the sample containing 2.3  $\text{H}_2\text{O}$  per  $\text{FePO}_4$  ( Figure 10b & c and Figure 11b & c). Presumably, the electronic properties as well as ionic conductivities are very different in these two samples. Concomitantly, also the capacities are much higher in the less

hydrated sample even at higher currents; compare Figure 10d and Figure 11d. Although, these two samples have been cycled with different C-rates, that is C-rate based on practical capacities for  $\text{FePO}_4 \cdot 2.3 \text{H}_2\text{O}$  and C-rates based on the theoretical C-rate for  $\text{FePO}_4 \cdot 1.1 \text{H}_2\text{O}$  we can still compare the capacities exhibited by the samples. For example, the charge current for the  $\text{FePO}_4 \cdot 2.3 \text{H}_2\text{O}$  was  $\sim 15 \text{ mA/g}$  ( $C/2$ ) and for  $\sim 17 \text{ mA/g}$  for  $\text{FePO}_4 \cdot 1.1 \text{H}_2\text{O}$  at  $C/10$ . For these very similar currents the difference in specific capacity is large;  $30 \text{ mAh/g}$  vs.  $140 \text{ mAh/g}$  respectively.

### Conclusion

Using a genetically modified bio template to synthesize amorphous  $\text{FePO}_4$  could be achieved in a low energy consuming manner. The obtained material adopted the shape of the filamentous bio template but contained a significant amount of water. While the water content seems to influence the redox potentials and usable capacity of the material, it is surprisingly stable and suggests that samples dried at temperatures as low as  $60^\circ\text{C}$  could be used as active material in Li ion batteries. For a better performing material, vacuum drying a higher temperature was necessary. Interestingly, if chemically lithiated, the material shows a very high ionic conductivity. Considering the diffusion-restricting crystal structure of crystalline  $\text{LiFePO}_4$ , the increased ionic conductivity in the amorphous sample is attributed to the more open structure of the amorphous state.

### References

1. Lee, Y. J.; Yi, H.; Kim, W.-J.; Kang, K.; Yun, D. S.; Strano, M. S.; Ceder, G.; Belcher, A. M. *Science* **2009**, 324, (5930), 1051-1055.
2. Dang, X.; Yi, H.; Ham, M.-H.; Qi, J.; Yun, D. S.; Ladewski, R.; Strano, M. S.; Hammond, P. T.; Belcher, A. M. *Nat Nano* **2011**, 6, (6), 377-384.
3. Birnboim, H. C.; Doly, J. *Nucleic acids research* **1979**, 7, (6), 1513-1523.
4. Mandel, M.; Higa, A. *Journal of Molecular Biology* **1970**, 53, (1), 159-162.
5. Lee, Y. J.; Belcher, A. M. *Journal of Materials Chemistry* **2011**, 21, (4), 1033-1039.
6. Neltner, B.; Peddie, B.; Xu, A.; Doenlen, W.; Durand, K.; Yun, D. S.; Speakman, S.; Peterson, A.; Belcher, A. *ACS Nano* **2010**, 4, (6), 3227-3235.

7. Monninger, M. K.; Nguessan, C. A.; Blancett, C. D.; Kuehl, K. A.; Rossi, C. A.; Olschner, S. P.; Williams, P. L.; Goodman, S. L.; Sun, M. G. *Journal of Virological Methods* **2016**, 238, 70-76.
8. Zhang, T.; Ding, L.; Ren, H.; Guo, Z.; Tan, J. *Journal of Hazardous Materials* **2010**, 176, (1-3), 444-450.
9. Fytianos, K.; Voudrias, E.; Raikos, N. *Environmental Pollution* **1998**, 101, (1), 123-130.
10. Scaccia, S.; Carewska, M.; Prosini, P. P. *Thermochimica Acta* **2004**, 413, (1), 81-86.
11. Scaccia, S.; Carewska, M.; Di Bartolomeo, A.; Prosini, P. P. *Thermochimica Acta* **2002**, 383, (1-2), 145-152.
12. Desai, N. B.; Byrappa, K.; Gopalakrishna, G. S.; Srikantaswamy, S.; Kulkarni, A. B. *Bulletin of Materials Science* **1987**, 9, (5), 317-321.
13. Bragatto, C. B.; Cassar, D. R.; Peitl, O.; Souquet, J. L.; Rodrigues, A. C. M. *Journal of Non-Crystalline Solids* **2016**, 437, 43-47.
14. Metselaar, R.; Oversluizen, G. *Journal of Solid State Chemistry* **1984**, 55, (3), 320-326.
15. Zaghbi, K.; Mauger, A.; Goodenough, J. B.; Gendron, F.; Julien, C. M. *Chemistry of Materials* **2007**, 19, (15), 3740-3747.
16. Shahid, R.; Murugavel, S. *Physical Chemistry Chemical Physics* **2013**, 15, (43), 18809-18814.
17. Sidebottom, D. L. *Physical Review Letters* **1999**, 83, (5), 983-986.
18. Zaghbi, K.; Julien, C. M. *Journal of Power Sources* **2005**, 142, (1), 279-284.

### Electronic Supplementary Information

For reference purposes, we also assembled cells using electrodes made of carbon-coated crystalline  $\text{LiFePO}_4$  (Clariant,  $<1.6 \mu\text{m}$ ). The electrochemical characterization of the reference material is shown in Figure S1.

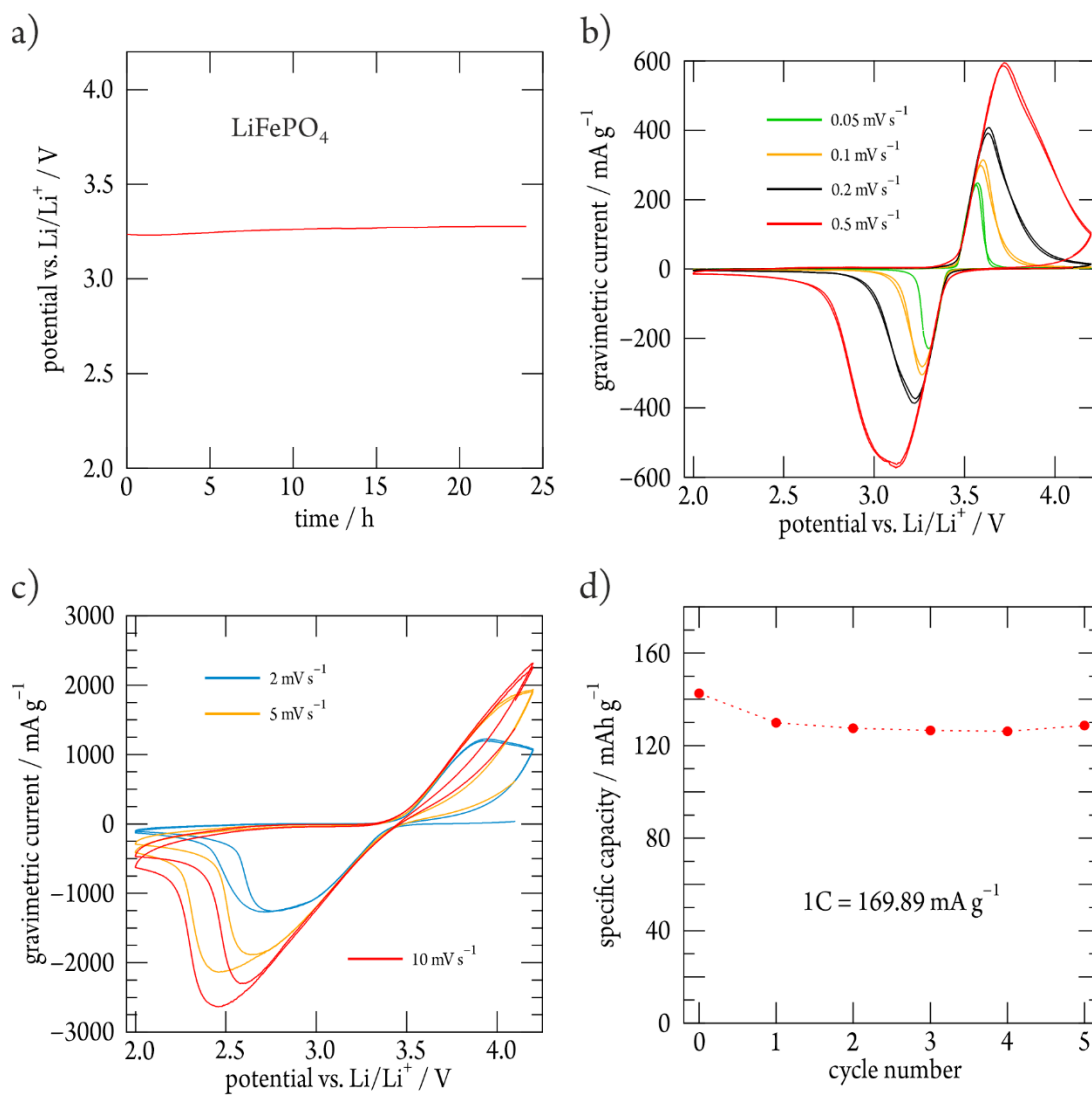


Figure S1: Open circuit voltage (OCV) of carbon coated crystalline  $\text{LiFePO}_4$  vs. the  $\text{Li}/\text{Li}^+$  redox couple. b) and c) cyclic voltammograms at different scan rates and d) galvanostatic cycling at a rate of 1 C between 2 V and 4.2 V vs  $\text{Li}/\text{Li}^+$





## 4 Conclusion and Outlook

---

I believe the goal of probably every PhD-thesis is at least two-fold:

- A personal goal is to train a student, a person, a mind.
- A global goal is to fulfil the need or desire to accumulate knowledge to gain a deeper understanding of nature and its laws.

With the aim of fulfilling both, within this dissertation various classes of solids were synthesized, modified and characterized with a strong emphasis on the ion conduction behaviour. While the focus was set on ionic conductivity, especially of  $\text{Li}^+$ , also the conduction via electronic or polaronic charge transport was assessed.

Ionic conductivity was foremost studied via impedance spectroscopy while NMR spectroscopic methods gave additional information except for  $\text{Li}_4\text{C}_{60}$  which was solely studied by NMR methods.

By careful analysis of the impedance spectra as well as structural characterization, it was possible to identify important parameters affecting ionic conductivity in solids. While in the case of the glassy petalite, a model using entropic contributions explained the peculiar decrease in conductivity seen during mechanical-induced structural relaxation. For the poorly conductive  $\text{LiTaO}_3$ , on the other hand, high energy ball-milling, and the introduction of defects along with nanosizing lead to orders of magnitude increased conductivity. Various annealing experiments revealed, via a combined effort using PALS and EXAFS along with impedance spectroscopy, that bond-disorder is most important for ionic conductivity.

For  $\text{Li}_7\text{La}_3\text{Zr}_2\text{O}_{12}$  stabilized in the highly conductive cubic phase by Ga-doping the ionic as well as the electronic conductivity was assessed. Making use of single crystals of this material, we could probe the electronic conductivity without the influence of grain boundaries and impurity phases as had thus access to the true materials property. Using potentiostatic long-time polarisation measurements, the electronic conductivity was found to be lower than reported for polycrystalline samples in the recent literature.

While defects in various form can significantly increase the ionic conductivity, especially in poor ionic conductors, also reduced dimensionality of diffusion may evoke fast ion conduction. If the

ions are guided between two sheets, their diffusivity may be much higher than in a material offering 3-dimensional diffusion.  $\text{Li}_4\text{C}_{40}$  represents a fast ion conductor with putative 2-dimensional ion diffusion. These Buckminster fullerenes, polymerized via lithiation from 2D polymers with  $\text{Li}^+$  ion residing between the large  $\text{C}_{60}$  monomers. Making use of various NMR-based  $^7\text{Li}$  relaxation techniques complex  $\text{Li}^+$  ion dynamics could be revealed. The results point to fast localized motion of the dilute  $\text{Li}^+$  ions. The long-range diffusion of the ions, however, seems to be restrained to two dimensions.

While exclusive ionic conductivity is the sole purpose of a solid electrolyte, it is also an important factor in active materials for Li-ion batteries. High ionic conductivity in an active material is especially important if high C-rate capability or thick electrodes are considered.  $\text{Li}_4\text{Ti}_5\text{O}_{12}$ , which is currently employed as anode material in LiB, shows very poor ionic and even lower electronic conductivity. Nonetheless, this material shows fast reaction kinetics in LiB. Combining in situ annealing with impedance spectroscopy, we could find evidence for a fast localized conduction processes that is enhanced by oxygen vacancies. Being present also in the pristine material, this conduction mechanism may represent feature responsible for the fast reaction kinetics of this material.

The active-material lithium iron phosphate,  $\text{LiFePO}_4$ , is intrinsically a very poor ionic and electronic conductor. Its drawbacks can be overcome by decreasing the length of the diffusion pathway (nanoparticles) and by coating the particles with carbon to increase the electronic conductivity. In its crystalline state, the  $\text{Li}^+$  ion diffusion is restrained to one dimension by the crystal structure. Upon delithiation, a new phase,  $\text{FePO}_4$ , forms and continuously grows. This two-phase mechanism leads to a very flat potential during dis-/charging but hinders the formation of a highly conductive  $\text{Li}_x\text{FePO}_4$  solid solution. Using a genetically adapted bio template allows for the synthesis of amorphous  $\text{FePO}_4$  nanowires. The material obtained from aqueous solutions adopts the filamentous shape of the bio template. This low-energy consuming process yields amorphous  $\text{FePO}_4$  that could be used directly in a Li-metal battery. Importantly, we found that this material shows much higher conductivity in its lithiated state compared to the crystalline material. First electrochemical tests revealed the clear lack of the two-phase reaction and could allow the determination of the SOC of this material from a simple OCV measurement. While here this material was only tested for its use in Li ion batteries other reports suggested that amorphous  $\text{FePO}_4$

is also a viable cathode material for  $\text{Na}^+$  and even  $\text{K}^+$  ion batteries. Its amorphous structure not only allows for much higher ionic conductivity in its lithiated state, but also allows the incorporation of much larger cations such as  $\text{K}^+$  and  $\text{Na}^+$  making it an optimal active material already suited for a possible post-lithium era.

---

*The problem of the world is that fools and fanatics are always so certain of themselves, and wiser people so full of doubts.*

— Bertrand Russell

---



## 5 Appendix

---

### 5.1. Equipment

**Incubator:** Grant-Instruments™ compact Shaker-Incubator including a P6-250 platform for Erlenmeyer flasks and a P-16-88 platform for small culture tubes.

**Autoclave:** Certoclave autoclave classic for heat sterilization

**Thermocycler:** GeneAmp PCR System(Perkin Elmer) was used as temperature controller for PCR

**Thermogravimeter:** Netzsch STA Model STA-449F1 coupled with a QMS-403C mass spectrometer

**UV-VIS spectrometer:** UV/Vis Spectrophotometer LSE-331, Model 7800 (JasCo)

**FT-IR Spectrometer:** ALPHA FT-IR platinum-ATR (Bruker)

**Centrifuge:** Sigma 2-16 KL centrifuge including rotors 12148-H and 12181

**High-energy planetary ball mill:** FRITSCH Pulverisette Premium Line 7 with gastight sealable 45 mL ZrO<sub>2</sub> beakers with ZrO<sub>2</sub> milling balls.

**Glove Boxes:** MBraun 150B-G and MBraun Labstar with Argon atmosphere; H<sub>2</sub>O and O<sub>2</sub> both below 1 ppm

**Sputter coater:** LEICA EM SCD 050 equipped with an EM QSG 100 to measure the deposited film thickness.

**Ovens:** REETZ Model LOBA 1200-45-400-1-OW tube furnace with an OMRON E5CK-T temperature regulation unit  
BÜCHI Glasoven B-585 Drying;

**Potentiostat/Galvanostat:** Multichannel VMP-3 and MPG-2 from BioLogic Science instruments

**Impedance spectrometer:** Novocontrol Concept 80 in combination with a ZGS active measurement cell.

**NMR spectrometer:** BRUKER AVANCE III 300WB with a 7 T cryomagnet

BRUKER AVANCE III Ultrashield 500WB with a 11 T cryomagnet

**Potentiostat:** PARStat MC (Princeton applied Research) including a low current interface with current resolution below the Picoampere range.

**X-ray Diffractometer:** Rigaku MiniFlex

## 5.2. Software

**WinDETA 5.73 (NOVOCONTROL):** Programme used to control the impedance spectrometer.

**HighScore X'Pert Plus (PANALYTIC):** Software package used for analysis of XRPD data and Rietveld Refinement.

**Vesta 3.4.7 (JP-Minerals):** Programme used to visualize and analyse crystal structures.

**TopSpin 3.1 (BRUKER):** Software used to control the NMR spectrometer.

**EC-Lab software V.11.30 (BioLogic):** Programme used to control the potentiostat/galvanostat.

**IGOR Pro 6.37 (WaveMetrics):** Software used to analyse data and to plot data.

**CorelDRAW Graphic suite 2019:** Graphics programme used for preparing figures for publications, posters, and presentations.

**JalView:** Programme used for sequence alignment, visualisation and analysis

**SerialCloner V.2.6 (SerialBasics):** Programme used to visualize and analyse DNA as well as for in silico cloning.

**PyMol:** Programme used for visualizing the protein sequences.

**EndNote X7.8:** Reference management software

### 5.3. List of Publications

#### Articles

##### **Glass in Two Forms: Heterogeneous Electrical Relaxation in Nanoglassy Petalite**

Gadermaier, B.; Stanje, B.; Wilkening, A.; Hanzu, I.; Heitjans, P.; Wilkening, H. M. R., The Journal of Physical Chemistry C 2019, 123, 10153-10162.

##### **Influence of defects on ionic transport in $\text{LiTaO}_3$ – a study using EXAFS and positron annihilation lifetime spectroscopy**

Gadermaier B.; Resch L.; Pickup D. M.; Hanghofer I.; Hanzu I.; Heitjans P.; Sprengel W.; Würschum R.; Chadwick A. V.; Wilkening H. M. R., Solid State Ionics (under revision)

##### **Fast Rotational Dynamics in Argyrodite-Type $\text{Li}_6\text{PS}_5\text{X}$ (X: Cl, Br, I) as Seen by $^{31}\text{P}$ Nuclear Magnetic Relaxation On Cation Anion Coupled Transport in Thiophosphates**

Hanghofer, I.; Gadermaier, B.; Wilkening, H. M. R., Chemistry of Materials 2019, 31, 4591-4597.

##### **Nuclear Spin Relaxation in Nanocrystalline $\beta\text{-Li}_3\text{PS}_4$ Reveals Low-Dimensional Li Diffusion in an Isotropic Matrix**

Prutsch, D.; Gadermaier, B.; Brandstätter, H.; Pregartner, V.; Stanje, B.; Wohlmuth, D.; Epp, V.; Rettenwander, D.; Hanzu, I.; Wilkening, H. M. R., Chemistry of Materials 2018, 30, 7575-7586.

##### **Lithium ion dynamics in $\text{LiZr}_2(\text{PO}_4)_3$ and $\text{Li}_{1.4}\text{Ca}_{0.2}\text{Zr}_{1.8}(\text{PO}_4)_3$**

Hanghofer, I.; Gadermaier, B.; Wilkening, A.; Rettenwander, D.; Wilkening, M., Dalton Transactions 2019.



**The Electronic Conductivity of Single Crystalline Ga-Stabilized Cubic  $\text{Li}_7\text{La}_3\text{Zr}_2\text{O}_{12}$  — A Technologically Relevant Parameter for All-Solid-State Batteries**

Philipp M.; Gadermaier B.; Posch P.; Hanzu I.; Ganschow S.; Meven M.; Rettenwander D.; Redhammer G. J.; Wilkening H. M. R., Advanced Materials Interfaces (under revision)

**Ion dynamics in Al-Stabilized  $\text{Li}_7\text{La}_3\text{Zr}_2\text{O}_{12}$  single crystals - Macroscopic transport and the elementary steps of ion hopping**

Posch, P.; Lunghammer, S.; Berendts, S.; Ganschow, S.; Redhammer, G. J.; Wilkening, A.; Lerch, M.; Gadermaier, B.; Rettenwander, D.; Wilkening, H. M. R., Energy Storage Materials 2019.

Unpublished manuscripts:

**Fast Li-ion dynamics in local bulk processes revealed by impedance spectroscopy in  $\text{Li}_4\text{Ti}_5\text{O}_{12}$**

Gadermaier B.; Wilkening H.M.R.

**NMR spectroscopic investigations into the  $\text{Li}^+$  dynamics of  $\text{Li}_4\text{C}_6\text{O}$**

B. Gadermaier and H. Martin R. Wilkening

**Li-ion dynamics in biotemplated amorphous  $\text{LiFePO}_4$  nanowires**

Gadermaier B.; Hanzu I.; Wilkening H.M.R.

Oral presentations at conferences & meeting

**When batteries go viral – a nanobiotechnological approach**

Gadermaier B.; Hanzu I.; Wilkening H.M.R.

European Materials Research Society: Fall Meeting, 18 – 21.09.2017, Warsaw, Poland

**When batteries go viral a bionanotechnological approach**

Gadermaier B.; Wilkening H.M.R.

DocDays 2018, 04 - 05.04.2018, Graz, Austria.

**How a virus can help to improve cathode materials**

Gadermaier B.; Hanzu I.; Wilkening H.M.R.

EUROMAT 2019: European Congress and Exhibition on Advanced Materials and Processes, 1 – 5.09.2019, Stockholm, Sweden

**Glass in two forms: heterogeneous electrical relaxation in nanoglassy petalite**

Gadermaier B.; Hanzu I.; Heitjans P.; Wilkening H. M. R.

EUROMAT 2019: European Congress and Exhibition on Advanced Materials and Processes, 1 – 5.09.2019, Stockholm, Sweden

Poster presentation at conferences & meetings

**When batteries go viral - a bionanotechnological approach**

Gadermaier B.; Hanzu I.; Wilkening H.M.R.

19<sup>th</sup> International Meeting on Lithium Batteries, 17 – 22.06.2018, Kyoto, Japan

### Awards and prices

**Best Oral Presentation Award** in Area I : Bio-based Materials at the EUROMAT 2019 for the talk  
**“How a virus can help to improve cathode materials”**

## 6 Bibliography

---

1. Zachariassen, W. H. *Journal of the American Chemical Society* **1932**, 54, (10), 3841-3851.
2. Chandra, A.; Bhatt, A.; Chandra, A. *Journal of Materials Science & Technology* **2013**, 29, (3), 193-208.
3. Jackson, R. B.; Friedlingstein, P.; Andrew, R. M.; Canadell, J. G.; Le Quéré, C.; Peters, G. P. *Environmental Research Letters* **2019**, 14, (12), 121001.
4. Lackner, M., Energy Efficiency: Comparison of Different Systems and Technologies. In *Handbook of Climate Change Mitigation and Adaptation*, Lackner, M.; Sajjadi, B.; Chen, W.-Y., Eds. Springer New York: New York, NY, 2020; pp 1-65.
5. Haruyama, J.; Sodeyama, K.; Tateyama, Y. *ACS Applied Materials & Interfaces* **2017**, 9, (1), 286-292.
6. Haruyama, J.; Sodeyama, K.; Han, L.; Takada, K.; Tateyama, Y. *Chemistry of Materials* **2014**, 26, (14), 4248-4255.
7. Kim, M.-J.; Park, J.-W.; Kim, B. G.; Lee, Y.-J.; Ha, Y.-C.; Lee, S.-M.; Baeg, K.-J. *Scientific Reports* **2020**, 10, (1), 11923.
8. Yubuchi, S.; Nakamura, W.; Bibienne, T.; Rousselot, S.; Taylor, L. W.; Pasquali, M.; Dolle, M.; Sakuda, A.; Hayashi, A.; Tatsumisago, M. *Journal of Power Sources* **2019**, 417, 125-131.
9. Fantin, R.; Trevisanello, E.; Ruess, R.; Pokle, A.; Conforto, G.; Richter, F. H.; Volz, K.; Janek, J. *Chemistry of Materials* **2021**.
10. Zaghbi, K.; Dontigny, M.; Guerfi, A.; Charest, P.; Rodrigues, I.; Mauger, A.; Julien, C. M. *Journal of Power Sources* **2011**, 196, (8), 3949-3954.
11. Ganapathy, S.; Wagemaker, M. *Nat. Energy* **2020**, 5, (6), 424-425.
12. Zachau-Christiansen, B.; West, K.; Jacobsen, T.; Atlung, S. *Solid State Ionics* **1990**, 40-41, 580-584.
13. Ryu, H.-H.; Sun, H. H.; Myung, S.-T.; Yoon, C. S.; Sun, Y.-K. *Energy & Environmental Science* **2021**, 14, (2), 844-852.
14. Li, W.; Cho, Y.-G.; Yao, W.; Li, Y.; Cronk, A.; Shimizu, R.; Schroeder, M. A.; Fu, Y.; Zou, F.; Battaglia, V.; Manthiram, A.; Zhang, M.; Meng, Y. S. *Journal of Power Sources* **2020**, 473, 228579.
15. Mauger, A.; Julien, C. M. *Batteries* **2018**, 4, (3), 39.
16. A. K. Padhi, K. S. N. a. J. B. G. *Journal of The Electrochemical Society* **1997**, 144, (4), 1188.
17. Zhu, C.; Weichert, K.; Maier, J. *Advanced Functional Materials* **2011**, 21, (10), 1917-1921.
18. Delmas, C.; Maccario, M.; Croguennec, L.; Le Cras, F.; Weill, F. *Nature Materials* **2008**, 7, (8), 665-671.

19. Malik, R.; Abdellahi, A.; Ceder, G. *Journal of The Electrochemical Society* **2013**, 160, (5), A3179-A3197.
20. Wang, J.; Sun, X. *Energy & Environmental Science* **2012**, 5, (1), 5163-5185.
21. Huria, T.; Ludovici, G.; Lutzemberger, G. *Journal of Power Sources* **2014**, 249, 92-102.
22. Gutzow, I.; Dobрева, A. *Journal of Non-Crystalline Solids* **1991**, 129, (1), 266-275.
23. Bragatto, C. B.; Cassar, D. R.; Peitl, O.; Souquet, J. L.; Rodrigues, A. C. M. *Journal of Non-Crystalline Solids* **2016**, 437, 43-47.
24. Ojovan, M. I. *Advances in Condensed Matter Physics* **2008**, 2008, 23.
25. Stebbinss Jonathan, F., Glass structure, melt structure, and dynamics: Some concepts for petrology. In *American Mineralogist*, 2016; Vol. 101, p 753.
26. Prutsch, D.; Breuer, S.; Uitz, M.; Bottke, P.; Langer, J.; Lunghammer, S.; Philipp, M.; Posch, P.; Pregartner, V.; Stanje, B.; Dunst, A.; Wohlmuth, D.; Brandstätter, H.; Schmidt, W.; Epp, V.; Chadwick, A.; Hanzu, I.; Wilkening, M., Nanostructured Ceramics: Ionic Transport and Electrochemical Activity. In *Zeitschrift für Physikalische Chemie*, 2017; Vol. 231, p 1361.
27. Dunst, A.; Sternad, M.; Wilkening, M. *Materials Science and Engineering: B* **2016**, 211, 85-93.
28. Lin, S.-S.; Liao, C.-N. *Journal of Applied Physics* **2011**, 110, (9), 093707.
29. West, A. R., *Solid state chemistry and its applications*. 2<sup>nd</sup> ed.; WILEY: 2014.
30. Kröger, F. A.; Vink, H. J., Relations between the Concentrations of Imperfections in Crystalline Solids. In *Solid State Physics*, Seitz, F.; Turnbull, D., Eds. Academic Press: 1956; Vol. 3, pp 307-435.
31. Brown, R. *The Philosophical Magazine* **1828**, 4, (21), 161-173.
32. Dependence of Diffusion on Temperature and Pressure. In *Diffusion in Solids: Fundamentals, Methods, Materials, Diffusion-Controlled Processes*, Springer Berlin Heidelberg: Berlin, Heidelberg, 2007; pp 127-149.
33. Murch, G. E.; Dyre, J. C. *Critical Reviews in Solid State and Materials Sciences* **1989**, 15, (4), 345-365.
34. Beijeren, H. v.; Kehr, K. W. *Journal of Physics C: Solid State Physics* **1986**, 19, (9), 1319-1328.
35. Compaan, K.; Haven, Y. *Transactions of the Faraday Society* **1956**, 52, (0), 786-801.
36. Metzler, R.; Jeon, J.-H.; Cherstvy, A. G.; Barkai, E. *Physical Chemistry Chemical Physics* **2014**, 16, (44), 24128-24164.
37. Dyre, J. C. *Journal of Applied Physics* **1988**, 64, (5), 2456-2468.
38. Funke, K. *Progress in Solid State Chemistry* **1993**, 22, (2), 111-195.
39. Funke, K. *Journal of Non-Crystalline Solids* **1994**, 172-174, 1215-1221.

40. Ngai, K. L. *Comments, Solid State Phys.* **1979**, *9*, (4), 127-140.
41. Habasaki, J.; León, C.; Ngai, K. L., Theories and Models of Ion Diffusion. In *Dynamics of Glassy, Crystalline and Liquid Ionic Conductors: Experiments, Theories, Simulations*, Springer International Publishing: Cham, 2017; pp 9-60.
42. Fleig, J.; Jamnik, J.; Maier, J.; Ludvig, J. *Journal of The Electrochemical Society* **1996**, *143*, (11), 3636-3641.
43. Veal, B. W.; Baldo, P. M.; Paulikas, A. P.; Eastman, J. A. *Journal of The Electrochemical Society* **2015**, *162*, (1), H47-H57.
44. Ngai, K. L.; Jonscher, A. K.; White, C. T. *Nature* **1979**, *277*, (5693), 185-189.
45. Schönhals, A.; Kremer, F., Analysis of Dielectric Spectra. In *Broadband Dielectric Spectroscopy*, Kremer, F.; Schönhals, A., Eds. Springer Berlin Heidelberg: Berlin, Heidelberg, 2003; pp 59-98.
46. Kidner, N. J.; Homrighaus, Z. J.; Ingram, B. J.; Mason, T. O.; Garboczi, E. J. *Journal of Electroceramics* **2005**, *14*, (3), 283-291.
47. Kidner, N. J.; Homrighaus, Z. J.; Ingram, B. J.; Mason, T. O.; Garboczi, E. J. *Journal of Electroceramics* **2005**, *14*, (3), 293-301.
48. M. Samet; V. Levchenko; G. Boiteux; G. Seytre; A. Kallel; Serghei, a. A. *The Journal of Chemical Physics* **2015**, *142*, (19), 194703.
49. Emmert, S.; Wolf, M.; Gulich, R.; Krohns, S.; Kastner, S.; Lunkenheimer, P.; Loidl, A. *The European Physical Journal B* **2011**, *83*, (2), 157.
50. Breuer, S.; Prutsch, D.; Ma, Q.; Epp, V.; Preishuber-Pflügl, F.; Tietz, F.; Wilkening, M. *Journal of Materials Chemistry A* **2015**, *3*, (42), 21343-21350.
51. Elliott, S. R. *Solid State Ionics* **1988**, *27*, (3), 131-149.
52. Almond, D. P.; Duncan, G. K.; West, A. R. *Solid State Ionics* **1983**, *8*, (2), 159-164.
53. Almond, D. P.; Hunter, C. C.; West, A. R. *Journal of Materials Science* **1984**, *19*, (10), 3236-3248.
54. Sidebottom, D. L. *Physical Review Letters* **1999**, *83*, (5), 983-986.
55. Francisco, B. E.; Stoldt, C. R.; M'Peko, J.-C. *The Journal of Physical Chemistry C* **2015**, *119*, (29), 16432-16442.
56. Ahmad, M. M. *Rsc Advances* **2015**, *5*, (33), 25824-25829.
57. Hairetdinov, E. F.; Uvarov, N. F.; Patel, H. K.; Martin, S. W. *Physical review. B, Condensed matter* **1994**, *50*, (18), 13259-13266.
58. Murch, G. E. *Solid State Ionics* **1982**, *7*, (3), 177-198.
59. Martin Steve, W.; Yao, W.; Berg, K., Space Charge Polarization Measurements as a Method to Determine the Temperature Dependence of the Number Density of Mobile Cations in Ion Conducting Glasses. In *Zeitschrift für Physikalische Chemie*, 2009; Vol. 223, p 1379.

60. Beaumont, J. H.; Jacobs, P. W. M. *Journal of Physics and Chemistry of Solids* **1967**, 28, (4), 657-667.
61. Tomozawa, M.; Shin, D.-W. *Journal of Non-Crystalline Solids* **1998**, 241, (2), 140-148.
62. Funke, K.; Hackenberg, R. *Berichte der Bunsengesellschaft für physikalische Chemie* **1972**, 76, (9), 883-885.
63. Stuhmann, C. H. J.; Kreiterling, H.; Funke, K. *Physical Chemistry Chemical Physics* **2001**, 3, (13), 2557-2558.
64. Denoyelle, A.; Duclot, M. J.; Souquet, J.-L. **1990**, 31, 98-102.
65. Clément, V.; Ravaine, D.; Déportes, C.; Billat, R. *Solid State Ionics* **1988**, 28-30, 1572-1578.
66. Morimoto, T.; Nagai, M.; Minowa, Y.; Ashida, M.; Yokotani, Y.; Okuyama, Y.; Kani, Y. *Nature Communications* **2019**, 10, (1), 2662.
67. Jonscher, A. K. *Journal of Physics D: Applied Physics* **1999**, 32, (14), R57-R70.
68. Funke, K.; Singh, P.; Banhatti, R. D. *Physical Chemistry Chemical Physics* **2007**, 9, (41), 5582-5590.
69. Preishuber-Pflügl, F.; Epp, V.; Nakhil, S.; Lerch, M.; Wilkening, M. *physica status solidi c* **2015**, 12, (1-2), 10-14.
70. Han, F.; Westover, A. S.; Yue, J.; Fan, X.; Wang, F.; Chi, M.; Leonard, D. N.; Dudney, N. J.; Wang, H.; Wang, C. *Nat. Energy* **2019**, 4, (3), 187-196.
71. Scherrer, P., Bestimmung der inneren Struktur und der Größe von Kolloidteilchen mittels Röntgenstrahlen. In *Kolloidchemie Ein Lehrbuch*, Springer Berlin Heidelberg: Berlin, Heidelberg, 1912; pp 387-409.
72. Langford, J. I.; Wilson, A. J. C. *Journal of Applied Crystallography* **1978**, 11, (2), 102-113.
73. Determination and Refinement of the Unit Cell. In *Fundamentals of Powder Diffraction and Structural Characterization of Materials*, Springer US: Boston, MA, 2009; pp 407-495.
74. Toby, B. H. *Powder Diffraction* **2012**, 21, (1), 67-70.
75. Rehr, J. J.; Albers, R. C. *Reviews of Modern Physics* **2000**, 72, (3), 621-654.
76. Newville, M. *Reviews in Mineralogy and Geochemistry* **2014**, 78, (1), 33-74.
77. Sayers, D. E.; Stern, E. A.; Lytle, F. W. *Physical Review Letters* **1971**, 27, (18), 1204-1207.
78. Dalba, G.; Fornasini, P. *Journal of Synchrotron Radiation* **1997**, 4, (4), 243-255.
79. Olsen, J. V.; Kirkegaard, P.; Pedersen, N. J.; Eldrup, M. *physica status solidi c* **2007**, 4, (10), 4004-4006.
80. Hofschneider, P. H. *Zeitschrift für Naturforschung B* **1963**, 18, (3), 203-210.
81. Smeal, S. W.; Schmitt, M. A.; Pereira, R. R.; Prasad, A.; Fisk, J. D. *Virology* **2017**, 500, 275-284.

82. Berkowitz, S. A.; Day, L. A. *Journal of Molecular Biology* **1976**, 102, (3), 531-547.
83. Dang, X.; Yi, H.; Ham, M.-H.; Qi, J.; Yun, D. S.; Ladewski, R.; Strano, M. S.; Hammond, P. T.; Belcher, A. M. *Nat Nano* **2011**, 6, (6), 377-384.
84. Woodall, C. A., Electroporation of *E. coli*. In *E. coli Plasmid Vectors: Methods and Applications*, Casali, N.; Preston, A., Eds. Humana Press: Totowa, NJ, 2003; pp 55-59.
85. Chan, W.-T.; Verma, C. S.; Lane, D. P.; Gan, S. K.-E. *Bioscience reports* **2013**, 33, (6), e00086.
86. Swords, W. E., Chemical Transformation of *E. coli*. In *E. coli Plasmid Vectors: Methods and Applications*, Casali, N.; Preston, A., Eds. Humana Press: Totowa, NJ, 2003; pp 49-53.
87. Mandel, M.; Higa, A. *Journal of Molecular Biology* **1970**, 53, (1), 159-162.
88. Birnboim, H. C.; Doly, J. *Nucleic acids research* **1979**, 7, (6), 1513-1523.
89. Dominy, C. N.; Andrews, D. W., Site-Directed Mutagenesis by Inverse PCR. In *E. coli Plasmid Vectors: Methods and Applications*, Casali, N.; Preston, A., Eds. Humana Press: Totowa, NJ, 2003; pp 209-223.
90. Stanje, B.; Bottke, P.; Breuer, S.; Hanzu, I.; Heitjans, P.; Wilkening, M. *Materials Research Express* **2018**, 5, (3), 035202.
91. Riess, I.; Safadi, R.; Tuller, H. L. *Solid State Ionics* **1994**, 72, 3-6.
92. Riess, I. *Solid State Ionics* **1996**, 91, (3), 221-232.
93. Tubandt, C.; Eggert, S. *Zeitschrift für anorganische und allgemeine Chemie* **1920**, 110, (1), 196-236.
94. Hebb, M. H. *The Journal of Chemical Physics* **1952**, 20, (1), 185-190.
95. Wagner, C. *The Journal of Chemical Physics* **1953**, 21, (10), 1819-1827.
96. Wagner, J. B.; Wagner, C. *The Journal of Chemical Physics* **1957**, 26, (6), 1597-1601.
97. Ohzuku, T.; Ueda, A.; Yamamoto, N. *Journal of The Electrochemical Society* **1995**, 142, (5), 1431-1435.
98. Maniwa, Y.; Ikejiri, H.; Tou, H.; Yasukawa, M.; Yamanaka, S. *Synthetic Metals* **2001**, 121, (1), 1105-1106.
99. Pontiroli, D.; Riccò, M.; Shiroka, T.; Belli, M.; Ruani, G.; Palles, D.; Margadonna, S. *Fullerenes, Nanotubes and Carbon Nanostructures* **2006**, 14, (2-3), 391-400.
100. Margadonna, S.; Pontiroli, D.; Belli, M.; Shiroka, T.; Riccò, M.; Brunelli, M. *Journal of the American Chemical Society* **2004**, 126, (46), 15032-15033.
101. Ailion, D.; Slichter, C. P. *Physical Review Letters* **1964**, 12, (7), 168-171.





## **Acknowledgement**

I would like to sincerely thank my fellow and former colleagues for their support and help and most importantly, for providing such a nice working environment. A special thank you goes to my former office colleagues, Marlena Uitz, Denise Tapler, Isabel Hanghofer and Katharina Hogrefe. It was a joy working alongside them as well as alongside Stefan Breuer, Roman Zettl, Maria Gombotz, Marina Brinek, Caroline Hiebl, Lukas Ladenstein and Veronika Pregartner. I am grateful for the interesting scientific discussions we had. At this I would like to express my gratitude to Ass. Prof. Ilie Hanzu with whom I could share my passion for discussing scientific phenomena and puzzling findings.

Last but certainly not least I would like to express my sincere gratitude to Prof. Martin Wilkening for offering me the opportunity to conduct my PhD thesis in his research group. He was an excellent supervisor and always encouraged me take a closer look. I am thankful for the many opportunities to participate at international conferences where I presented the newest findings. Furthermore, I appreciate the involvement in the various research projects where I could familiarize myself with the applied research facete of science as well as the management of such projects.

While all the work-related support was undoubtedly a significant factor making this thesis possible, the most important support was given by my family. I am especially in dept to my wife and my son which always backed me during tougher times.